$$\rho\left(\frac{\partial v}{\partial t} + v \cdot \nabla v\right) = -\nabla p + \nabla \cdot T + f$$

$$e^{i\pi} + 1 = 0$$

THÈSE DE DOCTORAT

Vortex quantiques, statistiques de la circulation de la vitesse et excitations dans la turbulence superfluide

Nicolás P. Müller

Laboratoire Lagrange, Observatoire de la Côte d'Azur

Quantum vortices, statistics of velocity circulation and excitations in superfluid turbulence

Vortex quantiques, statistiques de la circulation de la vitesse et excitations dans la turbulence superfluide

Jury

Rapporteurs

- Laurent Chevillard, Chercheur CNRS, ENS Lyon, Lyon, France
- Alessandra Lanotte, Directeur de Recherche CNR, Nanotec, Lecce, Italia

Examinateurs

- Jérémie Bec, Directeur de Recherche CNRS, MINES ParisTech, Nice, France
- Bérengère Dubrulle, Directeur de Recherche CNRS, SPHYNX Laboratory, SPEC, CEA Saclay, France
- Marco La Mantia, Associate Professor, Charles University, Prague, Czech Republic
- Katepalli R. Sreenivasan, Full Professor, NYU Tandon School of Engineering, New York, USA

Directeur de thèse

- Giorgio Krstulovic, Chercheur CNRS, Observatoire de la Côte d'Azur, Nice, France

Quantum vortices, statistics of velocity circulation and excitations in superfluid turbulence

Abstract   Superfluidity is a fascinating state of matter characterized by the absence of viscosity and the presence of topological defects with a quantized velocity circulation. These fundamental structures of the flow, also known as quantum vortices, interact and reconnect following very complex dynamics. The chaotic and disordered motion of these structures is known as quantum turbulence. They display rich multi-scale physics and some similarities with classical turbulence, such as the presence of a Kolmogorov-like energy cascade at large scales in certain regimes. Some typical examples of superfluids are Bose-Einstein condensates and superfluid helium at very low temperatures.

In this Thesis, we study numerically and analytically some statistical properties of quantum turbulence. We present a generalized Gross–Pitaevskii equation that takes into account strong and non-local interactions between bosons. In particular, this model allows us to consider the roton minimum in the excitation spectrum observed in superfluid helium. Performing extensive direct numerical simulations of this model, we address two specific problems: the study of quantum turbulence properties of the flow and the process of vortex nucleation and roton emission in the wake of an obstacle moving at different velocities.

The main scope of this Thesis is the study of velocity circulation statistics. This quantity, defined as the line integral of the velocity field around a closed loop, is a measure of the local rotation of the flow at a given scale. The goal is to characterize the intermittent nature of circulation statistics in quantum turbulence, provide a comparison with classical turbulence, and develop some analytical models to describe both systems. To achieve this, we generate and analyze data from high-resolution direct numerical simulations of three models: the Gross–Pitaevskii equation for low-temperature quantum fluids, the Navier–Stokes equations for incompressible classical fluids, and a two-fluid model for finite-temperature superfluids. We also analyze data from superfluid helium experiments. Finally, we present some preliminary studies on velocity circulation in two-dimensional quantum turbulence.

Keywords   Quantum turbulence, Superfluids, Quantum vortices, Intermittency, Velocity circulation

---

Quantum vortices, statistics of velocity circulation and excitations in superfluid turbulence

Résumé   La superfluidité est un état fascinant de la matière caractérisé par l'absence de viscosité et la présence de défauts topologiques avec une circulation de vitesse quantifiée. Ces structures fondamentales de l'écoulement, également appelées vortex quantiques, peuvent interagir et se reconnecter suivant une dynamique très complexe. Le mouvement chaotique et désordonné de ces structures est connu sous le nom de turbulence quantique. Ces structures présentent une physique multi-échelle riche et certaines similitudes avec la turbulence classique, tel que la présence d'une cascade d'énergie de type Kolmogorov à grande échelle. Quelques exemples typiques de superfluides sont les condensats de Bose-Einstein et l'hélium superfluide à très basse température.

Dans cette Thèse, nous étudions numériquement et analytiquement les propriétés statistiques de la turbulence quantique. Nous introduisons une équation de Gross–Pitaevskii généralisée qui prend en compte des interactions fortes et non locales entre les bosons. En particulier, ce modèle permet de considérer le minimum des rotons dans le spectre d'excitation observé dans l'hélium superfluide. En effectuant des simulations numériques directes, nous abordons deux problèmes spécifiques dans ce modèle : l'étude des propriétés de turbulence quantique de l'écoulement d'une part, et le processus de nucléation de vortex et d'émission des rotons dans le sillage d'un obstacle se déplaçant à différentes vitesses d'autre part.

La Thèse traite principalement de l'étude des statistiques de la circulation de la vitesse. Cette quantité, définie par l'intégrale de lignes du champ de vitesse autour d'une boucle fermée, mesure la rotation locale dans l'écoulement à une échelle donnée. L'objectif est de caractériser la nature intermittente des statistiques de circulation dans la turbulence quantique, de fournir une comparaison avec la turbulence classique et de développer des modèles analytiques pour décrire les deux systèmes. Pour ce faire, nous analysons les données de simulations numériques directes à haute résolution de trois modèles : l'équation de Gross–Pitaevskii pour les fluides quantiques à basse température, les équations de Navier–Stokes pour les fluides classiques incompressibles et un modèle à deux fluides pour les superfluides à température finie. Nous analysons également des données expérimentales obtenues avec de l'hélium superfluide. Enfin, nous présentons quelques études préliminaires sur la circulation des vitesses dans la turbulence quantique bidimensionnelle.

Mots-Clés   Turbulence quantique, Superfluides, Vortex quantiques, Intermittence, Circulation de vitesse

Acknowledgements

This manuscript is the ending point of my PhD Thesis that was carried out between 2019 and 2022 at the Observatoire de la Côte d'Azur in Nice, France, funded by the research project ANR GIANTE.

First of all and most important, I would like to thank my supervisor Giorgio Krstulovic, who gave me the opportunity to come to Nice to be his student. I felt really comfortable working with you since the first day and I appreciate your help at navigating the french burocracy since my arrival. I really appreciate your enthusiasm when we discuss about physics, and also the freedom you gave me to explore my own ideas. Your supervision during my PhD really improved me as a person and researcher. All the results achieved during this Thesis wouldn't have been possible without your guidance.

I would like to thank the all my PhD Jury members Jérémie Bec, Laurent Chevillard, Bérengère Dubrulle, Alessandra Lanotte, Marco La Mantia and Katepalli R. Sreenivasan for taking their time to read the manuscript and for their assertive and constructive feedback. I want to highlight Laurent and Alessandra who acted as referees and wrote detailed and valuable reports on the manuscript. I am also grateful to the Fluids and Plasma Turbulence Team at the Observatory, in particular to Silvio Cerri, Yannick Ponty and Emanuele Tassi for their advise during my PhD and for making days in the office more pleasant. To my office mate Vincent Labarre, thanks for the discussions we had on wave turbulence and for the many rides down from the Obs. I'd like to thank the coauthors of my papers Yuan Tang and Wei Guo, and specially to Juan Ignacio "Nacho" Polanco with whom I also enjoyed some very nice hikes around Nice. I thank Pablo Mininni who helped me get in contact with Giorgio to get this position.

During the 3 years of my PhD, I met many people that made my time in Nice really enjoyable. I would like to do a special mention to Max Mahlke and Camille Granier. We started the PhD at the same time and did this journey together, including surviving a world pandemic. I really enjoyed the time we spent together. I'd also like to thank to Julia Maia and Saburo Howard for your company at the coffee breaks when we were the only people at the Obs. Thank you Marco Raffaelli for the very nice moments we had at the French course and outside it. There is a large list of people that are also worth mentioning in this acknowledgements, and I am afraid I will probably leave someone behind, but I will try to list them all here in alphabetical order: Adrien, Chiara, Emma, Fabiola, George, Jon, Kate, Marco, Marie, Marjorie, Pablo, Pedro, Philippine, Tobias, and Umberto. I want to thank the chef of the Observatory's restaurant Khaled, who enlightened me with the subtleties of french language.

Esto también está dedicado a mi familia, que más allá de la distancia están siempre presentes para bancarme incondicionalmente. También agradecer a Flor, con quien recorrimos un camino similar pero en distintos puntos de Francia, y con quien pude compartir las ventajas y desventajas de vivir en este país lejano. Y por último, a todo ese grupo de amigos que cada vez que vuelvo a Argentina me reciben como si nunca me hubiera ido: Agus, Andy, Bren, Gon, Juanchi, Kevin, Lei, Lu, Nico, Santa y Sofi.

List of publications

Most of the results presented in this manuscript have been published in different peer-reviewed journals. These publications are integrally reported throughout the manuscript.

P1 - N. P. Müller, and G. Krstulovic, Kolmogorov and Kelvin wave cascades in a generalized model for quantum turbulence, *Physical Review B* **102**, 134513 (2020).
https://doi.org/10.1103/PhysRevB.102.134513 [MK20]

P2 - N. P. Müller, J. I. Polanco, and G. Krstulovic, Intermittency of Velocity Circulation in Quantum Turbulence, *Physical Review X* **11**, 011053 (2021).
https://doi.org/10.1103/PhysRevX.11.011053 [MPK21]

P3 - J. I. Polanco, N. P. Müller, and G. Krstulovic, Vortex clustering, polarisation and circulation intermittency in classical and quantum turbulence, *Nature Communications* **12**, 7090 (2021).
https://doi.org/10.1038/s41467-021-27382-6 [PMK21]

P4 - N. P. Müller, and G. Krstulovic, Critical velocity for vortex nucleation and roton emission in a generalized model for superfluids, *Physical Review B* **105**, 014515 (2022).
https://doi.org/10.1103/PhysRevB.105.014515 [MK22]

P5 - N. P. Müller, Y. Tang, W. Guo, and G. Krstulovic, Velocity circulation intermittency in finite-temperature turbulent superfluid helium, *Physical Review Fluids* **11**, 011053 (2022).
https://doi.org/10.1103/PhysRevFluids.7.104604 [MTG$^+$22]

Note that this is the chronological order in which they were published, but it is not necessarily the same order in which they are presented in this Thesis.

Contents

Introduction

Superfluidity is a fascinating state of matter characterized by a fluid with zero viscosity. This phenomenon is typically observed at temperatures close to the absolute zero, when quantum effects dominate the properties of fluids. Some examples are liquid ^{4}He below the critical temperature 2.17 K [Don91], liquid ^{3}He below the millikelvins [Leg04], and Bose–Einstein condensates (BEC) of ultracold atoms typically at temperatures below 10 μK [PS16; PS08]. Nowadays, there are other systems that manifest superfluid properties that can be found at higher temperatures, as quantum fluids of light in non-linear media at room temperature [CC13] and it is theorized that it can take place at the core neutron stars at temperatures up to 10^{10} K [PA85]

In the 1920s, it was observed that the liquid state of ^{4}He exists in two states: a high temperature phase called helium I, and a low temperature state originally called helium II. The transition between these two phases takes place at the critical temperature $T_\lambda = 2.17$ K at saturated vapour pressure, known as lambda point due to the shape of the specific heat anomaly at T_λ [Don91]. The first phase was obtained experimentally in 1908 when helium was first liquefied below the boiling temperature of 4.2 K [Onn08], at which helium behaves like an ordinary viscous fluid. Helium is the only chemical element that exists in a liquid state at extremely low temperatures at standard pressure, being the ideal framework to study low-temperature fluids. In 1938, it was first observed by Kapitza and independently by Allen and Misener that below the lambda point, the viscosity of helium II decreases abruptly [Kap38; AM38]. Kapitza named this phase superfluidity by analogy with superconductors. Due to its very low viscosity values, superfluid helium exhibits some fascinating behaviors, like the fountain effect [AM38], the creeping effect [RS39], and it can leak through porous media that ordinary fluids are not able to pass through [MZ68]. Based on these observations, Tisza and Landau developed a two-fluid model to describe the phenomenology of superfluid ^{4}He [Tis38; Lan41]. They proposed that helium II at finite temperatures can be described as a mixture of two fluids: a normal component that behaves as an ordinary viscous fluid whose density vanishes at zero temperature, and an irrotational superfluid component with zero viscosity and entropy whose density vanishes above T_λ. The dynamics of these two fluids is coupled by a mutual friction, proportional to the velocity difference between both components, called counterflow. This model predicts the propagation of density-pressure waves, known as first sound, and an exotic kind of waves given by temperature-entropy fluctuations, known as second sound, with the entropy carried completely by the normal component [LL87].

In 1938, London suggested that the transition observed in superfluid ^{4}He around the lambda point might be a manifestation of BEC, establishing a connection between both phenomena [Lon38]. The history of BECs dates back to 1924, when Bose and Einstein developed the statistical description of a non-interacting gas of bosons [Bos24; Ein25]. They predicted the occurrence of a phase transition at low temperatures, associated with the condensation of atoms in the state of lowest energy, a phenomenon resulting from the quantum nature of bosons. The experimental realization of a BEC was achieved in 1995 in dilute atomic gases trapped by magnetic

fields [AEM$^+$95; DMA$^+$95], leading to great advances in the study of quantum gases, quantum optics and condensed-matter physics [Leg01; BDZ08]. The macroscopic occupation of the ground state leads to a long-range correlation, and the condensate can be described by a macroscopic complex field that acts as an order parameter.

Contrary to the paradigm of classical flows, in which vortices have finite sizes, Lars Onsager and Richard Feynman proposed that vorticity can be concentrated in lines as topological defects of this order parameter [Ons49; Fey55]. The circulation around these topological defects, given by the line integral of the velocity field around a closed loop, is discrete and proportional to h/m, with m the mass of the bosons and h Planck constant. The vorticity is thus concentrated along lines known as quantum vortices. The typical core size of these peculiar structures in superfluid ^{4}He is about 1 Å, while in BECs is typically about 1 μm [TTC$^+$16]. The first experimental evidence of quantum vortices in superfluid helium was achieved by Hall and Vinen in 1956 [HV56], with the first images obtained in 1974 [WP74], and directly visualized in 2006 using solidified hydrogen particles and particle tracking velocity techniques [BLS06].

In classical three-dimensional (3D) fluids, vortices have a different nature as the circulation around them takes continuous values. The non-linear interaction between vortices and eddies might lead to a complex and chaotic spatiotemporal dynamics, known as turbulence. This phenomenon is found in a wide variety of systems in nature, going from the air circulating in our lungs to the interstellar media. One of the main properties of 3D turbulence is the existence of the Richardson cascade, in which energy is transferred from large to small scales until it reaches the viscous scales where it is dissipated as heat. This phenomenon is also known as direct energy cascade. In 1941, under the assumption of self-similarity, Kolmogorov proposed a theory for 3D turbulence (known as K41) that describes the moments of velocity increments [Kol41]. He derived the famous four-fifths law, an exact relation for the third order moment of velocity increments in 3D homogeneous isotropic turbulence (HIT) [MYL81]. The K41 phenomenology appears to describe successfully some of the statistical properties in the so-called inertial range of scales, taking place at scales much larger than viscous scale and smaller than the integral scale. However, it was later argued that the self-similar hypothesis is broken due the intermittent nature of turbulent flows, in the sense that for some periods of time and in some regions of the flow, the velocity fluctuations may take some extreme values [Vas15; Dub19]. Intermittency has been studied on the basis of some phenomenological assumptions, like multifractality and energy cascades [Fri95], but there is still a lack of first-principles theoretical framework able to describe the dynamics 3D turbulence, being sometimes called the oldest unsolved problem in classical physics.

Turbulence can also take place in superfluids despite their lack of viscosity, and is currently one the main research topics in superfluid ^{4}He and BECs [VN02; TTC$^+$16]. This phenomenon leads to the development of non-linear interactions between quantum vortices, such as reconnections, consisting of two vortex filaments that approach to each other, touch at one point and then separate, changing the topology of the flow [ZCB$^+$12; GBP$^+$19]. Quantum vortices also support the presence of helical displacements that propagate along them, known as Kelvin waves [FMO$^+$14]. Both of these interactions redistribute the energy in the system and excite sound waves. The phenomenology of quantum turbulence is very rich, showing fundamental differences as well as quantitative connections with classical turbulence [BSS14]. For instance, the large-scale dynamics of superfluid turbulence in certain regimes exhibits Kolmogorov turbulence, with a direct energy cascade and a same power law for the energy spectrum than classical turbulent flows [MT98; NAB97a]. For this reason,

there is a great interest in the study of quantum fluids. The presence of vortices as topological defects may be useful to the development of analytical theories for quantum turbulence, that might also be applied in classical turbulence. At small scales, the phenomenology differs due to the quantum nature of vortices and the presence of Kelvin waves [CMB17]. At finite temperatures, counterflow-driven turbulence develops anisotropies at small scales, leading to a quasi-2D flow [BKL+19a; PK20a].

The motion of superfluids is very complex due to the different temperature regimes and the large scale separation at play, which in superfluid ^{4}He can reach up to 10 decades between the largest scale of the flow and the vortex core size [RBD+14]. Therefore, there is no unique theoretical framework able to capture the complete dynamics of the system. For instance, to describe the large-scale dynamics of superfluid ^{4}He at finite temperatures, one can use a two-fluid description, for instance the well-known Hall-Vinen-Bekarevich-Khalatnikov (HVBK) model [HV56; BK61]. Here, the superfluid vorticity is coarse-grained at large scales, losing thus the notion of quantized circulation and valid only at large scales. Nevertheless, this model is useful for the study of finite temperature effects, counterflow, quantum turbulence and the interaction between particles and the superfluid [Don91; VN02; GML+14].

Another model that is valid at intermediate scales is the vortex filament model (VFM) [Sch85; Sch88]. Here, the low-temperature dynamics of the superfluid is governed by a collection of mutually-interacting vortex lines, where the velocity field of each vortex is prescribed by the Biot-Savart law. It is necessary to introduce a cut-off at the scale of the vortex core to avoid divergences of the velocity field. Thus, this model describes the dynamics of vortex filaments when the radius of curvature of vortices is larger than their core size. Reconnections are not naturally captured by this model, and they have to be included implementing some *ad hoc* mechanisms. At finite temperatures, it can be coupled with a normal velocity field, introducing some dissipation mechanisms in the flow. Thus, this model is very popular for theoretical and numerical studies of superfluid turbulence at large scales and Kelvin wave turbulence [ATN02; BDL+11; BLB12].

The HVBK and the vortex filament models are based on phenomenological assumptions, like the two-fluid description, and the existence of quantized vortices with *ad hoc* mechanisms for reconnection. A first-principles approach very popular for the study of BECs is the Gross–Pitaevskii (GP) equation, a non-linear Schrödinger equation (NLSE) that describes the dynamics of a weakly interacting gas of bosons at zero temperature. This microscopic model is based on the idea that at very low temperatures, there is a macroscopic occupation of the energy ground-state energy and the condensate can then be described by a macroscopic wavefunction. This complex field acts as the superfluid order parameter and captures the existence of quantum vortices as topological defects having quantized circulation. Indeed, this model was original derived by Gross and Pitaevskii to study the properties of quantum vortices [Gro61; Pit61]. The GP equation allows an hydrodynamic description of the condensate, connecting it with a compressible, barotropic, irrotational, and inviscid fluid. As it naturally describes the dynamics of quantum vortices, it is the ideal framework for the study of low-temperature quantum fluids, quantum vortex reconnections, Kelvin waves and quantum turbulence. In particular, it is expected to provide a good qualitative description of superfluid ^{4}He, even though the interaction between bosons in this system is strong. Moreover, the GP equation is not able to capture some of the properties of superfluid ^{4}He such as rotons, an elementary excitation that manifests as a minimum in the dispersion relation, and is only valid at zero temperature.

The GP equation is in particular the main model I used to obtain most of the

results reported in this manuscript for the study of quantum vortices and quantum turbulence. In particular, I study the properties of a generalized GP (gGP) model that admits rotons and that considers strong interactions between bosons in an attempt to provide a more realistic approach of superfluid ^{4}He. This model is based on phenomenological assumptions and has been used to study the dynamics of rotons, quantum vortices and reconnections [PR93; BR99; RSC18]. During this Thesis, I addressed different specific problems to study the statistical properties of quantum turbulence in 3D superfluids. To focus on this phenomenon, I performed extensive direct numerical simulations (DNS) of different superfluid models and realized different analytical treatments. The DNS of the GP model are performed using the parallel code "FROST" (Full solveR Of Superfluid Turbulence), that implements a pseudo-spectral scheme to solve partial differential equations in periodic domains, and a fourth-order Runge Kutta method for the time stepping. In particular, I implemented an hybrid openMP-MPI version of the code, which allowed me to perform high-resolution DNS in national clusters like Jean-Zay and Occigen using more than 8000 CPUs. I also analyzed data from numerical simulations of the incompressible Navier–Stokes (NS) and the two-fluid HVBK equations. These simulations were performed in my group for the specific problem I had to address. Thus, with the GP and HVBK models I have been able to compare different temperature regimes and length scales of quantum turbulence, and also with classical turbulence provided by the NS equations. I also had the chance to analyze data from dedicated experimental runs in superfluid ^{4}He, carried out by collaborators in Tallahassee, Florida.

The present manuscript is structured in five chapters. The first two are introductory chapters, in which I present the fundamental concepts of superfluids and turbulence. The other three chapters correspond to the main body of this manuscript, in which I present the main original results carried out during this Thesis. In particular, I address different properties of quantum turbulence, focusing mostly on Kolmogorov and Kelvin-wave turbulence, vortex nucleation and intermittency of velocity circulation.

In chapter 1, I first review the phenomenology of superfluid helium, and introduce the main notions of Bose–Einstein condensation in an ideal Bose gas using tools of statistical mechanics. The main body of this chapter is devoted to the derivation of the mean-field Gross–Pitaevskii equation and to provide a complete description of the properties of quantum fluids, including the conserved quantities in this system, the hydrodynamic description, quantum vortex solutions, and the effects of beyond mean-field corrections. I also describe the vortex filament and the two-fluid HVBK models, and provide a brief review of Kelvin waves and quantum vortex reconnections.

Chapter 2 is devoted to reviewing the phenomenology and the main results in classical and quantum turbulence. I first introduce the main notions of fluid dynamics, presenting the incompressible Navier–Stokes equations, the concept of turbulence and the balance equations. I present the Kolmogorov picture of turbulence based on the notion of Richardson cascade, and discuss the different hypotheses of this theory. I include a derivation of exact results obtained from the Navier–Stokes equations, such as the four-fifths law. Then, I present the phenomenology of quantum turbulence, including the different regimes that can be found in superfluids. Finally, I review the main concepts of intermittency, where I discuss the notions of fractal dimensions and introduce the monofractal and multifractal models. I also present a small discussion on the intermittency of velocity circulation.

Then, I start presenting the main results obtained during this Thesis. In chapter 3, I discuss the general properties of quantum turbulence in a model with rotons. I first motivate and describe the phenomenology of low temperature quantum turbulence, emphasizing on direct numerical simulations. Here, I present the generalized Gross–Pitaevskii model, in which I consider a non-local interaction potential between bosons that is chosen to reproduce the roton minimum in the excitation spectrum of superfluid ^{4}He, and a high-order non-linear term that represents strong interactions [BR99] or quantum fluctuations through beyond mean-field corrections [LHY57; DGP$^+$99]. This last term is also useful to mitigate the development of instabilities that lead to a crystallization state in which the background superfluid vanishes. In publication [MK20], I first verify that the introduction of the roton minimum modifies the density profile of quantum vortices, exhibiting some well-known modulations around the ground state [BR99; RSC18]. In a quantum turbulent regime, the system still reproduces Kolmogorov turbulence, showing that the introduction of rotons and beyond mean-field corrections do not modify the phenomenology of the flow at large scales. At small scales, however, there is an enhancement of the Kelvin-wave cascade, and we observe a good agreement with the weak-wave turbulence prediction for Kelvin waves. The simultaneous observation of these two energy cascades is a challenging task as it requires a large scale separation in the flow, achieved by high-resolution DNS.

Chapter 4 is devoted to the study of velocity circulation statistics in classical and quantum turbulence, and I present three articles [MPK21; PMK21; MTG$^+$22]. I first start the chapter with a motivation and a brief historical review of velocity circulation statistics, where I discuss some theoretical and numerical results. I include a discussion and comparison between velocity increments and circulation moments. The first publication [MPK21] is devoted to the study of velocity circulation moments in quantum turbulence described by the generalized GP equation, in which vortices naturally account for a discretized circulation. Using high-resolution DNS, we show that the statistical behavior of velocity circulation at small scales strongly differs from classical turbulence, exhibiting a highly intermittent scaling due to the discrete nature of quantum vortices. More strikingly, at large scales both systems display a very similar behavior, with the same anomalous deviations in the scaling exponents of circulation moments. This is particularly surprising as the NS and the GP equations have different mathematical structures. Motivated by these results, in publication [PMK21] we propose a discrete Markovian model for circulation in which the moments scaling depends on the polarization of vortices, recovering K41 theory for a partial polarization. We also develop an algorithm that identifies the position and orientation of each quantum vortex, and analyze the distribution of vortices. We show that the number of vortices inside a loop and the coarse-grained energy dissipation are related, and therefore both display a log-normal distribution [Dub19]. We propose that the intermittent behavior of velocity circulation can be understood as a composition of two effects: a partial polarization between vortices leading to K41 scaling, and a complex spatial distribution of vortices responsible for the intermittent nature of turbulence. In the last publication of this chapter [MTG$^+$22], I analyze the circulation statistics obtained from experimental data of superfluid ^{4}He at two different temperatures, provided by the group of Wei Guo in Tallahassee. I show that intermittency of circulation in turbulent superfluid ^{4}He is similar to classical fluids, and is independent of temperature. I also analyze data from numerical simulations of the coarse-grained HVBK equations at temperatures between 1.3 K and 2.1 K performed in my group. We provide a more detailed analysis on the temperature

dependence and on high-order moments. Again, the numerical data exhibit no temperature dependence, and scaling exponents compatible with GP and NS numerical simulations. These results suggest that circulation intermittency in superfluid ^{4}He is temperature independent on one side, and that the intermittent properties of quantum and classical turbulence share similarities on the other side, consistent with previous experimental observations [RCS$^+$17]. Along this chapter, I also report the low-order moments of velocity circulation in the generalized GP model, I compare the circulation statistics between the standard and generalized GP models, and provide further properties of the Markovian model. At the end of this chapter, I report some preliminary results on velocity circulation in two-dimensional quantum turbulence, focusing on the inverse energy cascade and the direct enstrophy cascade.

Finally, in chapter 5, I present the last publication [MK22] where I study the process of vortex nucleation in the gGP model. I first discuss the Landau criterion for superfluidity, which states that there is a critical velocity above which a moving impurity would perturb the flow creating some elementary excitation slowing the obstacle down. In a weakly-interacting BEC this critical velocity is given by the speed of sound, while in superfluid ^{4}He it is given by the velocity of roton propagation, which is smaller than the speed of sound by a factor 4. However, this criterion does not consider the possibility of vortex nucleation, that takes place for slower velocities in the wake of a moving obstacle [FPR92; HB97]. Implementing a Newton-Raphson method of the gGP model in two dimensions, I characterize the bifurcation diagrams of stable and unstable stationary solutions of the flow with an obstacle of different sizes moving at different velocities. For large obstacles sizes, I show that the critical velocity for superfluidity in the gGP and the standard GP models results from the process of vortex nucleation, recovering similar values for this velocity in both cases. For small obstacles sizes, the critical velocity in the gGP model is given by the rotons velocity, provided by Landau criterion, and differing from the standard GP model where the critical velocity is still determined by the process of vortex nucleation. I also show that in three dimensions the results are qualitatively the same.

At the end of the manuscript, I present some further concluding considerations of this Thesis and provide some outlook and perspectives.

Chapter 1

Superfluidity and Bose–Einstein condensation

In this chapter, we introduce the fundamental notions of quantum fluids. We first introduce the phenomenology of superfluid helium, one of the greatest exponents of superfluidity, a fascinating state of matter characterized by the lack of viscosity. We also present the phenomenon of Bose–Einstein condensation in the case of a non-interacting boson gas using statistical mechanics, and provide a link with superfluidity. We then derive the Gross–Pitaevskii equation, a mean-field model for weakly interacting bosons at very low temperatures, framework in which most of the work of this Thesis is carried out. We introduce the main properties of this model, such as its hydrodynamical picture, the elementary excitations taking place in condensates, and the physics of quantum vortices, one of the most interesting features of superfluids and key ingredient in quantum turbulence. We then discuss the different models there are to describe the motion of superfluids, like the vortex filament model, based on the dynamics of individual vortex lines, and the two-fluid fluid model. Finally, we introduce the main interactions taking place between vortices, such as reconnections and Kelvin waves.

1.1   Superfluid helium

Helium is the only chemical element in nature that can not be solidified at normal atmospheric pressure. Indeed, it becomes liquid at the very low temperature of 4.2 K. Its normal liquid state, known as He I, was first observed by Kamerlingh Onnes in 1908, who was awarded by the Nobel prize in 1913 [Onn08]. In the 1920s, it was found that when liquid helium is cooled down below temperatures around 2.3 K, it changed to an unusual form named He II. In 1938, Kapitza [Kap38] and Allen and Misener [AM38] realized that below the so-called lambda-point temperature $T_\lambda = 2.17$ K, liquid helium undergoes through a phase transition into a regime that they called superfluid helium due to the abrupt drop in the fluid viscosity. This observation and further studies in low-temperature physics led Pyotr Kapitza to the Nobel Prize in 1978.

The phase diagram of liquid helium is shown in Fig. 1.1 (a), where the transition between He I and He II is shown. Note that helium solidifies only at pressures above 25 bar. The critical temperature at which this transition takes place at saturated vapour pressure is called lambda point due to the shape of the specific heat transfer curve near this temperature, where it presents a strong peak (Fig. 1.1 (b)). The physical transition is shown in Fig. 1.2. At a temperature above the lambda point and below the boiling point, helium is in a normal liquid state. When it is cooled down to the lambda point, it starts boiling and after it crosses the transition it
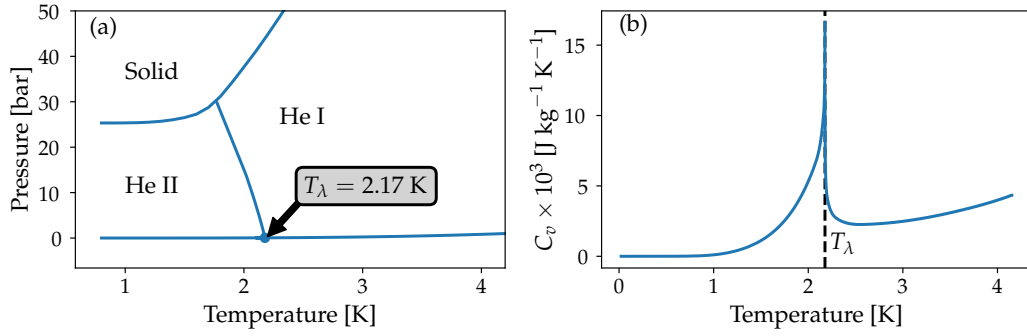
Figure 1.1: Properties of liquid helium. Data extracted from [DB98]. (a) Phase diagram of liquid helium showing the lambda-point temperature and the transition between He I and He II. (b) Heat capacity at constant volume of liquid helium across the lambda point.
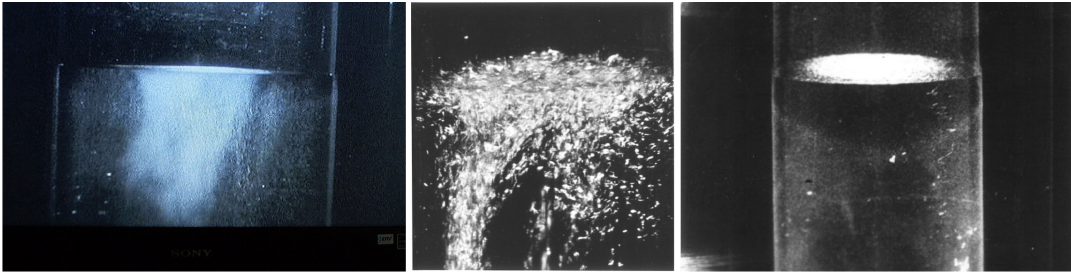
Figure 1.2: Visualization of the transition from He I to He II. (a) He I at 4.2 K and 1 bar. (b) He I close to the lambda point temperature $T_\lambda = 2.17$ K. (c) He II below 2.17 K. Extracted from Wikimedia Commons, the free media repository.

becomes still. The boiling process below the lambda point stops as the thermal conductivity increases abruptly and the heat is transferred so quickly that vaporization only takes place on the free surface.

Superfluidity is a fascinating quantum phenomenon that leads to spectacular macroscopic effects, like the fountain effect [AM38], the creeping effect [RS39], and the leak through a porous medium [MZ68]. In 1938, London suggested that superfluid helium is a manifestation of the Bose–Einstein condensation process [Lon38], taking place in weakly interacting Bose gases (see Sec. 1.2). Based on this idea and motivated by all these observations, Tisza and Landau proposed in 1941 the two-fluid model for superfluid helium [Tis38; Lan41]. This model proposes that He II can be regarded as a mixture of a normal viscous fluid and an inviscid superfluid component with a total density ρ [Don91]

$$\rho = \rho_{\mathrm{n}} + \rho_{\mathrm{s}}, \tag{1.1}$$

with ρ_{n} and ρ_{s} the normal and superfluid densities, respectively. The density fraction of each fluid component depends on temperature T, with the normal component vanishing at zero temperature, and the superfluid component vanishing above the lambda point. Their experimental values are shown in Fig. 1.3 (a). The dynamics of both fluids is coupled by a mutual friction force that transfers momentum between each component in both ways.

As in many other fluids, superfluid helium supports the propagation of pressure-density waves, known as first sound, that travel at a speed of 238 ms^{-1}. As a consequence of the quantum mechanical nature of superfluid helium, the system allows

also the propagation of entropy-temperature waves, known as second sound, and whose speed strongly depends on temperature. In particular, it goes to zero at temperatures above the lambda point, meaning that classical fluids do not support the propagation of second sound. For more details on the two-fluid model, see Sec. 1.3.3.

Another important flow predicted by this model is the thermal counterflow. Let us consider a superfluid container attached to a heat source on one end and closed at the other end. When a heat flux q is applied into the system, the normal component will start to carry the heat away from the source at an average speed $v_n = q/(\rho s T)$, with T the temperature of the heater and s the entropy per unit of mass. As there is no total momentum in this experiment $\mathbf{j} = \rho_s \mathbf{v}_s + \rho_n \mathbf{v}_n = 0$, the superfluid component $\mathbf{v}_s$ will start moving in the opposite direction with respect to the normal fluid, towards the heat source, generating thus a counterflow. If the heat flux is large enough, the coupling between both components becomes important due to mutual friction, entering a regime of counterflow superfluid turbulence, as will be discussed in chapter 2.

This model can also predict the macroscopic phenomena mentioned before. For instance, as a consequence of the lack of viscosity of the superfluid component, He II can form liquid layers thin enough that can flow through porous media that a classical viscous fluid could not, and also it can creep out the walls of a container beating the gravitational force. On the other hand, the fountain effect can be explained as a thermo-mechanical effect. When the superfluid is heated, the expansion pushes up the free surface of the liquid through a long capillary forming a fountain.

In Landau's theory of superfluidity, helium is composed by an irrotational, inviscid fluid with thermal excitations coming from the normal fluid. If the temperature is low enough to be able to neglect the normal fluid and viscous effects, then a moving object would experience no drag force. Landau proposed that there exists a critical velocity below which this is true, and above which it would generate some elementary excitations in the superfluid carrying an energy $\epsilon_\mathbf{p}$ and a momentum $\mathbf{p}$, and superfluidity would break down. This is known as Landau's criterion for superfluidity. Let us consider a superfluid moving at a constant velocity $\mathbf{u}$ along a pipe. The process of spontaneous creation of an excitation is possible only if it is energetically favorable, that is, if the excitation energy in the laboratory frame of reference is negative

$$\epsilon'_\mathbf{p} = \epsilon_\mathbf{p} + \mathbf{p} \cdot \mathbf{u} < 0, \tag{1.2}$$

which leads to the critical velocity

$$u_c = \min_\mathbf{p} \left(\frac{\epsilon_\mathbf{p}}{|\mathbf{p}|} \right). \tag{1.3}$$

As a consequence, an impurity moving above this critical velocity starts to generate elementary excitations in the flow. The excitation spectrum of superfluid helium is thus relevant for the definition of the critical velocity. Figure 1.3 (b) shows the excitation spectrum of superfluid helium obtained experimentally by inelastic scattering of neutrons. For small wavenumbers, there is a linear relation between the energy and the wavenumber $\epsilon_p = c_s p$, related with phonon excitations, and whose slope is proportional to the speed of sound of superfluid helium $c_s = 238 \text{ ms}^{-1}$. Around $k \approx 20 \text{ nm}^{-1}$, the excitation spectrum exhibits a minimum known as *roton minimum*, associated to roton excitations, that may be approximated by

$$\epsilon_\mathbf{p} = \Delta + \frac{(p - p_0)^2}{2m^*}, \tag{1.4}$$
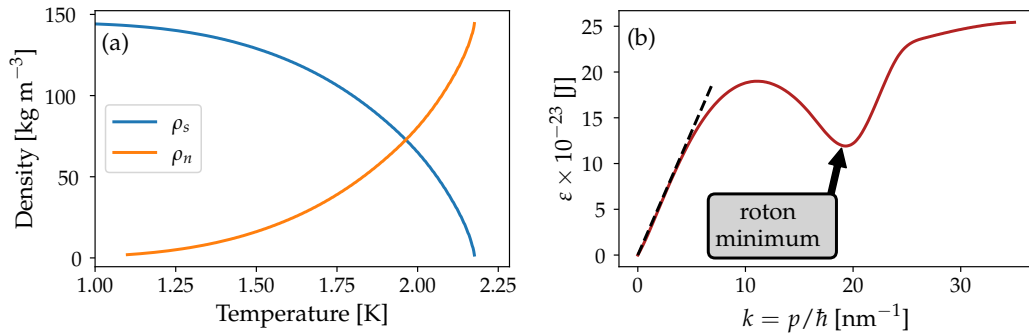
Figure 1.3: Experimental measurements in superfluid helium extracted from [DB98]. (a) Normal fluid and superfluid densities as a function of the temperature. (b) Excitation spectrum as a function of the wavenumber. The slope of the black dashed line is related with the speed of sound $c = 238$ ms^{-1}.

where p_0 is the momentum of the roton minimum and m^* a constant with mass dimensions. Landau's criterion for superfluidity in He II is given by the roton minimum in the excitation spectrum and corresponds to a critical velocity of $v_c \approx 60$ ms^{-1} which is approximately $c_s/4$. In other superfluid systems the excitation spectrum might be different, leading to a different critical velocity. For instance, in Bose–Einstein condensates (treated in Secs. 1.2 and 1.3), the dispersion relation is monotonically increasing and the critical velocity is given by the speed of sound of the gas.

Further discussions on elementary excitations in superfluids are presented in chapter 5, where I introduce the publication [MK22] where I study the critical velocity at which vortex nucleation and roton emission take place in a generalized Gross–Pitaevskii model.

1.2   Bose gases and Bose–Einstein condensation

In this section we will introduce the quantum statistical description of an ideal Bose gas [PS16; PB11; Hua87]. This theory was originally developed by Bose (1924) and Einstein (1924, 1925), who stated that in low-temperature regimes, a non-interacting Bose gas could "surpass" a transition to a condensate state. In this phase, there is a macroscopic occupation of the ground state, which is not observed in classical gases [Bos24; Ein25]. In 1938, London suggested that the transition between He I and He II around the lambda-point temperature might be a manifestation of a Bose–Einstein condensation (BEC) [Lon38]. The first experimental observation of a BEC was realized in 1995, and led to the attribution of the Nobel Prize in 2001 to Eric A. Cornell, Wolfgang Ketterle and Carl E. Wieman [AEM$^+$95; DMA$^+$95].

Let us consider a gas of N identical particles of mass m at a temperature T, each of them moving at a velocity v_i. In the thermodynamic limit, we can assume that in average there is an equipartition of kinetic energy

$$E_{\text{kin}} = \frac{1}{2}m\langle v^2 \rangle = \frac{\langle p^2 \rangle}{2m} = \frac{3}{2}k_{\text{B}}T, \tag{1.5}$$

where k_{B} is the Boltzmann constant and $p = mv$ is the particles momentum, that can also be related to the de Broglie wavelength $p = h/\lambda_{\text{dB}}$, with h Planck's constant.

We can thus obtain a mean value of the wavelength of the particles at a temperature T

$$\lambda_{\text{dB}}(T) = \frac{h}{\sqrt{3mk_{\text{B}}T}}. \tag{1.6}$$

For a system with a particles density $n = N/V$ we can define the inter-particle distance as $d = n^{-1/3}$. In the limit of de Broglie wavelength much smaller than the inter-particle distance $\lambda_{\text{dB}} \ll d$ usually recovered at high temperatures, particles can be considered as points and the system can be considered as a classical gas following a Maxwell-Boltzmann distribution. However, in the limit $\lambda_{\text{dB}} \sim d$ (low temperatures), there is an overlap between the particles wavelength, and quantum effects become important. In this limit, one can obtain a first approximation of the critical temperature at which this transition takes place as

$$T_{\text{c}} = \frac{4\pi^2\hbar^2}{3mk_{\text{B}}}n^{2/3}. \tag{1.7}$$

If we take some typical parameters for superfluid helium like $m = 6.65 \times 10^{-24}$ g and $n = 2.18 \times 10^{22}$ cm^{-3}, together with $\hbar = 1.05 \times 10^{-27}$ g cm^2 s^{-1} and $k_{\text{B}} = 1.38 \times 10^{-16}$ g cm^2 s^{-2} K^{-1}, we obtain a critical temperature of $T_c = 3.96$ K, which is a good first estimation of the lambda point temperature in superfluid helium $T_\lambda = 2.17$ K, considering that we only used equipartition of energy. In the following section, we will use statistical mechanics to provide a formal description of a Bose gas and the transition to a Bose–Einstein condensate.

1.2.1 Statistical description in the grand canonical ensemble

In the grand canonical ensemble, the probability of having a system of N particles in a volume V with an energy ε is

$$\mathcal{P}_N(\varepsilon) = \frac{z^N e^{-\beta\varepsilon}}{Z(\beta, z, V)} \tag{1.8}$$

where $z = e^{\beta\mu}$ is the fugacity with μ the chemical potential and $\beta = 1/k_{\text{B}}T$. The grand canonical partition function is defined as

$$Z(z, V, T) = \sum_{N=0}^{\infty} z^N \mathcal{Q}_N(V, T), \tag{1.9}$$

with $\mathcal{Q}_N(V, T) = \sum_\varepsilon e^{-\beta\varepsilon}$ the canonical partition function. The natural variables of the grand canonical ensemble are temperature, chemical potential and volume of the system. For an ideal Bose gas, in which each particle does not interact with each other having a Hamiltonian $h_i = p_i^2/(2m)$, the grand canonical partition function can be expressed as a product of different energy states

$$Z(z, V, T) = \prod_\varepsilon \frac{1}{1 - ze^{-\beta\varepsilon}}. \tag{1.10}$$

This partition function represents the statistical ensemble of all possible states of a non-interacting Bose gas in thermodynamical equilibrium. All thermodynamical quantities of the system can be obtained from it, like the equation of state, the total number of particles or the total energy respectively as

$$\frac{PV}{k_{\mathrm{B}}T} = \ln Z = -\sum_{\varepsilon} \ln(1 - z e^{-\beta\varepsilon}), \tag{1.11}$$

$$N = \sum_{\varepsilon} n_{\varepsilon} = -\sum_{\varepsilon} \frac{\partial}{\partial(\beta\varepsilon)} \ln Z = \sum_{\varepsilon} \frac{1}{z^{-1}e^{\beta\varepsilon} - 1}, \tag{1.12}$$

$$E = \sum_{\varepsilon} n_{\varepsilon}\varepsilon = \sum_{\varepsilon} \frac{\varepsilon}{z^{-1}e^{\beta\varepsilon} - 1}. \tag{1.13}$$

Here, P is the total pressure of the gas. The number of particles N is a strictly positive quantity, so it provides the physical constraint $z^{-1}e^{\beta\varepsilon} > 1$. In particular, this means that the energy of the ground state has to be larger than the chemical potential $\varepsilon_0 > \mu$. For free particles, $\varepsilon_0 = 0$ so the chemical potential is strictly negative. If the chemical potential approaches the ground state energy, then the occupation number of the ground state

$$N_0 = \frac{1}{z^{-1}e^{\beta\varepsilon_0} - 1} \tag{1.14}$$

increases exponentially. This macroscopic occupation into a single state $\varepsilon = 0$ leads to the phenomenon of Bose–Einstein condensation. Therefore, it is convenient to write the total number of particles as

$$N = N_0 + N_{\mathrm{exc}}, \tag{1.15}$$

with $N_{\mathrm{exc}} = \sum_{\varepsilon \neq \varepsilon_0} n_{\varepsilon}$ the occupation number of excited states.

In the thermodynamic limit of large volume $V = L^3$, the discrete energy levels provided by the free particle hamiltonian $H = p^2/(2m)$ can be approached as a continuous quantity. The momentum also satisfies the relation $|\mathbf{p}| = \hbar k = 2\pi n\hbar/L$ with n an integer. Then, the summation in the continuous limit becomes $\sum_{\mathbf{p}} \to V/(2\pi\hbar)^2 \int \mathrm{d}^3p$. Using isotropy and the transformation $p^2 = 2mk_{\mathrm{B}}Tx$, we obtain the excited occupation number

$$N_{\mathrm{exc}} = \frac{V}{\lambda_{\mathrm{th}}^3} g_{3/2}(z), \tag{1.16}$$

where we have introduced the thermal wavelength

$$\lambda_{\mathrm{th}} = \sqrt{\frac{2\pi\hbar^2}{mk_{\mathrm{B}}T}}, \tag{1.17}$$

and the 3/2-Bose function

$$g_{3/2}(z) = \frac{2}{\sqrt{\pi}} \int_0^{\infty} \frac{x^{1/2}\mathrm{d}x}{z^{-1}e^x - 1}. \tag{1.18}$$

This function increases monotonically, and for $0 \leq z \leq 1$ is bounded taking its maximum at $g_{3/2}(1) = \zeta(3/2) \simeq 2.612$, with $\zeta(x)$ the Riemann zeta function. As a consequence, for a fixed value of the temperature, the occupation number of excited is bounded by

$$N_{\mathrm{exc}}(T, z) \leq N_{\mathrm{exc}}(T, 1) \equiv N_c(T) = \frac{V\zeta(3/2)}{\lambda_{\mathrm{th}}^3}. \tag{1.19}$$

If the total number of particles is smaller than this critical value, then N_0 can be neglected. However, when the particles number increases, there is a macroscopic occupation of the ground state, known as Bose–Einstein condensation (BEC). The condition for the formation of a BEC is $N > N_c$. If we hold N and V constant and vary T, this condition leads to a critical temperature for the transition

$$T_c = \frac{2\pi\hbar^2}{mk_B} \left(\frac{n}{\zeta(3/2)} \right)^{2/3}, \tag{1.20}$$

with $n = N/V$ the particles density. For temperatures below this critical value, following Eqs. (1.16) and (1.20), the particles fraction in excited states and in the condensate are (see Fig. 1.4)

$$\frac{N_{\text{exc}}}{N} = \left(\frac{T}{T_c} \right)^{3/2} \quad ; \quad \frac{N_0}{N} = 1 - \left(\frac{T}{T_c} \right)^{3/2}. \tag{1.21}$$

We can further characterize the BEC transition studying the internal energy, defined as $U = -\frac{\partial}{\partial\beta}\ln Z$. Here, it is not necessary to separate the contribution of the ground state as it is negligible against the excited states. Hence, taking the thermodynamic limit of the equation of state (1.11) yields

$$\ln Z = \frac{PV}{k_B T} = \frac{V}{\lambda_{\text{th}}^3} g_{5/2}(z), \tag{1.22}$$

where we made use of the property $g_p(z) = z\frac{dg_{p+1}}{dz}$ and the 5/2-Bose function is defined as

$$g_{5/2}(z) = \frac{4}{3\sqrt{\pi}} \int_0^\infty \frac{x^{3/2}dx}{z^{-1}e^x - 1}. \tag{1.23}$$

Then, the internal energy of the system is defined as a function of the temperature as

$$U(z, V, T) = -\frac{\partial}{\partial\beta}\ln Z = \begin{cases} \frac{3}{2}k_B T \frac{V}{\lambda_{\text{th}}^3} g_{5/2}(z) & \text{if } T > T_c \\ \frac{3}{2}k_B T \frac{V}{\lambda_{\text{th}}^3} g_{5/2}(1) & \text{if } T < T_c \end{cases}. \tag{1.24}$$

The variation of the internal energy of the temperature gives the heat capacity of the gas at a constant volume $C_v(T) = \partial U/\partial T$. For $T < T_c$, it is straightforward to calculate this derivative. Above the critical temperature, we need to consider also the temperature dependence of the fugacity (or the chemical potential). In this limit, it is easier to study the temperature dependence of the 3/2-Bose function directly from Eq. (1.16) as $N = N_{\text{exc}}$. Then, we can see that $g_{3/2}(z) \sim T^{-3/2}$ and use the following relations

$$\frac{\partial g_{3/2}(z)}{\partial T} = -\frac{3}{2T}g_{3/2}(z) \quad ; \quad z\frac{\partial g_{3/2}(z)}{\partial z} = g_{1/2}(z) \tag{1.25}$$

to obtain an expression for the temperature derivative of the fugacity

$$\frac{1}{z}\frac{\partial z}{\partial T} = -\frac{3}{2T}\frac{g_{3/2}(z)}{g_{1/2}(z)}. \tag{1.26}$$

Finally, using these relations, we obtain the heat capacity of an ideal Bose gas
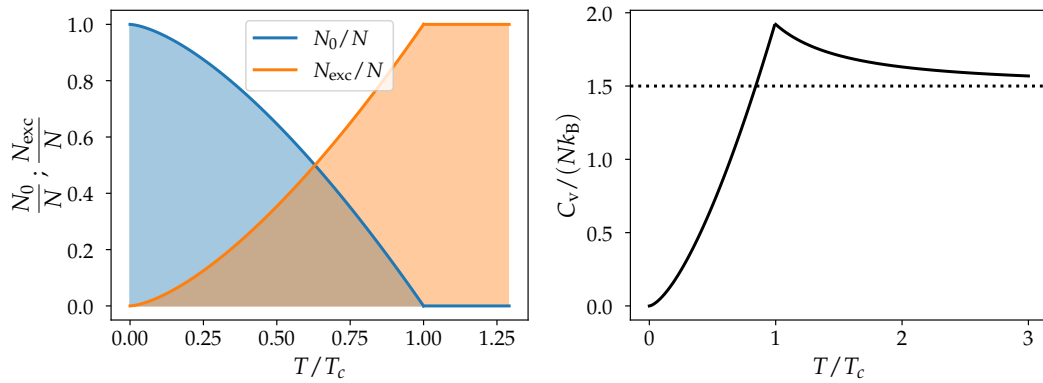
Figure 1.4: Bose–Einstein condensation in an ideal gas. (a) Occupation number of the excited N_{exc} and the ground N_0 states as a function of the temperature of the gas. (b) Heat capacity of the gas around the transition. The dotted line indicates the classical result $C_v = 3Nk_B/2$.

$$\frac{C_v}{Nk_B} = \begin{cases} \frac{15}{4}\frac{v}{\lambda_{th}^3}g_{5/2}(z) - \frac{9}{4}\frac{g_{3/2}(z)}{g_{1/2}(z)} & \text{if } T > T_c \\ \frac{15}{4}\frac{v}{\lambda_{th}^3}g_{5/2}(1) & \text{if } T < T_c \end{cases}, \tag{1.27}$$

with $v = V/N$ the specific volume. In the limit $T \to \infty$ the Bose functions $g_p(z) \to z$ and obtain the classical behavior $\lim_{T\to\infty} C_v/(Nk_B) = 3/2$.

Figure 1.4 shows the temperature dependence of the heat capacity, showing that the function is continuous at the critical point, where it takes a maximum value. The heat capacity of an ideal Bose gas is qualitatively similar to the one observed in superfluid helium (Fig. 1.1 (b)). This lead London (1938) to suggest that superfluid helium might be a manifestation of Bose–Einstein condensation taking place in liquid helium. Indeed, if we replace some typical values for superfluid helium (see end of Sec. 1.2), we obtain a value of the critical temperature $T_c = 3.14$ K, which is of the same order of the lambda point temperature $T_\lambda = 2.17$ K. This interpretation also provides some theoretical basis for the two-fluid model used in superfluid helium (see Sec. 1.1).

We finally remark that condensation in two-dimensions (2D) is formally prevented because of the Mermin-Wagner-Hohenberg theorem [MW66; Hoh67], but it originates as a finite size effect. In a 2D Bose gas, the occupation number of excited states is

$$N_{exc} = \frac{L^2}{\lambda_{th}^2} \int \frac{dx}{z^{-1}e^x - 1} \tag{1.28}$$

which differs from the 3D case given by Eq. (1.16). For $z = 1$ the integral in Eq. (1.28) diverges, preventing the macroscopic occupation of the ground state, and condensation does not occur. The physical explanation of this effect is given by Mermin, Wagner [MW66] and Hohenberg [Hoh67]. Their theorem states that in dimensions $D \leq 2$, no stable ordered phase at finite temperature can exist if the system is invariant under a continuous symmetry. The Mermin-Wagner-Hohenberg theorem is valid in the thermodynamic limit, when the system size $L \to \infty$. However, if L is finite, condensation can still occur as a finite size effect.

1.3 Models for superfluids

Superfluidity can be found in several systems in nature that vary in length scales and temperature. For instance, Bose–Einstein condensation is achieved experimentally by confining a dilute gas of bosons in sizes of the order of the μm and at temperatures of the order of the μK [TTC+16]. Superfluid ^{4}He can arise in systems of size of the order of a meter, and finite temperature effects are usually relevant for its dynamics [RBD+14]. ^{3}He, a rare isotope of the helium atom with spin 1/2, also presents superfluid properties as a consequence of the formation of Cooper pairs at temperatures of the order of mK [Leg04]. Superfluidity can also take place at room temperature in quantum fluids of light, triggered by photon-photon interactions obtained in non-linear optical media [CC13]. It is also theorized that in the core of neutron stars superfluidity can arise as a consequence of neutrons forming Cooper pairs. This system takes place at very high densities and temperatures up to $T \sim 10^{10}$ K, and it is extremely complex as it is under the effects of a strong magnetic field and rotation [Cha17].

All these systems where superfluidity arises are governed by different interactions, take place at very different temperature regimes, and present very different characteristic length scales. Therefore, there is not a unique model able to describe all of these systems for all length scales and temperatures. In this section we will introduce some of these models, focusing mainly in BECs and superfluid ^{4}He at finite temperatures. In Sec. 1.3.1 we introduce a first principles model for a dilute gas of weakly interacting bosons known as Gross–Pitaevskii equation, in Sec. 1.3.2 we discuss a model based on the interaction of vortex filaments, fundamental structures of superfluids, and finally in Sec. 1.3.3 we formalize the two-fluid model.

1.3.1 The Gross–Pitaevskii equation

In this section, we will derive the Gross–Pitaevskii (GP) equation, a model for a weakly interacting Bose gas at low temperature. This model was developed by Gross and Pitaevskii in 1961 to study vortex solutions in superfluids [Gro61; Pit61]. For its derivation, we will use the second quantization formalism and perform a mean-field approximation [PS16; DGP+99; PS08; PJ08; FW12; Bog47].

1.3.1.1 Mean-field theory

Consider a system of N interacting bosons of mass m described by the N-body wavefunction $\Phi(\mathbf{r}_1, \ldots, \mathbf{r}_N, t)$. We can describe its dynamics using the Schrödinger equation

$$i\hbar \frac{\partial}{\partial t} \Phi(\mathbf{r}_1, \ldots, \mathbf{r}_N, t) = H_N \Phi(\mathbf{r}_1, \ldots, \mathbf{r}_N, t), \tag{1.29}$$

where the hamiltonian can be written as a sum of a single-particle hamiltonian $\hat{h}_0(\mathbf{r}_i) = -\frac{\hbar^2}{2m}\nabla_i^2 + V_{\text{ext}}(\mathbf{r}_i, t)$, with V_{ext} an external potential, and a two-body interaction potential V_{I}

$$H_N = \sum_{i=1}^{N} \hat{h}_0(\mathbf{r}_i) + \frac{1}{2}\sum_{i,j=1}^{N} V_{\text{I}}(\mathbf{r}_i, \mathbf{r}_j). \tag{1.30}$$

The 1/2 factor ensures that the interaction between each particles pair is counted just once. For general many-body systems, this equation is very complicated to solve as

it involves ND degrees of freedom, with D the spatial dimension, and requires to take care of the symmetrization properties of bosonic wavefunctions.

An alternative way consists on reformulating the problem using a different basis that explicitly considers that particles are indistinguishable, the wavefunction for bosons is symmetric, and avoiding the idea of keeping track of each individual particle. Thus, we can make use of the second quantization formalism, involving the bosonic field operator $\hat{\Psi}(\mathbf{r},t) = \sum_i \Psi_i(\mathbf{r},t)\hat{a}_i$ expressed as a linear combination of single-particle wavefunctions, with $\hat{a}_i$ and $\hat{a}_i^\dagger$ the annihilation and creation operators for bosons defined as

$$\hat{a}_i \ket{n_0, n_1, \ldots, n_i, \ldots} = \sqrt{n_i}\ket{n_0, n_1, \ldots, n_i - 1, \ldots} \tag{1.31}$$

$$\hat{a}_i^\dagger \ket{n_0, n_1, \ldots, n_i, \ldots} = \sqrt{n_i + 1}\ket{n_0, n_1, \ldots, n_i + 1, \ldots}, \tag{1.32}$$

where $\ket{n_0, \ldots, n_i, \ldots}$ is a complete orthonormal basis set where n_i denotes the number of particles in state i. The number of atoms occupying a level i can be obtained applying the number operator $\hat{N} = \hat{a}_i^\dagger \hat{a}_i$. The annihilation and creation operators satisfy the commutation relations

$$\left[\hat{a}_i, \hat{a}_j^\dagger\right] = \delta_{ij}, \quad \left[\hat{a}_i, \hat{a}_j\right] = \left[\hat{a}_i^\dagger, \hat{a}_j^\dagger\right] = 0, \tag{1.33}$$

where the brackets denote $[A, B] = AB - BA$ and δ_{ij} is the Kronecker delta function.

The many-body Hamiltonian describing N interacting bosons in the second quantization formalism is given by

$$\hat{H} = \int \hat{\Psi}^\dagger(\mathbf{r},t) \left[-\frac{\hbar^2}{2m}\nabla^2 + V_{\text{ext}}(\mathbf{r},t) \right] \hat{\Psi}(\mathbf{r},t)d\mathbf{r} +$$

$$+ \frac{1}{2} \int \int \hat{\Psi}^\dagger(\mathbf{r},t)\hat{\Psi}^\dagger(\mathbf{r}',t)V_{\text{I}}(\mathbf{r} - \mathbf{r}')\hat{\Psi}(\mathbf{r}',t)\hat{\Psi}(\mathbf{r},t)d\mathbf{r}d\mathbf{r}', \tag{1.34}$$

where we made an explicit assumption that the two-body interaction potential depends only on the distance between the bosons, and $\hat{h}_o = \frac{\hbar^2}{2m}\nabla^2 + V_{\text{ext}}(\mathbf{r},t)$ is the single-particle hamiltonian for a boson of mass m under an external potential $V_{\text{ext}}(\mathbf{r},t)$. Solving the equation of motion for $\hat{\Psi}(\mathbf{r},t)$ in the Heisenberg picture allows us to obtain the time evolution of the system

$$i\hbar\frac{\partial\hat{\Psi}(\mathbf{r},t)}{\partial t} = \left[\hat{\Psi}(\mathbf{r},t), \hat{H}\right] =$$

$$= \left[-\frac{\hbar^2}{2m}\nabla^2 + V_{\text{ext}}(\mathbf{r},t) + \int \hat{\Psi}^\dagger(\mathbf{r}',t)V_{\text{I}}(\mathbf{r} - \mathbf{r}')\hat{\Psi}(\mathbf{r}',t)d\mathbf{r}' \right] \hat{\Psi}(\mathbf{r},t). \tag{1.35}$$

To describe the dynamics of a Bose–Einstein condensate, it is convenient to separate the contribution of the ground state $\hat{\psi} = \Psi_0(\mathbf{r},t)\hat{a}_0$ from the non-condensed atoms $\delta\hat{\Psi} = \sum_{i\neq 0}\Psi_i(\mathbf{r},t)\hat{a}_i$. Thus, we have the exact decomposition

$$\hat{\Psi}(\mathbf{r},t) = \hat{\psi}(\mathbf{r},t) + \delta\hat{\Psi}(\mathbf{r},t). \tag{1.36}$$

The non-condensed atoms come from thermal excitations, quantum fluctuations or atoms in higher energy states due to interactions. In a BEC, there is a macroscopic

occupation of particles in the ground state. As a consequence, the ratio between the number of particles in the ground state $N_0 \gg 1$ and the total number of particles N becomes finite in the thermodynamic limit $N \to \infty$. In this limit, we can approximate the creation and annihilation operators as real numbers $\hat{a}_0 = \hat{a}_0^\dagger \approx \sqrt{N_0}$ as states with N_0 and $N_0 \pm 1 \approx N_0$ number of atoms correspond to the same physical configuration. Note also that now the first commutation rule in Eq. (1.33) is broken in the thermodynamic limit and becomes $\left[\hat{a}_0^\dagger, \hat{a}_0 \right] = 0$. The condensate wavefunction can thus be written in terms of a classical field $\psi(\mathbf{r}, t) = \sqrt{N_0} \Psi_0(\mathbf{r}, t)$ with the total field operator

$$\hat{\Psi}(\mathbf{r}, t) = \psi(\mathbf{r}, t) + \delta \hat{\Psi}(\mathbf{r}, t), \tag{1.37}$$

where all the operator dependence is now in the fluctuation term $\delta \hat{\Psi}$.

Using Eq. (1.37), the particles density is obtained by

$$n(\mathbf{r}, t) = \langle \hat{\Psi}^\dagger(\mathbf{r}, t) \hat{\Psi}(\mathbf{r}, t) \rangle = n_0(\mathbf{r}, t) + n_{\text{exc}}(\mathbf{r}, t), \tag{1.38}$$

where $n_0(\mathbf{r}, t) = V^{-1} \int |\psi|^2 d\mathbf{r}$ is the particles density in the ground state and the second term $n_{\text{exc}}(\mathbf{r}, t) = V^{-1} \int \delta \hat{\Psi}^\dagger \delta \hat{\Psi} d\mathbf{r}$ is the particles density of excited states produced by the non-condensed particles, with V the volume of the system. In the limit of zero temperature, we can assume that the non-condensed fraction, describing a thermal cloud, is negligible compared to the ground state. As a consequence, one obtains a mean-field approximation for the field operator $\hat{\Psi}(\mathbf{r}, t) \approx \psi(\mathbf{r}, t)$, where the classical field $\psi(\mathbf{r}, t)$ plays the role of the order parameter describing the BEC transition. In this limit, replacing the macroscopic wavefunction into Eq. (1.35) yields the following equation for the order parameter

$$i\hbar \frac{\partial \psi}{\partial t}(\mathbf{r}, t) = \left[-\frac{\hbar^2}{2m} \nabla^2 + V_{\text{ext}}(\mathbf{r}, t) + \int V_{\text{I}}(\mathbf{r} - \mathbf{r}') |\psi|^2(\mathbf{r}', t) d\mathbf{r}' \right] \psi(\mathbf{r}, t). \tag{1.39}$$

In the case of dilute gases, we can assume that the interaction between bosons is weak and comes only from two-body collisions. In this limit, the effective two-body interatomic potential can be written as

$$V_{\text{I}}(\mathbf{r} - \mathbf{r}) = g\delta(\mathbf{r} - \mathbf{r}'), \quad g = \frac{4\pi\hbar^2 a_s}{m} \tag{1.40}$$

where $\delta(\mathbf{x})$ is a delta-function and a_s is the s-wave scattering length of bosons. The dilute gas limit is expected to occur when the product between the particles density and the scattering volume is very small $n|a_s|^3 \ll 1$. Thus, in the limit of zero-temperature $T \to 0$ and weakly interacting bosons, we obtain the so-called Gross–Pitaevskii (GP) equation

$$i\hbar \frac{\partial \psi}{\partial t}(\mathbf{r}, t) = \left[-\frac{\hbar^2}{2m} \nabla^2 + V_{\text{ext}}(\mathbf{r}, t) + g|\psi|^2(\mathbf{r}, t) \right] \psi(\mathbf{r}, t), \tag{1.41}$$

also known as non-linear Schrödinger equation (NLSE). This system is the main model to study the dynamics of dilute BECs from a macroscopic point of view, as it is obtained from first principles.

The ground state of this system can be obtained by separating the spatial and time dependence from the wavefunction as $\psi(\mathbf{r}, t) = \phi(\mathbf{r}) \exp(-iE_0 t)$ with $E_0 = \mu/\hbar$

the energy of the ground state and μ the chemical potential of the condensate. Introducing this wavefunction into Eq. (1.41) and assuming a time-independent external potential yields

$$\mu\phi(\mathbf{r}) = \left[-\frac{\hbar^2}{2m}\nabla^2 + V_{\text{ext}}(\mathbf{r}) + g|\phi|^2(\mathbf{r}, t)\right]\phi(\mathbf{r}). \tag{1.42}$$

1.3.1.2 Variational formulation and conserved quantities

The Hamiltonian density $\mathcal{H}$ and the Lagrangian density $\mathcal{L}$ that describe the Gross–Pitaevskii Eq. (1.41) are respectively [NAB97a; SS04]

$$\mathcal{H}[\psi, \boldsymbol{\nabla}\psi, \psi^*, \boldsymbol{\nabla}\psi^*] = \frac{\hbar^2}{2m}|\boldsymbol{\nabla}\psi|^2 + \frac{g}{2}|\psi|^4 + V_{\text{ext}}(\mathbf{r}, t)|\psi|^2, \tag{1.43}$$

$$\mathcal{L}[\psi, \boldsymbol{\nabla}\psi, \partial_t\psi, \psi^*, \boldsymbol{\nabla}\psi^*, \partial_t\psi^*] = \frac{i\hbar}{2}\left(\psi^*\frac{\partial\psi}{\partial t} - \frac{\partial\psi^*}{\partial t}\psi\right) - \mathcal{H}[\psi, \boldsymbol{\nabla}\psi, \psi^*, \boldsymbol{\nabla}\psi^*]. \tag{1.44}$$

Integrating over time and space the Lagrangian density leads to the Gross–Pitaevskii action functional

$$\mathcal{S} = \int\int \mathcal{L}[\psi, \boldsymbol{\nabla}\psi, \partial_t\psi, \psi^*, \boldsymbol{\nabla}\psi^*, \partial_t\psi^*]\mathrm{d}\mathbf{r}\mathrm{d}t = \tag{1.45}$$

$$= \int\int\left[\frac{i\hbar}{2}\left(\psi^*\frac{\partial\psi}{\partial t} - \frac{\partial\psi^*}{\partial t}\psi\right) - \left(\frac{\hbar^2}{2m}|\boldsymbol{\nabla}\psi|^2 + \frac{g}{2}|\psi|^4 + V_{\text{ext}}(\mathbf{r}, t)|\psi|^2\right)\right]\mathrm{d}\mathbf{r}\mathrm{d}t.$$

Its variation over infinitesimal perturbations $\delta\psi$ and $\delta\psi^*$, after integrating by parts, leads to the expression

$$\delta\mathcal{S} = \mathcal{S}[\psi + \delta\psi, \psi^* + \delta\psi^*] - \mathcal{S}[\psi, \psi^*] \tag{1.46}$$

$$= \int\int \delta\psi\left[\frac{\partial\mathcal{L}}{\partial\psi} - \boldsymbol{\nabla}\cdot\left(\frac{\partial\mathcal{L}}{\partial\boldsymbol{\nabla}\psi}\right) - \partial_t\left(\frac{\partial\mathcal{L}}{\partial\partial_t\psi}\right)\right]\mathrm{d}\mathbf{r}\mathrm{d}t + \left[\frac{\partial\mathcal{L}}{\partial\partial_t\psi}\delta\psi\right]_{t_0}^{t_1} + \text{c.c.},$$

where c.c. indicates the complex conjugate, and $\frac{\partial\mathcal{L}}{\partial\boldsymbol{\nabla}\psi}$ denotes the vector of components $\frac{\partial\mathcal{L}}{\partial\partial_i\psi}$ with $i = 1, \ldots, d$ and d the dimension of the system. The principle of least action states that extrema of the action functional yield the equations of motion for the system. Thus, we can recover the Euler-Lagrange equations of the system by minimizing the integrand

$$\frac{\partial\mathcal{L}}{\partial\psi} = \boldsymbol{\nabla}\cdot\left(\frac{\partial\mathcal{L}}{\partial\boldsymbol{\nabla}\psi}\right) + \partial_t\left(\frac{\partial\mathcal{L}}{\partial\partial_t\psi}\right), \tag{1.47}$$

that reduces to the Gross–Pitaevskii equation when the Lagrangian density (1.44) is used. Minimizing the term of the integrand in the complex conjugate term leads to the equation for ψ^*, corresponding to the complex conjugate of Eq. (1.41). Similarly, finding extrema of the Hamiltonian $H = \int\mathcal{H}\mathrm{d}\mathbf{r}$ leads to the Hamiltonian equations, that in the complex form are written as

$$i\hbar\frac{\partial\psi}{\partial t} = \frac{\delta\mathcal{H}}{\delta\psi^*}. \tag{1.48}$$

Now, consider any infinitesimal transformation applied to the wavefunction, space and time, such that

$$t' = t + \delta t, \quad \mathbf{r}' = \mathbf{r} + \delta \mathbf{r}, \quad \psi' = \psi + \delta \psi, \quad \psi'^* = \psi^* + \delta \psi^*. \quad (1.49)$$

According to Noether's theorem, any transformation that conserves the action functional invariant leads to a conservation law

$$\partial_t \left(\mathcal{L} \delta t + \frac{\partial \mathcal{L}}{\partial \partial_t \psi} \delta \psi + \frac{\partial \mathcal{L}}{\partial \partial_t \psi^*} \delta \psi^* \right) + \boldsymbol{\nabla} \cdot \left(\mathcal{L} \delta \mathbf{r} + \frac{\partial \mathcal{L}}{\partial \boldsymbol{\nabla} \psi} \delta \psi + \frac{\partial \mathcal{L}}{\partial \boldsymbol{\nabla} \psi^*} \delta \psi^* \right) = 0, \quad (1.50)$$

and integrating in space we obtain the following conserved quantity

$$\int \left[\frac{\partial \mathcal{L}}{\partial \partial_t \psi} \left(\partial_t \psi \delta t + \boldsymbol{\nabla} \psi \cdot \delta \mathbf{r} - \delta \psi \right) + \frac{\partial \mathcal{L}}{\partial \partial_t \psi^*} \left(\partial_t \psi^* \delta t + \boldsymbol{\nabla} \psi^* \cdot \delta \mathbf{r} - \delta \psi^* \right) - \mathcal{L} \delta t \right] \mathrm{d} \mathbf{r}. \quad (1.51)$$

This result can be applied to the GP system, for which $\frac{\partial \mathcal{L}}{\partial \partial_t \psi} = i\hbar \psi^* / 2$, to obtain different symmetries and conserved quantities. For instance, applying a global phase shift transformation, also known as $\mathcal{U}(1)$ symmetry,

$$t' = t, \quad \mathbf{r}' = \mathbf{r}, \quad \psi'(\mathbf{r}', t') = e^{i\phi/\hbar} \psi(\mathbf{r}, t), \quad (1.52)$$

corresponding to an infinitesimal transformation of the wavefunction with $\delta \psi = i\frac{\phi}{\hbar} \psi$ and $\delta \psi^* = -i\frac{\phi}{\hbar} \psi^*$, yields a conservation law when replacing in Eq. (1.50)

$$\partial_t |\psi|^2 + \frac{i\hbar}{2m} \boldsymbol{\nabla} \cdot (\psi \boldsymbol{\nabla} \psi^* - \psi^* \boldsymbol{\nabla} \psi) = 0. \quad (1.53)$$

Note that this expression is a continuity equation, as we shall see in Sec. 1.3.1.4, and therefore it leads to the conservation of the total number of particles

$$N = \int |\psi|^2 \mathrm{d} \mathbf{r}. \quad (1.54)$$

In the case that the external potential is time-independent $V_{\mathrm{ext}}(\mathbf{r}, t) = V_{\mathrm{ext}}(\mathbf{r})$, the GP action is invariant by an infinitesimal time translation

$$t' = t + \delta t, \quad \mathbf{r}' = \mathbf{r}, \quad \psi'(\mathbf{r}', t') = \psi(\mathbf{r}, t), \quad (1.55)$$

with $\delta \mathbf{r} = \delta \psi = \delta \psi^* = 0$. Replacing this transformation in Eq. (1.51), it leads to the conservation of the Hamiltonian

$$H = \int \left[\frac{i\hbar}{2} (\psi^* \partial_t \psi - \psi \partial_t \psi^*) - \mathcal{L} \right] \mathrm{d} \mathbf{r} = \int \mathcal{H} \mathrm{d} \mathbf{r}, \quad (1.56)$$

associated with the conservation of energy in the system.

Another symmetry of the GP action is obtained by applying a space translation in the case that te external potential is independent of the space coordinates $V_{\mathrm{ext}}(\mathbf{r}, t) = V_{\mathrm{ext}}(t)$

$$t' = t, \quad \mathbf{r}' = \mathbf{r} + \delta \mathbf{r}, \quad \psi'(\mathbf{r}', t') = \psi(\mathbf{r}, t), \quad (1.57)$$

with $\delta t = \delta \psi = \delta \psi^* = 0$, leading to the conservation of linear momentum

$$\mathbf{P} = \int \frac{i\hbar}{2} \left(\psi \boldsymbol{\nabla} \psi^* - \psi^* \boldsymbol{\nabla} \psi \right) d\mathbf{r}. \tag{1.58}$$

The last symmetry that we are going to introduce in this work corresponds to the Galilean invariance obtained by applying the transformation

$$t' = t, \quad \mathbf{r}' = \mathbf{r} + \mathbf{v}t, \quad \psi'(\mathbf{r}', t') = \psi(\mathbf{r}, t) e^{-i\frac{m}{\hbar} \left(\mathbf{v} \cdot \mathbf{r}' + \frac{1}{2} v^2 t' \right)}, \tag{1.59}$$

with $\mathbf{v}$ a constant velocity field, and we take $V_{\text{ext}}(\mathbf{r}, t) = 0$ for the sake of simplicity. Considering that the velocity field is small, the leading order of the wavefunction becomes $\psi'(\mathbf{r}', t') = \psi(\mathbf{r}, t) - i\frac{m}{\hbar} \mathbf{v} \cdot \mathbf{r}$, with $\delta\psi = -i\frac{m}{\hbar} \mathbf{v} \cdot \mathbf{r}$ and $\delta\psi^* = i\frac{m}{\hbar} \mathbf{v} \cdot \mathbf{r}$. This transformation also keeps the GP action invariant and leads to the conservation of linear momentum of the center of mass.

The GP action presents other symmetries, like space rotation, scale invariance for power law non-linearities, and pseudo-conformal invariance at critical dimension [SS04]. However, these are not going to be discussed in this work.

1.3.1.3   Ground state and dispersion relation

As discussed in the previous Sec. 1.3.1.2, the Gross–Pitaevskii equation Eq.(1.41) can also be derived using a variational method for the Hamiltonian leading to Eq. (1.48). We can also define the free energy functional $\mathcal{F} = \mathcal{H} - \mu N$ defined as

$$\mathcal{F}[\psi] = \int d\mathbf{r} \left[\frac{\hbar^2}{2m} |\boldsymbol{\nabla}\psi|^2 + V_{\text{ext}}(\mathbf{r}, t) + \frac{g}{2} |\psi|^4 - \mu |\psi|^2 \right], \tag{1.60}$$

and use the variational method with this quantity

$$i\hbar \frac{\partial \psi}{\partial t} = \frac{\delta \mathcal{F}}{\delta \psi^*}. \tag{1.61}$$

The free energy functional introduces the chemical potential μ as a Lagrange multiplier, showing explicitly that the number of particles in the condensate is not fixed and that it quantifies the amount of energy required to add a particle in the condensate. This variational method leads to the dynamical GP model

$$i\hbar \frac{\partial \psi}{\partial t}(\mathbf{r}, t) = \left[-\frac{\hbar^2}{2m} \nabla^2 + V_{\text{ext}}(\mathbf{r}, t) + g|\psi|^2(\mathbf{r}, t) - \mu \right] \psi(\mathbf{r}, t), \tag{1.62}$$

that now involves the chemical potential μ in its evolution. Assuming a flat condensate $\psi(\mathbf{r}, t) = \psi_0$ and no external potential, the ground state of the system becomes

$$gn_0 = \mu, \tag{1.63}$$

where $n_0 = |\psi_0|^2$. Let us now consider the ground state with small perturbations $\psi = \psi_0 + \delta\psi$. Replacing this into the GP Eq. (1.62) with no external potential, using the relation for the ground state given in (1.63), and keeping only linear perturbations yields

$$i\hbar \partial_t \delta\psi = \left[-\frac{\hbar^2}{2m} \nabla^2 + gn_0 \right] \delta\psi + g\psi_0^2 \delta\psi^*. \tag{1.64}$$

We assume now that the small perturbations can be written as a linear combination of planar waves of wavenumber $\mathbf{k}$ and frequency ω

$$\delta\psi(\mathbf{r},t) = \sum_{\mathbf{k}} u_{\mathbf{k}} e^{i(\mathbf{k}\cdot\mathbf{r}-\omega t)} + v_{\mathbf{k}}^* e^{-i(\mathbf{k}\cdot\mathbf{r}-\omega t)}. \tag{1.65}$$

We can thus obtain a linear system for the perturbation amplitudes

$$\begin{pmatrix} \frac{\hbar k^2}{2m} + \frac{gn_0}{\hbar} & \frac{gn_0}{\hbar} \\ -\frac{gn_0}{\hbar} & -\frac{\hbar k^2}{2m} - \frac{gn_0}{\hbar} \end{pmatrix} \begin{pmatrix} u_{\mathbf{k}} \\ v_{\mathbf{k}}^* \end{pmatrix} = \omega \begin{pmatrix} u_{\mathbf{k}} \\ v_{\mathbf{k}}^* \end{pmatrix}. \tag{1.66}$$

This linear system leads to the dispersion relation of Bogoliubov excitations

$$\omega_{\mathrm{B}} = \pm\sqrt{\frac{\hbar k^2}{2m}\left(\frac{\hbar k^2}{2m} + \frac{2gn_0}{\hbar}\right)}, \tag{1.67}$$

that has two clear limits. In the small wavenumber limit, the dispersion relation exhibits an acoustic regime $\omega_{\mathrm{B}} \approx \pm ck$ with

$$c = \sqrt{\frac{gn_0}{m}} \tag{1.68}$$

the speed of sound of the superfluid. On the other hand, for large wavenumbers, a free particle regime describes the dispersion relation $\omega_{\mathrm{B}} \approx \pm\hbar k^2/(2m)$. Comparing the kinetic term and the ground state energy, one can obtain the dispersive scale ξ in which both regimes are relevant

$$\frac{\hbar^2}{2m}\nabla^2 \sim \frac{\hbar^2}{2m\xi^2} = gn_0 \rightarrow \xi = \frac{\hbar}{\sqrt{2gmn_0}}. \tag{1.69}$$

The healing or coherence length ξ estimates the correlation of the system and is also proportional to the core size of vortices, that we shall introduce in Sec. 1.3.1.5. We can thus write Bogoliubov dispersion relation in terms of these two relevant parameters of the system as

$$\omega_{\mathrm{B}} = \pm ck\sqrt{\frac{\xi^2 k^2}{2} + 1}. \tag{1.70}$$

1.3.1.4 Hydrodynamic description of the GP model

The complex wavefunction described by the Gross–Pitaevskii equation can be prescribed by a real function $R(\mathbf{r},t)$ and an arbitrary phase $\phi(\mathbf{r},t)$ as

$$\psi(\mathbf{r},t) = R(\mathbf{r},t)e^{i\phi(\mathbf{r},t)}. \tag{1.71}$$

This wavefunction must satisfy the normalization condition $N = \int |\psi|^2 d\mathbf{r}$ and it determines the momentum density as

$$\mathbf{j} = \rho\mathbf{v} = \frac{\hbar}{2mi}\left[\psi^*\boldsymbol{\nabla}\psi - \psi\boldsymbol{\nabla}\psi^*\right]. \tag{1.72}$$

These two conditions prescribe a relation between the wavefunction, the mass density and the velocity field of the superfluid via the so-called Madelung transformation [Mad26]

$$\psi(\mathbf{r},t) = \sqrt{\frac{\rho(\mathbf{r},t)}{m}}e^{i\phi(\mathbf{r},t)}, \quad \mathbf{v}(\mathbf{r},t) = \frac{\hbar}{m}\boldsymbol{\nabla}\phi(\mathbf{r},t), \tag{1.73}$$

where $\rho(\mathbf{r}, t) = mn(\mathbf{r}, t) = m|\psi|^2$. The first consequence of this transformation is that the velocity field is prescribed by a potential flow, so the superfluid is irrotational

$$\boldsymbol{\nabla} \times \mathbf{v} = \boldsymbol{\nabla} \times \boldsymbol{\nabla} \phi = 0. \tag{1.74}$$

Inserting this expression into Eq. (1.41) yields the continuity and a modified Bernoulli equations for an inviscid dispersive fluid

$$\frac{\partial \rho}{\partial t} + \boldsymbol{\nabla} \cdot (\rho \mathbf{v}) = 0, \tag{1.75}$$

$$\frac{\partial \phi}{\partial t} + \frac{\hbar}{2m}(\boldsymbol{\nabla}\phi)^2 + \frac{g\rho}{\hbar m} - \frac{\hbar}{2m}\left(\frac{\nabla^2 \sqrt{\rho}}{\sqrt{\rho}}\right) = 0. \tag{1.76}$$

The continuity equation leads to mass (or particle) conservation, while the inviscid modified Bernoulli equation leads to energy conservation. From this equation it is possible to identify a term for the hydrodynamic pressure p_h and an extra term, absent in classical fluids, known as quantum pressure p_q. These two quantities are defined as

$$p_h = \frac{g\rho^2}{m^2}, \quad p_q = -\frac{\hbar^2 \rho}{2m^2}\left(\frac{\nabla^2 \sqrt{\rho}}{\sqrt{\rho}}\right), \quad p = p_h + p_q. \tag{1.77}$$

The quantum pressure becomes important in regions of the flow with strong density variations that, as we shall see in Sec. 1.3.1.5, are close to the core of quantum vortices. Note that in the notation we use, with the velocity field defined by a dimensionless phase as $\mathbf{v} = \hbar \boldsymbol{\nabla}\phi/m$, the Bernoulli equation might look different from the expression usually found in the literature. However, if we redefine the phase so that it is no longer dimensionless $\phi \rightarrow m\tilde{\phi}/\hbar$, then the usually expression is recovered

$$\frac{\partial \tilde{\phi}}{\partial t} + \frac{1}{2}(\boldsymbol{\nabla}\tilde{\phi})^2 + \frac{g\rho}{m^2} - \frac{\hbar^2}{2m^2}\left(\frac{\nabla^2 \sqrt{\rho}}{\sqrt{\rho}}\right) = 0, \tag{1.78}$$

where it is explicitly shown that the quantum pressure is the only term depending on $\hbar$. The mapping between the GP equation and the hydrodynamic equations for an ideal, compressible fluid may mislead to think that these two systems are equivalent. However, as we shall see in Sec. 1.3.1.5, this is not true due to the existence of singularities in the wavefunction that lead to the presence of vortices with a quantized circulation, structures that the modified Bernoulli equation fails to describe.

As described in Sec. 1.3.1.2, the GP model conserves the Hamiltonian obtained by integrating in space Eq. (1.43) if the external potential is independent of time. For simplicity, we set this potential as $V_{\text{ext}}(\mathbf{r}, t) = 0$. In this case, the total energy per unit of volume $e_{\text{tot}} = E_{\text{tot}}/V$ can be decomposed as

$$e_{\text{tot}} = e_{\text{kin}} + e_{\text{int}} + e_{\text{q}}, \tag{1.79}$$

where the kinetic, internal and quantum energies are defined as

$$e_{\text{kin}} = \frac{E_{\text{kin}}}{V} = \frac{1}{V} \int \frac{\left(\sqrt{\rho}\mathbf{v}\right)^2}{2} \mathrm{d}\mathbf{r} \tag{1.80}$$

$$e_{\text{int}} = \frac{E_{\text{int}}}{V} = \frac{1}{V} \int \frac{g\rho^2}{2m^2} \mathrm{d}\mathbf{r} \tag{1.81}$$

$$e_{\text{q}} = \frac{E_{\text{q}}}{V} = \frac{1}{V} \int \frac{\hbar^2}{2m^2} \left(\boldsymbol{\nabla}\sqrt{\rho}\right)^2 \mathrm{d}\mathbf{r}. \tag{1.82}$$

Furthermore, the kinetic energy can be separated into the compressible and incompressible parts using the Helmholtz decomposition $\sqrt{\rho}\mathbf{v} = (\sqrt{\rho}\mathbf{v})^{\text{i}} + (\sqrt{\rho}\mathbf{v})^{\text{c}}$. The compressible velocity field satisfies $\boldsymbol{\nabla} \times (\sqrt{\rho}\mathbf{v})^{\text{c}} = 0$, while the incompressible component satisfies $\boldsymbol{\nabla} \cdot (\sqrt{\rho}\mathbf{v})^{\text{i}} = 0$ and is associated with quantum vortices, described in Sec. 1.3.1.5.

In the case that one is not interested on the interaction between the superfluid with walls, one could consider a periodic system of size L. As each energy component is a quadratic quantity, they can be written in Fourier space using Parseval's theorem in d-dimensions

$$\int |\hat{f}(\mathbf{k})|^2 \mathrm{d}\mathbf{k} = \frac{1}{L^d} \int |f(\mathbf{r})|^2 \mathrm{d}\mathbf{r}, \tag{1.83}$$

where the Fourier transform is defined as $\hat{f}(\mathbf{k}) = L^{-d} \int f(\mathbf{r})e^{i\mathbf{k}\cdot\mathbf{r}}\mathrm{d}\mathbf{r}$ with the normalization $f(\mathbf{r}) = \int \hat{f}(\mathbf{k})e^{-i\mathbf{k}\cdot\mathbf{r}}\mathrm{d}\mathbf{k}$ and f a generic function. Therefore, the energy spectra are defined as

$$e_{\text{kin}}^{\text{i}}(k) = \frac{1}{2L^d} \int \left|\int e^{i\mathbf{k}\cdot\mathbf{r}}(\sqrt{\rho}\mathbf{v})^{\text{i}}\mathrm{d}\mathbf{r}\right|^2 k^{d-1}\mathrm{d}\Omega_k, \tag{1.84}$$

$$e_{\text{kin}}^{\text{c}}(k) = \frac{1}{2L^d} \int \left|\int e^{i\mathbf{k}\cdot\mathbf{r}}(\sqrt{\rho}\mathbf{v})^{\text{c}}\mathrm{d}\mathbf{r}\right|^2 k^{d-1}\mathrm{d}\Omega_k, \tag{1.85}$$

$$e_{\text{int}}(k) = \frac{g}{2m^2 L^d} \int \left|\int e^{i\mathbf{k}\cdot\mathbf{r}}\rho\mathrm{d}\mathbf{r}\right|^2 k^{d-1}\mathrm{d}\Omega_k, \tag{1.86}$$

$$e_{\text{q}}(k) = \frac{\hbar}{2m^2 L^d} \int \left|\int e^{i\mathbf{k}\cdot\mathbf{r}}(\nabla\sqrt{\rho})\mathrm{d}\mathbf{r}\right|^2 k^{d-1}\mathrm{d}\Omega_k, \tag{1.87}$$

where $\mathrm{d}\Omega_k$ is the solid angle differential in Fourier space. The energy components satisfy the relations $E_{\text{kin}} = \int \mathrm{d}k E_{\text{kin}}(k)$, $E_{\text{int}} = \int \mathrm{d}k E_{\text{int}}(k)$ and $E_{\text{q}} = \int \mathrm{d}k E_{\text{q}}(k)$. Finally, if we now consider an external potential independent of time, energy will still be conserved and it will present an extra term associated to this external potential defined as

$$E_{\text{ext}} = \int V_{\text{ext}}(\mathbf{r})\frac{\rho}{m}\mathrm{d}\mathbf{r}. \tag{1.88}$$

1.3.1.5   Quantum vortex solutions

One of the most important features of superfluids is the presence of vortices as topological defects, with zero mass density in its core and a quantized circulation around them. The idea of vortices in superfluids with a quantized circulation proportional to $\hbar$ was first proposed in 1949 by Onsager [Ons49]. Later, Richard Feynman in 1955

formalized this idea and proposed that vorticity should be concentrated along vortex lines [Fey55]. The first experimental evidences of the existence of quantum vortices were obtained by the end of the 1950s and beginnings of the 1960s by Hall and Vinen, with the studies of the angular momentum of a rotating superfluid helium [Hal58; Vin61]. These observations renewed the interest on the existence of quantum vortices, which by that time was surrounded by some skepticism [Don91]. In fact, one of the main motivations on the development of the Gross–Pitaevskii model in 1961 was to study quantum vortex solutions in weakly interacting Bose–Einstein condensates [Gro61; Pit61]. The first photographs of quantum vortices were realized years later in 1970s in rotating superfluid helium [WP74; YGP79]. Nowadays, using particle tracking velocimetry techniques, it is possible to directly visualize quantum vortices in superfluid ^{4}He [BLS06; GML$^+$14; FSL19].

The Madelung transformation (1.73) provides a relation between the condensate wavefunction and the velocity field of the superfluid via the gradient of the phase. The velocity circulation around a closed loop $\mathcal{C}$ is then

$$\Gamma = \oint_{\mathcal{C}} \mathbf{v} \cdot d\mathbf{l} = \frac{\hbar}{m} \oint_{\mathcal{C}} \boldsymbol{\nabla}\phi \cdot d\mathbf{l} = \frac{2\pi\hbar q}{m}, \qquad (1.89)$$

with q an integer number. Here, we used that the phase can vary by a factor multiple of 2π when integrated around a closed loop, keeping the wavefunction invariant. We thus obtain that the velocity circulation is a multiple of the quantum of circulation κ defined as

$$\kappa = \frac{h}{m} = 2\pi\sqrt{2}c\xi. \qquad (1.90)$$

Another consequence of the Madelung transformation is that the flow is potential, meaning that it is irrotational in the sense $\boldsymbol{\nabla} \times \mathbf{v} = 0$. Using Stokes theorem, it is possible to relate the line integral (1.89) with a surface integral of the rotational of the velocity field.

$$\Gamma = \oint_{\mathcal{C}} \mathbf{v} \cdot d\mathbf{l} = \iint_{S} (\boldsymbol{\nabla} \times \mathbf{v}) \cdot d\mathbf{S} = 0, \qquad (1.91)$$

with S a simply connected surface contained by the closed loop $\mathcal{C}$. However, if the surface is not simply connected, i.e., if the velocity presents singularities given by a divergence of this field, then the Stokes theorem cannot be applied and the circulation is non-zero. These singularities take place in nodal points of the wavefunction with $\mathrm{Re}\{\psi\} = \mathrm{Im}\{\psi\} = 0$ where the phase is not well defined. Thus, these two equations tell us that vorticity is concentrated along lines in three-dimensions and in single points in two-dimensions. The velocity field of a straight vortex line in the z axis expressed in cylindrical coordinates is given by

$$\mathbf{v}_{\mathrm{v}}(\mathbf{r}) = \frac{\Gamma}{2\pi r}\hat{e}_{\theta} = \frac{\hbar}{m}\frac{q}{r}\hat{e}_{\theta} \qquad (1.92)$$

with r the perpendicular distance to the vortex core and $\hat{e}_{\theta}$ the azimuthal direction.

The velocity field generated by a vortex line diverges in its core. Nevertheless, these are points where the mass density vanishes and, as we shall see, the combination of these two effects regularize the energy associated to a vortex line. To obtain the density profile of a quantum vortex, we will assume a straight vortex line in the z direction in a stationary state. We can write the wavefunction in cylindrical coordinates as $\psi(r, \theta, z) = R(r)e^{iq\theta}$ with q the quantum integer associated to the circulation charge and $R(r) = \sqrt{\rho(r)/m}$. Replacing it into the GP equation (1.62) we obtain

$$\xi^2 \frac{d^2 R}{dr^2} + \frac{\xi^2}{r} \frac{dR}{dr} + \left(1 - \frac{\xi^2 q^2}{r^2} - \frac{R^2}{n_0}\right) R = 0, \tag{1.93}$$

in terms of the healing length ξ (1.69) and the particles density of the ground state n_0. This equation has no exact analytical solution, but it is possible to study some limits. As boundary conditions we know that $R(r \to 0) = 0$ and $R(r \to \infty) = \sqrt{n_0}$. For $r \to 0$, we can neglect the first and third term inside parenthesis of Eq. (1.93) to obtain

$$\frac{d^2 R}{dr^2} + \frac{1}{r} \frac{dR}{dr} - \frac{q^2}{r^2} R = 0. \tag{1.94}$$

This equation admits solutions of the type $R(r) = a_0 (r/\xi)^\alpha$ with $\alpha = |q|$ and the amplitude $a_0 = a_0(q)$ that depends on the charge of the vortex. On the other hand, in the limit $r \to \infty$ we can expand the solution as a power series $R(r) = \sqrt{n_0} \sum_{i=0}^\infty b_i r^{-i}$ and obtain up to the second order $b_0 = 1$, $b_1 = 0$ and $b_2 = -\xi^2 q^2$. Thus, we obtain two asymptotic solutions

$$\lim_{r \to 0} R(r) = a_0 \left(\frac{r}{\xi}\right)^{|s|}, \quad \lim_{r \to \infty} = 1 - \frac{\xi^2 q^2}{r^2}. \tag{1.95}$$

Numerical integration of Eq. (1.93) for $q = 1$ gives a value $a_0 = 0.5827811878$ [Ber04]. A picture of the density profile of a single-charged quantum vortex is shown in Fig. 1.5.

The energy of a straight vortex can be obtained by replacing the cylindrical wavefunction into the free energy (1.60) in the absence of an external potential and integrating in a cylinder of length L and radius $\mathcal{R}$, and subtracting the energy corresponding to a flat condensate $\mathcal{F}[\psi_0] = -g n_0^2 V / 2$, with $V = \pi \mathcal{R}^2 L$ the volume of the cylinder [PS16; PS08]. Using that the chemical potential satisfies $\mu = g n_0$ and adimensionalizing in the sense $R^2 = n_0 \tilde{R}^2$ and $\eta = r/\xi$, leads to the quantum vortex energy $E_v = \mathcal{F} - \mathcal{F}_0$,

$$E_v = \frac{L m n_0 \kappa^2}{4\pi} \int_0^{\mathcal{R}/\xi} \left[\left(\frac{d\tilde{R}}{d\eta}\right)^2 + \frac{q^2}{\eta^2} \tilde{R}^2 + \frac{1}{2}(\tilde{R}^2 - 1)^2\right] \eta \, d\eta, \tag{1.96}$$

that explicitly depends on the quantum of circulation $\kappa = 2\pi\sqrt{2} c\xi$ and the charge of the vortex q. In the limit $\mathcal{R}/\xi \gg 1$, the second term in the integral dominates and leads to the approximate result

$$E_v \simeq \frac{q^2 L m n_0 \kappa^2}{4\pi} \ln\left(\frac{\mathcal{R}}{|q|\xi}\right), \tag{1.97}$$

The energy corresponding to multiply-charged vortices is larger than for single-charged vortices, meaning that if a multiply-charged vortex is let to evolve freely, it usually decays into q single-charged vortices, that corresponds to a lower energy state [KHO+06; TTF+22].

1.3.1.6 Beyond mean-field corrections and generalized GP model

In the last 20 years, there has been some evidence that, in some particular configurations, the beyond mean-field interactions become important in the dynamics of BECs. For example, in attractive Bose-Bose mixtures, it has been observed both theoretically [Pet15] and experimentally [CTS+18; SFM+18] that the collapse of quantum
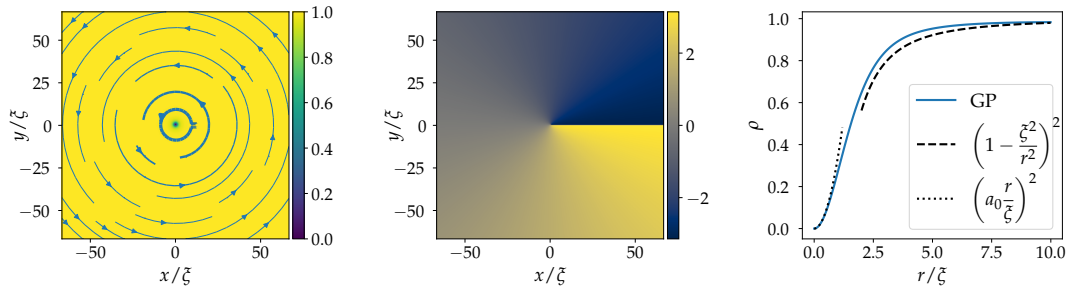
Figure 1.5: Quantum vortex solution in the Gross–Pitaevskii model. (a) Two dimensional mass density of a quantum vortex with the streamlines of the velocity field. Thicker lines indicate a stronger velocity field. (b) Phase generated by a quantum vortex. (c) Density profile obtained from numerical simulations of the Eq. (1.93). Dotted and dashed lines correspond to the limits of small and large r of Eq. (1.93), respectively.

droplets is suppressed by the beyond mean-field interaction between bosons. In dipolar BECs, characterized by the non-local interaction between bosons, the formation of these quantum droplets is also possible and is stabilized by the beyond mean-field interactions [CFF+23]. Currently, this system has attracted the interest of the low-temperature physics community due to the observation of supersolidity, a state that satisfies superfluidity properties in a self-organized crystalline structure [CPI+19; BSW+19; TLF+19].

The Gross–Pitaevskii equation describes the dynamics of a dilute gas of weakly interacting bosons, valid in the limit of $n|a_s|^3 \ll 1$, with a_s the scattering length and n the particles density. This quantity also corresponds to the ratio between the scattering length a_s and the coherence length ξ that, from Eqs. (1.69) and (1.40), can be also defined as

$$\xi = \frac{1}{\sqrt{8\pi n_0 a_s}}, \qquad (1.98)$$

with n_0 the ground state particles density. This means that a dilute BEC has a coherence length much larger than the typical length scale of the interaction between bosons.

In the limit of a weakly interacting boson gas, the chemical potential of the condensate in the absence of an external potential is $\mu = g n_0$. When the interactions between bosons become stronger, one has to go back in the derivation of the GP model to expression (1.37), before the mean-field approximation is performed. In this case, one needs to include the contribution of quantum fluctuations $\delta\hat{\Psi}$ from the Bogoliubov prescription $\hat{\Psi} = \psi + \delta\hat{\Psi}$, that lead to corrections proportional to a/ξ. The first order of the beyond mean-field correction to the chemical potential was first introduced by Lee, Huang and Yang in 1957 and goes as [LHY57; DGP+99; PS08]

$$\mu = g n_0 \left[1 + \frac{32}{3\sqrt{\pi}} (n_0 a_s^3)^{1/2} \right]. \qquad (1.99)$$

For the dynamical equation, the contribution of quantum fluctuations is also involved in the form of an extra high-order non-linear term proportional to $n^{3/2} = |\psi|^3$. The beyond mean-field Gross–Pitaevskii equation is [Sal18]

$$i\hbar \frac{\partial \psi}{\partial t} = \left[-\frac{\hbar^2}{2m} \nabla^2 + V_{\text{ext}} - \mu + g|\psi|^2 + g\frac{32}{3\sqrt{\pi}} a_s^{3/2} |\psi|^3 \right] \psi. \qquad (1.100)$$

The expression studied here takes into account only the first order contribution of quantum fluctuations. If we want to include the contribution of other effects, and to include a generic non-local interaction potential between bosons, we can write an effective generalized GP (gGP) model [BR99; BBP14]

$$ i\hbar \frac{\partial \psi}{\partial t} = \left[-\frac{\hbar^2}{2m} \nabla^2 + V_{\text{ext}} + g V_{\text{I}} * |\psi|^2 - (1+\chi)\mu + g\chi \frac{|\psi|^{2(\gamma+1)}}{n_0^\gamma} \right] \psi. \qquad (1.101) $$

with χ and γ two dimensionless parameters describing the amplitude and order of the extra non-linear term, respectively. The symbol $*$ denotes the convolution $V_{\text{I}} * |\psi|^2 = \int V_{\text{I}}(\mathbf{r} - \mathbf{r}')|\psi(\mathbf{r}')|^2 d\mathbf{r}'$. The interaction potential is normalized such that $\int V_{\text{I}} d\mathbf{r} = 1$. The chemical potential is redefined so that for a flat condensate in the absence of external potentials, it is independent of the beyond mean-field parameters χ and γ and equal to $\mu = gn_0$.

Perturbing Eq. (1.101) around the ground state and following the same procedure as in Sec. 1.3.1.3, we obtain a generalized dispersion relation

$$ \omega(k) = \tilde{c}k \sqrt{\frac{\tilde{\xi}^2 k^2}{2} + \frac{\hat{V}_{\text{I}}(k) + \chi(\gamma+1)}{1 + \chi(\gamma+1)}} \qquad (1.102) $$

where $\hat{V}_{\text{I}}(\mathbf{k}) = \int e^{i\mathbf{k}\cdot\mathbf{r}} V_{\text{I}}(\mathbf{r}) d\mathbf{r}$ is the Fourier transform of the interaction potential such that $\hat{V}_{\text{I}}(k=0) = 0$. In this model, the speed of sound and the healing length are now redefined as

$$ \tilde{c} = c\sqrt{1 + \chi(\gamma+1)} \qquad (1.103) $$

$$ \tilde{\xi} = \frac{\xi}{\sqrt{1 + \chi(\gamma+1)}} \qquad (1.104) $$

The gGP model introduced here is the one that I used in publications [MK20; MPK21; PMK21; MK22], where we study how the beyond mean-field terms affect the dynamics of the system, independently to the introduction of rotons.

1.3.1.7 Type of non-local interaction potentials

The choice of the non-local interaction potential in the Gross–Pitaevskii model depends on the microscopic physics of the system one wants to study. For instance, for a dilute gas, it is reasonable to assume that the interaction between bosons is weak and use the local potential $V_{\text{I}}(\mathbf{r} - \mathbf{r}') = g\delta(\mathbf{r} - \mathbf{r}')$. This is in fact a good approximation for BECs, however, for superfluid helium it is not the case as it fails to reproduce the roton minimum in the excitation spectrum discussed in Sec. 1.1. In particular, in a recent work of Reneuve et al. [RSC18], the authors studied the process of vortex reconnections in a regime with a roton minimum using an effective isotropic potential

$$ \hat{V}_{\text{I}}(\mathbf{k}) = \left[1 - V_1 \left(\frac{k}{k_{\text{rot}}} \right)^2 + V_2 \left(\frac{k}{k_{\text{rot}}} \right)^4 \right] \exp\left(-\frac{k^2}{2k_{\text{rot}}^2} \right), \qquad (1.105) $$

where k_{rot} is the wavenumber associated to the roton minimum, and V_1 and V_2 are two dimensionless parameters that are chosen to reproduce the excitation spectrum of superfluid helium shown in Fig. 1.3. They observed that, even though some of

the properties of the quantum vortices change with the introduction of the roton minimum, like the density profile, the reconnection process remains statistically the same as in the local GP model. In this Thesis, we will revisit this interaction potential including also beyond mean-field corrections as in Eq. (1.101), to include also the fact that interactions in liquid helium are strong. In particular, this model will be revisited in chapters 3-5, where we introduce publications [MK20; MPK21; PMK21; MK22]. In this framework, we study the statistical properties of quantum turbulence, Kolmogorov and Kelvin wave cascades, statistics of velocity circulation, intermittency, and the process of roton creation and vortex nucleation.

Another system in which the interaction between bosons is non-local are dipolar BECs. Here, the interaction is given by the anisotropic dipole-dipole potential [LMS⁺09; CFF⁺23]

$$V_{\mathrm{dd}}(\mathbf{r} - \mathbf{r}') = \frac{\mu_0 \mu^2}{4\pi} \frac{1 - 3\cos^2(\theta)}{|\mathbf{r} - \mathbf{r}'|^3} \tag{1.106}$$

where μ_0 is the magnetic permeability in vacuum, μ the magnetic dipole moment and θ is the angle between the vector distance between the dipoles and the polarization direction. One interesting remark on the dipole-dipole interaction potential is that, when the dipolar BEC is confined in at least one direction, the excitation spectrum starts exhibiting a roton minimum [SSL03].

1.3.2 Vortex filament model

The GP model, introduced in Sec. 1.3.1, predicts the presence of quantized vortices as topological defects with a quantized circulation $\Gamma = \oint_C \mathbf{v}_{\mathrm{s}} \cdot d\mathbf{l} = n\kappa$. This is a first principles model that allows one to study the physics at microscopic scales, of the order of the vortex core size. At these scales we find some relevant processes like vortex nucleation [FPR92; HB97; Ric01; VS18] and vortex reconnections [KL93; BLS06; SGI⁺17; VPK17; VPK20]. For larger systems with an increasing number of vortices, solving the GP equation might become too expensive and what happens at microscopic scales might become less relevant than macroscopic scales. On the other hand, there is the two-fluid model, introduced in Sec. 1.1 and discussed more in detail in Sec. 1.3.3, that is able to describe phenomena at macroscopic scales and finite temperatures like second sound [Don91]. However, the presence of quantum vortices is not captured in this model. Also, at very low temperatures, the two-fluid model starts to fail as the normal component vanishes, and the interaction between quantum vortices is what dominates the dynamics of the flow. Therefore, there is an interest in developing a model at mesoscopic scales that captures the dynamics of vortex lines. The vortex filament model (VFM) was introduced by Schwarz in 1985 [Sch85] and since then several works were done to study vortex reconnection [Sch85; ZCB⁺12], Kelvin waves along vortex lines [KVS⁺01; BDL⁺11; BB11; BL14], superfluid turbulence [Sch88; BSB⁺97; ATN02; BLB12; KKL⁺15], topology of vortex knots [RSB99], among other interesting topics. In this model, the vorticity field of the superfluid is considered as a collection δ-supported structures with the same circulation value, which in Helium II is $\kappa \approx 10^{-3}$ cm²s⁻¹.

For a single vortex line, the vorticity is given by the rotational of the superfluid velocity field [Don91; BDV⁺01; Nem13]

$$\boldsymbol{\omega}(\mathbf{r}, t) = \boldsymbol{\nabla} \times \mathbf{u}_{\mathrm{s}} = \kappa \int \mathbf{s}'(\chi, t)\delta(\mathbf{r} - \mathbf{s}(\chi, t))d\chi, \tag{1.107}$$

with $\mathbf{s}(\chi, t)$ the parametrization of the vortex filament, and the prime denotes differentiation over the arc length χ. The self-induced velocity field of a vortex line in the absence of boundaries can be obtained using the Biot-Savart law

$$\mathbf{v}_{\mathrm{s}}(\mathbf{r}, t) = \frac{\kappa}{4\pi} \int \frac{\mathbf{s}' \times (\mathbf{r} - \mathbf{s}(\chi, t)) \mathrm{d}\chi}{|\mathbf{r} - \mathbf{s}(\chi, t)|^3}. \tag{1.108}$$

In superfluid helium, the vortex core size is of the order $a_0 \sim 10^{-8}$ cm. This expression for the velocity field assumes infinitely thin vortices, hence it only applies far away from the lines, in the limit $|\mathbf{s} - \mathbf{r}| \gg a_0$. In fact, it is easily seen that the velocity field on each line $\mathbf{r} = \mathbf{s}$ diverges. This behavior is also observed in the GP context, but the divergence of the velocity field comes together with a vanishing density at the vortex core, regularizing thus the energy (see Sec. 1.3.1.5). In the VFM, this divergence needs to be regularized using the vortex core size a_0 as a cutoff [KKL+15]. An interesting remark is that the Biot-Savart equation (1.108) can be obtained systematically from the GP equation in the limit of the curvature radius of the vortex lines and the intervortex distance ℓ much larger than the healing length ξ, in the absence of background noise [BN15].

To obtain the time evolution of an individual vortex line, we need to know all the forces acting on it. At zero temperature, the only force acting on the filament is the Magnus force $\mathbf{f}_{\mathrm{M}}$, that arises from a body with an intrinsic circulation moving within the flow. Indeed, the circulation creates a pressure imbalance around the vortex and generates a force that can be written as

$$\mathbf{f}_{\mathrm{M}} = \rho_{\mathrm{s}} \kappa \mathbf{s}' \times (\dot{\mathbf{s}} - \mathbf{v}_{\mathrm{tot}}). \tag{1.109}$$

Here, ρ_{s} is the superfluid density and $\mathbf{v}_{\mathrm{tot}}$ the total velocity of the surrounding superfluid, given by the sum of the self-induced velocity field (1.108) and any externally applied velocity $\mathbf{v}_{\mathrm{tot}} = \mathbf{v}_{\mathrm{s}} + \mathbf{v}_{\mathrm{ext}}$. Using that the sum of all forces is equal to zero $\mathbf{f}_{\mathrm{M}} = 0$ as the inertia of the vortex can be neglected, we obtain an expression for the evolution of the vortex line at zero temperature

$$\dot{\mathbf{s}} = \mathbf{v}_{\mathrm{s}} + \mathbf{v}_{\mathrm{ext}}. \tag{1.110}$$

The computation of the self-induced velocity field (1.108) is, in general, complicated as it is non-local, meaning that the velocity of each point of the vortex line depends explicitly on the position of the whole filament. One way of simplifying this integral is to perform the so-called Local Induction Approximation (LIA) that, as the name suggests, considers only local contributions to the velocity field [Don93; AH65]. In this approximation, one assumes that each point of the filament has a local radius of curvature R. Performing a Taylor expansion of the vortex filament $\mathbf{s}(\chi + \epsilon) \approx \mathbf{s}(\chi) + \mathbf{s}'(\chi)\epsilon$ and replacing it in the Biot-Savart integral (1.108) one obtains

$$\mathbf{v}_{\mathrm{s}}(\mathbf{r}, t) \approx \mathbf{v}_{\mathrm{LIA}}(\mathbf{r}, t) = \frac{\kappa}{4\pi} \ln\left(\frac{L}{a_0}\right) \mathbf{s}' \times \mathbf{s}''. \tag{1.111}$$

where the choice of L to obtain a good approximation of the original integral depends on the configuration of the vortices. The cross product $\mathbf{s}' \times \mathbf{s}''$ has the magnitude $1/R$, with R the local curvature at the point $\mathbf{s}(\xi)$.

At finite temperatures, we need to consider an extra force acting on the vortex lines due to the mutual friction with the normal fluid component: the drag force $\mathbf{f}_{\mathrm{D}}$.

This term depends on the superfluid temperature, and is proportional to the normal fluid velocity $\mathbf{v}_n$

$$\mathbf{f}_D = -\alpha \rho_s \kappa \mathbf{s}' \times \left[\mathbf{s}' \times (\mathbf{v}_n - \mathbf{v}_s - \mathbf{v}_{\text{ext}}) \right] - \alpha' \rho_s \kappa \mathbf{s}' \times (\mathbf{v}_n - \mathbf{v}_s - \mathbf{v}_{\text{ext}}). \qquad (1.112)$$

Here, α and α' are two temperature dependent dimensionless parameters written in terms of the mutual friction coefficients B and B' defined by $\alpha(T) = \rho_n(T)B(T)/(2\rho)$ and $\alpha'(T) = \rho_n(T)B'(T)/(2\rho)$. The mutual friction coefficients are related to the parallel and perpendicular exchange of moments, respectively, and are determined experimentally [SD90]. Again, using that the sum of all forces equals zero $\mathbf{f}_M + \mathbf{f}_D = 0$, we obtain that the vortex filament obeys the following equation of motion

$$\dot{\mathbf{s}} = \mathbf{v}_s + \mathbf{v}_{\text{ext}} + \alpha \mathbf{s}' \times (\mathbf{v}_n - \mathbf{v}_s - \mathbf{v}_{\text{ext}}) + \alpha'(\mathbf{v}_n - \mathbf{v}_s - \mathbf{v}_{\text{ext}}) \qquad (1.113)$$

As discussed before, the VFM is good at describing the physics of quantum vortices and superfluid turbulence at mesoscales [BLB12; BL14]. However, as the physics of microscales is not taken into account, vortex reconnections have to be included in the model in an *ad hoc* manner. The usual technique is to force a reconnection process whenever two vortex lines are closer than some parameter δ. Another process that the VFM is not able to capture are sound waves. These are density perturbations of the superfluid, and are usually triggered when vortices reconnect. However, in this model the density of the system is flat and constant in time, so only the superfluid component can be studied.

One last remark on the VFM at finite temperatures is that usually the normal fluid velocity $\mathbf{v}_n$ is prescribed and taken constant in time, neglecting the back-reaction with vortices. The dynamics of the normal fluid velocity is given by the incompressible Navier–Stokes equations

$$\rho_n \left[\frac{\partial \mathbf{v}_n}{\partial t} + (\mathbf{v}_n \cdot \boldsymbol{\nabla})\mathbf{v}_n \right] = -\frac{\rho_n}{\rho} \boldsymbol{\nabla} p - \rho_s s \boldsymbol{\nabla} T + \mu \nabla^2 \mathbf{v}_n + \mathbf{F}_{\text{ns}} \qquad (1.114)$$

$$\boldsymbol{\nabla} \cdot \mathbf{v}_n = 0 \qquad (1.115)$$

where p is the pressure, μ the dynamic viscosity, s the entropy per unit of mass, T the temperature and $\mathbf{F}_{\text{ns}}$ the mutual friction force. The idea of coupling the VFM with the Navier–Stokes equations in a self-consistent way was first proposed in 2000 to study the dynamics of simple vortex configurations [IWB+00; KBS00], like the propagation of a superfluid vortex ring. Later, there were also some attempts to study two-dimensional systems [GSB15; GSB17] and decaying superfluid turbulence [Kiv15]. One of the main disadvantages of this model is that the coupling between these two models becomes computationally very expensive, and therefore the spatial resolution to solve the Navier–Stokes equations or the number of vortex filaments that can be introduced in the superfluid are limited. However, in the last few years, the state-of-the-art of numerical simulations of this system has improved steadily [YTK18; YKT+20; IT21; GBB+20; GKB23]. This model is good to study how is the interaction between the superfluid and the normal fluid components. For example, it can be useful to develop better models for the mutual friction, and to characterize the transition to turbulence of each fluid component independently, known as T1-T2 transition [MT83].

1.3.3 The two-fluid HVBK equations

As introduced in Sec. 1.1, the basis of the phenomenology of superfluid helium is that, at temperatures below the lambda point and above zero, helium behaves as a mixture of two fluid components, the inviscid superfluid and the viscous normal fluid [LL87]. The total density of the fluid is $\rho = \rho_s + \rho_n$ with ρ_s and ρ_n the density of the superfluid and normal components, respectively. The relative fraction of superfluid and normal fluid depends on temperature, with the superfluid component vanishing at $T = T_\lambda$, and the normal fluid vanishing at $T = 0$. The experimental temperature dependence of helium II is shown in Fig. 1.3.

The dynamics of the normal fluid component $\mathbf{v}_n$ is given by the Navier–Stokes equations, while the superfluid component $\mathbf{v}_s$ follows Euler equations due to its inviscid nature. The total dynamics of superfluid helium is then described by the so-called Hall-Vinen-Bekarevich-Khalatnikov (HVBK) equations

$$\rho_n \left[\frac{\partial \mathbf{v}_n}{\partial t} + (\mathbf{v}_n \cdot \boldsymbol{\nabla}) \mathbf{v}_n \right] = -\boldsymbol{\nabla} p_n - \rho_s s \boldsymbol{\nabla} T + \mu \nabla^2 \mathbf{v}_n - \mathbf{F}_{ns} \qquad (1.116)$$

$$\rho_s \left[\frac{\partial \mathbf{v}_s}{\partial t} + (\mathbf{v}_s \cdot \boldsymbol{\nabla}) \mathbf{v}_s \right] = -\boldsymbol{\nabla} p_s + \rho_s s \boldsymbol{\nabla} T + \mathbf{F}_{ns} \qquad (1.117)$$

where T is the temperature, s the entropy per unit of mass, μ the dynamic viscosity of the normal fluid, and $p_{n,s} = (\rho_{n,s}/\rho)p$ with p the hydrodynamic pressure. The mutual friction force $\mathbf{F}_{ns}$ couples the dynamics between the normal and superfluid components that, mediated by quantized vortices, transfers momentum between them. These equations take the name HVBK due to the contribution of the authors in the understanding of the mutual friction force [HV56; BK61], which can be approximated as $\mathbf{F}_{ns} \simeq \alpha \rho_s \Omega_0 (\mathbf{v}_n - \mathbf{v}_s)$. Here, $\alpha = \alpha(T)$ is a temperature dependent mutual friction parameter, and Ω_0 a frequency that, following the phenomenological approach of Stalp et al. [SSD99], can be estimated as $\Omega_0 \approx \kappa \mathcal{L}$ with $\mathcal{L}$ the vortex line density and κ the quantum of circulation. A key aspect of the HVBK equations is that they describe the dynamics of superfluid helium at a macroscopic scale, smoothing out the discrete nature of vortices. This model then is not able to capture some interesting interactions between quantum vortices like reconnections or Kelvin waves (see Sec. 1.4). Instead, it introduces a coarse-grained superfluid vorticity field $\boldsymbol{\omega}_s$ that allows us to account for the fluid motion at scales larger than the mean intervortex distance ℓ. The frequency Ω_0 (and the vortex line density) can be estimated using this superfluid vorticity field as $\Omega_0^2 \approx \langle \omega_s^2 \rangle / 2$ [BLN+15; BKL+18; PK20b]. It is important to remark that this relation is not obtained from first principle and is just a phenomenological estimation.

The superfluid is also considered to be irrotational $\boldsymbol{\nabla} \times \mathbf{v}_s = 0$, with zero entropy, and if the dissipation processes are small, we can assume conservation of mass and entropy [LL87; Don91]

$$\frac{\partial \rho}{\partial t} + \boldsymbol{\nabla} \cdot \mathbf{j} = 0 \qquad (1.118)$$

$$\frac{\partial (\rho s)}{\partial t} + \boldsymbol{\nabla} \cdot (\rho s \mathbf{v}_n) = 0 \qquad (1.119)$$

with the total momentum $\mathbf{j} = \rho_n \mathbf{v}_n + \rho_s \mathbf{v}_s$. Note that the entropy is carried only by the normal fluid. We can apply some small perturbations into the two-fluid equations (1.116)-(1.119) around equilibrium values ρ, ρ_s, ρ_n, T and s and linearize to

obtain some wave propagation. Indeed, we obtain that the system allows two kind of waves, known as first and second sound, that respectively propagate at speeds

$$u_1^2 = \frac{\partial p}{\partial \rho} \quad ; \quad u_2^2 = \frac{Ts^2 \rho_s}{C_v \rho_n} \tag{1.120}$$

with C_v the heat capacity at constant volume. The first sound is associated to the classical pressure-density waves, while the second sound is a quantum mechanical phenomenon corresponding to entropy-temperature waves. Note that at the lambda-point temperature, the second sound speed goes to zero as the superfluid density ρ_s vanishes.

The two-fluid HVBK equations (1.116)-(1.117) can be used to study the properties of superfluid turbulence by performing numerical simulations [BSS14]. For this matter, an effective superfluid kinematic viscosity ν_s is usually introduced into the system to account for the damping of superfluid vorticity taking place at scales smaller than the intervortex distance, due to quantum vortex reconnections and Kelvin waves. It is also useful to prevent possible numerical instabilities. The normal and superfluid components are also considered to be incompressible. Numerical simulations of the incompressible HVBK equations of superfluid turbulence have shown that some of the phenomenology of classical and quantum turbulence are similar, as the presence of a Kolmogorov-like cascade [RBL09; BKL+18]. It was observed that introducing a mean counterflow generates some large-scale anisotropic structures in the flow, that have been also associated with the presence of a quasi-bidimensionalization of the flow with evidence of an inverse energy cascade [BKL+19a; PK20a].

1.4 Vortex interactions

In this section, we will focus on the different type of vortex interactions taking place in a superfluid. In particular, in Sec. 1.4.1 we introduce Kelvin waves, helical displacements that propagate along vortex lines. In Sec. 1.4.2, we describe the process of vortex reconnection, taking place when two vortices approach to each other and interact changing their topology. These kind of interactions govern the dynamics of a superfluid at small scales and are also relevant in superfluid turbulence, as will be discussed in chapter 2.

1.4.1 Kelvin waves

When a disturbance is introduced into a straight vortex, the perturbation will start to propagate along it. These helicoidal excitations can be triggered in a superfluid due to interaction with thermal fluctuations, with large heavy particles, external forcings, or in extreme events such as vortex reconnections [FMO+14; BSS14; GK19; VPK20]. Sir William Thomson (better known as Lord Kelvin) predicted the existence of these excitations and studied how is the dispersion relation of the perturbation for vortices of different nature [Tho80]. Here, we will focus only in the case of hollow core vortices in an ideal fluid. The dispersion relation in this case is

$$\omega_{KW}(k) = \frac{\kappa}{2\pi a_0^2} \left[1 - \sqrt{1 + ka_0 \frac{K_0(ka_0)}{K_1(ka_0)}} \right] \tag{1.121}$$
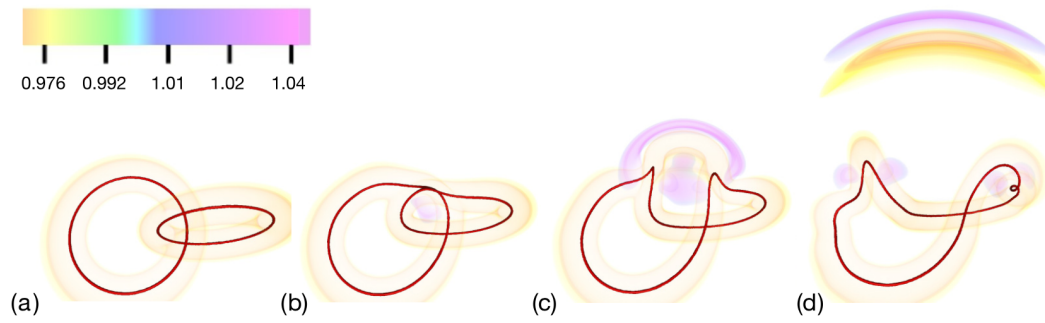
Figure 1.6: Snapshots of the density field during a quantum vortex reconnection process at different times. The initial state corresponds to a Hopf link. As the system evolves, vortices approach each other until they touch and reconnect, emitting a sound pulse. Extracted from [PK20c].

where a_0 is the vortex core radius and K_n is the modified modified Bessel function of order n. Expanding the Bessel functions in the limit of $ka_0 \ll 1$, we obtain the simplified expression for the Kelvin waves dispersion relation

$$\omega_{\text{KW}}(k) = -\frac{\kappa}{4\pi}k^2 \left[\ln\left(\frac{2}{ka_0}\right) - \gamma \right] \tag{1.122}$$

with $\gamma = 0.5772$ the Euler's constant.

In the Gross–Pitaevskii framework, the vortex core size is taken as $a_0 = 1.1265\xi$ [Rob03; GK20]. Numerical simulations of this model have been used to study the dispersion relation of Kelvin waves generated by individual quantum vortices or tangles of vortices, how it affects the energy spectrum of the system, and how particles can be used to try to sample these excitations [Krs12; CMB16; GK20]. Similar studies were also performed in numerical simulations of the vortex filament model [BL14]. Experimentally, Kelvin waves have been observed by tracking the motion of submicron particles in superfluid helium [FMO+14]. Kelvin waves can also interact between themselves non-linearly, a phenomenon that is described using the weak wave turbulence theory [Naz11]. Further discussions on Kelvin waves in superfluid turbulence is presented in chapter 2, where I introduce publication [MK20], and I study the Kelvin-wave cascade in a generalized GP model with the presence of a roton minimum in the excitation spectrum.

1.4.2 Quantum vortex reconnections

Kelvin's circulation theorem states that in a classical ideal flow, the circulation around a closed loop

$$\Gamma = \oint_{\mathcal{C}} \mathbf{u} \cdot d\mathbf{l} \tag{1.123}$$

is a conserved quantity along a material curve $\mathcal{C}$. As a consequence, vortex reconnections are forbidden in inviscid fluids. In a superfluid, in spite of its lack of viscosity, reconnections are still allowed as the density of the superfluid vanishes at the core of quantum vortices, introducing a discontinuity in the velocity field. This picture was first suggested in 1955 by Feynman [Fey55], and later confirmed by numerical simulations of the Gross–Pitaevskii equation [KL93]. Since then, reconnections have

been experimentally observed in superfluid helium [BPS$^+$08; PFS$^+$08; ŠLM19] and in
BECs [SGI$^+$17; GBP$^+$19].

The process of quantum vortex reconnection consists in two vortices that approach to each other, touch in one point, reconnect by changing their topology and separate (see Fig.1.6). It is a very important process in superfluid turbulence as it acts as a dissipative mechanism at small scales [VN02; Nem13]. In particular, when vortices reconnect, they emit a sound pulse, transferring thus part of their energy into sound. This behavior was confirmed by numerical simulations of the GP equation [LWS$^+$01; PK20c; VPK20]. During the reconnection event, Kelvin waves are triggered, which then interact in a non-linear way redistributing the energy into different scales. When energy reaches the smallest scale of the system, i.e. the healing length ξ, it is radiated into sound [PL11]. Even though the vortex filament model does not capture directly quantum vortex reconnections, they can be incorporated as an *ad hoc* process to reproduce some quantitative results also observed in the GP model [KBL11; ZCB$^+$12].

One of the simplest ways of characterizing a reconnection event is by studying how the minimal distance between these two vortices varies on time. Using dimensional analysis, one can assume that the only magnitude relevant for the reconnection is the quantum circulation κ. Then, it is easy to see that the vortex filaments approach and separate following

$$\delta^{\pm}(t) = A^{\pm}(\kappa|t - t^*|)^{1/2} \tag{1.124}$$

where $A^{\pm}$ is a dimensionless parameter of order one before (-) and after (+) the reconnection time t^*. The scaling $\delta \sim t^{1/2}$ for vortex reconnections has been observed experimentally in superfluid ^{4}He using particle tracking velocimetry techniques [PFL10; FSL19]. In recent works, it was shown by numerical simulations of the GP model that these amplitudes satisfy $A^+ > A^-$ exhibiting a time asymmetry, that can be understood by the sound emission during the reconnection as an irreversible energy transfer mechanism [PK20c; VPK20].

Chapter 2

Classical and quantum turbulence

In this chapter, we introduce the main concepts on fluid dynamics and turbulence. We first present the Navier–Stokes equations and the basic notions of classical fluids, such as viscosity, vorticity, Reynolds number and energy balance equations. We discuss the phenomenology of turbulent flows taking place in the limit of infinite Reynolds number and introduce the concepts of Richardson cascade, energy flux and structure functions. We derive the famous four-fifths law, exact result for homogeneous and isotropic turbulence, and discuss the phenomenology of two-dimensional turbulence, characterized by the presence of an inverse energy cascade. We then present the phenomenology of quantum turbulence, the complex and chaotic dynamics of quantum vortex tangles. We describe the different regimes taking place in this system, some of them resembling classical flows like Kolmogorov turbulence, and some of them differing, like Kelvin wave, Vinen and counterflow turbulence. The phenomenology of two-dimensional quantum turbulence is also discussed. Finally, we introduce the main notions of intermittency in turbulence. We present some properties of scaling exponents of structure functions, and provide a review of different multifractal models used to describe the anomalous scaling of turbulent flows. We discuss the role of velocity circulation in intermittency.

Classical and quantum fluids are, in principle, very different systems. The former is a viscous flow while in the latter viscosity is identically zero, meaning that it can flow freely without loss of kinetic energy. Vorticity has a very different nature in classical and quantum fluids, taking continuous values in the former, while in the latter it is concentrated along lines with a quantized circulation. In this work, we will consider only the phenomenology of incompressible classical fluids, while quantum fluids are compressible supporting density fluctuations and acoustic emissions. At finite temperatures, superfluids can be described as a two fluid system, while classical fluids consist only of one component. In spite of all these differences, in certain regimes both systems present great resemblances when it comes to turbulence.

In Sec. 2.1 we will introduce the Navier–Stokes equations, discuss its phenomenology and present some exact results of classical turbulence, both in two and three dimensions. In Sec. 2.2 we will introduce the phenomenology of superfluid turbulence, including a short review on the experimental and numerical results on two and three dimensions. We focus on the similarities and differences with classical turbulent flows and the different regimes present in this system. Finally, in Sec. 2.3 we introduce the basic concepts of intermittency, showing some of the properties of scaling exponents of structure functions. We also introduce the main phenomenological models describing the anomalous scaling.

2.1   Classical turbulence

Turbulence is the disordered and chaotic spatiotemporal motion of fluids. This phenomenon takes place in a wide variety of systems in nature, for example in biological fluids like blood circulatory system or at the wake of the wings of birds and insects. It also takes place in engineering, like in liquids flowing inside pipes, or in the air around planes. At larger scales, it is observed in geophysical fluids like in rivers, atmospheres and oceans, or in astrophysical flows, like interstellar or intergalactic media. These systems are characterized by very different length scales, from a few centimeters to astronomical units. In this section, we will introduce some of the universal properties of turbulence in two and three dimensions [MYL81; Fri95; Pop00; Bat00; Dav13].

2.1.1   The Navier–Stokes equations

The dynamics of an incompressible viscous fluid is given by the Navier–Stokes (NS) equations [Bat00; Dav13]

$$\frac{\partial \mathbf{u}}{\partial t} + (\mathbf{u} \cdot \boldsymbol{\nabla})\mathbf{u} = -\frac{1}{\rho}\boldsymbol{\nabla}p + \nu\nabla^2\mathbf{u} + \mathbf{f}, \tag{2.1}$$

$$\boldsymbol{\nabla} \cdot \mathbf{u} = 0, \tag{2.2}$$

with $\mathbf{u} = (u_x(\mathbf{r}, t), u_y(\mathbf{r}, t), u_z(\mathbf{r}, t))$ the velocity field, $p(\mathbf{r}, t)$ the pressure, ρ the fluid mass density, ν the kinematic viscosity and $\mathbf{f}(\mathbf{r}, t)$ an external forcing per unit of mass. To solve this equations, it is necessary to provide initial and boundary conditions. The second term of the l.h.s of Eq. (2.1) is the advective or non-linear term, while the second one of the r.h.s is the diffusive term. By comparing these two terms, we can define the famous dimensionless Reynolds number

$$\mathrm{Re} \sim \frac{|(\mathbf{u} \cdot \boldsymbol{\nabla})\mathbf{u}|}{|\nu\nabla^2\mathbf{u}|} \sim \frac{UL}{\nu}, \tag{2.3}$$

where U and L are a characteristic velocity and length scale, respectively. In the limit of low Reynolds numbers $\mathrm{Re} \ll 1$, the diffusive term dominates the dynamics of the fluid, attenuating velocity gradients. A flow in this regime is said to be laminar. For $\mathrm{Re} \gg 1$, the inertial term becomes dominant and the fluid enters into a turbulent regime.

Taking the curl in Eq. (2.1), leads to an equation for the temporal evolution of the vorticity field $\boldsymbol{\omega} = \boldsymbol{\nabla} \times \mathbf{u}$, that for a barotropic flow ($\boldsymbol{\nabla} \times \frac{1}{\rho}\boldsymbol{\nabla}p = 0$) is

$$\frac{\partial \boldsymbol{\omega}}{\partial t} + (\mathbf{u} \cdot \boldsymbol{\nabla})\boldsymbol{\omega} = (\boldsymbol{\omega} \cdot \boldsymbol{\nabla})\mathbf{u} + \nu\nabla^2\boldsymbol{\omega} + \mathbf{f}_\omega, \tag{2.4}$$

where $\mathbf{f}_\omega = \boldsymbol{\nabla} \times \mathbf{f}$. The first term of the r.h.s corresponds to vortex stretching. Note that in two dimensions, this term is identically zero as $\mathbf{u}$ and $\boldsymbol{\omega}$ are perpendicular.

Multiplying the NS Eqs. (2.1) by $\mathbf{u}$ and integrating over a volume V using periodic boundary conditions leads to an energy balance equation

$$\frac{\mathrm{d}E}{\mathrm{d}t} = -2\nu\Omega, \tag{2.5}$$

with $E = V^{-1}\int\frac{|\mathbf{u}|^2}{2}\mathrm{d}V$ the energy per unit mass and $\Omega = V^{-1}\int\frac{|\boldsymbol{\omega}|^2}{2}\mathrm{d}V$ the mean enstrophy.

For periodic flows in a cubic system of size $L = 2\pi$, the velocity and pressure fields can be written as a linear combination of the Fourier modes as [Fri95; Pop00]

$$\mathbf{u}(\mathbf{r}, t) = \sum_{\mathbf{k}} \hat{\mathbf{u}}_{\mathbf{k}}(t) e^{i\mathbf{k}\cdot\mathbf{r}}, \tag{2.6}$$

$$p(\mathbf{r}, t) = \sum_{\mathbf{k}} \hat{p}_{\mathbf{k}}(t) e^{i\mathbf{k}\cdot\mathbf{r}}, \tag{2.7}$$

with the Fourier transform defined as $\hat{\mathbf{u}}_{\mathbf{k}} = (2\pi)^{-3} \int \mathbf{u}(\mathbf{r}) e^{-i\mathbf{k}\cdot\mathbf{r}} d\mathbf{r}$ and $\mathbf{k} \in \frac{2\pi}{L}\mathbf{Z}$ the wavenumbers. Replacing this decomposition into Eq. (2.1), we can write the Navier–Stokes equations in Fourier space

$$\partial_t \hat{\mathbf{u}}_{\mathbf{k}} + \sum_{\mathbf{p}+\mathbf{q}=\mathbf{k}} (\hat{\mathbf{u}}_{\mathbf{p}} \cdot i\mathbf{q}) \hat{\mathbf{u}}_{\mathbf{q}} = -i\mathbf{k}\hat{p}_{\mathbf{k}} - \nu k^2 \hat{\mathbf{u}}_{\mathbf{k}} + \hat{\mathbf{f}}_{\mathbf{k}}, \tag{2.8}$$

valid for each Fourier mode $\mathbf{k}$. Note that the non-linear term establishes that the interaction between modes takes place in triads satisfying the relation $\mathbf{p} + \mathbf{q} = \mathbf{k}$. Multiplying Eq. (2.8) by $\mathbf{k}$ and using the incompressibility condition $\mathbf{k} \cdot \hat{\mathbf{u}}_{\mathbf{k}} = 0$ leads to an expression for the pressure

$$\hat{p}_{\mathbf{k}} = \frac{i\mathbf{k} \sum_{\mathbf{p}+\mathbf{q}=\mathbf{k}} (\hat{\mathbf{u}}_{\mathbf{p}} \cdot i\mathbf{q}) \hat{\mathbf{u}}_{\mathbf{q}}}{k^2}. \tag{2.9}$$

Defining the projector $\mathcal{P}_{\mathbf{k}} = (1 - \mathbf{k}\frac{\mathbf{k}}{k^2}\cdot)$ that removes the compressible component from the velocity field, we can rewrite the NS equations only in terms of the velocity modes as

$$\partial_t \hat{\mathbf{u}}_{\mathbf{k}} = -\mathcal{P}_{\mathbf{k}} \left[\sum_{\mathbf{p}+\mathbf{q}=\mathbf{k}} (\hat{\mathbf{u}}_{\mathbf{p}} \cdot i\mathbf{q}) \hat{\mathbf{u}}_{\mathbf{q}} \right] - \nu k^2 \hat{\mathbf{u}}_{\mathbf{k}} + \hat{\mathbf{f}}_{\mathbf{k}} \tag{2.10}$$

Multiplying Eq. (2.10) by $\hat{\mathbf{u}}_{\mathbf{k}}^*$ and integrating over shells of radius k given by the solid angle $\int_{S_k} dS_k$ leads to the scale-by-scale energy budget

$$\frac{dE}{dt}(k) = T(k) - 2\nu\Omega(k) + F(k) \tag{2.11}$$

with the energy spectrum per unit of mass $E(k) = V^{-1} \int_{S_k} \frac{|\hat{\mathbf{u}}_{\mathbf{k}}|^2}{2} dS_k$, the energy transfer function scale-by-scale $T(k) = \int_{S_k} \int\int_{\mathbf{p}+\mathbf{q}=\mathbf{k}} \{\hat{\mathbf{u}}_{\mathbf{k}}^* \cdot \mathcal{P}_{\mathbf{k}} [(\hat{\mathbf{u}}_{\mathbf{p}} \cdot i\mathbf{q})\hat{\mathbf{u}}_{\mathbf{q}}] + c.c.\} d\mathbf{p}d\mathbf{q}dS_k$ where *c.c.* denotes the complex conjugate, the enstrophy spectrum $\Omega(k) = k^2 E(k)$ and the forcing $F(k) = \int \hat{\mathbf{u}}_{\mathbf{k}}^* \cdot \hat{\mathbf{f}}_{\mathbf{k}} dS_k$. The energy transfer function $T(k)$ is conservative, and a positive (negative) sign of this quantity determines an increase (decrease) of the energy of the mode k. The total energy and enstrophy are given by $E = \int E(k)dk$ and $\Omega = \int \Omega(k)dk$, respectively.

As the transfer function is conservative, it can be written as the gradient of a potential $T(k) = -\partial_k \Pi(k)$. Then, integrating Eq. (2.11) up to a wavenumber K in the absence of an external forcing leads to an explicit equation for the energy flux Π

$$\frac{dE^<}{dt}(K) = -\Pi(K) - 2\nu\Omega^<(K), \tag{2.12}$$

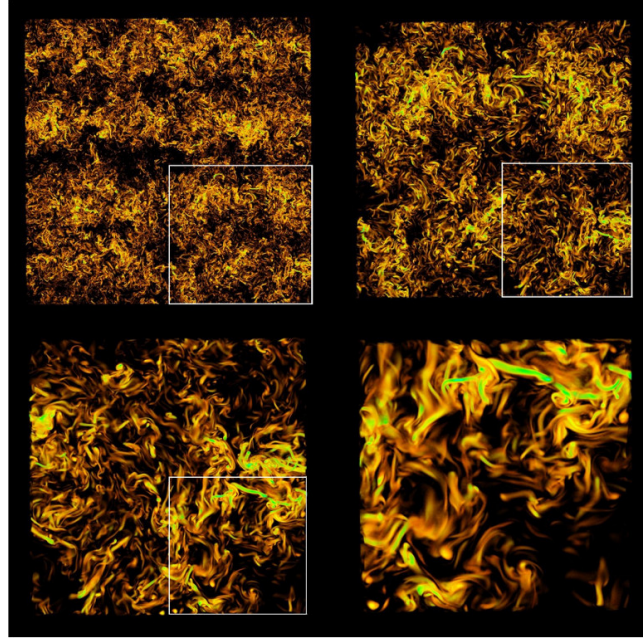where $g^<(K) = \int_0^K g(k)dk$ is a low-pass filtered function.

Figure 2.1: Visualization of vorticity in a numerical simulation of homogeneous isotropic turbulence using 2048^3 collocation points. From left to right, the white square shows the region that is zoomed in. Extracted from [MAP08].

2.1.2   Phenomenology of three-dimensional turbulence

One of the most relevant processes in turbulence is the phenomenon of energy cascade. Richardson proposed a picture of turbulence in which the fluid is composed by a set of whirls or eddies, structures of the flow of size r with a characteristic velocity u_r and a time scale $t_r = r/u_r$. The largest eddy has a characteristic length scale L_0 comparable with the size of the system L with a velocity $u_0 \sim u_{\text{rms}} = \sqrt{2E/3}$. In this picture, the largest eddies interact between themselves creating smaller ones, that also break down becoming smaller and smaller eddies. This process continues until the eddies reach scales small enough such that energy is dissipated as heat due to viscosity.

In 1941, Kolmogorov formalized this picture of turbulence [Kol41; MYL81; Fri95; Pop00]. He first assumed three hypotheses for turbulence. From now on, we will call this theory K41. The first of these hypotheses is that, in the limit Re $\gg$ 1, the small-scale turbulent motions are statistically homogeneous and isotropic. Here, by small scales we mean $L_0 \gg r \gg \eta$, with η the scale where dissipation starts acting on the eddies. This range of scales is known as *inertial range*. Before discussing about homogeneity and isotropy, let us introduce the velocity increments

$$\delta \mathbf{u}(\mathbf{x}, \mathbf{r}) = \mathbf{u}(\mathbf{x} + \mathbf{r}) - \mathbf{u}(\mathbf{x}), \tag{2.13}$$

where $\mathbf{r}$ is the distance between two points in space. By homogeneity we mean that $\delta \mathbf{u}(\mathbf{x} + \mathbf{x}', \mathbf{r})$ and $\delta \mathbf{u}(\mathbf{x}, \mathbf{r})$ are statistically equivalent, sharing the same probability distribution functions, while isotropy means that the statistical properties of velocity increments remain invariant under simultaneous rotations of $\mathbf{r}$ and $\delta \mathbf{u}$.

Kolmogorov's second hypothesis states that in the limit of Re $\gg$ 1, the turbulent flow is self-similar in the inertial range of scales in the sense

$$\delta \mathbf{u}(\mathbf{x}, \lambda \mathbf{r}) = \lambda^h \delta \mathbf{u}(\mathbf{x}, \mathbf{r}) \tag{2.14}$$

with h the scaling exponent known as Hölder exponent. To support the idea of self-similarity within the inertial range of turbulent flows, in Fig. 2.1 we show a visualization of a turbulent flow obtained from direct numerical simulations (DNS) of the incompressible Navier–Stokes equations [MAP08]. As we zoom in into different regions of the turbulent flow, it seems to be scale invariant. When we reach very small scales, the scale invariance breaks down. Finally, the third hypothesis proposes that, under the assumptions of the first two hypotheses, a turbulent flow has a non-vanishing mean energy dissipation rate

$$\epsilon = \langle \epsilon(\mathbf{x}) \rangle = \langle \frac{\nu}{2} \sum_{i,j} \left(\frac{\partial u_j}{\partial x_i} + \frac{\partial u_i}{\partial x_j} \right)^2 \rangle, \tag{2.15}$$

and that in the inertial range the statistical properties are determined by the length scale r and by ϵ. The fact that in the limit of infinite Reynolds number ϵ does not vanish is known as dissipation anomaly or zeroth law of turbulence [Vas15; Dub19]. In fully developed turbulence, the energy dissipation rate is given by $dE/dt = -\epsilon$. From Eq. (2.5) we obtain that in the limit of infinite Reynolds number, $\nu \to 0$ so the enstrophy Ω, quantity associated to velocity gradients, has to diverge to keep ϵ finite.

One straightforward consequence of these hypotheses is that, using just dimensional analysis arguments, one can obtain a scaling law for the structure functions of order p

$$S_p(r) = \langle (\delta \mathbf{u})^p \rangle \sim \epsilon^{p/3} r^{p/3} \tag{2.16}$$

where the angle brackets $\langle \rangle$ indicate average over space. One can follow the same procedure to obtain a scaling for the energy spectrum

$$E(k) = C_K \epsilon^{2/3} k^{-5/3}, \tag{2.17}$$

valid in the inertial range $k_0 \ll k \ll k_\eta$ with $k_0 = 2\pi/L_0$ and $k_\eta = 2\pi/\eta$. Eq. (2.17) is known as Kolmogorov's 5/3 law, and the universal dimensionless constant $C_K \approx 1.6$ [Sre95; IGK09]. In the inertial range, the energy flux is independent of the wavenumber and matches the energy dissipation rate $\Pi(k) = \epsilon$. A schematic picture of the energy spectrum and energy flux is shown in Fig. 2.2.

By the end of the inertial range, we have the dissipation length scale η, also known as Kolmogorov scale, that is obtained by assuming that $\text{Re}_\eta \sim 1$, leading to

$$\eta \sim \left(\frac{\nu^3}{\epsilon} \right)^{1/4}. \tag{2.18}$$

The size of the inertial range is given by the ratio L_0/η. Using Eq. (2.18) and the scaling $\epsilon \sim u_0^3/L_0$, we obtain

$$\frac{L_0}{\eta} \sim \text{Re}^{3/4}. \tag{2.19}$$

This relation shows that as the Reynolds number increases, the size of the inertial range also does. This means that for numerical simulations, where the number of grid points in three dimensions scales as $N \sim (L_0/\eta)^3 \sim \text{Re}^{9/4}$, the degrees of freedom in a turbulent flow increase with the Reynolds number. Earth's atmosphere
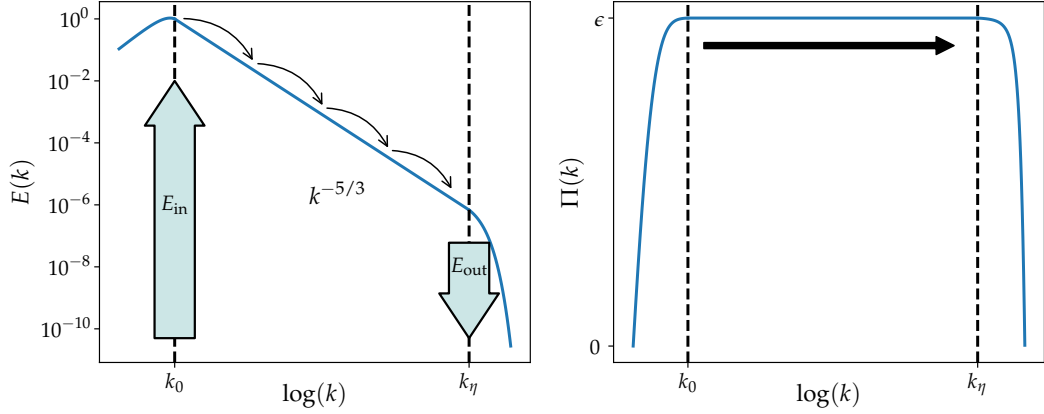
Figure 2.2: Schematic picture of energy spectrum $E(k)$ and energy flux $\Pi(k)$ in a 3D turbulent flow. Energy is injected at k_0 and transferred towards larger wavenumbers (smaller scales) with a constant energy rate ϵ until it reaches k_η, where energy is dissipated.

can have some typical values for the Reynolds number of Re $\sim 10^7$ while for astrophysical flows it can be larger, showing the challenge of performing real numerical simulations of such flows.

Another dimensionless number that is very useful to characterize turbulent flows is the Taylor microscale Reynolds number [TL72; Pop00; Fri95]

$$\mathrm{Re}_\lambda = \frac{U_{\mathrm{rms}}\lambda_{\mathrm{T}}}{\nu}, \tag{2.20}$$

with $U_{\mathrm{rms}} = \sqrt{2E/3}$ the root-mean-square velocity field, $\lambda_{\mathrm{T}} = U_{\mathrm{rms}}/\sqrt{\langle \partial u_1/\partial x_1 \rangle} = \sqrt{15\nu/\epsilon}U_{\mathrm{rms}}$ the Taylor microscale, and ν the kinematic viscosity. The Taylor microscale is associated with the curvature of the spatial autocorrelation, and length scales larger than this one are not strongly affected by viscosity [TL72]. From these definitions, it is obtained that the scale separation between the Taylor microscale and the integral length scale L_0 and Kolmogorov length scale η scale with the integral scale Reynolds number as

$$\frac{\lambda_{\mathrm{T}}}{L_0} = \sqrt{15}\mathrm{Re}^{-1/2}, \tag{2.21}$$

$$\frac{\lambda_{\mathrm{T}}}{\eta} = \sqrt{15}\mathrm{Re}^{1/4}. \tag{2.22}$$

2.1.3 Homogeneous isotropic turbulence (HIT)

One of the most important results of K41 theory on turbulence is the so-called four-fifths law, an exact relation for the third order longitudinal structure function. This result is based on the Kármán-Howarth-Monin (KHM) equation, an evolution equation for the two-point correlation function $C(\mathbf{r}, t) = \langle \mathbf{u}(\mathbf{x} + \mathbf{r}) \cdot \mathbf{u}(\mathbf{r}) \rangle$ obtained from the incompressible Navier–Stokes equations (2.1) for homogeneous flows in the absence of external forcing [Fri95; Dav13; Dub19]. It reads

$$\partial_t C(\mathbf{r}, t) = \frac{1}{2}\boldsymbol{\nabla}_{\mathbf{r}} \cdot \langle |\delta\mathbf{u}(\mathbf{r})|^2 \delta\mathbf{u}(\mathbf{r}) \rangle + 2\nu\boldsymbol{\nabla}_{\mathbf{r}}^2 C(\mathbf{r}, t), \tag{2.23}$$

where $\mathbf{r}$ is the increment vector. Using the relation between the velocity increments and the correlation function $\langle \mathbf{u}' \cdot \mathbf{u} \rangle = \langle (\mathbf{u})^2 \rangle - \langle (\delta \mathbf{u})^2 \rangle / 2$ and $\partial_t \langle (\mathbf{u})^2 \rangle = -2\epsilon$, it can be rewritten completely in terms of velocity increments as

$$\partial_t \langle (\delta \mathbf{u})^2 \rangle = -\boldsymbol{\nabla}_{\mathbf{r}} \cdot \langle |\delta \mathbf{u}(\mathbf{r})|^2 \delta \mathbf{u}(\mathbf{r}) \rangle - 4\epsilon + 2\nu \boldsymbol{\nabla}_{\mathbf{r}}^2 \langle (\delta \mathbf{u})^2 \rangle. \tag{2.24}$$

Note that both expressions (2.23) and (2.24) are completely equivalent and valid for anisotropic turbulence. Assuming statistically stationary flows in the limit of high Reynolds numbers, one obtains from (2.24) Kolmogorov's four-thirds law for anisotropic turbulence

$$\langle (\delta \mathbf{u})^2 \delta \mathbf{u} \rangle = -\frac{4}{3}\epsilon \mathbf{r}. \tag{2.25}$$

In the case of homogeneous and isotropic turbulence (HIT), from Eq.(2.23) it is possible to obtain the famous Kolmogorov four-fifths law for the third order longitudinal structure function

$$S_3(r) = \langle (\delta v_{\parallel})^3 \rangle = -\frac{4}{5}\epsilon r, \tag{2.26}$$

with $\delta v_{\parallel}(r) = [\mathbf{u}(\mathbf{x} + \mathbf{r}) - \mathbf{u}(\mathbf{x})] \cdot \hat{\mathbf{r}}$ the longitudinal velocity increments, and the prefactor $-4/5$ a universal constant, in the sense that it is independent of the flow. One of the main consequences of this result is the non-Gaussianity of velocity increments, as for zero-mean Gaussian distributions, odd moments are exactly zero, and in particular the third order moment $\langle \delta v^3 \rangle = 0$.

Making use of K41 theory introduced in Sec. 2.1.2, one is tempted to extend the validity of this result for all moments of order p of the longitudinal structure function as

$$S_p = \langle (\delta v_{\parallel})^p \rangle = C_p (\epsilon r)^{\zeta_p}, \tag{2.27}$$

where the scaling exponents in the K41 self-similar picture of turbulence are $\zeta_p = p/3$, with $\zeta_3 = 1$ and $C_3 = -4/5$ to satisfy Eq. (2.26). However, it has been observed both numerically and experimentally that the scaling exponents of the longitudinal structure functions deviate from K41 theory as it neglects strong intermittent fluctuations of the velocity increments [Fri95]. Further discussions on intermittency are presented in Sec. 2.3.

2.1.4 Two-dimensional turbulence

The case of two-dimensional (2D) turbulence is of particular interest as it can be found in different situations in nature. In particular, atmospheres or oceans at large scales are under the influence of mechanisms acting on the fluid, like stratification or rotation, that suppress the fluctuations in one direction generating an effective quasi-2D flow [Dav13; BE12; AB18]. A system under such conditions develops a different phenomenology as in 3D turbulence, and also presents a simplified framework in the sense that numerical simulations become less expensive.

As mentioned in Sec. 2.1.1, the equation for the evolution of vorticity in 3D is described by Eq. (2.4). In two dimensions, the first term on the r.h.s vanishes as there is no vortex stretching, which leads to the following balance equations for 2D flows

$$\frac{\mathrm{d}E}{\mathrm{d}t} = -2\nu\Omega = -\epsilon, \tag{2.28}$$

$$\frac{\mathrm{d}\Omega}{\mathrm{d}t} = -2\nu P = -\beta, \tag{2.29}$$

where we introduced the palinstrophy $P = \int |\mathbf{\nabla} \times \boldsymbol{\omega}|^2 dV/2$, and the enstrophy dissipation rate β. In the case of vanishing viscosity, there are two quadratic quantities that are conserved. One of the main consequences of the conservation of enstrophy (2.29) is that now the zeroth law of three dimensional turbulence, meaning that the energy dissipation rate stays finite even for vanishing viscosity, does not hold true for 2D turbulence. This is because now, as a consequence of Eq. (2.29), the enstrophy decreases monotonically and is bounded from above by its initial value, which implies that $\lim_{\mathrm{Re}\to\infty} \epsilon = 0$ [Dav13; BE12; Tab02].

To generate statistically stationary 2D turbulence, one needs to consider an external forcing $\mathbf{f}$ acting on a length scale $L_f = 2\pi/k_f$ and to introduce dissipation at large scales, for example a friction term $-\alpha\mathbf{u}$. In 1967, Kraichnan proposed that in fully developed 2D turbulence, the system admits two inertial ranges where the energy spectrum satisfies [Kra67]

$$E(k) \sim \epsilon^{2/3} k^{-5/3} \quad \text{for} \quad k_0 \ll k \ll k_f, \tag{2.30}$$

$$E(k) \sim \beta^{2/3} k^{-3} \quad \text{for} \quad k_f \ll k \ll k_\eta. \tag{2.31}$$

The range in which the energy spectrum obeys the $k^{-5/3}$ scaling corresponds to an inverse energy cascade, that is, the energy is transferred towards larger scales. For larger wavenumbers, there is a second range with a k^{-3} scaling that exhibits a direct enstrophy cascade, with the enstrophy being transferred towards smaller scales with a zero energy flux. This behavior is completely different to the one observed in 3D turbulence, where there are direct energy and helicity cascades taking place in the same inertial range. The presence of an inverse energy cascade and a direct enstrophy cascade can be understood using the Fjortoft argument as follows [Fjø53; BE12]. In a statistically steady state, the energy injected into the flow ϵ_f has to balance the dissipated one, that in principle can be at large scales ϵ_0 or at small scales ϵ_η. The same situation must hold true for the enstrophy injection and dissipation, leading to the balance relations for the energy $\epsilon_f = \epsilon_0 + \epsilon_\eta$ and for the enstrophy $\beta_f = \beta_0 + \beta_\eta$. Assuming the relation between the energy and enstrophy dissipation rates at a scale r given by $\epsilon_r \sim r^2\beta_r$, one obtains that the ratio between large and small scale dissipations are

$$\frac{\epsilon_\eta}{\epsilon_0} = \left(\frac{\eta}{L_f}\right)^2 \frac{1 - (L_f/L_0)^2}{1 - (\eta/L_f)^2} \tag{2.32}$$

$$\frac{\beta_0}{\beta_\eta} = \left(\frac{L_f}{L_0}\right)^2 \frac{1 - (\eta/L_f)^2}{1 - (L_f/L_0)^2}. \tag{2.33}$$

In the limit of infinite Reynolds number, we can assume a large separation of scales $L_0 \gg L_f \gg \eta$ and obtain from Eq. (2.32) that the energy dissipation ratio $\epsilon_\eta/\epsilon_0 \to 0$, meaning that all the energy cascades towards large scales where it is dissipated. Furthermore, from Eq. (2.33) one obtains $\beta_0/\beta_\eta \to 0$, showing that the enstrophy

dissipates at small scales. A schematic picture of the energy spectrum and the fluxes is shown in Fig. 2.3. Note that the energy flux takes negative values to transfer energy to larger scales, while the enstrophy flux is positive. This behavior has been confirmed by numerical simulations of stationary 2D turbulence with a resolution up to $32,768^2$ [BM10] and in freely decaying 2D turbulence [MP13], although in both cases the authors observed a slope for the direct cascade a bit steeper than k^{-3}.

One important remark regarding the direct enstrophy cascade range is that to obtain the energy spectrum (2.31) one assumes that the interaction between eddies is local in k space, meaning that only structures of similar wavenumbers interact exchanging enstrophy. However, this assumption is not fully consistent as non-local interaction between wavenumbers are relevant in the direct enstrophy cascade. Taking into account this non-locality, Kraichnan introduced a logarithmic correction into the energy spectrum [Kra67]

$$E(k) \sim \beta^{2/3} k^{-3} \left[\ln(k/k_\eta) \right]^{-1/3}. \tag{2.34}$$

Another interesting property of two-dimensional turbulence is the behavior of the velocity increments $\delta\mathbf{u}$ within the direct and inverse inertial ranges. In particular, it was observed via direct numerical simulations of the NS equations that for the inverse energy cascade, the velocity increments exhibit close to Gaussian probability distribution functions (PDFs), indicating an absence of intermittency, both in experiments [PT98; Tab02] and numerical simulations [BCV00; BE12]. Note that the PDFs are not exactly Gaussian as the third order longitudinal structure functions obtained from the Kármán-Howarth-Monin equations in 2D are [Lin99; Ber99]

$$S_3(r) = \frac{3}{2}\epsilon r \quad \text{for} \quad L_0 \gg r \gg L_f \tag{2.35}$$

$$S_3(r) = \frac{1}{8}\beta r^3 \quad \text{for} \quad L_f \gg r \gg \eta, \tag{2.36}$$

for the inverse and direct cascades, respectively. The lack of intermittency has been associated to an extra symmetry 2D turbulent flows known as conformal invariance, a wider class of scale invariance that preserves angles but not necessarily lengths [BBC+06]. It has been observed some evidence of this property by analyzing vorticity isolines in the inverse cascade. The statistics of vorticity clusters was observed to display a behavior similar to other systems presenting this symmetry, like critical percolation [BBC+06; BE12]. At scales smaller than the forcing scale the situation differs, as the vorticity fluctuations show an intermittent behavior [Ber00; NOA+00; BCM+02].

2.2 Quantum turbulence

Richard Feynman in 1955 speculated about the nature of turbulence that could take place in superfluids [Fey55; Don91; Don93]. Making a comparison with classical fluids, he assumed that in a superfluid it is possible to have a collection of vortex lines that mutually interact and that, far away from their core, this interaction should be reminiscent to the one of classical vortices in viscous fluids.

The dynamics of quantum vortices and superfluid turbulence has been studied in superfluid helium at very low temperatures since the pioneering work of Hall & Vinen in 1956 in helium II [HV56], soon after its theoretical suggestion by R. Feynman in 1955. In that work, they studied the coupling between the two fluids due to
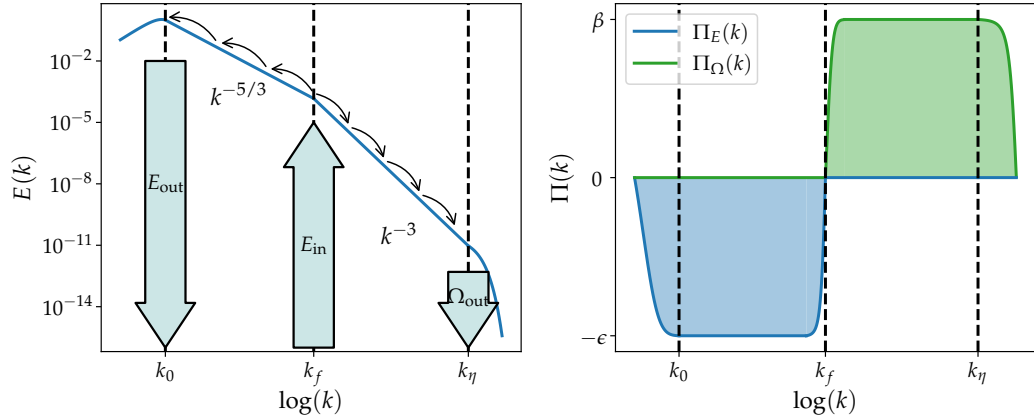
Figure 2.3: Schematic picture of two-dimensional turbulence. (a) Energy spectrum $E(k)$ and (b) energy $\Pi_E(k)$ and enstrophy $\Pi_\Omega(k)$ fluxes. The energy is injected at k_f and transferred towards smaller wavenumbers in an inverse energy cascade with a constant energy rate ϵ, while the enstrophy is transferred towards larger wavenumbers with a constant enstrophy rate β.

the mutual friction by attenuation of second sound. Since then, quantum turbulence has been widely studied in superfluid helium to understand the dissipation effects at low temperatures [WGH⁺07], the interaction between the superfluid and particles [PBS⁺05; PFS⁺08; LMS14; GK19], and counterflow turbulence [GML⁺14; MGG⁺15]. Quantum turbulence has also been reproduced experimentally in other systems, like He³ [FHG⁺01] and BECs [TTC⁺16], and it has also been studied using numerical simulations of different models, like the Gross–Pitaevskii equation [NAB97b; TH09], the vortex filament model [Sch88; ATN02; KVS⁺02], and the two-fluid model [RBL09; BKL⁺18].

2.2.1 Quasiclassical or Kolmogorov turbulence

Superfluids are characterized by the absence of viscous dissipation and by the concentration of vorticity along vortex filaments with a discrete circulation. Therefore, one would in principle expect that the classical picture of turbulence described in Sec. 2.1 should not apply directly. However, there are particular regimes of superfluid turbulence where this picture has been observed [BSS14].

A simplified low-temperature phenomenology of quantum turbulence in superfluid is shown in Fig. 2.4. When energy is injected at a large scale k_0, the incompressible kinetic energy E_{kin}^i is transferred towards small scales following the classical picture of turbulence given by the Kolmogorov energy cascade with a scaling $E(k) \sim k^{-5/3}$. This regime takes place at wavenumbers $k_0 \ll k \ll k_\ell$ with $k_\ell = 2\pi/\ell$ the wavenumber associated with the intervortex distance ℓ. At these scales, the discrete nature of vortices is not relevant, and they organize themselves in a coherent way forming large-scale structures (bundles) that follow Kolmogorov phenomenology [MT98; NAB97b; ATN02; KT05].

The total number of vortices in the system can be estimated by comparing the circulation at large scales $\Gamma \sim U_0 L_0$, where we neglected vortex cancellations, and the one generated by a single quantum vortex $\kappa \sim c\xi$, leading to [NAB97b]

$$N_v \sim \frac{U_0 L_0}{c\xi}. \tag{2.37}$$

This quantity can also be estimated using the intervortex distance, which by definition leads to

$$N_v \sim \frac{L_0^2}{\ell^2}. \tag{2.38}$$

From Eqs. (2.37) and (2.38), one obtains that the intervortex distance scales as

$$\ell \sim \sqrt{\frac{\xi L_0}{M}} \tag{2.39}$$

with $M = U_0/c$ the Mach number of the flow. Superfluid helium close to the critical point presents an effective viscosity $\nu_{\mathrm{cp}} \sim 0.25\kappa$ [GGV16]. Replacing this into Eq. (2.39) leads to

$$\frac{\ell}{L_0} \sim \mathrm{Re}_{\mathrm{cp}}^{-1/2}. \tag{2.40}$$

This expression is similar to Eq. (2.21), suggesting that in superfluid helium at temperatures above 1 K, the intervortex distance is of the same order as the Taylor microscale λ_T in classical turbulence [NAB97b]. In publication [MPK21], we show that indeed the intervortex distance ℓ in the GP framework plays the role of λ_T in classical turbulence.

   Once the energy reaches the intervortex distance, there is a bottleneck due to the transition between a strong and a weak cascade regime. Here, the energy is accumulated and it is distributed between wavenumbers $k \sim k_\ell$ following an equipartition energy distribution $E(k) \sim k^2$ [LNR07]. It is important to remark that a complete thermalization scaling in this regime has never been observed neither in numerical simulations nor experiments. Between the intervortex distance ℓ and the smallest characteristic scale of the system, the healing length ξ, the discrete nature of vortices becomes important. We will call this range of scales $\ell < r < \xi$ the quantum range. Here, the energy continues to be transferred downscale but now due to a different process triggered by the non-linear interaction between Kelvin waves along vortex lines. At these scales, quantum vortex reconnections also play an important role in the redistribution of energy and exciting Kelvin waves. One can describe the scaling of the Kelvin-wave cascade using weak wave turbulence theory to obtain the Kelvin waves energy spectrum $E_{\mathrm{KW}}(k) \sim k^{-5/3}$ [Naz11; LN10]. Note that the correspondence with the five-thirds law of Kolmogorov turbulence is pure coincidence as it is described by a different mechanism. At the smallest scales, energy is dissipated as sound or, more precisely, the incompressible kinetic energy is transferred to the compressible kinetic energy by the emission of a sound pulse [VPK20]. The existence of Kelvin waves in superfluid ^{4}He was observed for the first time in 2014 by tracking individual vortex lines before and after the reconnection process [FMO+14]. The experimental measurement of the energy spectrum of Kelvin waves is still being eluded as it requires very small scales measurements. For this, it is convenient to make use of numerical simulations of, for example, the GP equation [Krs12; VPK16; CMB17] and the vortex filament model [KVS+01; BDL+11; BB11; BL14], where there has been observed evidence of a $k^{-5/3}$ scaling of the energy spectrum.

   One important remark is that the scaling laws at large and small scales are usually studied independently. The Kelvin wave cascade is obtained by tracking individual vortex lines, while the Kolmogorov cascade is generated by injecting energy at large scales. The simultaneous observation of both regimes becomes more difficult as it requires very large numerical simulations and proper conditions for the flow to
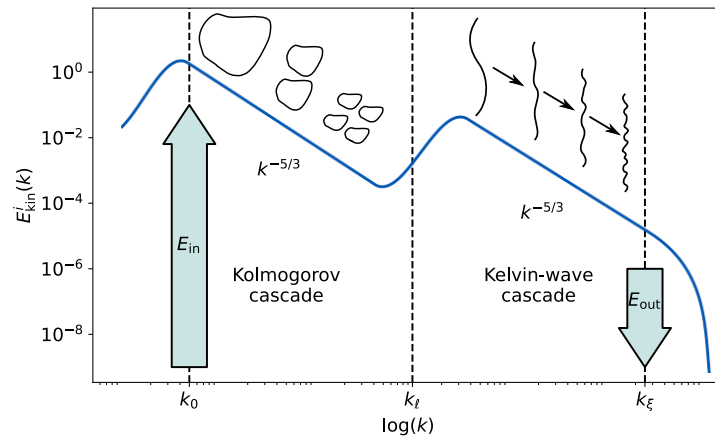
Figure 2.4: Simplified schematic picture of low-temperature quantum turbulence. Between the large wavenumber k_0 and the intervortex distance k_ℓ, the energy cascades towards smaller scales following a quasiclassical Kolmogorov behavior $E(k) \sim k^{-5/3}$. At the intervortex distance there is a bottleneck given by the transition between a strong and a weak cascade, and then energy keeps cascading towards smaller scales via the non-linear interaction of Kelvin waves. At these scales, quantum vortex reconnections also plays an important role in redistributing the energy and by exciting Kelvin waves. At wavenumbers larger than the healing length, associated with the wave vector k_ξ, energy is dissipated as sound.

obtain a large scale separation for the quasiclassical and quantum ranges. Note that, following Eq. (2.39), increasing the total scale separation L_0/ξ by a factor 2, leads to an increase in the scale separation of the quasiclassical and quantum ranges by a factor $\sqrt{2}$, difficulting the simultaneous observation of both scaling laws. Nevertheless, it has been achieved by studying helical flows that trigger the production of Kelvin waves, or by superposing different numerical simulations at different resolutions [CMB17; SMK$^+$19]. In chapter 3, I present publication [MK20] in which we observe the simultaneous development of these energy cascades in a generalized GP model that introduce the roton minimum in the excitation spectrum.

2.2.2   Kelvin wave turbulence

Kelvin waves (KWs) are helicoidal perturbations that propagate along vortex lines, that can interact between each other in a non-linear way. These waves are excited by quantum vortex reconnections, and coexist with first and second sound. The Kelvin-wave spectrum is described by the weak wave turbulence theory, which provides an equation for the evolution of the wave action $n(k)$, given by the amplitude of the waves along the vortex lines [Naz11]. In general, for a non-linear wave system, the specific dynamics of the wave action depends on the interaction between waves. If each interaction occurs between N waves, the resonant conditions for the energy and momentum conservation of the system are respectively

$$\omega(\mathbf{k}_1) \pm \cdots \pm \omega(\mathbf{k}_i) \pm \cdots \pm \omega(\mathbf{k}_N) = 0 \qquad (2.41)$$

$$\mathbf{k}_1 \pm \cdots \pm \mathbf{k}_i \pm \cdots \pm \mathbf{k}_N = 0. \qquad (2.42)$$

where the sign depends on the type of interaction. For example, in a $N = 4$-wave process there are two kind of interactions: the $2 \to 2$ and the $3 \to 1$. For the former type of interaction, two signs must be a $+$ and two a $-$, while for the latter three

of the signs must be a $+$ and the other one must be a minus. For Kelvin waves, the dispersion relation of the system is $\omega(k) = \kappa k^2 \log(1/ka)$ with κ the quantum of circulation of vortices and a proportional to the vortex core size. The first attempt to describe the KW spectrum assumed a 6-wave kind of process, with a $3 \to 3$ interaction [KS09]. Under this hypotheses, Kozik and Svistunov found the spectrum [KS09]

$$E_{\mathrm{KS}}(k) = C_{\mathrm{KS}} \kappa^{7/5} \Lambda \epsilon^{1/5} k^{-7/5}, \qquad (2.43)$$

with $\Lambda = \log(\ell/\xi)$ with ℓ the intervortex distance. Any Kolmogorov-Zakharov solution of the type $E(k) \sim k^\alpha$ must be local, in the sense that the collision integral must converge to ensure the physical realizability of the stationary state. It was later proven that this spectrum resulted to be non-local [LLN+10]. The dimensionless constant C_{KS} is therefore not properly defined. L'vov and Nazarenko developed an effective theory governed by a 4-wave process with a $3 \to 1$ kind of interaction that leads to the spectrum [LN10]

$$E_{\mathrm{LN}}(k) = C_{\mathrm{LN}} \kappa \Lambda \epsilon^{1/3} \Psi^{-2/3} k^{-5/3} \qquad (2.44)$$

with $\Psi = 8\pi E \Lambda^{-1} \kappa^{-2}$, the energy $E = \int E_{\mathrm{LN}}(k)\mathrm{d}k$, and the dimensionless constant $C_{\mathrm{LN}} = 0.304$ [BDL+11].

During several years, there was an agitated controversy on whether which one of these two predictions holds true. The similarity between the scaling $k^{-5/3}$ and $k^{-7/5}$ makes it challenging to discard one or another. The direct observation of Kelvin waves has been performed in superfluid helium, but a direct measurement of its energy spectrum still remains eluded [FMO+14]. Thanks to numerical simulations of the vortex filament model [BDL+11; BL14] and the Gross-Pitaevskii equation [Krs12; CMB17] there exists today a stronger support to the L'vov and Nazarenko (LN) spectrum (2.44).

In chapter 3 of this thesis, we show some more evidence on the LN spectrum of Kelvin waves by performing numerical simulations of quantum turbulence. In publication [MK20] we generate different flows, varying the values of ϵ and the intervortex distance ℓ (that modify also Λ) to study more in detail the dependence on the prefactors of energy spectrum (2.44). Here, we observe the simultaneous development of two inertial ranges, one of them displaying the quasiclassical Kolmogorov scaling and the other one exhibiting the LN Kelvin wave spectrum. In particular, we phenomenologically adapt Eq. (2.44), which is developed for an isolated vortex line, to a whole 3D turbulent flow.

2.2.3 Ultraquantum or Vinen turbulence and counterflow

The phenomenology of quantum turbulence discussed in Sec. 2.2.1 shows that at large scales, superfluid turbulence is similar to the one observed in classical fluids. This quasiclassical regime is characterized by the large-scale correlations in the polarization of vortex lines. In superfluid turbulence it is possible to generate a different regime in which vortex lines present no correlations at large scales, developing an energy spectrum that differs from Kolmogorov scaling. This regime is known as ultraquantum or Vinen turbulence due to his pioneering work on counterflow turbulence [Vin57]. Both Kolmogorov and Vinen turbulent regimes have been generated by injecting vortex rings of different sizes and at different rates in superfluid ^{4}He [WG08] and in numerical simulations of the vortex filament method [BLB12].

In these two regimes, the decaying of the vortex line density presents two different behaviors, as we describe in the following.

As vortices in quantum fluids are supported along filaments, the mean vorticity of the superfluid is given by $\langle \omega \rangle = \kappa \mathcal{L}$, with $\mathcal{L}$ the vortex line density. The intervortex distance is then $\ell = \mathcal{L}^{-1/2}$ [SSD99; VN02]. In classical fluids, the energy dissipation rate and the vorticity are related by $\epsilon = \nu \langle \omega^2 \rangle$. In a superfluid, we can use this expression as an estimation assuming that at small scales there is an effective viscosity ν_{eff} associated to the reduction of vorticity due to vortex reconnections and Kelvin waves, converting it into sound. Under this phenomenological assumption, one can approach the energy dissipation rate in a superfluid by [VN02; Tsu09]

$$\epsilon = \nu_{\text{eff}} \kappa^2 \mathcal{L}^2. \tag{2.45}$$

We will consider now that there is no external forcing, so the energy of the vortices decays in time. There are now two possible approaches one can take. On one hand, one can assume that the system is in a quasiclassical regime, i.e. it obeys the Kolmogorov energy spectrum $E(k) = C\epsilon^{2/3}k^{-5/3}$. The total energy is given to a good approximation by

$$E = \int_{k_0}^{k_\ell} E(k)\mathrm{d}k \approx \frac{3}{2}C\epsilon^{2/3}k_0^{-2/3} \tag{2.46}$$

where $k_\ell = 2\pi/\ell$ and $k_0 = 2\pi/L_0$ the integral wavenumber. By definition, the energy dissipation rate is

$$\epsilon = -\frac{\mathrm{d}E}{\mathrm{d}t} = -\frac{C}{\epsilon^{1/3}k_0^{2/3}}\frac{\mathrm{d}\epsilon}{\mathrm{d}t}. \tag{2.47}$$

Integrating this equation one obtains the time dependence of the energy dissipation rate and, using relation (2.45), the vortex line density

$$\epsilon(t) = 27C^3 k_0^{-2}(t + t_0)^3 \tag{2.48}$$

$$\mathcal{L}(t) = \frac{(3C)^{3/2}}{k_0 \kappa \nu_{\text{eff}}^{1/2}}(t + t_0)^{-3/2} \tag{2.49}$$

where t_0 is a constant with units of time. Equation (2.49) shows that the vortex line density in the quasiclassical regime decays as $\mathcal{L} \sim t^{-3/2}$. This behavior has been observed in superfluid ^{4}He at different temperatures [SSD99; SND00; WG08], in superfluid ^{3}He experiments [BCF+06], and in DNS of the vortex filament model [BLB12; BBS12].

The second possible approach that leads to a different vortex line density decay is to assume that the superfluid velocity field of a single vortex line at the intervortex distance is given by [TH09; Vin57]

$$u_s^2(l) = \frac{\kappa^2}{(2\pi)^2 \ell^2} = \frac{\kappa^2 \mathcal{L}}{(2\pi)^2}. \tag{2.50}$$

In the absence of external forcing and at low temperatures, one expects that during the turbulent regime energy will decay at a rate

$$\frac{\mathrm{d}u_s^2}{\mathrm{d}t} = -\chi \frac{u_s^3}{\ell} \tag{2.51}$$

with χ a dimensionless constant of order unity, and $t_\ell = \ell/u_s$. Equations (2.50) and (2.51) lead to the decay of the vortex line density

$$\frac{d\mathcal{L}}{dt} = -\chi\frac{\kappa}{2\pi}\mathcal{L}^2 \tag{2.52}$$

The original expression obtained by Vinen considers also a vortex amplification term relevant at finite temperature [Vin57], that is not shown here. Equation (2.52) leads to a solution

$$\mathcal{L}(t) = \left[\mathcal{L}_0 + \frac{\chi\kappa}{2\pi}(t - t_0)\right]^{-1} \tag{2.53}$$

This vortex line density decay $\mathcal{L} \sim t^{-1}$ differs from the one obtained assuming Kolmogorov scaling shown in (2.49). This regime is associated with an energy spectrum with a scaling $E(k) \sim k^{-1}$ due to the lack of large-scales correlations, and has been observed in superfluid ^{4}He [WG08], DNS of the vortex filament model in counterflow turbulence [BLB12; BBS12] and the GP model [VPK16; CWA$^+$17; MMC$^+$21; AEBM22].

The main reason for the different scaling between Vinen and Kolmogorov turbulence is the lack of correlation at large scales in the former regime. It is also argued that in Vinen turbulence there is no energy cascade, in the sense that energy is no longer transferred from larger to smaller scales [BSB16]. It is still not clear if the Vinen turbulence regime is unique to superfluids or if it can be observed in other systems. It is possible that it is a consequence of the discrete nature of vortices, which would mean that cannot take place in classical fluids.

Another regime that is also unique to superfluids is counterflow turbulence. This regime arises at finite temperatures, when both the normal and superfluid components have a significant density fraction. When a thermal gradient is introduced in superfluid ^{4}He, both fluid components will start flowing in opposite directions and, if their velocity is large enough, they can generate counterflow turbulence. This is an interesting regime as both fluid components can be turbulent simultaneously, with the vorticity of the superfluid component constraint to lines, while the normal fluid develops classical (viscous) turbulence. Both components are coupled by mutual friction, transferring energy among each other and increasing the complexity of their dynamics [BSS14]. Counterflow turbulence has been recently studied performing DNS of the HVBK equations and it was observed that when a strong counterflow is imposed, velocity fluctuations are suppressed in the direction of the counterflow, and the superfluid starts exhibiting some of the phenomenology taking place in quasi two-dimensional turbulence, like an inverse energy cascade and the formation of large-scale structures [BKL$^+$19b; PK20a].

2.2.4 Two-dimensional quantum turbulence

In two-dimensional superfluids, vortices are restricted into points in space. These point-vortices carry a circulation $\Gamma = \pm\kappa$ and can interact between themselves creating clusters or annihilating each other. Onsager proposed in 1949 a point-vortex model and used statistical mechanics tools to describe the dynamics of a point-vortex gas [Ons49; ES06]. In this model, the dynamics of each point-vortex located at $\mathbf{r}_i = (x_i, y_i)$ is given by the equations of motion

$$\rho_0\Gamma_i\frac{dx_i}{dt} = \frac{\partial H}{\partial y_i} \quad ; \quad \rho_0\Gamma_i\frac{dy_i}{dt} = -\frac{\partial H}{\partial x_i} \tag{2.54}$$

with ρ_0 the 2D fluid density and the incompressible kinetic energy of N vortices in an unbounded fluid given by

$$H = -\frac{\rho_0}{2\pi} \sum_{i<j} \Gamma_i \Gamma_j \ln\left(\frac{r_{ij}}{\xi}\right). \tag{2.55}$$

Here, $r_{ij} = |\mathbf{r}_i - \mathbf{r}_j|$ is the relative distance between vortices and ξ is a short range cutoff scale, which for a superfluid corresponds to the healing length. For a confined flow, the logarithm in Eq. (2.55) is replaced by a more general Green function of the Laplace equation with appropriate boundary conditions, where interactions of vortices with their images have to be considered.

Let us now consider the flow enclosed by a boundary, with the vortices confined to an area A. As the space coordinates x and y of each vortex are canonical conjugates, the phase space and the configuration space are identical, in the sense

$$d\Omega = dx_1 dy_1 \ldots dx_n dy_n. \tag{2.56}$$

The total phase-space volume is finite and given by $\int d\Omega = A^n$. The energy can, in principle, take all possible values, from $+\infty$ when two vortices of the same sign coincide in space, to $-\infty$ when two vortices of opposite sign coincide. The phase-space volume for states at a given energy is defined by

$$\Omega(E) = \int \prod_{i=1}^{N} \delta(H(\mathbf{r}_1, \ldots, \mathbf{r}_N) - E) d^2\mathbf{r} \tag{2.57}$$

We define a differentiable function given by

$$\Phi(E) = \int_{H<E} d\Omega = \int_{-\infty}^{E} \Phi'(E) dE, \tag{2.58}$$

with $\Phi(-\infty) = 0$ and $\Phi(\infty) = A^n$, by definition. The derivative $\Phi'(E) = \Omega(E)$ is therefore a non-negative function going to zero on both extremes with $\Omega(\pm\infty) = 0$. As a consequence, the function $\Omega(E)$ must have at least one maximum value at some energy E_m such that $\Omega'(E_m) = 0$, and with $\Omega'(E) > 0$ for $E < E_m$ and $\Omega'(E) < 0$ for $E > E_m$. The thermodynamic entropy and the inverse of the temperature of the point-vortex gas are given respectively by

$$S = k_B \ln \Omega(E), \tag{2.59}$$

$$\frac{1}{T} = \frac{\partial S}{\partial E}, \tag{2.60}$$

with k_B Boltzmann constant. The inverse of the temperature is then negative for $E > E_m$, positive for $E < E_m$ and zero for $E = E_m$. Negative temperature states are associated with the formation of large-scales, long-lived vortex clusters, also known as Onsager vortex clusters. A positive temperature state corresponds to a gas of vortex dipoles. It was recently shown that it is possible to derive the point vortex model from the two-dimension Gross-Pitaevskii equation, in the limit of well-separated vortices on a strong condensate [SLN22].

Onsager vortex clusters are structures that are observed in geophysical flows, like Jupiter's great red spot [YR17]. In particular, the point-vortex system becomes an ideal framework in superfluids due to the point-like nature of quantum vortices. The formation of Onsager clusters was studied numerically in the GP framework

[BRA+14; SA16; GSP+16] and observed experimentally in two-dimensional BECs [JGS+19; GRY+19]. The phenomenology of 2D quantum turbulence (2DQT) at scales larger than the intervortex distance is expected to be similar as in classical turbulence. Indeed, the formation of Onsager clusters can be associated to an inverse energy cascade, making vortices to rearrange and form large-scales structures. This cascade process and the energy spectrum was studied in the GP framework in different systems, like purely 2D quantum fluids including some forcing and dissipation [BA12; RBA+13], in thin layers [MBA+20] or in spherical shells geometries [KG21] in an attempt to recreate recent microgravity BECs experiments carried on at the NASA Cold Atom Laboratory, aboard the International Space Station [LCL+19]. The formation of vortex clusters and the inverse energy cascade was recently also studied in exotic quantum fluids, like binary BECs [MKD+21; DMM22] or superfluid of light [PMD+21; PCM+22].

As the vorticity on quantum fluids is given by a collection of δ-Dirac distributions, the enstrophy, being the square of vorticity, is not properly defined bringing into question the possibility of a direct enstrophy cascade. However, one can consider that introducing some cut-off length scale, like the healing length ξ for the vortex core size, the δ is regularized into some Gaussian distribution. In that case, the coarse-grained enstrophy will be given then by the total number of vortices in the system, that can decrease in time due to mechanisms taking place at small scales like vortex annihilation. Indeed, the presence of a direct enstrophy cascade, with a scaling in the energy spectrum of $E(k) \sim k^{-3}$ was observed in numerical simulations of the point-vortex models [BA12; RBY+17].

2.3 Intermittency

One of the main assumptions of K41 theory of turbulence is the self-similarity of velocity increments in the inertial range. This symmetry is actually broken because of the intermittent nature of the velocity field, in the sense that during a certain period of time and at certain regions of the fluid, the flow becomes inactive, while other regions of the flow are active and might exhibit violent events. In Fig. 2.5, we show that the energy dissipation and the enstrophy obtained from direct numerical simulations at taylor-microscale Reynolds number $\mathrm{Re}_\lambda = 675$ display this kind of behavior, with active and non-active regions of the flow [IGK09]. As a consequence of these extreme events, the scaling exponents of the structure function introduced in Eq. (2.27) deviate from K41 prediction $\zeta_p^{\mathrm{K41}} = p/3$ and a new interpretation needs to be introduced.

In this section, we will show some of the most important models of intermittency for homogeneous isotropic turbulence. It is important to remark that these models are not obtained from first principles, i.e., they are not obtained directly from the Navier–Stokes equations, but are phenomenological models based on different arguments, like the Richardson cascade process and multifractality.

2.3.1 Properties of scaling exponents

In homogeneous isotropic turbulence in the limit of high Reynolds number, the structure functions of velocity increments of even order $2p$ satisfy the scaling within the inertial range of scales [Fri95]

$$S_{2p} = \langle (\delta v)^{2p} \rangle \sim A_{2p} v_0^{2p} \left(\frac{l}{L_0} \right)^{\zeta_{2p}},$$
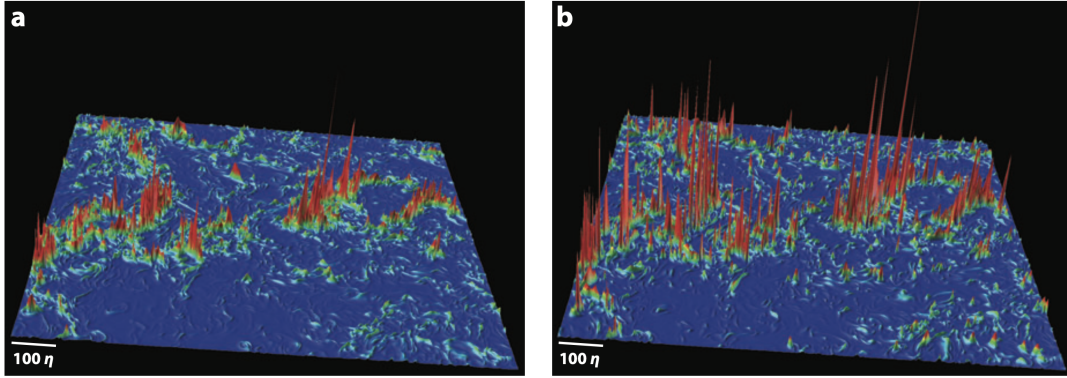(2.61)

Figure 2.5: (a) Energy dissipation and (b) enstrophy of a 2D snapshot from a turbulent 3D flow using 4096^3 grid points. Regions in red and blue indicate high and small values, respectively. Extracted from [IGK09]

with A_{2p} an amplitude independent on the increment l. We will assume that the velocity field is bounded, taking a maximum value $U_{\max}$, such that $|\delta v| \leq 2U_{\max}$. Using expression (2.61), we then have that

$$S_{2p+2} = A_{2p+2}v_0^{2p+2}\left(\frac{l}{L_0}\right)^{\zeta_{2p+2}} \leq 4U_{\max}^2 S_{2p} = 4U_{\max}^2 v_0^{2p}A_{2p}\left(\frac{l}{L_0}\right)^{\zeta_{2p}}, \qquad (2.62)$$

that leads to the inequality

$$\left(\frac{l}{L_0}\right)^{\zeta_{2p+2}-\zeta_{2p}} \leq 4\frac{A_{2p}}{A_{2p+2}}\left(\frac{U_{\max}}{v_0}\right)^2. \qquad (2.63)$$

In the limit of infinite Reynolds number, $l \ll L_0$ and assuming the velocity is bounded by $U_{\max} < \infty$ one obtains that

$$\zeta_{2p+2} \geq \zeta_{2p}, \qquad (2.64)$$

which means that the scaling exponents have to be non-decreasing. Today, there is some numerical evidence showing that for high-order moments the scaling exponents might saturate, in the sense that $\zeta_{2p+2} \approx \zeta_{2p}$ for $p \gg 1$ [ISY20]. Equation (2.64) and the four-fifths law (2.26) are important constraints for intermittency models that are introduced in the following sections.

2.3.2 β-model

One of the simplest models that tries to describe the intermittent behavior of turbulent flows is the β-model proposed in 1978 [FSN78; Fri95]. This model does not explain the origin of intermittency phenomena, but presents a simple way to link the anomalous scaling observed in the structure functions to geometrical properties of the turbulent flow.

This model is based on the idea that eddies follow a Richardson cascade process, that is, larger eddies break down to form smaller eddies. For instance, starting with a mother eddy of the system size L_0, it can break down into eddies of size $l_1 = rL_0$ with the fraction $r < 1$. Moreover, these eddies also interact in a non-linear way creating more daughter eddies of size $l_2 = rl_1 = r^2L_0$. In general, for a step n, the length scale is given by $l_n = r^nL_0$, with $n = \log(l_n/L_0)/\log r$. This process

takes place until the daughter eddies reach the Kolmogorov length scale η, where they are dissipated as heat. From now on, we will consider a turbulent flow in the limit of Re $\to \infty$, meaning that $L_0 \gg l_n \gg \eta$. The β-model introduces the idea of intermittency considering that only a fraction $\beta \leq 1$ of the larger eddies are active, in the sense that not all the eddies break down into smaller ones. Then, for a certain length scale l_n, that fraction is

$$\beta^n = \beta^{\frac{\log(l_n/L_0)}{\log r}} = \left(\frac{l_n}{L_0} \right)^{d-D} \tag{2.65}$$

where $d - D = \log \beta / \log r$ with D the fractal dimension of the eddies and d is the dimension of the system.

To understand the idea of fractal dimension, let us consider a cube (with $d = 3$) filled with different geometrical objects, like a point, a line or a surface. The first one has a dimension $D = 0$, the line a dimension $D = 1$ and the surface a dimension $D = 2$. Let us consider now that we introduce a ball of radius l and we would like to know what is the probability p_l of intersecting these different objects. For the surface, for example, the ball would have to be between a volume of thickness $2l$ around the surface. This geometrical observation leads to the probability $p_l \sim 2l$. For the line, the ball would have to be around it within a surface proportional to l^2, while for the point around a volume proportional to l^3. Thus, in three dimensions we have that the probability of intersecting a structure with a fractal dimension D is $p_l \sim l^{3-D}$. In general, for system of dimension d, this probability is proportional to

$$p_l \sim l^{d-D}, \tag{2.66}$$

with $Co = d - D$ the codimension of the geometrical object. In the Richardson cascade picture, the probability of an eddy being active at a given length scale l_n is associated with the volume fraction $p_{l_n} = \beta^n$. To lighten the notation, we will refer to this probability as p_l.

Now, we can make use of Kolmogorov's phenomenology of turbulence to associate the velocity difference $v_n \equiv \delta v_{l_n}$ for an active eddy of size l_n with the energy at this same length scale l_n considering that only a fraction of these structures are active

$$E_n \sim v_n^2 p_l = v_n^2 \left(\frac{l_n}{L_0} \right)^{d-D}. \tag{2.67}$$

The energy flux $\epsilon_n \sim E_n/t_n$, with the eddy turnover time defined as $t_n \sim l_n/v_n$, for active eddies is

$$\epsilon_n \sim \frac{v_n^3}{l_n} p_l = \frac{v_n^3}{l_n} \left(\frac{l_n}{L_0} \right)^{d-D}. \tag{2.68}$$

We can still assume that in the limit of high Reynolds number, the energy flux within the inertial range is independent of the length scale which leads to $\epsilon_n \sim \epsilon_0 \sim v_0^3/L_0$. This estimation of the energy dissipation rate ϵ together with Eqs. (2.67) and (2.68) leads to the scaling

$$v_n \sim \epsilon_0^{1/3} l_n^{1/3} \beta^{-n/3} = v_0 \left(\frac{l_n}{L_0} \right)^h \quad \text{with} \quad h = \frac{1}{3} - \frac{d-D}{3}, \tag{2.69}$$

where h is the Hölder exponent. We can now turn to study the structure functions of the turbulent flow. The structure functions, weighted by the probability of having an active eddy p_l, are

$$S_p(l) = \langle v_n^p \rangle = \langle \delta v_l^p \rangle \sim p_l (\delta v_l)^p = v_0^p \left(\frac{l}{L_0} \right)^{\zeta_p}, \tag{2.70}$$

$$\zeta_p = \frac{p}{3} + (d - D) \left(1 - \frac{p}{3} \right). \tag{2.71}$$

Note that the β-model gives a prediction for the scaling exponents that is linear in p. Therefore, if the fractal dimension of the eddies is space filling, meaning $D = d$, then the scaling exponents recover the self-similar K41 scaling for the structure functions $\zeta_p = p/3$. Another interesting fact is that for $p = 2$ the scaling exponent is $\zeta_2 = 2/3 + (d - D)/3$, which leads to an energy spectrum $E(k) \sim k^{-5/3+(d-D)/3}$ that is steeper than the five-thirds law. Note that the scaling exponents can also be rewritten in terms of the Hölder exponent h as

$$\zeta_p = hp + d - D, \tag{2.72}$$

with $h = 1/3 - (d - D)/3$.

2.3.3 Multifractal models

In the β-model we considered that there is a single type of characteristic structures described by a single fractal dimension D. In a more general way, one could consider that the nature of the active eddies depends on the length scale of the velocity increments. An equivalent way of seeing this is by relaxing the hypothesis of global scale invariance presented in Eq. (2.14) into a local scale invariance that is valid within a certain range of scales and that gives different values of h. As a consequence, we can define a fractal dimension that now depends on the Hölder exponent $D = D(h)$ [BPP+84; BMV08].

If one considers that a turbulent flow admits an infinite number of values of h, following the same steps as for the β-model, one obtains a scaling for the structure functions

$$S_p(l) = \langle \delta v_l^p \rangle \sim \int d\mu(h) \left(\frac{l}{L_0} \right)^{ph+d-D(h)}, \tag{2.73}$$

where $d\mu(h)$ is the weight corresponding to the different exponents. For high Reynolds numbers we have that $l \ll L_0$ and then the dominant scaling exponents correspond to

$$\zeta_p = \inf_h \left\{ ph + d - D(h) \right\}. \tag{2.74}$$

The weights $d\mu(h)$ disappear in the asymptotic expression of the structure functions. One important restriction to this expression is given by the four-fifths law $\zeta_3 = 1$. Equation (2.74) can be inverted using a Legendre transformation to obtain an expression for the fractal dimension

$$D(h) = \inf_p \left\{ ph + d - \zeta_p \right\}. \tag{2.75}$$

This allows one to study the fractal dimension of a turbulent flow based on experimental measurements of the scaling exponents.

The simplest case of multifractality (bifractality) is obtained by assuming that the turbulent flow presents two kind of active eddies with fractal dimensions D_1 and D_2 or, equivalently, two Hölder exponents h_1 and h_2. In this case, the scaling exponents reduce to

$$\zeta_p = \min_h \left\{ ph_1 + d - D_1, ph_2 + d - D_2 \right\}, \tag{2.76}$$

where, depending on the value of p, one scaling dominates over the other, and there is a competition between both of them. One model that exhibits bifractality is the one-dimensional ($d = 1$) Burgers equation [BK07]. Here, there is a competition between a smooth field and shock waves. In the first of these cases, applying a Taylor expansion on the velocity field leads to $h_1 = 1$, with space-filling structures of fractal dimension $D_1 = 1$. In contrast, shock waves generate sheet-like structures with $D_2 = 0$, which applying the β-model given by Eq. (2.72) leads to $h_2 = 0$. Then, for $p < 1$ one obtains K41 scaling, while for $p > 1$ the scaling exponents in three dimensions saturate to $\zeta_p = 1$.

2.3.4 Obukhov-Kolmogorov 1962

Landau's main criticism on the self-similar K41 theory is that, for moments of order p of the structure functions defined in Eq. (2.27), Kolmogorov considered only the mean value of the energy dissipation rate. As fluctuations are not taken into account in this theory, Landau argued that the dimensionless constants C_p for $p \neq 3$ are not universal, and that this is only valid for $p = 3$ as $\langle \epsilon^{p/3} \rangle = \langle \epsilon \rangle^{p/3}$.

In 1962, Obukhov [Obo62] and Kolmogorov [Kol62] proposed a coarse-grained energy dissipation rate defined as

$$\epsilon_l = \frac{3}{4\pi l^3} \int_{B(\mathbf{x},l)} \epsilon(\mathbf{x}') \mathrm{d}\mathbf{x}' \tag{2.77}$$

where $B(\mathbf{x}, l)$ is a ball of radius l centered at $\mathbf{x}$, and $\epsilon(\mathbf{x})$ is defined in (2.15). This positive quantity introduces the idea that dissipation depends on a characteristic scale l, and its moments follow a scaling

$$\langle \epsilon_l^q \rangle \sim \epsilon_0^q \left(\frac{l}{L_0} \right)^{\tau_q}. \tag{2.78}$$

Note that, by definition, the scaling exponents τ_q satisfy $\tau_0 = 0$, and $\tau_1 = 0$ as the energy flux is independent on the scale in the inertial range. To bridge the statistical properties of velocity increments and the coarse-grained dissipation, Obukhov and Kolmogorov, based on the K41 theory, proposed that $\delta u_l / (\epsilon_l l)^{1/3}$ is a universal quantity, with δu_l and ϵ_l statistically independent. This assumption is known as the refined similarity hypothesis (RSH). Then, the moments of the structure function should follow a scaling

$$S_p(l) = C_p \langle \epsilon_l^{p/3} \rangle l^{p/3}, \tag{2.79}$$

where now the moments of the energy dissipation become relevant. The anomalous scaling exponents of velocity increments are thus

$$\zeta_p = p/3 + \tau_{p/3}. \tag{2.80}$$

For $p = 3$ one recovers the four-fifths law (2.26) as $\tau_1 = 0$, with $C_3 = -4/5$. Many intermittency models try to prescribe a scaling for the coarse-grained energy dissipation rate and thus prescribe the anomalous scaling of velocity increments.

2.3.5 Random cascade model

One of the simplest ways to describe the scaling exponents of the coarse-grained energy dissipation rate τ_p is by considering a random cascade process, in the same spirit as for the velocity increments in the β-model, but now for the dissipation [Fri95]. We will assume that some structures are more dissipative than others, and that only a fraction of them is active, in the sense that the largest structure at L_0 has a dissipation ϵ_0. A smaller structure $l_1 = rL_0$ has a dissipation $\epsilon_1 = W_0\epsilon_0$ with W_0 a positive random variable. For a general length scale $l_n = r^n L_0$, one can build a multiplicative process for the energy dissipation as

$$\epsilon_{l_n} = \epsilon_0 W_0 W_1 \ldots W_n, \tag{2.81}$$

where $W_i \geq 0$ are identically distributed and independent random variables that satisfy $\langle W \rangle = 1$ due to energy flux conservation along the inertial range $\langle \epsilon_{l_n} \rangle = \langle W \rangle \epsilon_0 = \epsilon_0$ with non-divergent moments $\langle W^q \rangle < \infty$. Then, the moments of the energy dissipation rate follow a scaling

$$\langle \epsilon_l^q \rangle = \epsilon_0^q \langle W^q \rangle^n = \epsilon_0^q \left(\frac{l}{L_0} \right)^{\tau_q} \quad \text{with} \quad \tau_q = \frac{\log \langle W^q \rangle}{\log r}. \tag{2.82}$$

Benzi et al. [BPP$^+$84; BMV08] proposed in 1984 the so-called random β-model in which they make the phenomenological assumption that the probability distribution of the fraction volume β takes two values, β_1 with a probability x and β_2 with a probability $1 - x$

$$P(\beta) = x\delta(\beta - \beta_1) + (1 - x)\delta(\beta - \beta_2). \tag{2.83}$$

The scaling exponents of the dissipation are then given by

$$\tau_q = \frac{\log \langle W^q \rangle}{\log r} = \frac{\log(x\beta_1^q + (1 - x)\beta_2^q)}{\log r}, \tag{2.84}$$

where now x, β_1 and β_2 are free parameters that are fit to reproduce the experimental exponents of the velocity increments or dissipation. Note that if $x = 1$ and $\beta_1 = 1$ one recovers the K41 prediction, while for $x = 0$ and $\beta_2 = \beta$ one recovers the standard β-model.

There are many phenomenological models that fit different values of x, β_1 and β_2 to reproduce the scaling exponents of the structures functions observed either in experiments and in numerical simulations. One popular example is the so-called She–Lévêque model [SL94]. This model was first obtained assuming three main hypothesis. The first of them is the refined similarity hypothesis, in the sense that $\delta v_l / (\epsilon_l l)^{1/3}$ is a universal quantity. The second hypothesis is that the coarse-grained energy dissipation moments obey a hierarchical structure, with $\langle \epsilon_l^{p+1} \rangle = F(\langle \epsilon_l^p \rangle, \langle \epsilon_l^{p-1} \rangle)$, with F a well defined function. The third hypothesis proposes a quantity $\epsilon_l^{(\infty)}$ associated with the most intermittent dissipative structures. To obtain the She–Lévêque model, we will instead use the approach introduced in Dubrulle [Dub94], in which they propose that this model is a particular case of the random β-model. Here, we will assume that $x \ll 1$ and that the cascade proceeds with small steps, in the sense that

$r = 1 - x/Co$ with Co the codimension of structures associated to the intensity β_2. Under these assumptions and using that $\langle W \rangle = 1$ due to energy flux conservation, one obtains from Eqs. (2.80) and (2.84) the scaling exponents [Dub94; Bol02]

$$\zeta_p = \frac{p}{3} + Co \left[(\beta_1 - 1)\frac{p}{3} + 1 - \beta_1^{p/3} \right], \tag{2.85}$$

where now the number of free parameters is reduced to two: Co and β_1. In particular, assuming that the most dissipative structures are concentrated along filaments with $Co = 2$, and $\beta_1 = 2/3$, one obtains the She-Lévêque scaling exponents

$$\tau_p^{\text{SL}} = -\frac{2}{3}p + 2 \left[1 - \left(\frac{2}{3}\right)^p \right], \tag{2.86}$$

$$\zeta_p^{\text{SL}} = \frac{p}{9} + 2 \left[1 - \left(\frac{2}{3}\right)^{p/3} \right] \tag{2.87}$$

that fit to a good agreement the structure functions obtained from experiments and numerical simulations [Fri95; ISY20]. The probability function of the coarse-grained energy dissipation rate ϵ_l in the She–Lévêque model of intermittency is also related to log-Poisson statistics [Dub94; SW95].

There exist many models that try to describe the anomalous scaling of structures functions, many of them based on multifractality [MS87; SS95; Yak01]. Another intermittency model of historical relevance is the log-normal model, proposed by Obukhov and Kolmogorov [Obo62; Kol62] as a first attempt to consider intermittent corrections for the scaling of the structure functions. Here, the authors assumed that the energy dissipation rate follows a log-normal behavior, in the sense that $W_i = r^m$ with m a random variable obeying a Gaussian distribution with mean value $\overline{m}$ and standard deviation σ, and $r < 1$. Using that $\langle W \rangle = 1$ due to conservation of energy flux, one obtains a relation between the mean value and the standard deviation $2\overline{m} = \sigma^2 \log r$, and recovers the scaling exponents

$$\tau_p^{\text{ln}} = \frac{\mu}{2}(p - p^2), \tag{2.88}$$

$$\zeta_p^{\text{ln}} = \frac{p}{3} + \frac{\mu}{18}(3p - p^2), \tag{2.89}$$

with $\mu = 2\overline{m}$ the intermittency exponent, whose experimental value is $\mu = 0.17 \pm 0.01$ [TAD$^+$20]. Note that $\tau_2 = -\mu$ and the second order structure function presents a correction from K41 scaling of $\mu/9$. One important problem that presents the log-normal model is that for large order moments, the scaling exponents start to decrease, violating condition (2.64) obtained for bounded flows.

2.3.6 Velocity circulation

The search for universality in homogeneous and isotropic turbulence has been largely done by studying the statistical properties of velocity increments, since differences are presumed to eliminate large-scale effects. Alternatively, one could eliminate also these effects by studying the velocity circulation, a geometrical quantity given by the line integral of the velocity field around a closed loop $\mathcal{C}_l$ of linear size l or area $A \sim l^2$ defined as

$$\Gamma_l = \oint_{\mathcal{C}_l} \mathbf{u} \cdot \mathrm{d}\mathbf{r} = \int_{\mathcal{S}_A} \boldsymbol{\omega} \cdot \mathrm{d}\mathbf{S}, \tag{2.90}$$

where the second equality is obtained by applying Stokes theorem, with $\mathcal{S}_A$ a surface of area A enclosed by the loop $\mathcal{C}_l$. Instead of the moments of velocity increments, one could study the moments of Γ_l/l, both having the same dimensions. It is conjectured that the circulation around single vortex filaments may give rise to multifractal scaling [Fri95]. First studies on the intermittent behavior of velocity circulation showed that the scaling exponents differ from the structure functions in a non-trivial way [SJS95; CCS96].

One of the main properties of the velocity circulation is that it is a signed measure, meaning that it can also involve cancellation effects given by opposite-sign values. This phenomenon might lead to a statistical behavior that differs from the one of velocity increments, which can be characterized making use of cancellation exponents [ODS+92; IM10; ZSY19]. This method might also give some insight on whether vortex filaments carrying a circulation Γ_i are the main reason of multifractal scaling in turbulent flows, or if they are only one of the ingredients of a more complex system. Further discussions on the statistics of velocity circulation are introduced in chapter 4, where we present the main results on this thesis regarding the intermittent behavior of classical and quantum turbulent flows using the velocity circulation.

Chapter 3

Kolmogorov and Kelvin wave cascades in quantum turbulence

In this chapter, we study the properties of quantum turbulence in a generalized Gross–Pitaevskii equation, a phenomenological model that reproduces some of the properties of superfluid helium and dipolar BECs, like the roton minimum in the excitation spectrum. In this model, we consider an effective non-local interaction potential between bosons, and a beyond mean-field correction that models strong interactions. In particular, we present the publication "Kolmogorov and Kelvin wave cascades in a generalized model for quantum turbulence" [MK20], in which we study the quantum turbulent properties in a superfluid with rotons. We observe that the introduction of the roton minimum enhances the Kelvin-wave energy spectrum at small scales predicted by the weak wave turbulence theory. At large scales, the turbulent behavior reproduced by this model remains unchanged, exhibiting a Kolmogorov scaling for the incompressible energy spectrum and suggesting that small-scale modeling does not affect the large-scales dynamics.

3.1   Quantum turbulence in GP

The GP model describes the dynamics of an inviscid irrotational and compressible fluid, with the emergence of vorticity as topological defects supported along vortex filaments (see chapter 1). As the superfluid is inviscid, one would expect that the Kolmogorov picture of turbulence taking place in classical fluids should not apply directly to quantum turbulence, governed by the complex dynamics of a tangle of quantum vortices. However, depending on the temperature, the forcing or the initial conditions, one can observe a different phenomenology of superfluid turbulence, some of them resembling the properties of classical turbulence (see chapter 2). Here, we will only focus on the phenomenology at very low temperatures, described by the GP model, which is the framework studied later in publication [MK20].

The typical evolution of decaying quantum turbulence is shown in Fig. 3.1 (extracted from [KB11]) and can be understood as follows. Let us consider that the superfluid initially consists of a complex tangle of quantum vortices that prescribes a velocity field. As the system starts to evolve, vortices begin to interact and reconnect. These interactions redistribute the energy in the system and act as a dissipative mechanism on the vortices at small scales, as their energy is partially radiated into sound. At early stages, the dynamics of the superfluid is completely prescribed by the initial condition. As the system continues to evolve, the amount of interactions increases until eventually they reach a maximum, usually quantified by the incompressible energy dissipation rate $\epsilon = -\mathrm{d}E^I_{\mathrm{kin}}/\mathrm{d}t$. In this transient, the superfluid
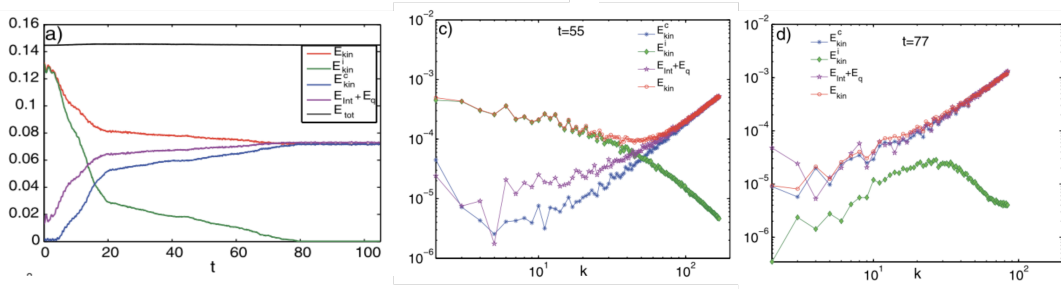
Figure 3.1: Evolution of the energy components in a quantum turbulent flow. The middle and right panels show the energy spectra at different times of the evolution. Extracted from [KB11].

displays a Kolmogorov turbulent regime at scales larger than the intervortex distance ℓ [NAB97a; KT05]. For $r < \ell$, the energy spectrum is determined by Kelvin waves propagating along individual vortices. This regime is described by the weak wave turbulence theory [Krs12; CMB17]. In this Thesis, we focus on the turbulent properties developed by the superfluid in this regime. At later stages, the vortex line density in the system decreases significatively. In this regime, vortices are usually arranged in rings and the system is described by Vinen turbulence, with an energy spectrum that satisfies k^{-1} and with a slower decay of the vortex line density [WG08; BBS12]. In Fig. 3.1 we show that, for an intermediate time $t = 55$ in which there is still some incompressible energy (i.e. there are some vortices), it follows a scaling at large scales close to k^{-1}, while the other energy components start to redistribute in equipartition. Finally, for a very late stage in the evolution $t = 77$, the superfluid thermalizes and waves satisfy an equipartition of energy with a scaling close to k^2 [KB11]. In this stage, the energy associated to vortices is negligible. The phenomenology of these regimes is described in chapter 2.

As classical fluids are dissipative, it is natural to study the properties of turbulence in a steady state in which the forcing and dissipative mechanisms are balanced. In the GP framework, the generation of stationary turbulence is more complicated. First of all, an external forcing would excite both vortices and sound waves. As the total energy of the system is conserved, one should introduced some damping mechanism into the system to prevent the energy to diverge. One way of doing this is to consider that the condensate is in contact with a thermal reservoir and interchanges particles with the thermal cloud [ZNG99; Tsu09]. This model, together with the introduction of a forcing, has been used to study statistical steady turbulence in two dimensions [RBA⁺13], or to study wave turbulence [PNO12]. One of the counterparts of this method is that this dissipation mechanism acts at all scales and over all energy components of the system, including vortices. Considering also the energy transfer to sound due to reconnections and Kelvin waves, it leads to a system that at very late stages of its evolution is dominated by acoustic waves, that may destroy the Kolmogorov phenomenology at large scales. For this reason, all the results obtained in this Thesis are performed studying decaying quantum turbulence (without forcing and damping) in a time window in which the Kolmogorov properties of the superfluid are manifest.

Note that a physical system that is naturally described by a driven-dissipative Gross–Pitaevskii equation is the exciton-polariton condensate, a paradigmatic family of quantum fluids of light [DHY10; PMD⁺21]. These are strictly 2D systems, confined in the plane of the superconductor microcavity in which polaritons are pumped with an amplitude F and momentum $\hbar \mathbf{k}_p$. The lifetime of this system is
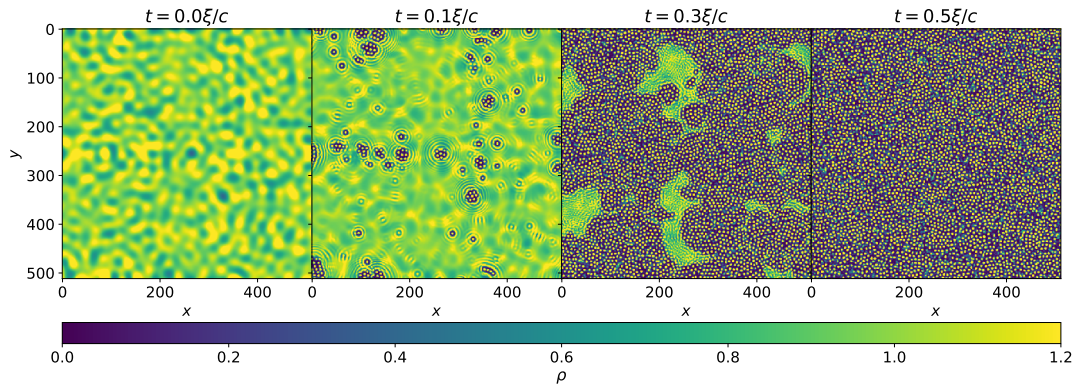
Figure 3.2: Evolution of the density field in a system with a roton minimum in the excitation spectrum in the absence of high-order non-linear terms. As the system evolves, small droplets are formed, leading to a crystallization state that destroys the background condensate.

usually very small (of the order of the picoseconds) due to the photon leakage from the microcavity, given at a rate γ. The effective dynamics of the polariton field ψ is given by

$$i\hbar\partial_t\psi = \left(-\frac{\hbar^2}{2m}\nabla^2 - i\frac{\gamma}{2} + V_{\text{ext}} + g|\psi|^2\right)\psi + Fe^{i\mathbf{k}_p\cdot\mathbf{x}} \tag{3.1}$$

with m the polariton effective mass, g the interaction strength, and V_{ext} an external potential. Note that experiments in BECs can also be reproduced by this model, as the loss of atoms in the condensate can also be interpreted as a dissipation mechanism [NGS+16; NEZ+19]. As this model counts with a source and a dissipation mechanism, it is an ideal framework for the study of weak-wave turbulence [Naz11].

In the publications [MK20; MPK21; PMK21], we study the decaying of a quantum Arnold-Bertrami-Childress (ABC) flow, described in detail in publication [MK20]. To properly generate the initial condition, we introduce this incompressible velocity field into a minimization method that prescribes the phase of the condensate wavefunction and the density profile of quantum vortices to minimize the acoustic contributions (see Appendix A for details on the numerical methods).

3.2 Crystallization in the generalized GP

The Bogoliubov dispersion relation, obtained from the GP model by perturbing the system around the ground state, does not reproduce the roton minimum in the excitation spectrum. Rotons are elementary excitations that originate from the competition between attractive and repulsive forces between atoms and are observed in systems like superfluid helium or dipolar BECs [DB98; SSL03]. A natural way of incorporating such excitations in the GP model is by considering a non-local two-particle potential V_I that reproduces the correct wavenumber and frequency of the roton minimum. In superfluid helium, it has a characteristic length scale $a_{\text{rot}} \approx 4\xi \approx 3.2$ Å. Many choices for V_I that satisfy these conditions are possible [VCC12]. In particular, in this work we use the isotropic interaction potential introduced by Reneuve, Salort, and Chevillard [RSC18]
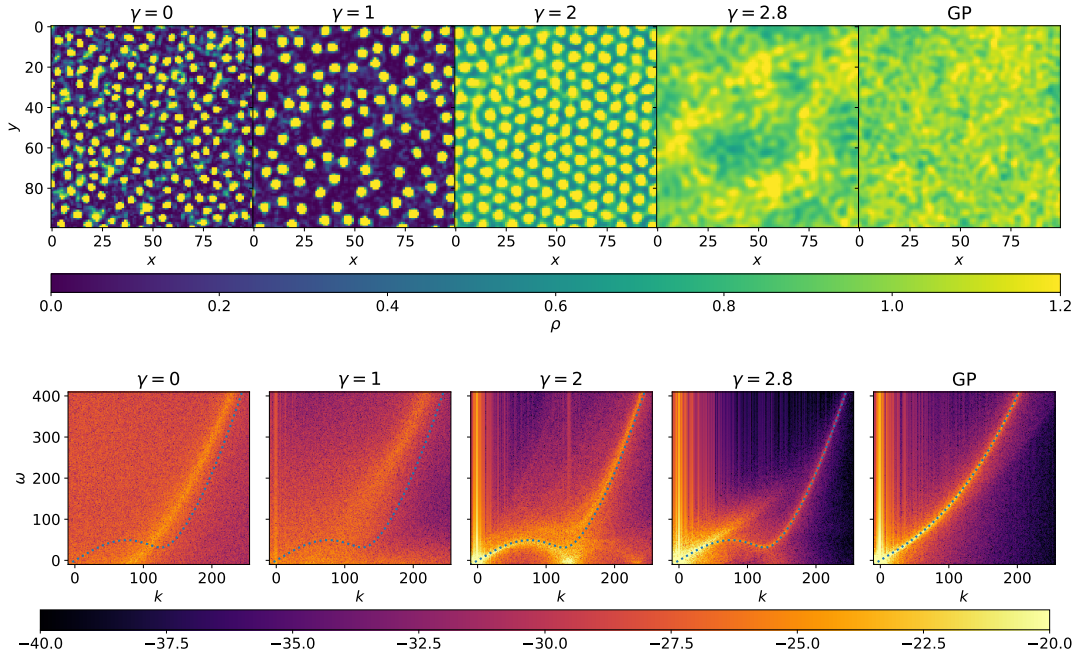
Figure 3.3: Density fields and spatio-temporal spectra for different values of the high-order exponent. Light colors indicate excited frequencies, and the dotted lines show the theoretical dispersion relation (3.4).

$$\hat{V}_{\mathrm{I}}(\mathbf{k}) = \left[1 - V_1 \left(\frac{k}{k_{\mathrm{rot}}}\right)^2 + V_2 \left(\frac{k}{k_{\mathrm{rot}}}\right)^4\right] \exp\left(-\frac{k^2}{2k_{\mathrm{rot}}^2}\right), \qquad (3.2)$$

where k_{rot} is the wavenumber associated to the roton minimum, and V_1 and V_2 two dimensionless parameters that are chosen to fit the dispersion relation of superfluid ^{4}He. In particular, it reproduces not only the position of the roton minimum, but also the speed of sound and the "maxon" energy observed in superfluid ^{4}He. This model was studied to understand the density profile of quantum vortices [BR99], how they reconnect [RSC18], the propagation of rotons [PR93], how different shapes of the interaction potential affect the properties of the superfluid [VCC12].

One of the counterparts of introducing the roton minimum is that, when the system is strongly perturbed, it develops some instabilities that lead to the formation of a crystal state in the absence of a background superfluid [RSC18]. This mechanism is shown in Fig. 3.2. We generate a 2D condensate with random waves using the non-local interaction potential (3.2) that reproduces the roton minimum in its excitation spectrum, and let it evolve following the GP equation using 1024^2 collocation points. Very quickly, we observe the formation of droplets with high values of density. Their typical size is given by the roton minimum distance. For late times, the system is fully crystallized and the background condensate vanishes.

To avoid the development of these instabilities, one can incorporate beyond mean-field corrections that model strong interactions between bosons. In particular, the generalize GP (gGP) model is then written as

$$i\hbar \frac{\partial \psi}{\partial t} = \left[-\frac{\hbar^2}{2m}\nabla^2 + V_{\mathrm{ext}} + gV_{\mathrm{I}} * |\psi|^2 - (1+\chi)\mu + g\chi \frac{|\psi|^{2(\gamma+1)}}{n_0^\gamma}\right]\psi. \qquad (3.3)$$

with χ and γ the amplitude and order of the extra non-linear term. Perturbing the condensate around the ground state leads to the generalized dispersion relation

$$\omega(k) = ck\sqrt{\frac{\xi^2 k^2}{2} + \frac{\hat{V}_{\mathrm{I}}(k) + \chi(\gamma+1)}{1 + \chi(\gamma+1)}} \qquad (3.4)$$

with c and ξ the speed of sound and the healing length of the superfluid, respectively. Using the effective non-local interaction potential (3.2) and fitting the parameters properly, this generalized dispersion relation reproduces the roton minimum [RSC18]. To show this effect, we study the dispersion relation and the density field in the gGP model for different values of the high-order exponent γ, with a fixed value of the amplitude of this term $\chi = 0.1$. The crystallization takes place for small values of this exponent $\gamma = 0$ and $\gamma = 1$. The dispersion relation in this case does not show the roton minimum as at this stage the background superfluid vanishes, so excitations are modified drastically and the roton minimum is lost. For $\gamma = 2$ we see an exotic behavior, similar to the one observed in supersolids [GRS+20]. In particular, we observe that the droplets are arranged in a triangular lattice immersed in a superfluid background. In this case, there are zero-frequency excitations that are triggered at the roton wave number. Finally, for $\gamma = 2.8$, we observe no droplets and the roton minimum is correctly reproduced. For this reason, in publication [MK20] we use this value for the high-order non-linear term to study some statistical properties of quantum turbulence. To compare, in Fig. 3.3 we also show the typical behavior of waves in the standard GP model.

3.3 Publication: *Kolmogorov and Kelvin wave cascades in a generalized model for quantum turbulence*

In this work, we study the properties of quantum turbulence in the generalized Gross–Pitaevskii (gGP) equation (3.3). This model reproduces the roton minimum in the excitation spectrum observed in superfluid helium, by considering a non-local interaction between bosons and a beyond mean-field correction that models strong interactions. To understand the role of each of these effects, we study separately the standard GP model, the local GP including a high-order non-linear term (without roton minimum), and the full gGP including the roton minimum.

We generate several initial conditions that follow the Arnold-Bertrami-Childress (ABC) velocity field, a flow characterized for having maximal helicity, using different spatial resolutions that go from 256^3 to 1024^3 collocation points and different values of the parameters controlling the high-order non-linear term. Once the flow is initialized, we let the system freely evolve in the absence of an external forcing. We study the quantum turbulent properties of the flow in a time window when contributions of initial condition are not dominant.

We first verify that the roton minimum introduces some density modulations in the vortex density profile around the ground state [BR99; RSC18] while, for the local case, the healing length is slightly modified with the high-order non-linearities. Nevertheless, these changes do not seem to affect qualitatively the evolution of different global quantities of the flow, like the intervortex distance or the different energy components. The energy spectra at large scales also show no significative difference between all the flows, suggesting that the modelling of bosonic interactions at small scales does not affect the dynamics of coherent structures in the Kolmogorov regime.

More strikingly, when the roton minimum is introduced, we observe that the incompressible energy spectrum at small scales shows a clear $k^{-5/3}$ power law given by the Kelvin wave prediction. In the standard GP model, this scaling is observed only for high-resolution numerical simulations [CMB17; SMK$^+$19]. This result suggests that this effect occurs as rotons perturb vortices triggering the excitation of Kelvin waves. Furthermore, we study the weak-wave turbulence prediction for Kelvin waves varying some properties of the flow like the values of ϵ, intervortex distance ℓ and healing length ξ. We observe that, not only the scaling with the wavenumber is compatible with the theory, but also the prefactor.

We conclude that the introduction of the roton minimum does not modify the dynamics of the system at large scales. Therefore, the specific choice of the non-local interaction potential between bosons is not relevant in the dynamics of Kolmogorov turbulence in quantum fluids. At small scales, however, rotons enhances the Kelvin-wave cascade, displaying scaling properties that reproduce the weak wave turbulence theory [LN10].

Kolmogorov and Kelvin wave cascades in a generalized model for quantum turbulence

Nicolás P. Müller and Giorgio Krstulovic
Université Côte d'Azur, Observatoire de la Côte d'Azur, CNRS, Laboratoire Lagrange,
Boulevard de l'Observatoire CS 34229 - F 06304 NICE Cedex 4, France

We performed numerical simulations of decaying quantum turbulence by using a generalized Gross-Pitaevskii equation that includes a beyond mean field correction and a nonlocal interaction potential. The nonlocal potential is chosen in order to mimic He II by introducing a roton minimum in the excitation spectrum. We observe that at large scales the statistical behavior of the flow is independent of the interaction potential, but at scales smaller than the intervortex distance a Kelvin wave cascade is enhanced in the generalized model. In this range, the incompressible kinetic energy spectrum obeys the weak wave turbulence prediction for Kelvin wave cascade not only for the scaling with wave numbers but also for the energy flux and the intervortex distance.

I. INTRODUCTION

One of the most fundamental phase transitions in low temperature physics is the Bose-Einstein condensation [1]. It occurs when a fluid composed of bosons is cooled down below a critical temperature. In that state, the system has long-range order and can be described by a macroscopic wave function. One of the most remarkable properties of a Bose-Einstein condensate (BEC) is that it flows with no viscosity. Well before the first experimental realization of a BEC by Anderson *et al.* [2], Kaptiza and Allen discovered that helium becomes superfluid below 2.17 K [3,4]. A couple of years later, London suggested that superfluidity is intimately linked to the phenomenon of Bose-Einstein condensation [5]. Since then, superfluid helium and BECs made of atomic gases have been extensively studied, both theoretical and experimentally. In particular, the fluid dynamics aspect of quantum fluids has renewed interest due the impressive experimental progress of the last fifteen years. Today it is possible to visualize and follow the dynamics of quantum vortices, one the most fundamental excitations of a quantum fluid [6,7].

Quantum vortices are topological defects of the macroscopic wave function describing the superfluid. They are nodal lines of the wave function and they manifest points and filaments in two and three dimensions, respectively. To ensure the monodromy of the wave function, vortices have the topological constraint that the circulation (contour integral) of the flow around the vortex must be a multiple of the Feynman-Onsager quantum of circulation $\kappa = h/m$, where h is the Planck constant and m is the mass of the Bosons constituting the fluid [1]. In superfluid helium their core size is of the order of 1 Å whereas in atomic BECs is typically of the order of microns [8]. Quantum vortices interact with other vortices similarly to classical ones. They move thanks to their self-induced velocity and interact with each other by hydrodynamics laws [9]. Unlike ideal classical vortices described by Euler equations,

quantum vortices can reconnect and change their topology despite the lack of viscosity of the fluid [10].

At scales much larger than the mean intervortex distance ℓ, the quantum nature of vortices is not very important as many individual vortices contribute to the flow. One could expect then that the flow is similar, in some sense, to a classical one. Indeed, if energy is injected at large scales, a classical Kolmogorov turbulent regime emerges. Such a regime has been observed numerically [11–13] and experimentally in superfluid helium [14,15]. In a three-dimensional turbulent flow, energy is transferred towards small scales in a cascade process [16]. In a low temperature turbulent superfluid, when energy reaches the intervortex distance, energy keeps being transferred to even smaller scales where it can be efficiently dissipated by sound emission. The mechanisms responsible for this transfer are vortex reconnections and the wave turbulence cascade of Kelvin waves, that have its origin in the quantum nature of vortices [17].

Describing a turbulent superfluid is not an easy task, in particular for superfluid helium. One of the main reasons is the gigantic scale separation existing between the vortex core size and the typical size of experiments, currently of the order of centimeters or even meters [18]. Their theoretical description began at the beginning of the 20th century by the pioneering works of Landau and Tisza where superfluid helium was modeled by two immiscible fluid components [19]. In this two-fluid model, the thermal excitations constitute the so-called normal fluid that is described by the Navier-Stokes equations whereas the superfluid component is treated as an inviscid fluid. It was later realized that the thermal excitations interact with superfluid vortices through scattering processes that lead to a coupling of both components by mutual friction forces [19]. Today the two-fluid description, known as the Hall-Vinen-Bekarevich-Khalatnikov model is understood as a coarse-grained model where scales smaller than the intervortex distance are not considered. The quantum nature aspects

of superfluid vortices are therefore lost. However, this model remains useful for describing the large scale dynamics of finite temperature superfluid helium. An alternative model was introduced by Schwarz [9], where vortices are described by vortex filaments interacting through regularized Biot-Savart integrals. However, the reconnection process between lines needs to be modeled in an ad-hoc manner and by construction the model excludes the dynamics of a superfluid at scales smaller than the vortex core size. Finally, for weakly interacting BECs in the limit of low temperature, a model of different nature can be formally derived which is the Gross-Pitaevskii (GP) equation, obtained from a mean field theory [1]. This model naturally contains vortex reconnections [10,20], sound emission [21,22], and is known to also exhibit a Kolmogorov turbulent regime at scales much larger than the intervortex distance [11]. Although this model is expected to provide some qualitative description of superfluid helium at low temperatures, it lacks of several physical ingredients. For instance, in GP, density excitations do not present any roton minimum as it does superfluid helium, where interactions between boson are known to be much stronger than in GP [23]. However, there have been some successful attempts to include such effects in the GP model. For instance, a roton minimum can be easily introduced in GP by using a nonlocal potential that models a long-range interaction between bosons [24–26]. The stronger interaction of helium can also be included phenomenologically by introducing high-order terms in the GP Hamiltonian. Note that these terms can be derived as beyond mean field corrections [27]. Some generalized version of the GP model has been used to study the vortex solutions [28,29] and some dynamical aspects such as vortex reconnections [26]. Intuitively, for a turbulent superfluid, we can expect that such generalization of the GP model might be important at scales smaller than the intervortex distance and with less influence at scales at which Kolmogorov turbulence is observed.

In this work, we study quantum turbulent flows by performing numerical simulations of a generalized Gross-Pitaevskii (gGP) equation. We compare the effect of high-order nonlinear terms and the effect of a nonlocal interaction potential in the development and decay of turbulence at scales both larger and smaller than the intervortex distance. Remarkably, by modeling superfluid helium with a nonlocal interaction potential and including high-order terms, the range where a Kelvin wave cascade is observed is extended and becomes manifest. Using the dissipation (or rate of transfer) of incompressible kinetic energy we are able to show that the weak wave turbulence results [30] are valid not only to predict the scaling with wave number but also with the energy flux and the intervortex distance.

The paper is organized as follows. Section II introduces the gGP model and discusses its basic properties and solutions. It also discusses how the vortex profile is modified in this generalized model. All useful definitions to study turbulence are also given here. Section III gives a brief overview of the predictions of quantum turbulence and the numerical methods used in this work. Also, it includes the results of different simulations at moderate and high resolutions by varying the different parameters of the beyond mean field correction and the introduction of a nonlocal potential. Finally in Sec. IV we present our conclusions.

II. THEORETICAL DESCRIPTION OF SUPERFLUID TURBULENCE

In this section we introduce the generalized Gross-Pitaevskii model used in this work. We also discuss and review some of the basic properties of the model such as its elementary excitations and its hydrodynamic description.

A. Model

The Gross-Pitaevskii equation describes the low temperature dynamics of weakly interacting bosons of mass m

$$i\hbar\frac{\partial \psi}{\partial t} = -\frac{\hbar^2}{2m}\nabla^2\psi - \mu\psi + g|\psi|^2\psi, \tag{1}$$

where ψ is the condensate wave function, μ the chemical potential, $\hbar = h/(2\pi)$, and $g = 4\pi\hbar^2 a_s/m$ is the coupling constant fixed by the s-wave scattering length a_s that models a local interaction between bosons. Note that the use of a local potential assumes a weak interaction between bosons, which certainly is not the case for other systems like He II and for dipolar gases [31].

A generalized model that is able to describe more complex systems can be obtained by considering a nonlocal interaction between bosons. With proper modeling [24–26], density excitations exhibit a roton minimum in their spectrum as the one observed in He II [23]. It also describes well the behavior of dipolar condensates [32,33]. In helium and other superfluids, the interaction between bosons is stronger and high-order nonlinearities are needed for proper modeling. For instance, in helium high-order terms are considered to mimic its equation of state [25] and in dipolar BECs beyond mean field terms are needed to describe the physics of recent supersolid experiments [34].

We consider the generalized Gross-Pitaevskii (gGP) model written as

$$i\hbar\frac{\partial \psi}{\partial t} = -\frac{\hbar^2}{2m}\nabla^2\psi - \mu(1+\chi)\psi \\ + g\left(\int V_{\mathrm{I}}(\boldsymbol{x}-\boldsymbol{y})|\psi(\boldsymbol{y})|^2 d^3y\right)\psi + g\chi\frac{|\psi|^{2(1+\gamma)}}{n_0^\gamma}\psi, \tag{2}$$

where γ and χ are two dimensionless parameters that determine the order and amplitude of the high-order terms, respectively. The interaction potential V_{I} is normalized such that $\int V_{\mathrm{I}}(\boldsymbol{x})d^3x = 1$. The chemical potential and the interaction coefficient of the high-order term have been renormalized such that $|\psi_0|^2 = n_0 = \mu/g$ is the density of particles for the ground state of the system for all values of parameters. The GP equation (1) is recovered by simply setting $V_{\mathrm{I}}(\boldsymbol{x}-\boldsymbol{y}) = \delta(\boldsymbol{x}-\boldsymbol{y})$ and $\chi = 0$. The gGP equation is not intended to be a first principle model of superfluid helium, but it has the advantage of at least introducing in a phenomenological manner some important physical aspects of helium.

B. Density waves

The dispersion relation of the GP model is easily obtained by linearizing equation (1) about the ground state. The waves obey the Bogoliubov dispersion that reads

$$\omega_B(k) = c_0 k \sqrt{\frac{\xi_0^2 k^2}{2} + 1}, \tag{3}$$

where k is the wave number, $c_0 = \sqrt{gn_0/m}$ is the speed of sound of the superfluid, and $\xi_0 = \hbar/\sqrt{2mgn_0}$ is the healing length at which dispersive effects become important. The healing length also fixes the vortex core size.

A similar calculation leads to the Bogoliubov dispersion relation in the case of the gGP model (2)

$$\omega(k) = ck \sqrt{\frac{\xi^2 k^2}{2} + \frac{\hat{V}_I(k) + \chi(\gamma + 1)}{1 + \chi(\gamma + 1)}}, \tag{4}$$

where $\hat{V}_I(\boldsymbol{k}) = \int e^{i\boldsymbol{k}\cdot\boldsymbol{r}} V_I(\boldsymbol{r}) d^3r$ is the Fourier transform of the interaction potential normalized such that $\hat{V}_I(k=0) = 1$. The inclusion of beyond mean field terms and a nonlocal potential

yields to a renormalized speed of sound and healing length. They are given in terms of c_0 and ξ_0 by

$$c = c_0 \sqrt{1 + \chi(\gamma + 1)} \tag{5}$$

$$\xi = \frac{\xi_0}{\sqrt{1 + \chi(\gamma + 1)}}. \tag{6}$$

Note that, in what concerns low amplitude density waves, the effect of high-order terms is a simple renormalization of the healing length and the speed of sound. Depending on the shape and properties of the nonlocal potential, the dynamics and steady solutions can be drastically modified. Note that the product between c and ξ remains constant because it is related to the quantum of circulation $\kappa = h/m = c\xi 2\pi\sqrt{2} = c_0\xi_0 2\pi\sqrt{2}$.

In order to be able to compare systems with different types of interactions, it is convenient to rewrite Eq. (2) in terms of its intrinsic length ξ and speed of sound c and the bulk density n_0. The gGP model then becomes

$$\partial_t \psi = -i \frac{c}{\xi\sqrt{2}(1 + \chi(\gamma + 1))} \left[-(1 + \chi(\gamma + 1))\xi^2 \nabla^2 \psi - (1 + \chi)\psi + \chi \frac{|\psi|^{2(1+\gamma)}}{n_0^{1+\gamma}}\psi + \frac{\psi}{n_0} \int V_I(\boldsymbol{x} - \boldsymbol{y})|\psi(\boldsymbol{y})|^2 d^3y \right]. \tag{7}$$

The only dimensional parameters of the model are the speed of sound c, the healing length ξ, and the bulk density n_0. They can be absorbed by a trivial rescaling of time, length, and density. The dimensionless parameters χ, γ and the nonlocal potential V_I should be chosen to model the physical system under study. In numerical simulations we will express lengths in units of the healing length ξ. A natural time scale to study excitations is the fast turnover time $\tau = \xi/c$. However, this small-scale based time is not appropriate for turbulent flows. For such flows, it is customary to use the large-eddy turnover time corresponding to the typical time of the largest coherent vortex structures. It will be defined later.

Modeling superfluid helium excitations

In this work, we aim at mimicking some properties of superfluid helium II, in particular, the roton minimum in the dispersion relation. For the sake of simplicity, we use an isotropic nonlocal interaction potential used in previous works [26,28]. With our normalization it reads

$$\hat{V}_I(\boldsymbol{k}) = \left[1 - V_1 \left(\frac{k}{k_{\text{rot}}}\right)^2 + V_2 \left(\frac{k}{k_{\text{rot}}}\right)^4 \right] \exp\left(-\frac{k^2}{2k_{\text{rot}}^2}\right), \tag{8}$$

where k_{rot} is the wave number associated with the roton minimum and $V_1 \geqslant 0$ and $V_2 \geqslant 0$ are dimensionless parameters to be adjusted to mimic experimental dispersion relation of helium II [23]. The effects of different functional forms of the nonlocal potential have been studied in previous works, showing that only a phase shift of ψ and the overall amplitude of the density depend on the precise form of the interaction [29].

In order to compare the dispersion relation (4) with the experimental data [23], we plot the helium dispersion relation in

units of the helium healing length $\xi_{\text{He}} = 0.8$ Å and its turnover time $\tau_{\text{He}} = \xi_{\text{He}}/c_{\text{He}} = 3.36 \times 10^{-13}$s, where $c_{\text{He}} = 238$ m/s is the speed of sound in He II. The experimental helium dispersion relation is displayed in Fig. 1 as green dotted lines. Note that by definition, the speed of sound of the gGP model and the one helium are equal to 1 (in units of ξ/τ.)

It was reported in Reneuve *et al.* [26] that introducing a roton minimum in the GP dispersion relation (without beyond mean field terms) that matches helium measurements leads to an unphysical crystallization under dynamical evolution of
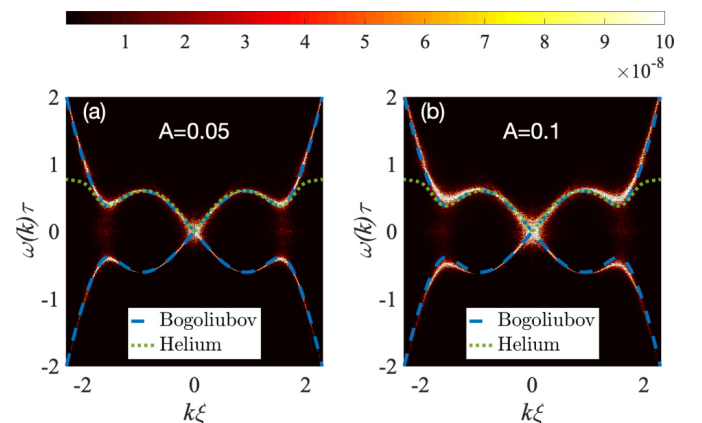

FIG. 1. Spatiotemporal dispersion relation for simulations with 1024^2 grid points with a nonlocal potential and beyond mean field corrections. Light zones correspond to excited frequencies. Figures (a) and (b) correspond to different amplitude of the perturbation A, both exhibiting a roton minimum. Experimental observations (green dotted line, see Ref. [23]) and theoretical dispersion following equation (4) (blue dashed line) are shown.

a vortex. We confirm such behavior in our simulations. In order to avoid such spurious effect of the model, in Ref. [26] the frequency associated to the roton minimum was set to higher values to be able to study vortex reconnections. We have numerically observed that this crystallization takes place even when a first order correction of the beyond mean field expansion is included, with values of $\chi = 0.1$ and $\gamma = 1$. For this reason, we chose a higher order expansion with $\gamma = 2.8$ for the simulations with a nonlocal potential, a value that was already used in the literature to study the vortex density profile in superfluid helium [25]. Furthermore, with this value no crystallization is observed for all test cases and all the simulations performed in this work.

The dispersion relation of a nonlinear wave system can be measured numerically by computing the spatiotemporal spectrum of the wave field [13]. As an example, in Fig. 1 we also display the spatiotemporal spectrum of small density perturbations of a numerical simulation of the gGP model in two dimensions using 1024^2 collocation points and with parameters set to $\gamma = 2.8$, $\chi = 0.1$, $V_1 = 4.54$, $V_2 = 0.01$, and $k_{rot}\xi = 1.638$ (see details on numerics later in Sec. III), for two different amplitude values A. Dark zones indicate that no frequencies are excited, while light zones correspond to the excited ones with the total sum normalized to one. The parameters have been set in a way such that they match qualitatively the dispersion relation measured in helium up to the roton minimum. As expected for weak amplitude waves, the numerical and theoretical dispersion relations coincide. For larger wave amplitudes, theoretical prediction (4) and numerical measurements slightly differ together with an apparent broadening of the curve. This is a typical behavior of nonlinear wave systems [35]. In the following sections, all simulations with a nonlocal interaction are performed with the aforementioned set of parameters.

C. Hydrodynamic description

The GP equation maps into a hydrodynamic description by introducing the Madelung transformation

$$\psi = \sqrt{\rho/m} \exp\left(\frac{i\phi}{\sqrt{2}c\xi}\right), \tag{9}$$

which allows the mapping of the wave function with the fluid mass density $\rho = m|\psi|^2$ and with the fluid velocity $\boldsymbol{v} = \boldsymbol{\nabla}\phi$. Replacing equation (9) into the gGP model (7) two hydrodynamic equations are obtained

$$\frac{\partial \rho}{\partial t} + \boldsymbol{\nabla} \cdot (\rho \boldsymbol{v}) = 0 \tag{10}$$

$$\frac{\partial \phi}{\partial t} + \frac{1}{2}(\boldsymbol{\nabla}\phi)^2 = -h[\rho] + (c\xi)^2 \frac{\nabla^2 \sqrt{\rho}}{\sqrt{\rho}}, \tag{11}$$

with

$$h[\rho] = -c_0^2(1+\chi) + c_0^2 \frac{V_1 * \rho}{\rho_0} + c_0^2 \chi \left(\frac{\rho}{\rho_0}\right)^{\gamma+1}. \tag{12}$$

Here $*$ denotes the convolution product and $\rho_0 = m|\psi_0|^2$ is the fluid mass density of the ground state. These equations correspond to the continuity and Bernoulli equations, respectively, of a fluid with an enthalpy per unit of mass $h[\rho]$ [11].
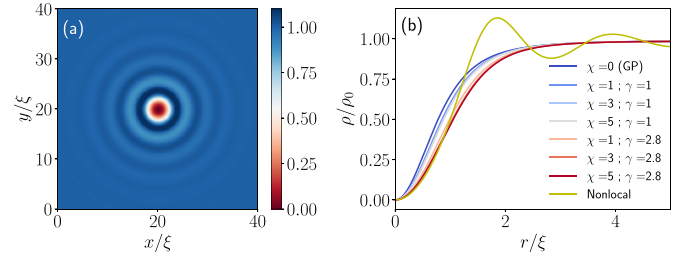

FIG. 2. (a) Mass density of a two-dimensional vortex with a nonlocal potential. (b) Density profile of a vortex for the gGP model with different values of the nonlinearity and a local potential, and a single profile with a nonlocal potential (yellow line). The vortex core size tends to increase with the nonlinearity.

The last term of equation (11) is called the quantum pressure. Note that hydrodynamic pressure is given by

$$p[\rho] = \frac{c_0^2 \rho}{\rho_0}\left[\frac{1}{2}V_1 * \rho + \chi \frac{\gamma+1}{\gamma+2}\frac{\rho^{\gamma+1}}{\rho_0^{\gamma}}\right]. \tag{13}$$

As expected, for large amplitude waves, the speed of sound reads $\frac{\partial p}{\partial \rho}\big|_{\rho_0} = c_0^2(1 + \chi(\gamma + 1)) = c^2$.

Although the fluid is potential, it admits vortices as topological defects of the wave function. A stationary vortex solution of (7) is a zero of the wave function where the circulation around it is quantized with values $\pm s\kappa$ with s an integer. Because of this last condition, topological defects are also called quantum vortices.

A quantum vortex has a vortex core size of the order of a healing length ξ and depends on the parameters of the gGP model. By replacing the Madelung transformation (9) into the gGP equation (7) and using cylindrical coordinates, a differential equation for the vortex profile is directly obtained

$$\frac{1}{r}\frac{d}{dr}\left(r\frac{dR}{dr}\right) + \left\{1 - \frac{s^2\xi_0^2}{r^2} - V_1 * R^2 + \chi(1 - R^{2\gamma+2})\right\}\frac{R}{\xi_0^2}$$
$$= 0, \tag{14}$$

where $R(r) = \sqrt{\rho(r)/\rho_0}$ defines the density profile of the vortex line in the radial direction r.

Figure 2(a) displays the mass density of a two-dimensional vortex in the case where the nonlocal interaction potential is included. The roton minimum introduces some density fluctuations around the center of the vortex which is a well-known pattern. The effect of a nonlocal potential has already been studied before, for example its interaction with an obstacle [24], the dynamics of vortex rings [25], and in reconnection processes [26]. Figure 2(b) shows the radial dependence of the density profile of a vortex for different parameters of the gGP model. Numerical simulations were performed with 4096^2 grid points with standard numerical methods (see Sec. III B for details). Even though all curves tend to collapse when plotted as a function of the healing length ξ, the vortex core size slightly increases (in units of ξ) when the nonlinearity of the system is increased. Note that for the present range of parameters, ξ_0/ξ varies in the range (1,4.4). The relatively good collapse of the vortex core size thus justifies the choice of ξ to parametrize the gGP model while varying the beyond mean field parameters.

D. Energy decomposition and helicity in superfluids

It is convenient to write the free energy per unit of mass $\mathcal{F}$ of a quantum fluid such that it vanishes when evaluated in the ground state of the system ($\psi = \sqrt{\rho_0/m} = \sqrt{n_0}$). For the gGP model in equation (7), it is given by

$$
\mathcal{F} = \frac{c_0^2}{n_0 V} \int \left[\xi_0^2 |\nabla \psi|^2 + \frac{|\psi|^2}{2n_0} (V_I * |\psi|^2) - (1 + \chi)|\psi|^2 \right.
$$
$$
\left. + \frac{\chi |\psi|^{2(\gamma+2)}}{n_0^{\gamma+1}(\gamma+2)} + \frac{n_0}{2} + \chi n_0 \frac{\gamma+1}{\gamma+2} \right] d^3r, \quad (15)
$$

with V the volume of the fluid. Following standard procedures applied in simulations of GP quantum turbulence [11], the free energy can be decomposed as $\mathcal{F} = E_{\text{kin}}^I + E_{\text{kin}}^C + E_q + E_{\text{int}}$ where $E_{\text{kin}}^I = \frac{1}{V\rho_0} \int ([\sqrt{\rho}\boldsymbol{v}]^I)^2 d^3r$, $E_{\text{kin}}^C = \frac{1}{V\rho_0} \int ([\sqrt{\rho}\boldsymbol{v}]^C)^2 d^3r$, and $E_q = \frac{c^2\xi^2}{V\rho_0} \int |\nabla\sqrt{\rho}|^2 d^3r$, with $[\sqrt{\rho}\boldsymbol{v}]^I$ the regularized incompressible velocity obtained via the Helmholtz decomposition and $[\sqrt{\rho}\boldsymbol{v}]^C = \sqrt{\rho}\boldsymbol{v} - [\sqrt{\rho}\boldsymbol{v}]^I$ the compressible one. The internal energy per unit of volume is defined in the gGP model as

$$
E_{\text{int}} = \frac{c_0^2}{V\rho_0} \int \left[\frac{1}{2\rho_0} (\rho - \rho_0) V_I * (\rho - \rho_0) \right.
$$
$$
\left. + \left(\frac{\rho}{\rho_0} \right)^{\gamma+1} \frac{\chi\rho}{\gamma+2} - \chi\rho + \chi \frac{\gamma+1}{\gamma+2}\rho_0 \right] d^3r. \quad (16)
$$

Note that $E_{\text{int}} = 0$ if $\rho = \rho_0$. The corresponding energy spectra are defined in a straightforward way for the quadratic quantities [11]. For the internal energy spectrum, it is defined as follows

$$
E_{\text{int}}(k) = \frac{c_0^2}{V\rho_0} \int \left[\frac{1}{2\rho_0} \widehat{(\rho - \rho_0)}_{-\mathbf{k}} \hat{V}_I(k) \widehat{(\rho - \rho_0)}_{\mathbf{k}} \right.
$$
$$
\left. + \frac{\chi}{\gamma+2} \hat{\rho}_{-\mathbf{k}} \widehat{\left(\frac{\rho}{\rho_0} \right)^{\gamma+1}}_{\mathbf{k}} + \left(\chi\rho_0 \frac{\gamma+1}{\gamma+2} - \chi\rho \right)_{\mathbf{k}} \right]
$$
$$
\times d\Omega_k, \quad (17)
$$

where $d\Omega_k$ is the element of surface of the shell $|\mathbf{k}| = k$ where the hat stands for the Fourier transform defined in the same way as in the nonlocal potential after equation (4). Note that this particular choice of the spectrum is not unique and has been made so that the ground state $\rho = \rho_0$ contributes with no internal energy to the system. It is also worth noting that with this definition, the internal energy spectrum may take negative values.

Besides the energies, there is another quantity in quantum turbulence that presents a great interest in the dynamics of quantum vortices [36–38], which is the central line helicity per unit of volume

$$
H_c = \frac{1}{V} \int \boldsymbol{v}(\boldsymbol{r}) \cdot \boldsymbol{\omega}(\boldsymbol{r}) d^3r. \quad (18)
$$

Note that $V H_c / \kappa^2$ is the total number of helicity quanta. Formally, this quantity is ill defined for a quantum vortex as the vorticity is δ supported on the filaments and the velocity is not defined on the vortex core. However, in the GP formalism, this singularity can be removed by taking proper limits [36]. We use the definition central line helicity proposed in Ref. [36] as its numerical implementation is tedious but straightforward and well behaved for vortex tangles.

III. EVOLUTION OF QUANTUM TURBULENT FLOWS

This section gives a brief overview about the predictions in quantum turbulence both at large and small scales, and details of the numerical methods used to run the simulations. There is also a description of the flow visualization in the presence of a nonlocal interaction potential, and the results of the flow evolution at moderate and high resolution are shown. In particular, it is studied the dependence of the different components of the energy and the helicity with beyond mean field parameters and with the introduction of a nonlocal interaction potential.

A. A brief overview of cascades in quantum turbulence

Quantum turbulence is characterized by the disordered and chaotic motion of a superfluid. Energy injected, or initially contained, at large scales is transferred towards small scales in a Richardson cascade process [16]. In the context of GP turbulence, the contribution of vortices to the global energy can be studied by looking at the incompressible kinetic energy E_{kin}^I and its associated spectrum. As the system evolves, vortices interact transferring energy between scales. Besides, the incompressible kinetic energy is transferred to the quantum, internal and compressible energy through vortex reconnections and sound emission [17,22]. After some time, acoustic excitations thermalize and act as a thermal bath providing a (pseudo)dissipative mechanism, so vortices shrink until they vanish [8,39,40].

Three-dimensional quantum turbulence presents two main statistical properties. At scales much larger than the intervortex distance ℓ, but much smaller than the integral scale L_0, the quantum character of vortices is not important and we can think as the system being coarse grained. At such scales the system presents a behavior that resembles classical turbulence with a direct energy cascade, that is the transfer of energy from large to small structures. As a consequence, in this range, the incompressible kinetic energy spectrum $E_{\text{kin}}^I(k)$ follows the Kolmogorov prediction [11,16,41,42]

$$
E_{\text{kin}}^I(k) = C_K \epsilon^{2/3} k^{-5/3}, \quad (19)
$$

where $C_K \sim 1$ and ϵ is the dissipation rate of the flow, which in GP quantum turbulence is associated with the rate of change of incompressible kinetic energy $\epsilon = -dE_{\text{kin}}^I/dt$, that is expressed in units of $[\epsilon] = \text{length}^2/\text{time}^3$.

In classical three-dimensional inviscid flows, helicity (18) is also conserved. Associated to this invariant, a second direct cascade is expected to be also present at large scales, obeying the scaling [43]

$$
H(k) = C_H \eta \epsilon^{-1/3} k^{-5/3}, \quad (20)
$$

where $C_H \sim 1$ and $\eta = -dH/dt$ is the dissipation rate of helicity. This dual cascade has been also observed in quantum turbulent flows described by the GP equation [44].

At scales smaller than the intervortex distance, each quantum vortex can be thought as if it were isolated. Hence, its behavior can be described, in principle, by the wave turbulence theory as such vortices admit hydrodynamic excitations known as Kelvin waves. Such waves propagate along vortices and interact nonlinearly among themselves. As a result, energy is transferred towards small scales through a process that can be described by the theory of weak wave turbulence [35]. An agitated debate arose some time ago concerning the prediction of the energy spectrum. Two independent groups leaded by L'vov and Nazarenko [30] and Kozik and Svistunov [45], starting from the same equations and applying the same theory derived different predictions. Even though, today there is more numerical data supporting L'vov and Nazarenko prediction [46–49], this issue is still debated [50–52]. We present here the L'vov and Nazarenko prediction as, we will see later, it was found to be in agreement with our numerical data. This theoretical prediction is derived for an almost straight vortex of period L_v and, as discussed in Ref. [50], some care is needed in order to apply the model to a turbulent vortex tangle. We partially reproduce here and adapt to our case the considerations of Ref. [50]. The wave turbulence L'vov and Nazarenko prediction is

$$e_{\mathrm{KW}}(k) = C_{\mathrm{LN}} \frac{\kappa \Lambda \epsilon_{\mathrm{KW}}^{1/3}}{\Psi^{2/3} k^{5/3}}, \qquad (21)$$

with $\Lambda = \log(\ell/\xi)$ and $C_{\mathrm{LN}} \approx 0.304$ [47]. Here $\epsilon_{\mathrm{KW}} = -de_{\mathrm{KW}}/dt$ is the mean energy flux per unit of length L_v and density ρ_0. Note their respective dimensions are $[\epsilon_{\mathrm{KW}}] = $ length^4/time^3 and $[e_{\mathrm{KW}}(k)] = $ length^5/time^2. The dimensionless number Ψ is given by

$$\Psi = \frac{(12\pi C_{\mathrm{LN}})^{3/5} \epsilon_{\mathrm{KW}}^{1/5}}{\kappa^{3/5} k_{\min}^{2/5}} = C_{\mathrm{LN}}^{3/5} \tilde{\Psi}, \qquad (22)$$

where $k_{\min}$ is the smallest wave number of the Kelvin waves that can be associated with the wave number of the intervortex distance $k_\ell = 2\pi/\ell$ in the case of a vortex tangle [50]. $\tilde{\Psi}$ is defined so that it is independent of the constant C_{LN}.

In order to compare this result with the incompressible kinetic energy, one can notice that the total energy of Kelvin waves is $L_v \rho_0 \int e_{\mathrm{KW}}(k)dk$, where now L_v is taken as the total vortex length in the system. As in a turbulent tangle the total vortex length is related to the mean intervortex distance by $L_v = V\ell^{-2}$, it follows that the mean kinetic energy spectrum per unit of mass is given by $E_{\mathrm{KW}}(k) = e_{\mathrm{KW}}(k)\ell^{-2}$. The same logic relates the energy flux ϵ_{KW} of the Kelvin wave cascade to the global energy flux ϵ of a tangle by $\epsilon_{\mathrm{KW}} = \epsilon\ell^2$. It follows from (21) and the previous considerations that

$$E_{\mathrm{KW}}(k) = C_{\mathrm{LN}}^{3/5} \frac{\kappa \Lambda \epsilon^{1/3} \ell^{-4/3}}{\tilde{\Psi}^{2/3} k^{5/3}}. \qquad (23)$$

Here we have made the assumption that the energy flux in the Kolmogorov range is the same as in the Kelvin wave cascade. This strong assumption might be questioned as energy could be already dissipated into sound by vortex reconnections at different scales diminishing this value [22,53]. Such extra sinks of energy are difficult to quantify and we will not take them into account. Finally, note that the theory of wave turbulence also predicts the value of the constant C_{LN} [47], however

in (23) several phenomenological considerations have been made and we do not expect an exact agreement. Nevertheless, the scaling with the global energy flux should remain valid.

B. Numerical methods

We perform numerical simulations of equation (7) using a pseudo-spectral method for the spatial resolution applying the "2/3 rule" for dealiasing [54], and a Runge-Kutta method of fourth order for the time stepping. The nonlinear term is dealiased twice following the scheme presented in [40] in order to also conserve momentum. Note that in the case of a nonlocal potential, this extra step has no extra numerical cost. All simulations were performed in a cubic L-periodic domain.

To observe a Kolmogorov range in GP turbulence it is customary to start from an initial vortex configuration with a minimal acoustic contribution. We prepared the initial condition by a minimization process such that the resulting flow is as close as possible to the targeted velocity field [11]. In this work we study the quantum Arnold-Bertrami-Childress (ABC) flow [44]. It is obtained from the velocity field $\boldsymbol{v}_{\mathrm{ABC}} = \boldsymbol{v}_{\mathrm{ABC}}^{(k_1)} + \boldsymbol{v}_{\mathrm{ABC}}^{(k_2)}$, where each ABC flow is given by

$$\boldsymbol{v}_{\mathrm{ABC}}^{(k)} = [B\cos(ky) + C\sin(kz)]\hat{x} + [C\cos(kz)$$
$$+ A\sin(kx)]\hat{y} + [A\cos(kx) + B\sin(ky)]\hat{z}. \qquad (24)$$

We set in this work $(A, B, C) = V_{\mathrm{amp}}(0.9, 1, 1.1)/\sqrt{3}$, with $V_{\mathrm{amp}} = 0.5c$. Each ABC flow is an L-periodic stationary solution of the Euler equation with maximal helicity, in the sense that $\nabla \times \boldsymbol{v}_{\mathrm{ABC}}^{(k)} = k\boldsymbol{v}_{\mathrm{ABC}}^{(k)}$. The mean kinetic energy associated with $\boldsymbol{v}_{\mathrm{ABC}}$ is $E_{\mathrm{kin}}^{\mathrm{ABC}} = (A^2 + B^2 + C^2) = 0.2517c^2$. Following Ref. [44], the wave function associated to this ABC flow is generated as $\psi_{\mathrm{ABC}} = \psi_{\mathrm{ABC}}^{(k_1)} \times \psi_{\mathrm{ABC}}^{(k_2)}$, where each mode is constructed as the product $\psi_{\mathrm{ABC}}^{(k)} = \psi_{A,k}^{x,y,z} \times \psi_{B,k}^{y,z,x} \times \psi_{C,k}^{z,x,y}$ with

$$\psi_{A,k}^{x,y,z} = \exp\left\{ i\left[\frac{A\sin(kx)}{c\xi\sqrt{2}}\right]\frac{2\pi y}{L} + i\left[\frac{A\cos(kx)}{c\xi\sqrt{2}}\right]\frac{2\pi z}{L} \right\}, \qquad (25)$$

where the brackets [ ] indicate the integer closest to the value to ensure periodicity. This ansatz gives a good approximation for the phase of the initial condition. In order to set properly the mass density and the vortex profiles, it is necessary to first evolve ψ_{ABC} using the generalized advected real Ginzburg-Landau equation (imaginary time evolution in a locally Galilean transformed system of reference) [11]

$$\partial_t \psi = -\frac{c_0}{\xi_0\sqrt{2}}\left\{ -\xi_0^2\nabla^2\psi - (1+\chi)\psi + \chi\frac{|\psi|^{2(1+\gamma)}}{\rho_0^{1+\gamma}}\psi \right.$$
$$\left. + \frac{\psi}{\rho_0}(V * |\psi|^2) \right\} - i\boldsymbol{v}_{\mathrm{ABC}} \cdot \nabla\psi - \frac{(\boldsymbol{v}_{\mathrm{ABC}})^2}{2\sqrt{2}c\xi}\psi. \qquad (26)$$

This equation is dissipative and its final state contains a minimal amount of compressible energy. This state is used as an initial condition for the gGP equation. Unless stated otherwise, we use a flow at the largest scales of the systems by setting $k_1 = 2\pi/L$ and $k_2 = 4\pi/L$ throughout this work.

The numerical simulations performed in this work are summarized in Table I and regrouped in two different sets. The first set of simulations (runs A1–A8) have been performed at a moderate spatial resolution of $N^3 = 256^3$ grid points to study

TABLE I. Table with the parameters of the different simulations. N is the linear spatial resolution, χ and γ are the amplitude and order of the beyond mean field interactions, L/ξ is the scale separation between the domain size L and the healing length ξ, $\tilde{k}_1 = k_1 L/2\pi$ and $\tilde{k}_2 = k_2 L/2\pi$ are the two wave numbers where the energy is concentrated for the initial condition, and a local or a nonlocal interaction potential is used in each of them.

	N	χ	γ	L/ξ	$\tilde{k}_1, \tilde{k}_2$	Interaction potential
A1	256	0	1	171	1,2	local
A2	256	1	1	171	1,2	local
A3	256	3	1	171	1,2	local
A4	256	5	1	171	1,2	local
A5	256	1	2.8	171	1,2	local
A6	256	3	2.8	171	1,2	local
A7	256	5	2.8	171	1,2	local
A8	256	0.1	2.8	171	1,2	nonlocal
B1	512	0	1	341	1,2	local
B2	512	0.1	2.8	171	1,2	nonlocal
B3	512	0.1	2.8	341	1,2	nonlocal
B4	512	0.1	2.8	341	2,3	nonlocal
B5	512	0.1	2.8	341	3,4	nonlocal
B6	1024	0.1	2.8	683	1,2	nonlocal

the effects introduced by the beyond mean field interactions and a nonlocal potential. Each of them has a different value of χ and γ with a local potential and were compared with a single simulation with a nonlocal interaction potential. The second set (runs B1–B6) has been performed to study the scaling of the energy spectra. In these runs, we used a spatial resolution of 512^3 and 1024^3 grid points, different scale separations, and initial conditions. These results were also compared with the GP model.

C. Flow visualization

The introduction of a nonlocal potential, as mentioned in Sec. II C, allows the system to reproduce the roton minimum in the excitation spectrum (see Fig. 1). As a consequence, the density profiles close to the quantum vortices have some fluctuations around the bulk value ρ_0 (see Fig. 2). These oscillations have been studied for the profile of a two-dimensional vortex [25,29] and have been also observed in three dimensions during vortex reconnections [26]. In the case of a helical vortex tangle, the roton minimum induces a remarkable pattern of density fluctuations around a vortex line. A visualization of the initial condition ψ_{ABC} for run B6 is displayed in Figs. 3(a) and 3(b). The red structures are isosurfaces of low density values $\rho = 0.1\rho_0$ and thus represent the vortex lines. The greenish rendering displays density fluctuations of the field above the bulk value ρ_0, that are only observed in the case of a nonlocal potential. In Fig. 3(a) we recognize the large scale structures of the ABC flow accompanied by some density fluctuations around the nodal lines. Figure 3(b) displays a zoom of the tangle where such fluctuations are clearly observed. Unlike the (local) GP model, density variations around a vortex line have a very specific pattern, rolling around the nodal lines in a helicoidal manner.
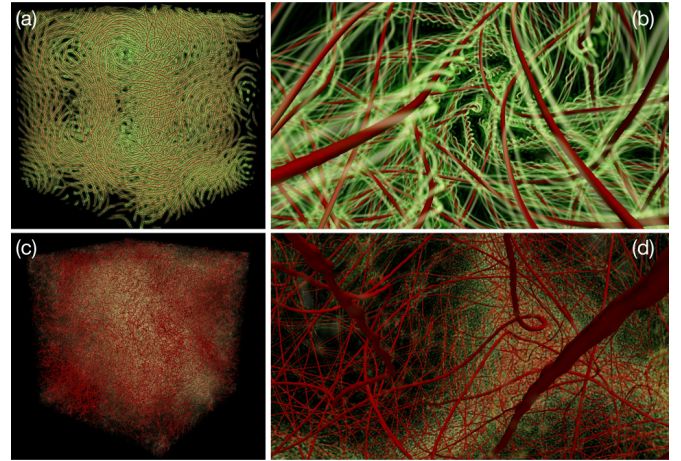

FIG. 3. (a)-(b) Visualization of an ABC flow at $t = 0$ and (c)-(d) for $t = 1.25\tau_L$ and $t = 0.4\tau_L$ respectively, for a resolution of 1024^3 grid points with a nonlocal potential. The isosurfaces of a small value the mass density shown in red correspond to the vortex lines, and in green are the values of the density fluctuations above ρ_0.

Such a pattern is a consequence of the maximal helicity initial condition produced by the ABC flow. Indeed, we have also produced a Taylor-Green initial condition [11] that has no mean helicity, and such helicoidal patterns in the density fluctuations are absent, although they are nevertheless developed after some vortex reconnections, as observed in Ref. [26] (data not shown). Finally, in Figs. 3(c) and 3(d) we display visualizations of the field for times $t = 1.25\tau_L$ and $t = 0.4\tau_L$, respectively. Time is expressed in units of the large-eddy turnover time $\tau_L = L_0/v_{\text{rms}}$ with $v_{\text{rms}} = \sqrt{2E_{\text{kin}}^I(t=0)/3}$ and L_0 its integral length scale given by $L_0 = 2\pi/k_2$ with k_2 the largest wave number used to generate the initial condition. $t = 1.25\tau_L$ corresponds to a time when turbulence is developed and $t = 0.4\tau_L$ to an early stage of the turbulent development for a better insight of the flow. As the system evolves, acoustic emissions are produced and the density fluctuations increase. In Fig. 3(c) we observe a turbulent tangle where a large scale structure is predominant. Figure 3(d) displays a zoom where reconnections and Kelvin waves propagating along vortices are clearly visible.

D. Temporal evolution of global quantities

In this section we study the behavior of the global quantities of an ABC flow driven by the gGP model (7) with both local and nonlocal potentials corresponding to runs A in Table I. Figure 4 shows the time evolution of the (a) incompressible kinetic energy and (b) the sum of the quantum, internal, and compressible kinetic components to the total energy. We notice that in Fig. 4(a) the values of amplitude and exponent of the beyond mean field interaction and the inclusion of roton minimum (runs A1–A8) have a negligible impact on the incompressible energy of the initial condition, and their effect is very small during the temporal evolution. On the other hand, as the fluid can be considered to be more incompressible due to stronger interactions, the density variations with respect to the bulk value ρ_0 yield larger values

FIG. 5. Time evolution of the intervortex distance of the system in units of the healing length. All curves correspond to the runs A in Table I. The green area corresponds to the window where the dissipation achieves a maximum and where the time averages were performed.
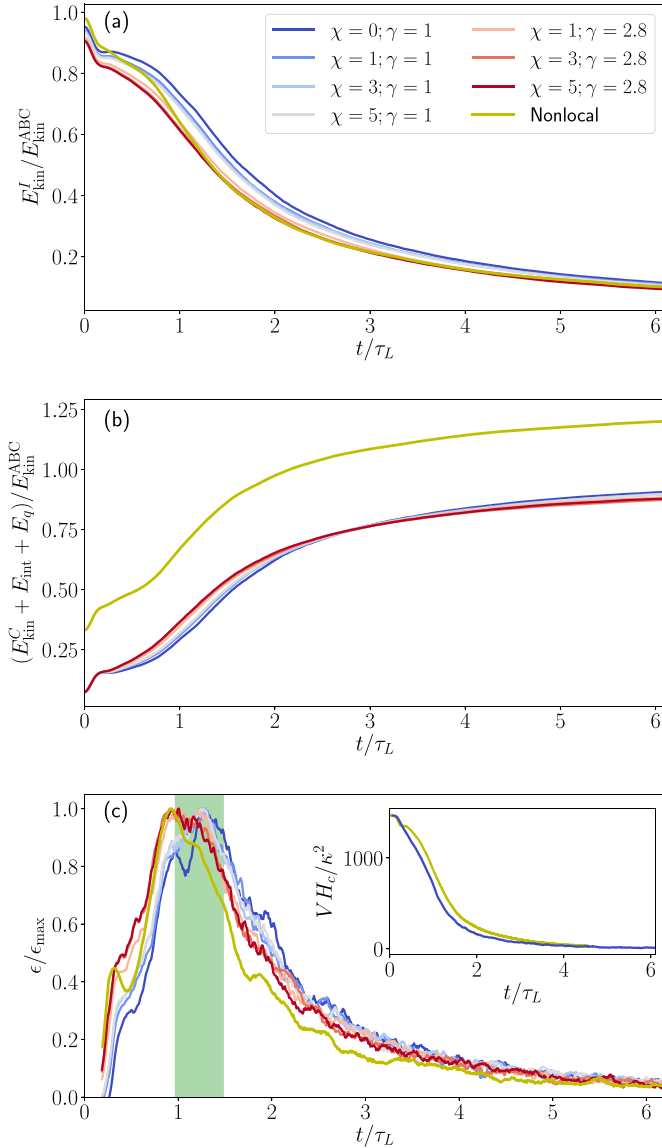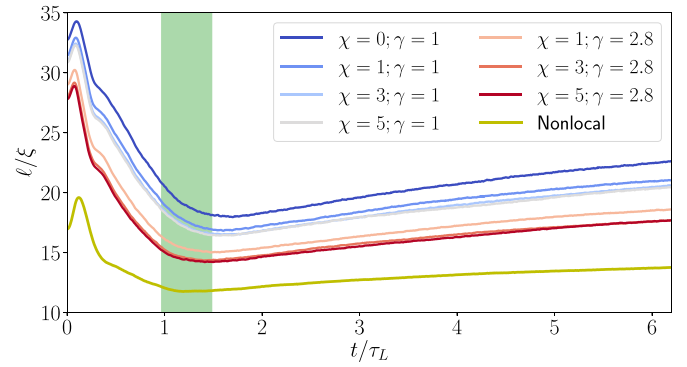

FIG. 4. Time evolution of the (a) incompressible kinetic energy, (b) the sum of the internal, quantum, and compressible kinetic energy, and (c) the dissipation rate of incompressible energy for runs A in Table I. The inset in (c) shows the evolution of the central line helicity. The green area corresponds to the window where the dissipation achieves a maximum and where the time averages were performed.

of the other energy component between the initial time and $t \approx 3\tau_L$ as displayed in Fig. 4(b). In particular, for the case of a nonlocal potential their values remain larger for the whole run. Nevertheless, for all runs during the first large-eddy turnover times the main contribution to energy comes from vortices. At later times, energy from vortices is converted into sound. As stated in Sec. III A, the decay of the incompressible energy can be used to estimate the energy dissipation rate ϵ. Its temporal evolution is displayed in Fig. 4(c). As in classical decaying turbulent flows, for quantum flows the Kolmogorov regime is more developed at times slightly after the maximum of dissipation is reached. The green zone in the figure depicts the temporal window where the system is considered to be in

a quasisteady state and a temporal average can be performed to improve statistics. The inset of Fig. 4(c) displays that the decay of the central line helicity is independent of the parameters of the gGP model and is consistent with the one reported in Ref. [44].

As a turbulent flow evolves, the total vortex length L_v varies in time in a competition between the vortex line stretching and the reconnection process. This quantity can be obtained from the incompressible momentum density of the flow $J^I(k)$ and of a two-dimensional point-vortex $J_{vort}^{2D}(k)$ as $L_v = 2\pi \sum_{k<k_{max}} k^2 J^I(k) / \int_0^{k_{max}} k^2 J_{vort}^{2D}(k) dk$ [11].

Figure 5 shows the time evolution of the intervortex distance $\ell = \sqrt{V/L_v}$. In the cases of a local and a nonlocal interaction, the intervortex distance achieves a minimum around one τ_L. The vortex line density of the system $\mathcal{L} = \ell^{-2}$ is expected to decay in time following either the Vinen's decay law [55] $\mathcal{L} \sim t^{-1}$, when flow is dominated by random rings, or the "quasiclassical" $\mathcal{L} \sim t^{-3/2}$ regime, when it is saturated by the container size [56]. In the GP framework, the Vinen's law has been clearly observed at very late times, where only a few rings are left [49]. To perform a clean study of the decay of the vortex line density, it is necessary to study the evolution of the system for much longer times that the ones presented in this work. In addition, the method implemented for the computation of the vortex length of the system is just an estimation and a more precise method needs be used to determine the scaling of the vortex length decay. Such a study is left for a future work.

Finally, in Fig. 6 we display the energy spectra for different runs of set A. Figure 6(a) shows the spectra of the incompressible kinetic energy and the sum of all the other components for different runs. Even though the range of scales is rather limited for this set of simulations, a Kolmogorov-like power law at large scales is observed in the incompressible kinetic energy. The spectra of the sum of the other energy components can be considered as the contribution of excitations that do not arise from vortices. Phenomenologically, we can consider that dynamics of the system is governed by vortices and is thus almost incompressible for scales down to the crossover between the two spectra plotted in Fig. 6(a). Such crossover wave
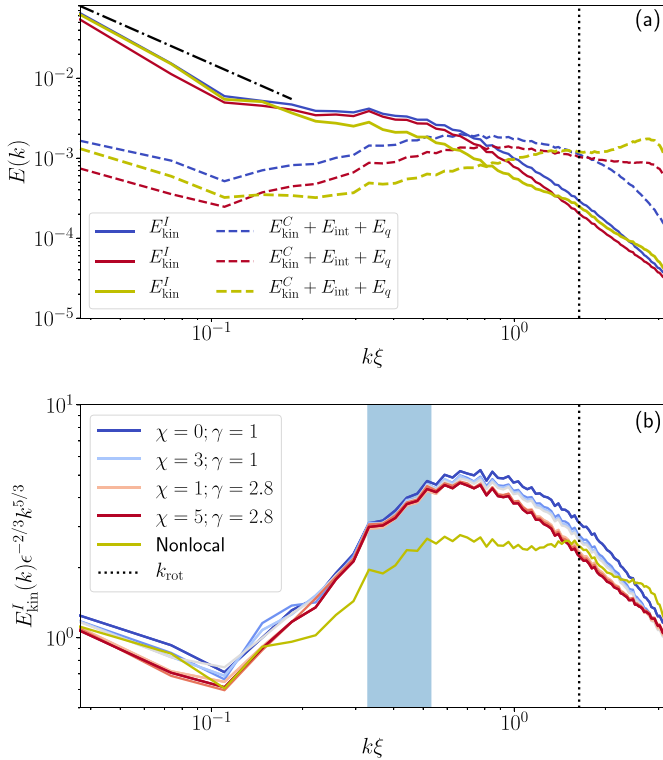
FIG. 6. (a) Time averaged spectra of the incompressible kinetic energy and the sum of the internal, quantum, and compressible kinetic energy for runs A1 (blue), A7 (red), and A8 (yellow) in Table I. (b) Compensated incompressible energy spectra for all the set of runs A. The filled blue area indicates the intervortex wave numbers $k_\ell \xi$ for the different simulations.

FIG. 7. (a) Helicity and energy spectra of the different components for the simulation with 1024^3 grid points (run B6). Vertical dotted lines indicate the wave numbers associated with the intervortex distance k_ℓ and the roton minimum $k_{\rm rot}$. (b) Helicity spectra compensated by Eq. (20) for runs B1–B3 and B6 shown in Table I.

number is decreased while introducing beyond mean field terms and a nonlocal potential. Figure 6(b) displays the incompressible energy spectra compensated by the Kolmogorov prediction $E_{\rm kin}^I \sim \epsilon^{2/3} k^{-5/3}$, where large scales collapse to values close to one. Remarkably, for the nonlocal potential run, a secondary plateau appears at smaller scales, below the intervortex distance (intervortex wave numbers for each run vary within the blue area). This range can be associated to the presence of Kelvin waves and it will be studied at higher resolutions in the next section.

E. Numerical evidence of the coexistence of Kolmogorov and Kelvin wave cascades

The Kelvin wave cascade discussed in Sec. III A is formally derived from an incompressible model in a very simplified theoretical setting. In the context of the GP model, the Kelvin wave cascade was first observed in Ref. [46] where a setting close to the theoretical prediction was used. In the case of turbulent tangles, there was first an indirect observation of the Kelvin wave cascade by making use of the spatiotemporal spectra [57]. In that work, the Kelvin wave dispersion relation was glimpsed and a space-time filtering of the fields was performed yielding a scaling in the energy spectrum compatible to the Kelvin wave cascade. Then, by using an accurate tracking algorithm of a turbulent tangle, in Ref. [49] the L'vov-Nazarenko prediction was clearly observed in the
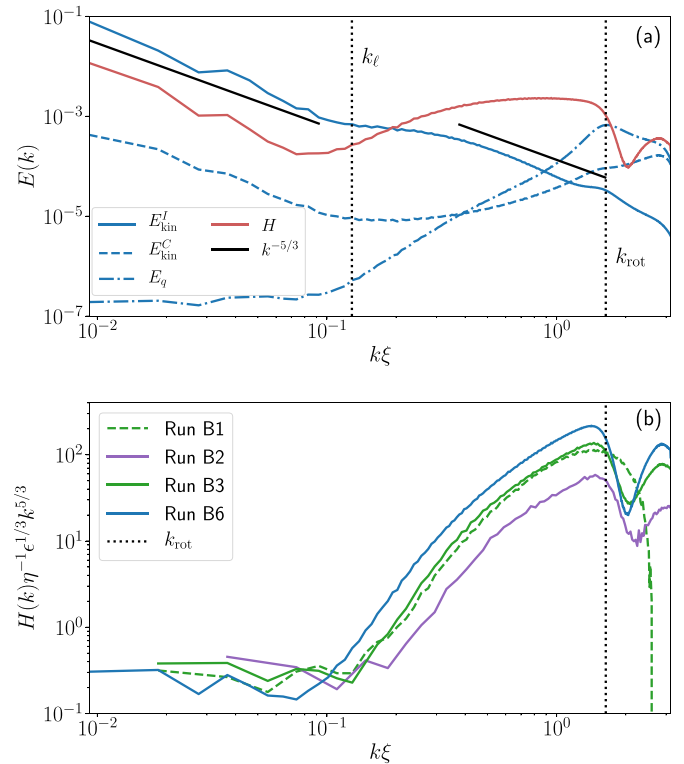
spectrum of large vortex rings extracted from the tangle. Later, in Refs. [13,44], by using high-resolution numerical simulations of the GP model, and by superposing different runs, a secondary scaling range compatible with Kelvin wave cascade predictions was observed. In this section, we focus on the scaling of the incompressible energy spectra and helicity for the case with a nonlocal potential (set of runs B) as it seems to present a much clearer scaling at scales smaller than the intervortex distance. We vary different parameters so the range of scales (system size, intervortex distance, healing length) and energy fluxes take different values.

The spectra for the different components constituting the kinetic energy and the helicity of the simulation with 1024^3 grid points are shown in Fig. 7(a). Clear power laws for the Kolmogorov and Kelvin wave range are observed simultaneously at large and small scales. A fit $k^{-\alpha}$ using the least squares method was performed for each cascade. We obtain a scaling $\alpha = 1.73$ in the range between $k\xi = 0.02$ and $k\xi = 0.12$, associated with the Kolmogorov cascade, and a scaling $\alpha = 1.65$ in the range between $k\xi = 0.33$ and $k\xi = 1.64$, associated with a Kelvin wave cascade. These two scaling laws are separated by the intervortex wave number k_ℓ. At this scale, a bottleneck between a strong and a weak cascade takes place and a plateau in the incompressible kinetic energy is observed. According to the warm cascade ideas [58], this bottleneck should display a k^2 scaling associated with the thermalization of the system. However, this behavior is not observed probably due to the fact that the separation of scales

TABLE II. Values of integral scale L_0, the quantum of circulation κ, the energy dissipation rate ϵ, and the intervortex distance, expressed in units of the box size $L = 2\pi$, and the speed of sound is fixed to $c = 1$.

Run	v_{rms}	L_0	κ	ϵ	ℓ
B1	0.395	$L/2$	0.163	0.012	0.412
B2	0.377	$L/2$	0.327	0.013	0.494
B3	0.398	$L/2$	0.163	0.012	0.255
B4	0.406	$L/3$	0.163	0.020	0.235
B5	0.403	$L/4$	0.163	0.029	0.227
B6	0.392	$L/2$	0.081	0.011	0.139

in the Kelvin wave range is not large enough. We will come back to this point later.

Concerning other energy components, the quantum energy shows a maximum at the scale associated with the roton minimum, whereas its contribution is negligible at large scales. The helicity spectrum also displays a Kolmogorov-like behavior at large scales, while at scales between the intervortex distance and the roton minimum it flattens. This flat range of the helicity spectrum appears in the range where the Kelvin wave cascade is dominant. Whether a direct relationship between the Kelvin wave cascade and the flattening of the central line helicity spectrum exists is still unclear. Figure 7(b) displays the compensated helicity spectrum according to (20) for different runs displaying different scale separations and with local and nonlocal potentials. The parameters of these simulations correspond to the runs B1–B3 and B6 shown in Table I. At large scales all curves collapse to a constant $C_H \sim 1$, while at smaller scales the system with a wider scale separation displays that the helicity contribution is more intense.

To analyze further the incompressible energy spectra, we have performed two runs varying the integral length of the initial condition so that the dissipation rate also changes (runs B4 and B5). We recall that in classical turbulence, the energy flux ϵ is fixed by the inertial range and varies as $\epsilon \sim v_{\mathrm{rms}}^3/L_0$. Our initial condition ψ_{ABC} keeps fixed, by construction, the value of v_{rms}. In Table II we present the values of different physical quantities relevant for a turbulent state. Such quantities are expressed, as customary in classical turbulence, in units of large scale quantities. In particular, the system size is $L = 2\pi$ and the speed of sound is $c = 1$. With such definitions, large scale quantities remain almost constant when increasing the scale separation between the box size and the smallest scale of the system, but the quantum of circulation takes smaller values.

Figure 8(a) shows the incompressible energy spectra compensated by $k^{-5/3}$. Two plateaux are clearly observed: one corresponding to the large scales Kolmogorov scaling and the other small-scale Kelvin wave cascade. It can be seen that the values of these plateaux differ by a factor of 3. By following the procedures introduced in Ref. [58], but using prediction of Eq. (23) for the Kelvin wave spectrum, the ratio between these two plateaux is expected to scale as

$$E_{KW}/E_{K41} \sim \Lambda^{22/15}, \tag{27}$$

where we recall that $\Lambda = \log \ell/\xi$. The previous derivation assumes that $\Lambda \gg 1$. In our simulations, this quantity takes a
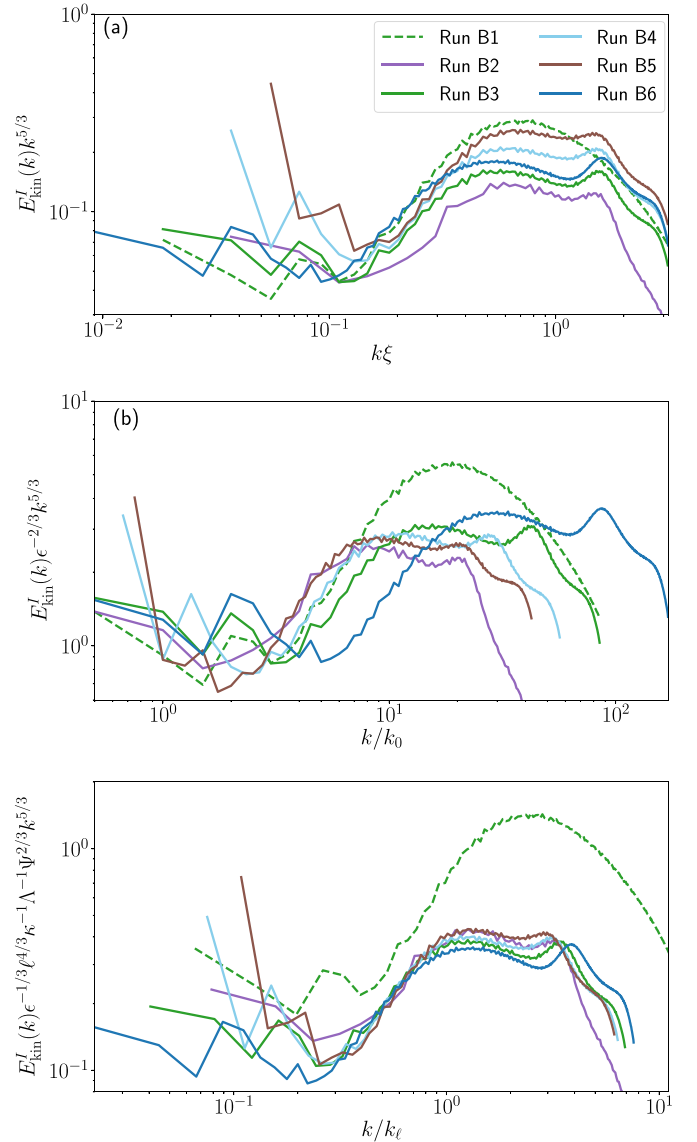

FIG. 8. Compensated incompressible kinetic energy spectra by (a) $k^{-5/3}$ scaling, (b) Kolmogorov scaling (19). and (c) L'vov-Nazarenko scaling for Kelvin waves (23).

value of $\Lambda \approx 2.7$, which cannot be considered large to apply the previous formula safely. It is nevertheless expected that if the inertial range of the Kelvin wave cascade is extended, the bottleneck joining the two regimes should be enhanced, eventually leading to a thermalized k^2 zone.

The energy spectra shown in Fig. 8(b) have been compensated by the Kolmogorov law (19) and displayed as a function of k/k_0, with $k_0 = 2\pi/L_0$ in order to emphasize the Kolmogorov regime. Once properly normalized, all runs present a plateau at large scales that collapse to values that fluctuate around a Kolmogorov constant $C_K \sim 1$, in agreement with previous simulations of the GP model [13,44]. In order to emphasize the Kelvin wave cascade, we make use of the L'vov and Nazarenko wave turbulence prediction (23). Figure 8(c) displays the incompressible energy spectra compensated by this theoretical prediction as a function of k/k_ℓ, with $k_\ell = 2\pi/\ell$. The collapse of the Kelvin wave

cascade is remarkable. All runs having a nonlocal potential display a plateau around a value $C_{LN}^{3/5} \approx 0.36$, which recovers a constant of $C_{LN} \approx 0.18$. Such a value is relatively close to the predicted one $C_{LN} = 0.304$, in particular considering all the phenomenological assumptions made in Sec. III A to adapt the theoretical prediction (21) to the case of a turbulent tangle in Eq. (23). It is also important to remark that Eq. (21) is obtained from the Biot-Savart model, while the dynamics studied in this work corresponds to the gGP model, with a nonlocal interaction potential and beyond mean field corrections. The GP run (with local interaction potential) displays a good Kolmogorov scaling at large scales. However, it does not clearly exhibit a Kelvin wave cascade range at the highest resolution used in this work for this model (512^3 grid points). Note that previous works reporting a secondary $k^{-5/3}$ range in local GP model after superposing different runs have used resolutions of 2048^3 and 4096^3 collocation points [13,44]. For the sake of completeness, the incompressible kinetic energy spectrum compensated by the Kozik and Svistunov prediction [45] is displayed in Appendix.

IV. CONCLUSIONS

We studied the properties of the freely decaying quantum turbulence of the generalized Gross-Pitaevskii (gGP) model (7) that includes beyond mean field corrections and considers a nonlocal interaction potential between bosons. This model pretends to give a better description of superfluid helium as it reproduces a roton minimum in the excitation spectrum.

The visualization of the flow with a nonlocal potential allowed us to observe the formation of helical structures around the vortices produced by density fluctuations, exhibiting the intrinsic property of maximal helicity of an ABC flow. These structures were not observed at initial times in a flow with no helicity like a Taylor-Green flow, but they develop as the system evolves (data not shown). However, it was seen that the behavior of the helicity is independent of the interaction potential. At large scales the helicity develops a spectrum that satisfies prediction (20), while at scales between the intervortex distance and the healing length a plateau is observed. This range is usually associated with the Kelvin wave cascade regime, but it is still not clear whether the formation of this plateau is associated with Kelvin waves or not.

By studying numerically the freely decaying quantum turbulence of an ABC flow, we observed that the statistical behavior of the system does not depend much on the parameters of the beyond mean field correction in the presence of a local interaction potential between bosons. This is manifest in the evolution of quantities such as the energy, the helicity, and the intervortex distance of the system. The introduction of a nonlocal potential does not modify significantly the behavior of the system at large scales, exhibiting a Kolmogorov-like scaling law for the incompressible kinetic energy. However, the situation changes at smaller scales when a nonlocal potential is implemented, between the intervortex distance ℓ and the healing length ξ, the range associated with the Kelvin wave cascade. Here, the nonlocal potential enhances a second scaling of the incompressible energy spectrum. This is observed even at a moderate resolution of 256^3 grid points, while in the case of a local GP model an energy spectrum compatible with

$k^{-5/3}$ scaling law begins to be recognizable from resolutions of 2048^3 collocation points [44], and even in this case the range of scales where it takes place is less than a decade. This stronger manifestation of the Kelvin wave cascade may be very useful for numerical and theoretical studies of wave turbulence. This clear difference with the local GP model may be used to compare if effectively this model better describes the dynamics of superfluid helium. However, experimental observation at scales smaller than the intervortex distance still remains a challenge.

We also studied the scaling of the Kelvin wave spectrum with the energy flux ϵ and the intervortex distance by varying the integral scale of the initial flow and its healing length. We observed that the different spectra tend to collapse to a constant according to L'vov and Nazarenko spectrum for Kelvin waves (23). The observed value of the constant is $C_{LN} \approx 0.18$ which is close to the predicted one $C_{LN} \approx 0.304$. This is surprising given that the theory is constructed using a Biot-Savart model considering a single vortex line, while here it is extended to a vortex tangle in the framework of the gGP model with a nonlocal interaction potential and including several phenomenological assumptions. The Kozik and Svistunov spectrum for Kelvin waves was also studied for these set of simulations, however, by compensating the energy spectra by this theory no clear plateau is observed (see Appendix). Furthermore, in the range of the Kelvin wave cascade the Kozik-Svistunov cascade would take values of $C_{KS} \approx 0.06$ which is not of order one, so it might imply that the energy spectrum is not described by this theory.

The overall results of this work show that both GP and gGP models describe a similar behavior at large scales, exhibiting a classical Kolmogorov law for the incompressible kinetic energy and helicity spectra. However, at small scales, the gGP model includes the roton minimum in the excitation spectrum, and the Kelvin wave cascade range is enhanced, showing an apparent discrepancy with the local GP model. In summary, the simulations of this generalized model allow for a simultaneous observation of the Kolmogorov and Kelvin wave cascades, at resolutions at which the (standard) GP model barely exhibit a Kelvin wave range. Further studies are needed to understand the effect of nonlocal interactions deeply.

APPENDIX: KOZIK-SVISTUNOV KELVIN SPECTRUM

The original Kozik and Svistunov prediction for the Kelvin wave cascade [45] was done with the same geometrical
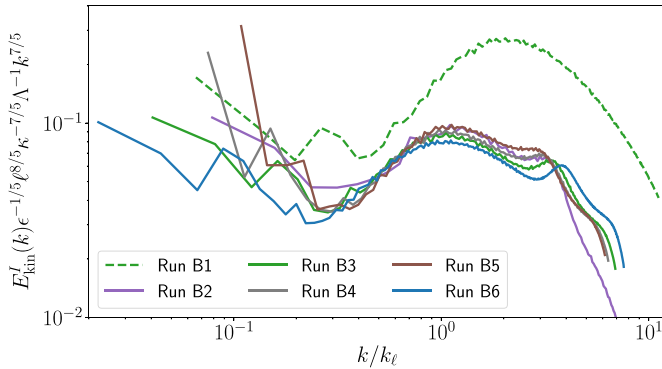
FIG. 9. Compensated incompressible kinetic energy spectra by the Kozik and Svistunov prediction for Kelvin waves.

considerations of L'vov and Nazarenko and it is also expressed in units of length^5/time^2. Applying the same considerations of Sec. III A to adapt this prediction to a turbulent three-

dimensional flow leads to the following Kelvin wave energy spectrum

$$E_{\mathrm{KW}}^{\mathrm{KS}}(k) = C_{\mathrm{KS}} \frac{\kappa^{7/5} \Lambda \epsilon^{1/5} \ell^{-8/5}}{k^{7/5}}, \tag{A1}$$

where the constant C_{KS} could be in principle determined by the theory if some integrals in the associated kinetic equation are convergent, but its value is still unknown. Figure 9 displays the incompressible kinetic energy spectrum compensated by prediction (A1). All the curves tend to collapse in the range associated with Kelvin waves, showing a proper scaling with the energy flux ϵ, the intervortex distance ℓ, and the quantum of circulation κ. However, although the Kelvin wave range is limited, a plateau is not clearly observed if the spectra are compensated by (A1), and even though a constant cannot be well defined, the energy spectra collapse to a mean value of $C_{\mathrm{KS}} \approx 0.06$, which is not of order one.

[1] L. P. Pitaevskii and S. Stringari, *Bose-Einstein Condensation and Superfluidity*, Vol. 164 (Oxford University Press, New York, 2016).

[2] M. H. Anderson, J. R. Ensher, M. R. Matthews, C. E. Wieman, and E. A. Cornell, Sci., New Ser. **269**, 198 (1995).

[3] P. Kapitza, Nature (London) **141**, 74 (1938).

[4] J. F. Allen and A. Misener, Nature (London) **141**, 75 (1938).

[5] F. London, Nature (London) **141**, 643 (1938).

[6] E. Fonda, D. P. Meichle, N. T. Ouellette, S. Hormoz, and D. P. Lathrop, Proc. Natl. Acad. Sci. **111**, 4707 (2014).

[7] S. Serafini, M. Barbiero, M. Debortoli, S. Donadello, F. Larcher, F. Dalfovo, G. Lamporesi, and G. Ferrari, Phys. Rev. Lett. **115**, 170402 (2015).

[8] C. F. Barenghi, L. Skrbek, and K. R. Sreenivasan, Proc. Natl. Acad. Sci. **111**, 4647 (2014).

[9] K. W. Schwarz, Phys. Rev. B **38**, 2398 (1988).

[10] J. Koplik and H. Levine, Phys. Rev. Lett. **71**, 1375 (1993).

[11] C. Nore, M. Abid, and M. E. Brachet, Phys. Fluids **9**, 2644 (1997).

[12] A. W. Baggaley, J. Laurie, and C. F. Barenghi, Phys. Rev. Lett. **109**, 205304 (2012).

[13] V. Shukla, P. D. Mininni, G. Krstulovic, P. C. di Leoni, and M. E. Brachet, Phys. Rev. A **99**, 043605 (2019).

[14] J. Maurer and P. Tabeling, Europhys. Lett. **43**, 29 (1998).

[15] J. Salort, B. Chabaud, E. Lévêque, and P.-E. Roche, Europhys. Lett. **97**, 34006 (2012).

[16] U. Frisch, *Turbulence: The Legacy of A.N. Kolmogorov*, 1st ed. (Cambridge University Press, Cambridge, 1995).

[17] W. F. Vinen, Phys. Rev. B **64**, 134520 (2001).

[18] B. Rousset, P. Bonnay, P. Diribarne, A. Girard, J. M. Poncet, E. Herbert, J. Salort, C. Baudet, B. Castaing, L. Chevillard, F. Daviaud, B. Dubrulle, Y. Gagne, M. Gibert, B. Hébral, T. Lehner, P.-E. Roche, B. Saint-Michel, and M. Bon Mardion, Rev. Sci. Instrum. **85**, 103908 (2014).

[19] R. J. Donnelly, *Quantized Vortices in Helium II* (Cambridge University Press, Cambridge, 1991).

[20] A. Villois, D. Proment, and G. Krstulovic, Phys. Rev. Fluids **2**, 044701 (2017).

[21] G. Krstulovic, M. Brachet, and E. Tirapegui, Phys. Rev. E **78**, 026601 (2008).

[22] A. Villois, D. Proment, and G. Krstulovic, Phys. Rev. Lett. **125**, 164501 (2020).

[23] R. J. Donnelly and C. F. Barenghi, J. Phys. Chem. Ref. Data **27**, 1217 (1998).

[24] Y. Pomeau and S. Rica, Phys. Rev. Lett. **71**, 247 (1993).

[25] N. G. Berloff and P. H. Roberts, J. Phys. A: Math. Gen. **32**, 5611 (1999).

[26] J. Reneuve, J. Salort, and L. Chevillard, Phys. Rev. Fluids **3**, 114602 (2018).

[27] T. D. Lee, K. Huang, and C. N. Yang, Phys. Rev. **106**, 1135 (1957).

[28] N. G. Berloff, M. Brachet, and N. P. Proukakis, Proc. Natl. Acad. Sci. **111**, 4675 (2014).

[29] S. Villerot, B. Castaing, and L. Chevillard, J. Low Temp. Phys. **169**, 1 (2012).

[30] V. S. L'vov and S. Nazarenko, JETP Lett. **91**, 428 (2010).

[31] T. Lahaye, C. Menotti, L. Santos, M. Lewenstein, and T. Pfau, Rep. Prog. Phys. **72**, 126401 (2009).

[32] A. Griesmaier, J. Phys. B: At., Mol. Opt. Phys. **40**, R91 (2007).

[33] L. Santos, G. V. Shlyapnikov, and M. Lewenstein, Phys. Rev. Lett. **90**, 250403 (2003).

[34] S. M. Roccuzzo, A. Gallemi, A. Recati, and S. Stringari, Phys. Rev. Lett. **124**, 045702 (2020).

[35] S. Nazarenko, *Wave Turbulence*, Lecture Notes in Physics No. 825 (Springer, Heidelberg, 2011).

[36] P. Clark di Leoni, P. D. Mininni, and M. E. Brachet, Phys. Rev. A **94**, 043605 (2016).

[37] S. Zuccher and R. L. Ricca, Phys. Rev. E **92**, 061001(R) (2015).

[38] M. W. Scheeler, D. Kleckner, D. Proment, G. L. Kindlmann, and W. T. M. Irvine, Proc. Natl. Acad. Sci. **111**, 15350 (2014).

[39] G. Krstulovic and M. Brachet, Phys. Rev. B **83**, 132506 (2011).

[40] G. Krstulovic and M. Brachet, Phys. Rev. E **83**, 066311 (2011).

[41] S. K. Nemirovskii, Phys. Rep. **524**, 85 (2013).

[42] L. Skrbek and K. R. Sreenivasan, Phys. Fluids **24**, 011301 (2012).

[43] A. Brissaud, Phys. Fluids **16**, 1366 (1973).

[44] P. Clark di Leoni, P. D. Mininni, and M. E. Brachet, Phys. Rev. A **95**, 053636 (2017).

[45] E. V. Kozik and B. V. Svistunov, J. Low Temp. Phys. **156**, 215 (2009).

[46] G. Krstulovic, Phys. Rev. E **86**, 055301(R) (2012).

[47] L. Boué, R. Dasgupta, J. Laurie, V. L'vov, S. Nazarenko, and I. Procaccia, Phys. Rev. B **84**, 064516 (2011).

[48] A. W. Baggaley and J. Laurie, Phys. Rev. B **89**, 014504 (2014).

[49] A. Villois, D. Proment, and G. Krstulovic, Phys. Rev. E **93**, 061103(R) (2016).

[50] V. Eltsov and V. S. L'vov, JETP Lett. **111**, 389 (2020).

[51] E. B. Sonin, Pis'ma Zh. Eksp. Teor. Fiz. **111**, 706 (2020) [JETP Lett. **111**, 598 (2020)].

[52] V. B. Eltsov and V. S. L'vov, JETP Lett. **111**, 600 (2020).

[53] D. Proment and G. Krstulovic, Phys. Rev. Fluids **5**, 104701 (2020).

[54] D. Gottlieb and S. A. Orszag, *Numerical Analysis of Spectral Methods: Theory and Applications* (SIAM, Philadelphia, 1977).

[55] W. F. Vinen, Proc. R. Soc. London, Ser. A **242**, 493 (1957).

[56] P. M. Walmsley and A. I. Golov, Phys. Rev. Lett. **118**, 134501 (2017).

[57] P. Clark di Leoni, P. D. Mininni, and M. E. Brachet, Phys. Rev. A **92**, 063632 (2015).

[58] V. S. L'vov, S. V. Nazarenko, and O. Rudenko, Phys. Rev. B **76**, 024520 (2007).

Chapter 4

Intermittency of velocity circulation in quantum and classical turbulence

In this chapter, we present the main results obtained in this Thesis on the intermittent nature of velocity circulation in quantum and classical turbulence. The velocity circulation statistics is studied in three different models: the Navier–Stokes equations for an incompressible classical fluid, the Gross–Pitaevskii equation describing a dilute gas of bosons at zero temperature, and the two-fluid HVBK equations describing superfluid helium at finite temperatures. We also analyze data from experiments in superfluid ^{4}He, performed by collaborators in Florida. The results are presented in three different publications [MPK21; PMK21; MTG$^+$22], where we highlight the similarities in the intermittent behavior of velocity circulation statistics in classical and quantum turbulence, and provide some tools to understand its nature.

The intermittent behavior of homogeneous and isotropic turbulence is usually studied in terms of velocity increments statistics. By computing velocity differences, the large-scales effects produced by a mean velocity field are removed, leaving only the turbulent fluctuations of the flow. The scaling exponents of structure functions present anomalous deviations from the mean-field K41 theory, known as anomalous scaling. This behavior is usually described using multifractal models, a phenomenological tool based on the local self-similarity of turbulent flows and expressed in terms of an infinite number of exponents. It is important to remark that there is still no first principles theory able to describe the intermittent nature of turbulent flows. To provide a deeper understanding of this phenomenon, we propose to study the intermittent behavior of velocity circulation statistics in quantum fluids. We present in this chapter the results obtained in three different publications carried out during this Thesis.

In the first of these publications [MPK21], presented in Sec. 4.2, we show that the scaling exponents of circulation moments obtained from high-resolution DNS of quantum turbulence at scales larger than the intervortex distance are similar to the ones observed in classical turbulence. At small scales, due to the discrete nature of circulation in quantum vortices, the scaling properties of classical and quantum fluids differ. In the second publication [PMK21], introduced in Sec. 4.3, we develop a discrete model for circulation that is able to describe the scaling exponents of circulation based on vortex proximity. We thus propose that the mean-field Kolmogorov scaling comes from a partial polarization of coherent structures at large scales, while the intermittent behavior can be understood as the complex spatial distribution between vortices. In the third publication [MTG$^+$22], presented in Sec. 4.4, we analyze

the circulation statistics from experimental data performed by the group of Wei Guo in Tallahassee, and compare them with DNS of the two-fluid HVBK equations at different temperatures. We show that the intermittent nature of superfluid turbulence is compatible with classical fluids, and is temperature independent. Finally, in Sec. 4.5, we report some preliminary results on the statistics of velocity circulation in two-dimensional quantum turbulence from DNS of the GP model. We show that the inverse cascade is characterized by a lack of intermittency, while the direct enstrophy cascade presents some anomalous deviations in the scaling exponents.

4.1   Velocity circulation

The velocity circulation is defined as the line integral of the velocity field $\mathbf{u}$ around a closed loop $\mathcal{C}_r$ of linear size r

$$\Gamma_r = \oint_{\mathcal{C}_r} \mathbf{u} \cdot d\mathbf{l} = \int_{\mathcal{S}_A} \boldsymbol{\omega} \cdot d\mathbf{S}. \tag{4.1}$$

The second equality is obtained using Stokes theorem, with $\partial \mathcal{S}_A = \mathcal{C}_r$ where $A \sim r^2$ is the area of the surface, and $\boldsymbol{\omega} = \nabla \times \mathbf{u}$ the vorticity field. The velocity circulation is a geometrical quantity that measures the strength of vortices passing through the loop $\mathcal{C}_r$.

Using only dimensional arguments, one would naively expect that the scaling exponents of circulation λ_p and velocity increments ζ_p were related as

$$\langle \Gamma_r^p \rangle \sim r^p \langle \delta v_r^p \rangle \sim r^{\zeta_p + p} \sim r^{\lambda_p}, \tag{4.2}$$

and therefore $\lambda_p = \zeta_p + p$, which in the case of K41 leads to $\lambda_p^{\text{K41}} = 4p/3$. One could also expect that circulation moments present an anomalous scaling that could be described on the basis of multifractal arguments for ζ_p. This relation was first studied by Cao et al. [CCS96] via DNS and showed that for high-order moments it fails, suggesting that the intermittent nature of velocity increments and circulation might differ.

By definition, the circulation around a square-planar loop of size r with opposite vertices at $(0,0)$ and (r,r) is

$$\Gamma_r = \int_0^r [u_x(x,0) - u_x(x,r)]dx + \int_0^r [u_y(0,y) - u_y(r,y)]dy, \tag{4.3}$$

showing that circulation is related with transverse velocity increments. Then, one would a priori expect that transverse structure functions and circulation moments are somehow related.

Velocity circulation is an integrated quantity, meaning that events with opposite signs can cancel out reducing thus the probability of finding high circulation values generated by vortex clusters. This phenomenon might lead to a statistical behavior that differs from velocity increments, and that might be characterized be the cancellation index [ODS+92; ZSY19]. It is speculated that turbulence can be understood as a collection of vortex filaments, each of them carrying a circulation Γ_i. Understanding the behavior of these singularities could provide some information on whether vortex filaments are the main reason of multifractality or if they are one of the components of a complex system [Fri95].
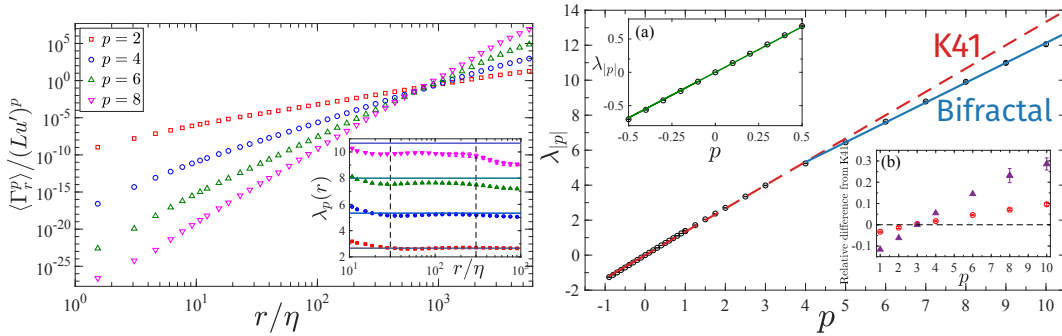
Figure 4.1: Left panel: Normalized circulation moments of even order p obtained from DNS of incompressible NS equations with $\mathrm{Re}_\lambda = 1300$. Moments are plotted as a function of the linear size of the loop r normalized by the Kolmogorov length scale η. Inset: Local slopes $\lambda_p(r) = \mathrm{d}\log\langle\Gamma_r^p\rangle/\mathrm{d}\log r$. Right panel: Scaling exponents of the absolute value of circulation moments. Red-dashed line shows K41 scaling $\lambda_p^{\mathrm{K41}} = 4p/3$ and blue-solid line shows the bifractal fit $1.1p + 0.8$ for $p > 3$. Inset (a) shows low-order scaling exponents. Inset (b) shows the relative deviations from K41 defined as $(\lambda_p^{\mathrm{K41}} - \lambda_p)/\lambda_p^{\mathrm{K41}}$. Red circles correspond to circulation exponents, while triangles to longitudinal velocity increments exponents. Extracted from [ISY19].

4.1.1 Historical aspects

The statistics of velocity circulation in incompressible fluids was first studied by Migdal [Mig94] based on a reduced Hopf generating functional. Within this framework, he derived an explicit functional equation for the tails of the circulation PDF in the WKB limit (from Wentzel-Kramers-Brillouin) of $\nu \to 0$ and in the absence of external forcing. He proposed the so-called area rule, which states that the tails of the PDF depend only on the minimal area of the closed loop, and not on its actual shape, as long as the characteristic length scale r of the loop is contained within the inertial range.

After the theoretical observations made by Migdal, several groups studied the statistics of velocity circulation. Using numerical simulations of the incompressible NS equations at modest Reynolds numbers, Umeki [Ume93] was the first to observe a scaling for the circulation standard deviation $\langle\Gamma_A^2\rangle^{1/2} \sim A^{2/3}$, with $A \sim r^2$ the minimal area enclosed by the loop. Later experimental and numerical investigations at low Reynolds numbers showed that scaling exponents of circulation and structure functions differ in a non-trivial way, in the sense that relation (4.2) fails in turbulent flows [SJS95; CCS96]. This observation was later contradicted by numerical studies on turbulent shear flows, showing that relation (4.2) actually holds true up to $p = 6$. Years later, experiments in turbulent Rayleigh-Bénard convection were carried out, showing that circulation is a very effective quantity for measuring local anisotropies of the flow [ZSX08]. It was also observed that for low-order moments, circulation and structure functions display the same scaling, consistent with the results of Benzi et al. [BBS+97], while for high-order moments the relative deviation of circulation was found to be larger, consistent with the results of Cao et al. [CCS96].

In 2019, there was a renewed interest in the topic after the work of Iyer et al. [ISY19]. In that article, the authors studied the statistics of velocity circulation using state-of-the-art DNS of the NS equation, with Taylor-microscale Reynolds numbers from $\mathrm{Re}_\lambda = 140$ to $\mathrm{Re}_\lambda = 1300$. They first tested the area rule of circulation, so they compared the circulation PDFs computed around rectangular loops of different sizes. They observed that when both of the sides of the loop are within the inertial range, the circulation PDFs are statistically equivalent. They also studied one of the

original questions of Migdal on whether circulation statistics depends on the scalar or vectorial sum of the closed loops. To do this, the authors computed the circulation around eight-shape loops, composed by two square loops with characteristic lengths L_1 and L_2 touching at a common vertex with an opposite orientation, and with a fixed distance $\Delta = L_1 - L_2$. If circulation is based on a scalar law, it should scale as $\langle \Gamma_r^2 \rangle \sim (L_1^2 + L_2^2)^{4/3} \sim r^{8/3}$, while if it were vectorial it should scale as $\langle \Gamma_r^2 \rangle \sim (L_1^2 - L_2^2)^{4/3} \sim [\Delta(L_1 + L_2)]^{4/3} \sim r^{4/3}$. The authors concluded that circulation statistics depends on the scalar sum of the areas. Further studies on the area rule showed that when circulation is computed using non-planar loops, its statistics depends on the minimal area of the surface enclosed by the loop [IBS21].

In addition to laying the fundamental bases on the study of circulation statistics, the main interpretation proposed by Iyer et al. [ISY19] is that scaling exponents of circulation moments λ_p is bifractal (Figure 4.1). It means that for low-order moments $p < 3$, the exponents follow K41 scaling of $\lambda_p = 4p/3$ associated to a set of space-filling fractal structures. For high-order moments $3 < p < 10$, the authors propose a monofractal fit $hp + 3 - D$ with $h = 1.1$ and $D = 2.2$. The fractal dimension of these structures is here associated to wrinkled vortex sheets. This behavior differs completely from the anomalous exponents observed for the structure functions of velocity increments, that is usually described using a multifractal model with an infinite set of fractal dimensions $D(h)$. The authors also studied the relative deviation of the scaling exponents λ_p from K41 prediction $\lambda_p^{\text{K41}} = 4p/3$ for different Reynolds numbers. They observed that the deviation decreases for increasing Reynolds numbers up to $\text{Re}_\lambda = 1300$. If this tendency holds true even for larger Reynolds numbers, the circulation flatness defined as $F(r) = \langle \Gamma_r^4 \rangle / \langle \Gamma_r^2 \rangle^2$ would approach a plateau for $\text{Re}_\lambda = 1900$, and the bifractal behavior of λ_p would start at higher p.

This strong claim motivated other groups to study the circulation statistics. For instance, Apolinário et al. [AMP+20] proposed a model based on a dilute vortex gas, combined with the OK62 phenomenological framework. In the vortex gas model, the velocity circulation in a domain $\mathcal{D}$ is expressed as

$$\Gamma(\mathcal{D}) = \sum_i \Gamma_i(\mathcal{D}) \quad \text{with} \quad \Gamma_i(\mathcal{D}) = f_{\mathcal{D}} \int_{\mathcal{D}} \mathrm{d}^2 \mathbf{r} \, g_\eta(\mathbf{r} - \mathbf{r}_i) \tilde{\omega}(\mathbf{r}_i). \tag{4.4}$$

Here, $\mathbf{r}_i$ is the position of each two-dimensional vortex structure. Their intensity is described by the convolution between Gaussian envelope $g_\eta(\mathbf{r}) = \exp[-\mathbf{r}^2/(2\eta^2)]$ regularized at the Kolmogorov length scale η, and a Gaussian random field $\tilde{\omega}(\mathbf{r})$ with a correlation that follows K41 statistics $\langle \tilde{\omega}(\mathbf{r})\tilde{\omega}(\mathbf{r}') \rangle \sim |\mathbf{r} - \mathbf{r}'|^{-4/3}$. The function $f_{\mathcal{D}} = A^{-1} \int_{\mathcal{D}} \mathrm{d}^2 \mathbf{r} \sqrt{\epsilon(\mathbf{r})/\epsilon_0}$ describes the intensity distribution of vortices within an area A determined by the domain $\mathcal{D}$. Based on this dilute vortex gas model and assuming the OK62 phenomenology, the authors obtained that the scaling exponents of circulation moments of order p follow

$$\lambda_p = \frac{4p}{3} + \tau_{p/2}. \tag{4.5}$$

To model the fluctuations of ϵ, Apolinário et al. [AMP+20] used the log-normal model introduced in chapter 2, which leads to a good approximation of the scaling exponents λ_p observed in Iyer et al. [ISY19]. This result interprets thus circulation intermittency as a multifractal system. We will show later in publication [PMK21] that we also propose a multifractal interpretation. In a follow-up work, the authors also assumed that vortices can be modelled as hard disks, which allows for a better description for small-scale properties [MPV22].
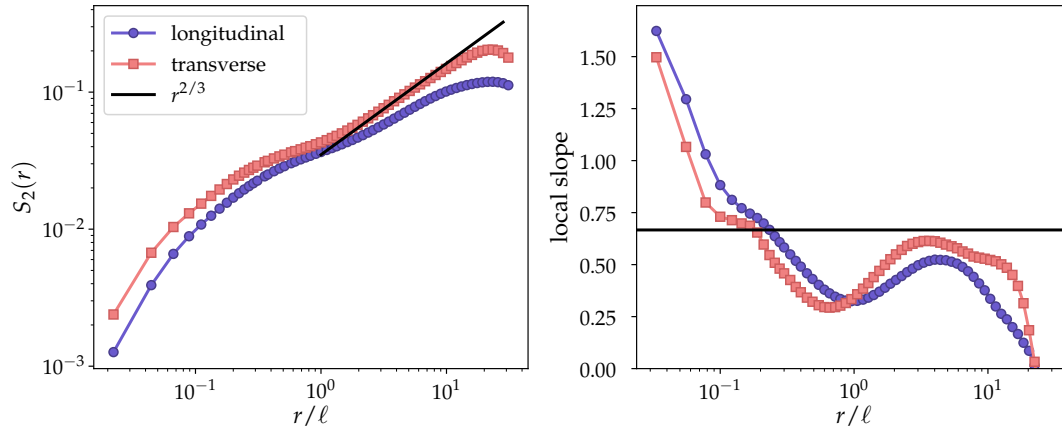
Figure 4.2: Longitudinal and transverse second order structure functions obtained from numerical simulations of the Gross–Pitaevskii equation. On the right, we show the local slopes defined as $\mathrm{d}\log S_2/\mathrm{d}\log r$.

4.1.2 Intermittency of velocity increments in the GP framework

The characterization of the intermittent behavior of quantum turbulence in the Gross–Pitaevskii framework is a challenging task. In particular, DNS of the GP equation lead to the evolution of the wavefunction of the condensate $\psi(\mathbf{r}, t) = \sqrt{n}\exp(im\phi/\hbar)$, with $n(\mathbf{r}, t)$ the particle density, m the mass of the bosons and $\phi(\mathbf{r}, t)$ the phase of the complex field. The mass density and velocity field are given by $\rho(\mathbf{r}, t) = m|\psi|^2$ and $\mathbf{u}(\mathbf{r}, t) = \nabla\phi$, respectively (see chapter 1). As the fluid is potential, it describes an irrotational flow with vorticity that emerges a consequence of singularities supported along a δ-distribution. As the fluid is compressible, the velocity can also be decomposed into a compressible and an incompressible component. The computation of structure functions in this framework requires a careful analysis, as the contribution of compressibility and singularities contaminate its behavior and its scaling properties. To simplify this picture, one could study the structure functions of a regularized and incompressible velocity field defined as

$$\mathbf{v} = (\sqrt{\rho}\mathbf{u})^{\mathrm{inc}}, \tag{4.6}$$

with $\nabla \cdot \mathbf{v} = 0$. This velocity field is the square root of the energy density and is regularized at small scales as the density profile of a quantum vortex goes as $\rho \sim r^2$ with r the distance to the vortex core, while the velocity field of a straight vortex is $u \sim r^{-1}$ (see chapter 1).

In Fig. 4.2 we show the second order structure functions of longitudinal and transverse velocity increments obtained from GP simulations with 2048^3 grid points, using the regularized velocity field (4.6). These results were obtained during this Thesis and are still an ongoing work. Following Kolmogorov phenomenology, one would expect to have a scaling $r^{2/3}$ at large scales $r > \ell$. However, we obtain a scaling slightly smaller than expected. It is interesting to remark that the second-order transverse structure function seems to display better scaling properties than the longitudinal one. This might be related with the fact that the velocity field of a quantum vortex is azimuthal, and longitudinal increments along lines passing through the vortex core are zero by definition. Studies on high-order moments of the regularized structure functions in GP simulations show a stronger intermittent behavior than in classical turbulence [Krs16]. However, experiments in superfluid helium at different temperatures have shown no difference between classical and

quantum turbulence in superfluid helium [MT98; RCS$^+$17]. For further discussions on intermittency at finite temperature, see Sec. 4.4.

The different observations on the intermittent nature of superfluid turbulence between experiments in ^{4}He and numerical simulations of the GP equation might have different interpretations. Superfluid helium is incompressible, so there are no spurious effects coming from compressibility that might modify the scaling properties of the structure functions. Simulations in the GP model are performed without forcing and dissipation, and the scaling properties are studied averaging in a time window where the flow is quasi-steady, while experiments are typically performed in steady turbulent flows. Also, experimental measurements in superfluid helium are performed with probes that resolve scales larger than the quantum vortex core (of the order of 1 Å), so singularities are naturally smoothed out.

All of these possible spurious effects that we can find for the structure functions in the GP model are naturally solved by the velocity circulation. First of all, by definition, the compressible component of the velocity field does not contribute to circulation, so there is no need in performing Helmholtz decomposition for the velocity field. The second important property, and probably the most important one, is that circulation is quantized, being $\pm\kappa$ if the loop encloses a quantum vortex (with $\kappa = h/m$ the quantum circulation), and zero if it does not. Singularities are thus the only structures that contribute to circulation, while for the structure functions are the main source divergences. Circulation around large loops is then an additive process given by $\Gamma = \kappa \sum_i^N s_i$ with s_i the sign of each quantum vortex. However, numerical computation of Γ requires special care, as we will see in the following Sec. 4.2, where we present the characterization of velocity circulation statistics in the GP model.

4.2 Publication: *Intermittency of velocity circulation in quantum turbulence*

Motivated by the work of Iyer et al. [ISY19], we decided to study velocity circulation statistics in quantum turbulence. Vortices in superfluids have a quantized circulation, showing the very different nature of this quantity in classical and quantum fluids. It is natural then to expect that circulation statistics in these two systems may present different properties, at least at small scales.

We performed direct numerical simulations of a generalized Gross–Pitaevskii equation using a pseudo-spectral method to solve in space and a fourth-order Runge-Kutta method for time evolution in a periodic and cubic domain using 2048^3 grid points. As discussed in chapter 3, the generalized GP equation allows us to introduce high-order non-linear terms and a non-local interaction potential that better reproduce the strong interactions and the roton minimum in the excitation spectrum of superfluid helium, respectively. These effects only affect the dynamics of the system at small scales, triggering the excitation of Kelvin waves. At large scales, the standard and generalized GP models behave statistically in an equivalent manner, as Kelvin waves only contribute to the dynamics at small scales. Note that Kelvin waves do not contribute to the statistical properties of Γ.

We compute the circulation around squared-planar loops of different sizes r at each point of each two-dimensional slab of the system, in the three different orientations to maximize the amount of statistics. More specifically, in our largest simulation we analyze 3×2048 two-dimensional slabs, and compute the circulation at each of the 2048^2 points of each slab. For the computation, we use the definition of circulation using the velocity field in Eq. (4.1), with the velocity field defined as the

gradient of the phase of the condensate wavefunction $\mathbf{u} = \nabla \phi$. This approach leads to four linear integrals along the squared loop with opposite vertices at (x_0, y_0) and $(x_1, y_1) = (x_0 + r, y_0 + r)$ that can be written as

$$\Gamma_r = [U_x(y_0)]_{x_0}^{x_1} - [U_x(y_1)]_{x_0}^{x_1} + [U_y(x_1)]_{y_0}^{y_1} - [U_y(x_0)]_{y_0}^{y_1} \tag{4.7}$$

with $[U_x(y)]_a^b = \int_a^b u_x(x', y) \mathrm{d}x'$. In the Fourier representation, the velocity field can be written as $u_x(x, y) = \sum_k \hat{u}_k(y) e^{ikx}$. Thus, each term of the circulation in Eq. (4.7) is

$$[U_x(y)]_a^b = (b - a)\hat{u}_0(y) - \sum_{k \neq 0} \frac{i}{k} \hat{u}_k(y)(e^{ikb} - e^{ika}), \tag{4.8}$$

which allows us to use spectral precision of our codes.

The velocity is a singular quantity at the vortex positions. When circulation is computed along a loop that passes close to a vortex core, it will introduce some numerical errors due to the divergence of the velocity field at these points. To improve the numerical precision of the computation of circulation, we perform a Fourier interpolation in each 2D slab of the velocity field of 2048^2 and increase its resolution up to 32768^2. This method allows us to resolve better each quantum vortex and thus reduce the amount of noisy measurements, increasing the amount of statistics in the discrete values of circulation and improving the scaling properties at small scales.

The main result of this work is that circulation moments in quantum turbulence present two different scaling laws. For small loop sizes, in the sense $r < \ell$ with ℓ the intervortex distance, the probability of enclosing more than one vortex is negligible, and therefore the circulation typically takes only the values $\Gamma = \pm 1$ and $\Gamma = 0$. Then, the moments are only dominated by the probability of finding a single quantum vortex within the loop, which is proportional to the normalized area of the loop r^2/ℓ^2. This scaling is the same for all moments p, and is a direct consequence of the discrete nature of circulation. At large scales $r > \ell$, vortices reorganize in a coherent way creating large-scale structures and the moments reproduce a scaling closer to K41 phenomenology for $p < 3$. This behavior is not completely unexpected as the incompressible energy spectrum in quantum turbulence also displays the Kolmogorov scaling $k^{-5/3}$ [NAB97b; KT05]. However, for high-order moments with $p > 3$, we observe that the exponents present an anomalous deviation from K41 phenomenology. We show that this behavior is very close to the one observed in classical turbulence [ISY19].

In conclusion, we show that the large-scale dynamics of velocity circulation statistics in classical and quantum turbulence are in principle the same in spite of the different nature of circulation in classical and quantum vortices. The anomalous exponents for $p > 3$ can, at first order, be approached with a monofractal fit associated to structures with fractal dimension $D = 2.2$, that can be linked to the formation of vortex bundles that interact coherently. This result reinforces the universal behavior of turbulent flows within the inertial range, and suggests that simpler systems, composed by a collection of individual identical structures, can be used to understand the behavior of classical turbulence. After the publication, we make a short discussion on a small difference between classical and quantum turbulence observed for $p \to 0$, and a comparison between the GP and the gGP models.

Intermittency of Velocity Circulation in Quantum Turbulence

Nicolás P. Müller◉, Juan Ignacio Polanco◉, and Giorgio Krstulovic◉

Université Côte d'Azur, Observatoire de la Côte d'Azur, CNRS, Laboratoire Lagrange,
Boulevard de l'Observatoire CS 34229-F 06304 NICE Cedex 4, France

The velocity circulation, a measure of the rotation of a fluid within a closed path, is a fundamental observable in classical and quantum flows. It is indeed a Lagrangian invariant in inviscid classical fluids. In quantum flows, circulation is quantized, taking discrete values that are directly related to the number and the orientation of thin vortex filaments enclosed by the path. By varying the size of such closed loops, the circulation provides a measure of the dependence of the flow structure on the considered scale. Here, we consider the scale dependence of circulation statistics in quantum turbulence, using high-resolution direct numerical simulations of a generalized Gross-Pitaevskii model. Results are compared to the circulation statistics obtained from simulations of the incompressible Navier-Stokes equations. When the integration path is smaller than the mean intervortex distance, the statistics of circulation in quantum turbulence displays extreme intermittent behavior due to the quantization of circulation, in stark contrast with the viscous scales of classical flows. In contrast, at larger scales, circulation moments display striking similarities with the statistics probed in the inertial range of classical turbulence. In particular, we observe the emergence of the power-law scalings predicted by Kolmogorov's 1941 theory, as well as intermittency deviations that closely follow the recently proposed bifractal model for circulation moments in classical flows. To date, these findings are the most convincing evidence of intermittency in the large scales of quantum turbulence. Moreover, our results strongly reinforce the resemblance between classical and quantum turbulence, highlighting the universality of inertial-range dynamics, including intermittency, across these two *a priori* very different systems. This work paves the way for an interpretation of inertial-range dynamics in terms of the polarization and spatial arrangement of vortex filaments.

Subject Areas: Fluid Dynamics, Nonlinear Dynamics,
Superfluidity

I. INTRODUCTION

The motion of vortices in fluid flows, including rivers, tornadoes, and the outer atmosphere of planets like Jupiter, has fascinated observers for centuries. Vortices are a defining feature of turbulent flows, and their dynamics and their mutual interaction are the source of very rich physics. One notable example of such an interaction is the reconnection between vortex filaments [1], the process by which a pair of vortices may induce a change of topology following their mutual collision. In inviscid classical fluids, Helmholtz's theorems [2] imply that a vortex tube preserves its identity over time, thus disallowing reconnections. An extension of this result is Kelvin's theorem [3], which states that the velocity circulation around a closed loop moving with the flow is conserved in time. The velocity circulation

around a closed loop $\mathcal{C}$ enclosing an area A, defined from the fluid velocity $\boldsymbol{v}$ by

$$\Gamma_A(\mathcal{C}; \boldsymbol{v}) = \oint_{\mathcal{C}} \boldsymbol{v} \cdot \mathrm{d}\boldsymbol{r}, \qquad (1)$$

is directly related to the vorticity flux across the loop via Stokes' theorem, and thus to the topology and the dynamics of vortex filaments. In nonideal classical flows, one effect of viscous dissipation is to smooth out the interface between vortices and the surrounding fluid. As a result, vortex reconnections become possible, and the circulation is no longer conserved around advected loops.

Superfluids, such as very-low-temperature liquid helium, have the astonishing property of being free of viscous dissipation. This property is closely related to Bose-Einstein condensation and is a clear manifestation of quantum physics at macroscopic scales. As a result, superfluids can be effectively described by a macroscopic wave function. This description supports the emergence of quantum vortices, topological defects where the wave function vanishes, which, in three-dimensional space, take the form
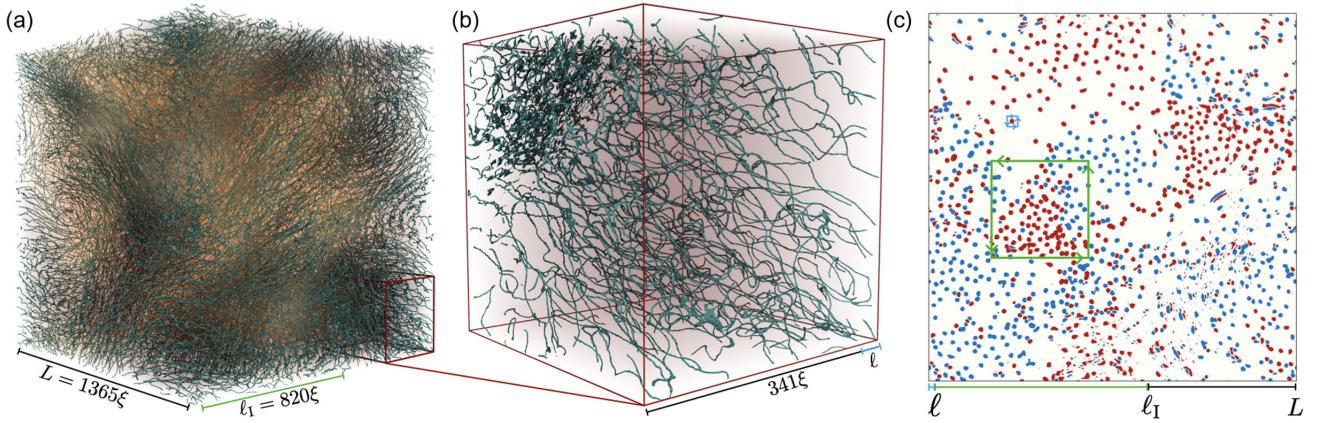
FIG. 1.   Visualization of a quantum turbulent vortex tangle from gGP simulations using 2048^3 collocation points. (a) Full simulation box. Quantum vortices are displayed as thin teal-colored filaments and correspond to isosurfaces of a vanishingly small density value. Density fluctuations around its bulk value are volume-rendered in shades of brown. The size of the box L is expressed in units of the healing length ξ, which is of the order of the vortex core size. Here, ℓ_I is the integral scale of the flow. (b) Zoom of the full box. The mean intervortex distance ℓ is indicated at the bottom of the figure. (c) Two-dimensional slice of the full box displaying the low-pass filtered vorticity field. Blue and red dots correspond to vortices of different signs. Also shown are two typical integration loops: a small blue path surrounding a single vortex, and a larger green path enclosing several vortices.

of thin filaments. Moreover, the velocity circulation around such vortices is quantized in units of the quantum of circulation $\kappa = h/m$, where h is Planck's constant and m is the mass of the bosons constituting the superfluid [4].

Despite the absence of viscosity, it is now well known that vortices in superfluids can reconnect. This possibility was initially suggested by Feynman [5] and was first verified numerically in the framework of the Gross-Pitaevskii (GP) model [6]. Quantum vortex reconnections were later visualized experimentally in liquid helium [7] as well as in trapped Bose-Einstein condensates [8]. Vortex reconnections are considered to be an essential mechanism for sustaining the whole turbulent process [9–11].

Quantum flows are capable of reaching a turbulent state not unlike high-Reynolds-number classical flows. Loosely speaking, quantum turbulence is described as a complex *tangle* of quantum vortices, as illustrated by the teal-colored filaments in the flow visualization in Fig. 1 (see details on the numerical simulations later). Such a turbulent tangle displays rich multiscale physics. At scales larger than the mean distance between vortices ℓ, the quantum nature of vortices is less dominant, and fluid structures, akin to those observed in classical fluids, are apparent [Fig. 1(a)]. In contrast, at scales smaller than ℓ, the dynamics of individual quantized filaments becomes very important. Figure 1(b) displays a zoom of the flow, where Kelvin waves (waves propagating along vortices) and vortex reconnections are clearly observed. Because of this multiscale physics, with discrete vortices at small scales and a classical-like behavior at large ones, quantum turbulence can be considered as the skeleton of classical three-dimensional turbulent flows [4,12]. Such ideas will

be further supported by the results discussed later in this work.

Classical turbulent flows are characterized by an inertial range of scales where, according to the celebrated Kolmogorov's K41 theory [13], statistics are self-similar and independent of the energy injection and dissipation mechanisms. In particular, the variance of the velocity circulation is expected to follow the power-law scaling $\langle \Gamma_A^2 \rangle \sim A^{4/3}$ when the loop area A is within the inertial range. This prediction, based on dimensional grounds, is equivalent to the two-thirds law for the variance of the Eulerian velocity increments [14]. The four-thirds scaling law for the circulation variance has been robustly observed in classical turbulence experiments [15,16] and numerical simulations [17–20]. Furthermore, as shown by these studies, higher-order circulation moments robustly deviate from K41 scalings. Such deviations result from the intermittency of turbulent flows [14,21], that is, the emergence of rare events of extreme intensity, associated with the breakdown of spatial and temporal self-similarity. Very recently, high-Reynolds-number simulations have shown that the intermittency of circulation may be described by a very simple bifractal model [20], which contrasts with the more complex multifractal description of velocity increment statistics. This study has renewed interest on the dynamics of circulation in classical turbulence [22–24].

As in classical flows, K41 statistics and deviations due to intermittency have indeed been observed in the large scales of quantum turbulence. In particular, superfluid helium experiments have shown that finite-temperature quantum turbulence is intermittent and that the scaling exponents of velocity increments might slightly differ from those in classical turbulence [25–28]. In zero-temperature

superfluids, numerical simulations of the GP model have shown evidence of a K41 range in the kinetic energy spectrum [29–31]. Noting that the GP velocity field is compressible and singular at the vortex positions, the energy spectrum is often computed using the incompressible part of a regularized velocity field [11]. This decomposition was used in Ref. [32] to show that, in quantum turbulence, the intermittency of velocity increments is enhanced with respect to classical turbulence. Note that such decomposition is not needed for circulation statistics since the compressible components of the velocity are, by definition, potential flows [29], and therefore, their contributions to the circulation vanish when evaluating the contour integral in Eq. (1). This absence of ambiguity, as well as its discrete nature, makes the circulation a particularly interesting quantity to study in low-temperature quantum turbulence.

The paper is organized as follows. In Sec. II, we present the model used in this work to simulate quantum turbulence, and we discuss the numerical methods to integrate it and to process data. Section III presents and discusses the main results concerning the scaling of circulation moments in quantum turbulence and its intermittency. Finally, Sec. IV discusses the implications of this work.

II. QUANTUM TURBULENCE SIMULATIONS

We numerically study the scaling properties of velocity circulation in quantum turbulence. The results are obtained from a database of high-resolution direct numerical simulations of a generalized GP (gGP) model, which describes, in more detail, the phenomenology of superfluid helium compared to the standard GP equation [31]. The simulation reported in this work uses 2048^3 grid points. In the following, we briefly introduce the gGP model used in this work. For details, the reader is referred to Ref. [31].

The gGP equation is written

$$
i\hbar\frac{\partial\psi}{\partial t} = -\frac{\hbar}{2m}\nabla^2\psi - \mu(1+\chi)\psi
$$
$$
+ g\left(\int V_{\mathrm{I}}(\boldsymbol{x}-\boldsymbol{y})|\psi(\boldsymbol{y})|^2\mathrm{d}^3y\right)\psi + g\chi\frac{|\psi|^{2(1+\gamma)}}{n_0^\gamma}\psi,
$$

(2)

where ψ is the condensate wave function describing the dynamics of a compressible superfluid at zero temperature. Here, m is the mass of the bosons, μ is the chemical potential, n_0 is the particle density, and $g = 4\pi\hbar^2 a_s/m$ is the coupling constant proportional to the s-wave scattering length. To model the presence of the roton minimum in superfluid ^{4}He, the governing equation includes a nonlocal interaction potential V_{I} that is described in Appendix B. This model also includes a beyond-mean-field correction controlled by two dimensionless parameters χ and γ, which

correspond to its amplitude and order, respectively. This term arises from considering a strong interaction between bosons [31]. Note that the standard Gross-Pitaevskii equation is recovered by setting $\chi = 0$ and $V_{\mathrm{I}}(\boldsymbol{x}-\boldsymbol{y}) = \delta(\boldsymbol{x}-\boldsymbol{y})$, where δ is the Dirac delta.

The connection between Eq. (2) and hydrodynamics is given by the Madelung transformation, $\psi = \sqrt{\rho/m}e^{im\phi/\hbar}$, which relates ψ to the velocity field $\boldsymbol{v} = \boldsymbol{\nabla}\phi$. Note that the phase ϕ is not defined at the locations where the density ρ vanishes, and hence, the velocity is singular along superfluid vortices [11]. When the system is perturbed around a flat state $\psi = \sqrt{n_0}$, the speed of sound is given by $c = \sqrt{gn_0(1+\chi(\gamma+1))/m}$ [31]. Nondispersive effects are observed at scales below the healing length $\xi = \hbar/\sqrt{2mgn_0(1+\chi(\gamma+1))}$. This length scale is also the typical size of the vortex core.

Equation (2) is solved using the Fourier pseudospectral code FROST in a periodic cube with a fourth-order Runge-Kutta method for the time integration. In this work, the simulation box has a size $L = 1365\xi$, and the initial condition is generated to follow the Arnold-Bertrami-Childress (ABC) flow used in Ref. [33]. The initial velocity wave function is generated as a combination of two ABC flows at the two largest wave numbers, as described in Ref. [31]. To reduce the acoustic emission, the initial condition is prepared using a minimization process [11]. Besides the integral length scale ℓ_{I}, which is associated with the largest scales of the initial condition, and the healing length, proportional to the vortex core size, in quantum flows, it is possible to define a third length scale ℓ associated with the mean intervortex distance. This scale can be estimated as $\ell = \sqrt{L^3/\mathcal{L}}$, where $\mathcal{L}$ is the total vortex length of the system. Numerically, $\mathcal{L}$ is estimated using the incompressible momentum density as in Refs. [11,31].

Evolving the initial setting under the gGP model [Eq. (2)] leads to the tangle of quantum vortices displayed in Fig. 1, whose energetic content decays at large times as vortices reconnect and sound is emitted [34]. Similar to decaying classical turbulence, this temporal decay is characterized by an intermediate stage, termed the turbulent regime, in which the rate of dissipation of incompressible kinetic energy is maximal and the mean intervortex distance ℓ is minimal [31]. In the present work, we only consider this regime, as its large-scale dynamics is most comparable with fully developed classical turbulence. In this stage, as discussed in Ref. [31], the incompressible kinetic energy spectrum of high-resolution gGP simulations presents a clear K41 scaling range, followed by a Kelvin wave cascade range at small scales. At this time, the integral scale is measured to be $\ell_{\mathrm{I}} \approx 820\xi$, and the intervortex distance is $\ell \approx 28\xi$, as illustrated in Fig. 1.

Throughout this work, the circulation is computed from its velocity-based definition in Eq. (1), as opposed to the

vorticity-based expression resulting from the application of Stokes' theorem (see Appendix A). Moreover, only planar square loops of area $A = r^2$ are considered. Thus, we refer to the circulation over a loop of area A as Γ_A or Γ_r, depending on the context. To take advantage of the spectral accuracy of the solver, the circulation is computed from the Fourier coefficients of the velocity field, as detailed in Appendix A. Moreover, to reduce spurious contributions from loops passing close to vortices, each two-dimensional slice where circulation is computed is resampled into a finer grid of resolution $32\,768^2$, using Fourier interpolation. Values of circulation are then filtered to keep only multiples of κ. Details on this procedure are given in Appendix A.

III. SCALING OF CIRCULATION IN QUANTUM TURBULENCE

The quantization of circulation is one of the defining properties of superfluids. However, despite its relevance, the behavior of circulation at scales much larger than the vortex core size ξ (about an Ångström in superfluid ⁴He) is currently poorly understood in quantum turbulence. Figure 1(c) displays a two-dimensional cut of the fluid where a low-pass filtered vorticity field is displayed. Vortices are visible as small dots, and their sign is colored in black and red. Intuitively, one can expect that the circulation will be allowed to take increasingly higher values as the area of the integration loop increases. For sufficiently small loops [such as the small path displayed in Fig. 1(c)], the probability of enclosing a quantum vortex (let alone many of them) is small, and the circulation will most likely take values in $\{0, \pm\kappa\}$. This strongly discrete distribution of circulation is in stark contrast with the continuous distribution found in viscous flows. For larger loops, typically larger than the mean intervortex distance ℓ, higher circulation values become possible, as more vortices may intersect the loop area, shown by the large green path in Fig. 1(c). Even though it remains quantized, the discreteness of circulation becomes less apparent as the set of possible values increases. Other effects, such as the cancellation of circulation contributions from antipolarized vortices, become important. Indeed, the relative orientation of quantum vortices is deeply linked to the emergence of K41 statistics in quantum turbulence [35,36] and is expected to play a major role in circulation statistics at large scales. The polarization of vortices is manifest in Fig. 1(c), where, at large scales, vortices of the same sign have a tendency to cluster.

A. Circulation at classical and quantum scales

We start by presenting one of the simplest circulation observables, that is, the variance of the circulation for loops of different sizes in quantum turbulence. The scaling of the circulation with the area of the loops is displayed in Fig. 2. For comparison purposes, we also perform direct
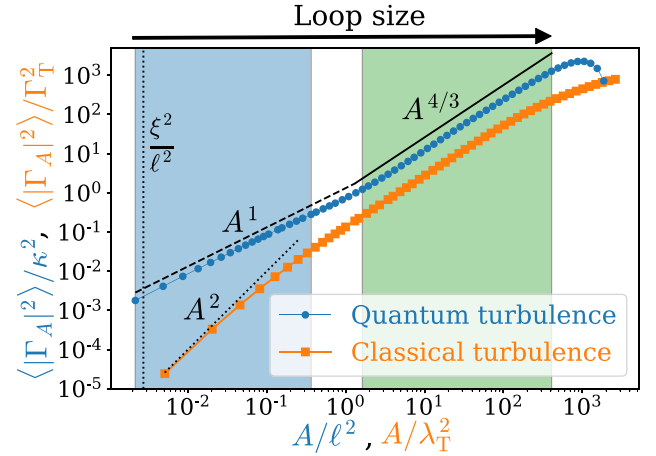

FIG. 2. Variance of the circulation around square loops of area $A = r^2$. The blue line shows the gGP simulation (resolution 2048^3), and the orange line shows the Navier-Stokes simulation (resolution 1024^3). The classical variance is rescaled by $\Gamma_T^2 = (\lambda_T^4/3)\langle|\boldsymbol{\omega}|^2\rangle$, with λ_T the Taylor microscale and $\boldsymbol{\omega}$ the vorticity field.

numerical simulations of the Navier-Stokes equations (see Appendix C). We then compute the scaling of the circulation variance in the steady state at a Taylor-scale Reynolds number of $\mathrm{Re}_\lambda \approx 320$. In the quantum flow, the circulation variance shows clear evidence of two scaling regimes. First, just like in the inertial range of classical turbulence, quantum turbulence displays a classical range, where the $\langle\Gamma_A^2\rangle \sim A^{4/3}$ scaling predicted by K41 theory is observed. This range corresponds to integration loops of linear dimension r such that $\ell \ll r \ll \ell_I$, where ℓ_I is the integral scale of the flow.

In quantum turbulence, the emergence of K41 statistics for $r \gg \ell$ requires the partial polarization of vortex filaments [35,36], which effectively form bundles of corotating vortices [4]. For instance, because of vortex cancellations, a tangle of randomly oriented vortices would be associated with $\langle|\Gamma_A|^2\rangle \sim A$ in the classical range [35], which is different from the K41 estimate $\langle|\Gamma_A|^2\rangle \sim A^{4/3}$ verified in Fig. 2. On the other side of the spectrum, a fully polarized tangle (as may be found in quantum flows under rotation) is associated with the estimate $\langle|\Gamma_A|^2\rangle \sim A^2$. Therefore, we see that K41 dynamics corresponds to a precise intermediate state between an isotropic and a fully polarized tangle.

At small scales, classical and quantum flows display different power-law scalings. Viscous flows are smooth at very small scales, and the vorticity field may be considered a constant within a sufficiently small loop. By isotropy, it follows that $\langle\Gamma_A^2\rangle \approx \langle|\omega_i A|^2\rangle = \frac{1}{3}\langle|\boldsymbol{\omega}|^2\rangle A^2$ for small A. Equivalently, such scaling can be obtained by invoking the smoothness of the velocity field and performing a Taylor expansion around the center of the loop [20]. This viscous scaling is indeed observed in Fig. 2 for $r \ll \lambda_T$.

Here, $\lambda_T = v_{\mathrm{rms}}/\sqrt{\langle(\partial_x v_x)^2\rangle}$ is the Taylor microscale, below which the dynamics of the flow is affected by viscosity in classical turbulence (see Ref. [37]). Note that we have used the Taylor microscale instead of the Kolmogorov length scale, which, for the present numerical simulations, is about 30 times smaller. This fact suggests that, in the correspondence between classical and quantum turbulence, the intervortex distance ℓ may be compared to the Taylor microscale.

On the contrary, for quantum turbulence, a less steep scaling is observed at small scales, which recalls the singular signature of the quantum vortex filaments. We will come back to this scaling later. In the following, we refer to the range $\xi \ll r \ll \ell$ as the *quantum* range since it strongly differs from the dissipative range of classical turbulence. The quantum and the classical ranges are highlighted by different background colors in Fig. 2. We have checked that the above results are also observed in low-resolution simulations of the standard Gross-Pitaevskii model (data not shown).

B. Circulation statistics and intermittency

In quantum flows, the velocity circulation takes discrete values (multiples of the quantum of circulation κ), which contrasts with the continuous space of possible values in viscous flows. In statistical terms, its probability distribution is described by a probability mass function (PMF), the discrete analog of a probability density function (PDF). The discreteness of the circulation is most noticeable for loop sizes r smaller than the mean intervortex distance ℓ, where the probability of a loop enclosing more than one vortex is vanishingly small, and Γ_r takes one of a small set of discrete values. This behavior is verified in Fig. 3(a), where the probability $\mathcal{P}_r(n)$ of having a circulation $\Gamma_r = n\kappa$, for small loop sizes, is shown. As expected, the PMFs are strongly peaked at $\Gamma_r = 0$ for very small loop sizes, indicating that it is very unlikely for such a loop to enclose more than one vortex (vortex cancellation is negligible at those scales). The PMF becomes wider as r increases, and more vortices are allowed within an integration loop.

The circulation PMF within the quantum range strongly differs from the (continuous) PDF of circulation in the small scales of classical turbulence. In isotropic flows, for a fixed loop size r in the dissipative range, the circulation PDF is equivalent to that of a vorticity component. Vorticity is a highly intermittent quantity in fully developed turbulence, and like other small-scale quantities, it is characterized by a strongly non-Gaussian distribution with long tails [39]. In that sense, and in regards to circulation, quantum turbulence presents a much simpler behavior despite its singular distribution of vorticity. Such a behavior could be useful for developing theoretical models of circulation.

For larger loops with $r/\ell > 1$, the circulation takes increasingly larger values, and its discrete nature becomes
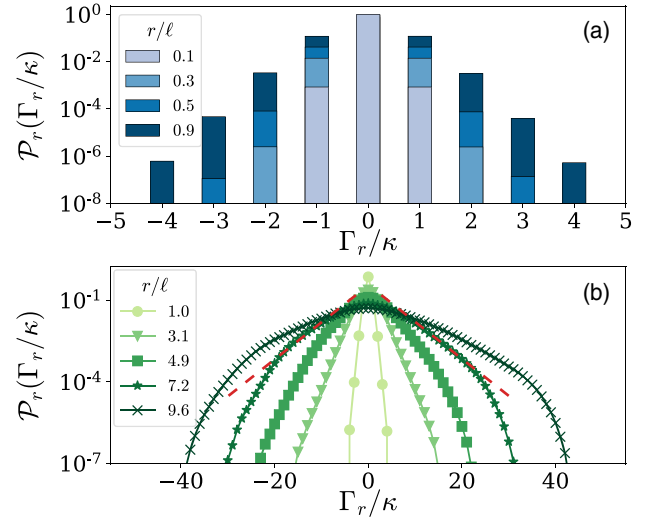

FIG. 3. PMF of the circulation in quantum turbulence for (a) loop sizes $r/\ell < 1$ and (b) loop sizes $r/\ell \geq 1$. The red dashed lines are a guide for the eye indicating exponential tails. Note that all distributions are discrete, as Γ_r/κ only takes integer values. In panel (a), bars for $\mathcal{P}_r(0)$ and $r/\ell \geq 0.3$ are hidden behind the $r/\ell = 0.1$ case. See Fig. 6 for details on $\mathcal{P}_r(0)$.

less apparent. This behavior is seen in the circulation PMFs shown in Fig. 3(b), which may be approximated by continuous distributions. Within the classical range, these distributions seem to display exponential-like tails (red dashed lines). These distribution tails are compatible with those found in the inertial range of classical turbulence, which may be fitted by stretched exponentials [20] or modified exponentials [24].

In classical turbulence, it is customary to characterize velocity intermittency by evaluating the departure of the moments of velocity increments from K41 self-similarity theory [14]. For the same purposes, a few studies have also considered the moments of circulation [15,16,18–20,24]. In the following, we consider the moments $\langle|\Gamma_r|^p\rangle$ in quantum turbulence resulting from the circulation distributions discussed in the previous section. The aims are to characterize the validity of K41 theory in the classical range, to provide evidence of possible departures due to intermittency, and to elucidate the statistics of circulation at small scales resulting from the quantum nature of the flow. This analysis extends the discussion relative to the circulation variance ($p = 2$), which is presented in Fig. 2 in the context of a comparison with classical flows.

Circulation moments $\langle|\Gamma_r|^p\rangle$ are shown in Fig. 4(a) as a function of the loop size r for different orders p. For each moment, a clear power-law scaling is identified in each of these ranges. We define the exponents of the power law as

$$\frac{\langle|\Gamma_r|^p\rangle}{\kappa^p} \approx \left(\frac{r}{\ell}\right)^{\lambda_p}. \tag{3}$$
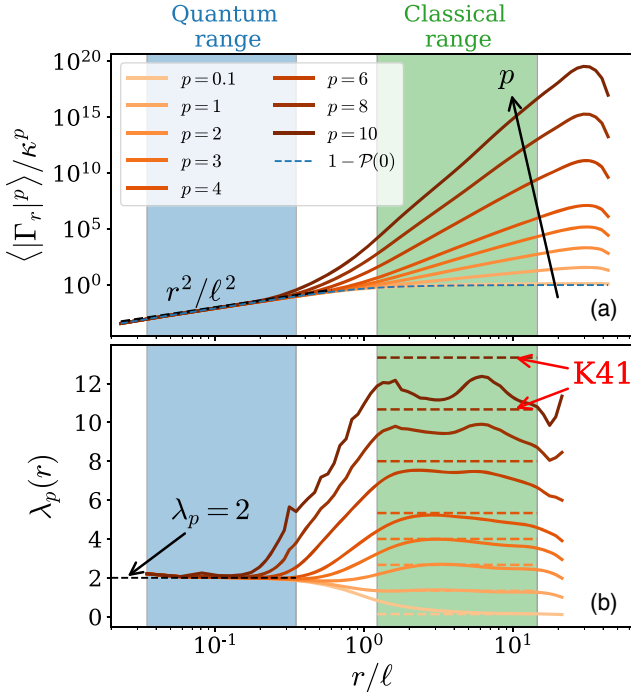
FIG. 4. (a) The p-order moments of the circulation over square loops of area $A = r^2$ from the gGP simulation. (b) Local scaling exponents $\lambda_p(r) = \mathrm{d}[\log\langle|\Gamma_r|^p\rangle]/\mathrm{d}[\log r]$. Dashed horizontal lines correspond to the K41 scalings $\lambda_p^{\mathrm{K41}} = 4p/3$. The blue dashed line shows $\mathcal{P}_r(\Gamma_r \neq 0) = 1 - \mathcal{P}_r(\Gamma_r = 0)$, which corresponds to the pth circulation moment in the limit $p \to 0^+$ [Eq. (6)]. The blue and green areas, respectively, illustrate the quantum and classical regimes.

To better characterize the exponents, one can compute the local scaling exponents $\lambda_p(r) = \mathrm{d}[\log\langle|\Gamma_r|^p\rangle]/\mathrm{d}[\log r]$, which, for pure power laws, are flat. The local scaling exponents are presented in Fig. 4(b), where two different plateaux are observed in both ranges for each order p.

1. Quantum range

At first glance, it is striking to note that all moments collapse in the quantum range, which suggests that circulation is extremely intermittent at these scales as a consequence of the quantum nature of the flow. Indeed, as inferred from Fig. 3 and discussed in the previous section, a random loop of characteristic length $r \ll \ell$ will almost never enclose more than a single vortex filament. By the definition of the intervortex distance ℓ, at such small scales, the probability of finding a vortex within a loop is simply $\beta_r = r^2/\ell^2$. From there, it follows that $\langle|\Gamma_r|^p\rangle = (0 \times \kappa)^p(1 - \beta_r) + (1 \times \kappa)^p\beta_r$ since only zero or one vortex might lie inside the loop. This simple model leads to the prediction

$$\frac{\langle|\Gamma_r|^p\rangle}{\kappa^p} \approx \left(\frac{r}{\ell}\right)^2 \quad \text{for } r \ll \ell, \tag{4}$$

which is precisely the law observed in Fig. 4 at small scales. Remarkably, the simulation results capture not only the predicted scaling exponent $\lambda_p = 2$ [as verified in Fig. 4(b)] but also the prefactor ℓ^{-2}.

The independence of the circulation scaling exponents λ_p on the moment order p translate the extreme intermittency of circulation at quantum scales. This result is a clear consequence of quantum physics, as it results from the quantization of circulation and the discrete nature of vortex filaments. As seen in Fig. 2, it is in stark contrast with the small-scale physics of viscous flows, characterized by smooth velocity fields, which lead to very different circulation statistics scaling as r^{2p}.

2. Classical range

For larger loops of size $\ell \ll r \ll \ell_{\mathrm{I}}$, circulation moments in Fig. 4 follow different power laws, with a scaling exponent λ_p that increases with the moment order p. Kolmogorov's phenomenology gives a prediction for the scaling of circulation moments in this regime. Assuming self-similarity across scales, the K41 predictions for the circulation moments about loops of area $A = r^2$ are of the form

$$\langle|\Gamma_r|^p\rangle = C_p\varepsilon^{p/3}r^{4p/3} \quad \text{for } \ell \ll r \ll \ell_{\mathrm{I}} \tag{5}$$

for positive moment order p, where ε is the incompressible kinetic energy dissipation rate per unit mass and C_p are, supposedly, universal constants. Similarly to classical K41 scalings, Eq. (5) results from dimensional arguments and the assumption that, within the classical range, the statistics of Γ_r depends only on ε and r.

The local scaling exponents displayed in Fig. 4(b) exhibit a plateau in the classical range, confirming the power-law behavior of circulation moments at those scales. For low-order moments ($p < 3$), the exponents approximately match the K41 prediction, plotted as dashed horizontal lines. This observation is consistent with the scaling of the circulation variance in Fig. 2. On the other hand, higher-order moments yield lower exponent values than those predicted by K41 theory. This departure is clear evidence of circulation intermittency in the classical range of quantum turbulence. Moreover, it is qualitatively consistent with the trends observed in the inertial range of classical turbulence [15,16,18–20]. A more quantitative comparison of the scaling exponents in classical and quantum flows is provided in the next section.

C. Scaling exponents in the classical regime

We finally quantify the anomalous exponents of the circulation in the classical range of the quantum turbulent tangle. With this aim, we average the local scaling exponents over a range of loop sizes within $\ell \ll r \ll \ell_{\mathrm{I}}$. The precise averaging range is given by the green area in
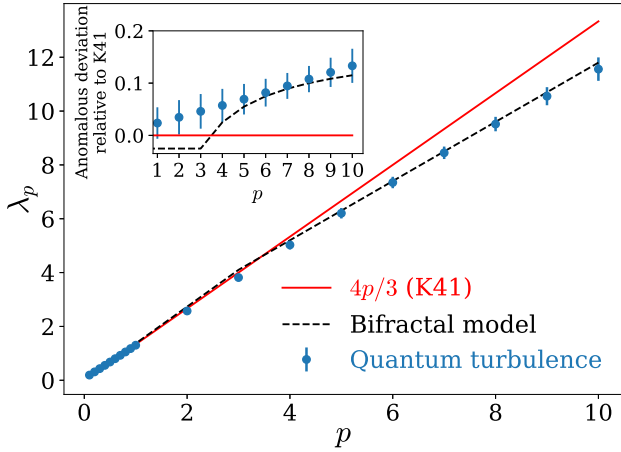
FIG. 5. Scaling exponents of the circulation moments for loop sizes within the classical range ($\ell \ll r \ll \ell_1$). Blue circles with error bars correspond to gGP simulations. The solid line shows K41 scaling $\lambda_p^{K41} = 4p/3$, and the dashed line shows the bifractal fit in classical turbulence [20]. Inset: relative deviation from K41 estimates, $(\lambda_p^{K41} - \lambda_p)/\lambda_p^{K41}$. Error bars indicate the standard deviation of each λ_p within the classical range.

Fig. 4. As in Ref. [20], we also compute fractional circulation moments. However, note that we do not include negative moments $p \in\,]-1, 0[$, as done in that work, because the discrete nature of the circulation distribution in quantum flows results in a finite probability of having $\Gamma_r = 0$, and thus negative order moments diverge.

The circulation scaling exponents λ_p obtained from our simulations are shown in Fig. 5. As suggested by the behavior of the circulation moments discussed in the previous section, the departure from K41 scaling (solid red line in the figure) is weak for low-order moments, while it becomes significant for orders $p \geq 3$.

Strikingly, the scaling exponents are consistent with the recent results in high-Reynolds-number classical turbulence [20] (dashed lines in Fig. 5). To give some relevant context, that work provides evidence of a bifractal behavior of the scaling exponents. Concretely, for low-order moments $p < 3$, the exponents grow linearly as $\lambda_p = \alpha p$, with $\alpha \approx 1.367$. This robust scaling, almost independent of Reynolds number, is close but not exactly equal to the $\alpha = 4/3$ predicted from K41 phenomenology. As for orders $p > 3$, they are accurately described by a monofractal fit $\lambda_p = hp + (3 - D)$, with a fractal dimension D and Hölder exponent h that display a weak-Reynolds-number dependence. At the highest Reynolds number studied in that work, they are estimated as $D \approx 2.2$ and $h \approx 1.1$. We stress that the above bifractal fit, which we adopt here for its simplicity, is empirically derived in Ref. [20] from direct numerical simulation data. Note that an alternative functional form of the scaling exponents λ_p in classical turbulence, which also closely matches the

numerical data, has recently been proposed based on a dilute vortex gas model [22].

For high-order moments, the anomalous exponents in the quantum-flow case display a behavior that is close to that observed in classical turbulence. The inset of Fig. 5 shows the relative deviation from K41 estimates, $(\lambda_p^{K41} - \lambda_p)/\lambda_p^{K41}$, and its comparison with the bifractal model fitted in Ref. [20]. For $p > 3$, the bifractal model lies between error bars of our data, which hints at the universality of inertial-range dynamics across different turbulent systems.

Low-order moments are particularly interesting. From a statistical point of view, the main contribution to those moments comes from loops having a very small circulation, which are the most probable ones (see Fig. 3). A loop with small circulation might either be the result of a region of the flow where there are few vortices or the opposite regime, where many vortices of opposite signs cancel each other's contributions to the circulation. The last case corresponds to a very rare intermittent event. Such an idea was invoked by Iyer et al. [20] to explain the intermittency of low-order moments.

In the case of quantum turbulence, the discrete nature of vortices is very important, and regardless of the size of the loop, there is always a nonzero probability of having a total zero circulation. In fact, we can relate low-order moments with such probability as

$$
\begin{aligned}
\langle |\Gamma_r|^p \rangle &= \sum_{n \neq 0} |\Gamma_r|^p \mathcal{P}_r(n) \\
&= 1 - \mathcal{P}_r(0) + p\langle \log |\Gamma_r| \rangle_{\neq 0} + o(p), \quad (6)
\end{aligned}
$$

where $\mathcal{P}_r(n)$ is the circulation PMF and $\langle \mathcal{O}[\Gamma_r] \rangle_{\neq 0} = \sum_{n \neq 0} \mathcal{O}[\Gamma_r]\mathcal{P}_r(n)$. The above expression results from the Taylor expansion $|\Gamma_r|^p = 1 + p \log |\Gamma_r| + o(p)$ around $p = 0$ and the fact that $\langle 1 \rangle_{\neq 0} = 1 - \mathcal{P}_r(0)$. Remarkably, the probability of having zero circulation displays a clear $r^{-4/3}$ power-law scaling in the classical regime, as shown in Fig. 6. This power law is related to a partial polarization of the quantum vortices. Indeed, in the case of a fully polarized tangle, we trivially have that $\mathcal{P}_r(0) = 0$, as all vortices have the same sign within a loop. In the opposite regime of a totally unpolarized tangle, we have that $\mathcal{P}_r(0) \sim r^{-1}$. This scaling results from considering $N \sim (r/\ell)^2$ homogeneously distributed uncorrelated vortices enclosed in a loop of size r and computing the probability of having exactly $N/2$ positive vortices among those N. Such probability is simply given by $2^{-N}\binom{N}{N/2} \approx \sqrt{2/N\pi} \sim (r/\ell)^{-1}$. The $r^{-4/3}$ scaling thus corresponds to a partial polarization of the tangle. Note that the transition between the quantum and the classical regimes is manifest. At small scales, we find that $\mathcal{P}_r(0) = 1 - (r/\ell)^2$, which corresponds to the probability of not finding any vortex.
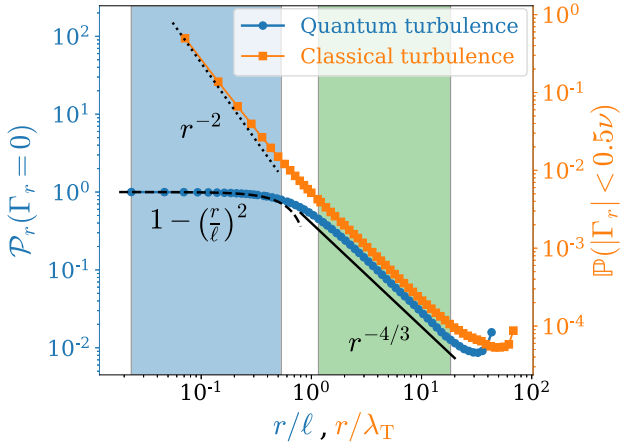
FIG. 6. Probability of having zero circulation in gGP simulations (blue line) and of having a weak circulation in Navier-Stokes simulations (orange line). The dashed lines show their respective predictions at large and small scales.

It is interesting that for classical flows, albeit the circulation takes continuous values, the probability $\mathbb{P}(|\Gamma_r| < \alpha\nu)$ of having low circulation values presents the same power law in the inertial range, as also reported in Fig. 6. For a classical flow, this scaling can be derived by invoking K41 phenomenology, which predicts that the statistics of $\gamma = \Gamma_r \varepsilon^{-1/3} r^{-4/3}$ is scale invariant in this range. It follows that

$$\mathbb{P}(|\Gamma_r| < \alpha\nu) = \mathbb{P}(|\gamma| < \alpha\nu\varepsilon^{-1/3} r^{4/3}) \sim \alpha\nu\varepsilon^{-1/3} r^{4/3} \quad (7)$$

for $\alpha \ll 1$. Here, we assume that the PDF of γ is finite at zero. Besides, for r much smaller than the Taylor microscale λ_T, one has that $\Gamma_r \sim \omega_i r^2$ (see Sec. III A) and a similar argument leads to $\mathbb{P}(|\Gamma_r| < \alpha\nu) \sim r^{-2}$, as is also displayed in Fig. 6 [40]. Again, the small scales of classical and quantum fluids strongly differ.

Finally, note that the asymptotic approach predicted in Eq. (6) is clearly verified in Fig. 4 for low-order moments. The finite value of $\mathcal{P}_r(0)$ in the quantum case implies a discontinuity of the moments when $p \to 0^+$ since $\langle|\Gamma_r|^0\rangle = 1$. The subdominant power-law term in Eq. (6) explains the reduced inertial range observed in Fig. (5) for low-order moments.

IV. SUMMARY AND DISCUSSION

The recent work of Iyer *et al.* [20] has sparked renewed interest in the statistics of velocity circulation in high-Reynolds-number classical turbulent flows. Their numerical results have showcased the relative simplicity of circulation statistics in the inertial range, despite the intermittency of these flows. This simplicity contrasts with the complexity of velocity increment statistics, as well as that of enstrophy or dissipation, which display multifractal statistics as a result of turbulence intermittency [14].

It has been long suggested that quantum turbulence shares many similarities with classical flows at scales much larger than those associated with individual quantum vortices. For instance, experimentalists have struggled to find significant differences between finite-temperature superfluid helium and classical flows at those scales [25,27,41]. Features of classical turbulence, most notably, the scaling of the energy spectrum $E(k) \sim k^{-5/3}$ resulting from Kolmogorov's self-similarity theory, have also been observed in low-temperature quantum turbulence [11,30,33,42–48]. However, for a few reasons detailed below, such observations only show a limited picture of inertial-range dynamics in quantum flows. First, most of these studies have looked at the scaling properties of the velocity field and its wave-number spectrum. The velocity field is a singular quantity that diverges at the vortex filament locations. This property has led to considering a regularized version of it, whose physical interpretation is less clear. Second, even though K41 scaling has been observed in low-temperature quantum turbulence, little is known regarding deviations from them due to intermittency. Indeed, despite a few works [27,28,32], because of numerical and experimental limitations, nonconclusive results exist for how the intermittency of those flows compares with classical turbulence. In numerical simulations, because of the two disjoint ranges of scales with nontrivial dynamics (as opposed to just one in classical turbulence), high resolutions are needed to obtain more than a decade of inertial range in wave-number space [31,33,49].

The differences between classical and quantum turbulence become more evident at smaller scales, as the regularity of classical flows at scales below the dissipative length is in stark contrast with the singular nature of quantized vortices. At those scales, quantization leads to enhanced intermittency of velocity statistics in superfluid helium [28,50] and in zero-temperature quantum turbulence [32]. Note that at quantum scales, both the singularity of the velocity field and compressible effects such as sound emission become important. As mentioned above, this leads to the necessity of regularizing and decomposing the velocity field into different contributions. In contrast, the velocity circulation considered in this work does not suffer from such limitations, as it is nonsingular and, by its definition, is exempt from contributions from compressible dynamics.

In this work, we have numerically investigated circulation statistics in low-temperature quantum turbulence. In superfluid flows, the velocity circulation is intimately linked to the quantum nature of the system. We have performed high-resolution numerical simulations of a generalized Gross-Pitaevskii model, allowing for a relatively large degree of scale separation between the vortex core size ξ, the mean intervortex distance ℓ, and the integral scale of the flow ℓ_I. The main objectives of this work have

been twofold: (1) to disentangle the differences between classical and quantum turbulence at small scales, and (2) to provide new evidence of the strong analogy between both physical systems at large scales, which, as we show, goes beyond self-similarity predictions and includes intermittent behavior. Our results strongly reinforce the view of quantum turbulence as the skeleton of classical flows, which can be used to provide a better understanding of the latter. Besides, note that the physics of the Kelvin wave cascade, which becomes important at quantum scales, should play no role in circulation statistics, as the circulation around a vortex is blind to the presence of such vortex excitations.

We have considered the circulation Γ_r integrated over square loops of varying area $A = r^2$. As is customary in classical turbulence, we have characterized the scaling properties of the circulation in terms of its moments $\langle |\Gamma_r|^p \rangle$ and their dependence on the scale r of the integration loop. We have shown that all circulation moments follow two distinctive power-law scalings, for r much smaller and much larger than the mean intervortex distance ℓ.

At small (or quantum) scales, our main finding is that circulation moments are independent of the moment order p, which translates the extreme intermittency of the circulation at these scales. This result is a consequence of the quantized nature of circulation and the discreteness of vortex filaments. The small-scale dynamics of circulation in quantum flows is in strong contrast with that in classical flows, where, as a result of viscosity, the velocity field is smooth at very small scales, leading to very different circulation statistics.

At scales larger than ℓ (the classical range), we have found that low-order circulation moments closely follow the predictions of K41 phenomenology theory, which were initially proposed by Kolmogorov for classical turbulence. This result, by itself, is very important, as it highlights the strong analogy between classical and quantum flows at large scales. While K41 scalings have previously been observed in the energy spectrum of zero-temperature quantum turbulence, this is the most convincing evidence to date of such behavior, as the circulation is a well-defined physical quantity in quantum turbulence, and the observed K41 range spans about one full decade in scale space.

In addition, our work provides unprecedented evidence of intermittency in the classical range of zero-temperature quantum turbulence. The circulation moments obtained from our simulations not only display intermittent behavior (in the form of deviation from K41 estimates), but they do so in a way that is quantitatively similar to the anomalous scaling of circulation in classical turbulence. The impressive similarity between these two *a priori* very different systems strongly reinforces the idea of universality of inertial-range dynamics in classical and quantum flows. Indeed, since Kolmogorov's pioneering works in 1941, it has been conjectured that such dynamics is independent of

the viscous dissipation mechanisms in classical fluids. The present work goes further to suggest that, more generally, inertial-range dynamics and intermittency are independent of the small-scale physics and, in particular, of the regularization mechanism. In classical turbulence, viscosity plays the role of smoothing out (or regularizing) the flow at small scales. In quantum flows, regularization results from dispersive effects taking place at scales smaller than the vortex core size. Note that in Ref. [51], it was suggested that for classical flows in the limit of infinite Reynolds numbers, the Kelvin theorem is violated and might be recovered only in a statistical sense, somehow as a consequence of the dissipative anomaly of turbulence [14]. It would be of great interest to study how this picture changes in quantum turbulence and to investigate whether an analog of the classical circulation cascade exists [52].

In previous classical turbulence experiments [15,16], circulation has been evaluated using the particle image velocimetry (PIV) technique, which provides a measure of the velocity field over a two-dimensional slice of the flow. While this technique has been applied in finite-temperature superfluid ^{4}He [53–55], the interpretation of PIV measurements in this system remains unclear [56,57]. As an alternative, variants of the particle tracking velocimetry (PTV) technique have been used in most recent studies of ^{4}He [56–64]. To our knowledge, no attempts have been made to compute the velocity circulation in superfluid experiments. While perhaps challenging, such a study would be of great interest to the turbulence community.

The emergence of K41 scalings in quantum turbulence results from the partial polarization of vortex filaments [35,36]. In quantum flows, because of the discrete nature of circulation, there is always a finite probability of having zero circulation, whose scale dependence also results from partial polarization. Such a behavior is also seen in classical flows and can be explained by invoking K41 phenomenology. This observation suggests that a possible stochastic modeling of classical and quantum turbulence, or at least of circulation statistics, could be based on a discrete combinatorial approach where spinlike vortices are generated with *ad hoc* correlations. For such a study, it will be important to gain a better understanding of the polarization of quantum turbulent tangles and of how this translates to classical flows. Alternatively, in Iyer *et al.* [20], the bifractal behavior of circulation intermittency has been related to the presence of "moderately wrinkled vortex sheets" with fractal dimension $D = 2.2$. It would be interesting to relate these ideas to the partial polarization and the arrangement of quantum vortices. Such ideas will be addressed in a future work.

ACKNOWLEDGMENTS

APPENDIX A: COMPUTATION OF CIRCULATION

Via Stokes' theorem, Eq. (1) around a closed loop $\mathcal{C}$ can be written in terms of the vorticity field $\boldsymbol{\omega} = \nabla \times \boldsymbol{v}$,

$$\Gamma_A = \iint_A \boldsymbol{\omega} \cdot \boldsymbol{n} \mathrm{d}S, \qquad (A1)$$

where A is the area enclosed by the loop and $\boldsymbol{n}$ its associated normal unit vector. Since the superfluid is irrotational away from vortices, this alternative form amounts to counting the contributions of the vortices enclosed within a loop. In quantum flows, the vorticity field is extremely irregular, being effectively represented by a sum of Dirac deltas. This property renders Eq. (A1) impractical for numerically evaluating the circulation in quantum flows.

For the above reasons, we compute the circulation in quantum and classical flows using its velocity-based form Eq. (1). The algorithm, described in the following, enables the evaluation of the line integral in Eq. (1) with high accuracy over rectangular loops aligned with the Cartesian axes of the domain. For simplicity, we consider a square loop of size $r \times r$, with sides respectively aligned with the x- and y-coordinate axes in a 2π-periodic domain. Here, we denote by $\boldsymbol{v}(\boldsymbol{x}) = (v_x(x, y), v_y(x, y))$ the in-plane velocity field.

The circulation over such a square loop with opposite corners at (x_0, y_0) and $(x_1, y_1) = (x_0 + r, y_0 + r)$ is given by

$$\Gamma_r = [V_x(y_0)]_{x_0}^{x_1} + [V_y(x_1)]_{y_0}^{y_1} - [V_x(y_1)]_{x_0}^{x_1} - [V_y(x_0)]_{y_0}^{y_1}, \qquad (A2)$$

where $[V_x(y)]_a^b = \int_a^b v_x(x', y) \mathrm{d}x'$ is the integral of v_x along the x direction. This notation, and what follows below, similarly applies to the y component of the velocity.

Using the Fourier representation of the velocity field, its v_x component can be written as $v_x(x, y) = \sum_k \hat{u}_k(y) e^{ikx}$. Then, its integral is $[V_x(y)]_a^b = (b-a)\hat{u}_0(y) + \sum_{k \neq 0} [-(i/k)\hat{u}_k(y)](e^{ikb} - e^{ika})$. However, note that the velocity field is singular at vortex locations, and as a result, the Fourier coefficients $\hat{u}_k$ decay slowly with the wave number k. Hence, compared to the complex wave function ψ, a large number of Fourier modes are needed to accurately describe the velocity field.
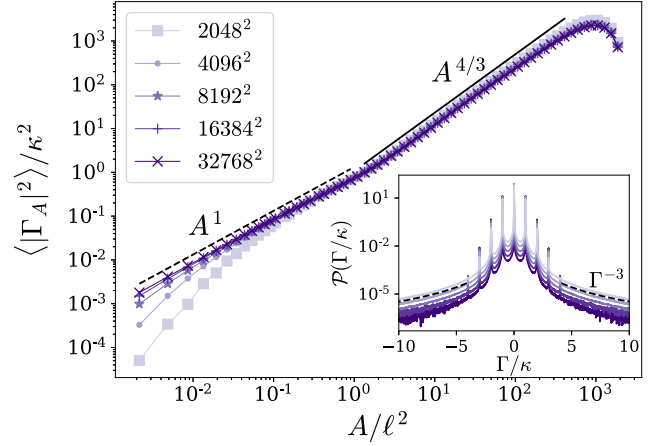

FIG. 7. Moments of order 2 for different values of the resampling in gGP simulations with $N^3 = 2048^3$. Resampling factors are $\beta = 1, 2, 4, 8,$ and 16. As the resampling increases, vortices are better resolved, and the expected scaling at small scales arises. At large scales, the system is less affected by resampling. Inset: probability distribution of the circulation for a loop size $r/\ell = 0.67$. Peaks are observed at small-circulation values which are multiples of κ. The separation between peaks and valleys is higher as the resampling increases. Tails exhibit a Γ_r^{-3} scaling.

In practice, to obtain an accurate representation of the velocity field on a given 2D cut of the 3D domain, we first evaluate the wave function $\psi(\boldsymbol{x})$ on a 2D grid that is β times finer, along each direction, than the original 2048^2 grid. This evaluation is performed exactly from the Fourier coefficients of ψ. In practice, this is done by zero-padding the Fourier representation of ψ (from 2048 to 2048β Fourier modes along each direction).

In Fig. 7, we present the variance of the velocity circulation obtained using different values of the resampling factor β. For small loop sizes, the scaling $\langle |\Gamma_A|^2 \rangle \sim A^1$ predicted by Eq. (4) is only observed when β is large enough ($\beta \geq 8$), while for small β, the small-scale moments are contaminated by spurious circulation values. Throughout this work, the value $\beta = 16$ is used; i.e., the velocity is computed on a 32768^2 grid for each 2D cut. Note that for loop sizes in the classical range (where the K41 scaling $\langle |\Gamma_A|^2 \rangle \sim A^{4/3}$ is observed), resampling becomes less important.

Finally, the inset of Fig. 7 shows the measured PDF of the circulation along loops in the quantum range, for the same values of β. In all cases, the PDFs display peaks at small integer values of Γ_r/κ, as expected from the underlying physics. However, intermediate noninteger values are also sampled in the distributions. These are a purely numerical artifact, mainly a consequence of the approximation error arising from the Fourier truncation of the velocity field. This error strongly decreases at high resampling factors, as evidenced by the increasing separation between peaks and valleys as β increases. Another source

of spurious circulations originates when vortices are present very close to an integration path. Such events lead to unphysical, very large circulation values sampling the r^{-1} divergence of the velocity, whose signatures are PDF tails exhibiting a Γ_r^{-3} scaling. As seen in the figure, resampling also helps reduce this error by a few orders of magnitude. In a second step, these spurious contributions to the circulation distributions are further suppressed by only considering the peaks of Γ_r/κ close to integer values, from which discrete PMFs are constructed. Only peaks that have a prominence of at least 3 orders of magnitude are considered; i.e., the value of the peaks should be at least 1000 times larger than their neighbors.

APPENDIX B: NONLOCAL INTERACTION POTENTIAL

To model the presence of the roton minimum in superfluid ^{4}He, the governing equation includes an isotropic nonlocal interaction potential [31,65]

$$\hat{V}_I(\boldsymbol{k}) = \left[1 - V_1 \left(\frac{k}{k_{\text{rot}}} \right)^2 + V_2 \left(\frac{k}{k_{\text{rot}}} \right)^4 \right] \exp \left(-\frac{k^2}{2k_{\text{rot}}^2} \right),$$

(B1)

where $\hat{V}_I(\boldsymbol{k}) = \int e^{i\boldsymbol{k}\cdot\boldsymbol{r}} V_I(\boldsymbol{r}) \mathrm{d}^3 r$ is the Fourier transform of the normalized interaction potential $\hat{V}_I(k=0) = 1$. The wave number associated with the roton minimum is denoted as k_{rot}, and $V_1 \leq 0$ and $V_2 \leq 0$ are two dimensionless parameters that are set to reproduce the dispersion relation of superfluid ^{4}He (see Ref. [31]). This model also includes a beyond-mean-field correction controlled by two dimensionless parameters χ and γ that correspond to its amplitude and order, respectively. This term arises from considering a strong interaction between bosons.

The parameters used in the simulations were set to $k_{\text{rot}}\xi = 1.638$, $V_1 = 4.54$, $V_2 = 0.01$, $\chi = 0.1$, and $\gamma = 2.8$ in order to mimic the dispersion relation of superfluid ^{4}He. The speed of sound and the particle density are fixed as $c = 1$ and $n_0 = 1$.

APPENDIX C: NAVIER-STOKES SIMULATIONS

Classical turbulence simulations are performed using the LaTu solver [66], which solves the incompressible Navier-Stokes equations

$$\frac{\partial \boldsymbol{v}}{\partial t} + \boldsymbol{v} \cdot \nabla \boldsymbol{v} = -\nabla p + \nu \nabla^2 \boldsymbol{v} + \boldsymbol{f}, \qquad \text{(C1)}$$

$$\nabla \cdot \boldsymbol{v} = 0 \qquad \text{(C2)}$$

using a standard Fourier pseudospectral method in a three-dimensional periodic domain of size $(2\pi)^3$, with a third-order Runge-Kutta scheme for the temporal discretization.

Here, ν is the fluid viscosity, p is the pressure field, and $\boldsymbol{f}$ is an external forcing that emulates a large-scale energy injection mechanism. The forcing is active within a spherical shell of radius $|\boldsymbol{k}| \leq 2$ in Fourier space.

Simulations are performed on a grid of $N^3 = 1024^3$ collocation points, at a Taylor scale Reynolds number $\text{Re}_\lambda \approx 320$. Circulation statistics are gathered once the simulation reaches a statistically steady state, when the energy injection and dissipation rates are in equilibrium. Circulation is computed from a set of velocity fields obtained from the simulations. As in the quantum turbulence simulations, circulation is computed from its velocity-based definition, Eq. (1), using the Fourier coefficients of the velocity field as described in Appendix A.

[1] S. Kida and M. Takaoka, *Vortex Reconnection*, Annu. Rev. Fluid Mech. **26**, 169 (1994).

[2] H. Helmholtz, *Über Integrale der Hydrodynamischen Gleichungen, Welche den Wirbelbewegungen Entsprechen*, J. Für Reine Angew. Math. **55**, 25 (1858).

[3] W. Thomson, *VI.—On Vortex Motion*, Earth Environ. Sci. Trans. R. Soc. Edinb. **25**, 217 (1868).

[4] C. F. Barenghi, L. Skrbek, and K. R. Sreenivasan, *Introduction to Quantum Turbulence*, Proc. Natl. Acad. Sci. U.S.A. **111**, 4647 (2014).

[5] R. P. Feynman, *Application of Quantum Mechanics to Liquid Helium*, in *Progress in Low Temperature Physics*, edited by C. J. Gorter (Elsevier, New York, 1955), Vol. 1, pp. 17–53.

[6] J. Koplik and H. Levine, *Vortex Reconnection in Superfluid Helium*, Phys. Rev. Lett. **71**, 1375 (1993).

[7] G. P. Bewley, M. S. Paoletti, K. R. Sreenivasan, and D. P. Lathrop, *Characterization of Reconnecting Vortices in Superfluid Helium*, Proc. Natl. Acad. Sci. U.S.A. **105**, 13707 (2008).

[8] S. Serafini, L. Galantucci, E. Iseni, T. Bienaimé, R. N. Bisset, C. F. Barenghi, F. Dalfovo, G. Lamporesi, and G. Ferrari, *Vortex Reconnections and Rebounds in Trapped Atomic Bose-Einstein Condensates*, Phys. Rev. X **7**, 021031 (2017).

[9] K. W. Schwarz, *Three-Dimensional Vortex Dynamics in Superfluid ^{4}He: Homogeneous Superfluid Turbulence*, Phys. Rev. B **38**, 2398 (1988).

[10] R. J. Donnelly, *Quantized Vortices and Turbulence in Helium II*, Annu. Rev. Fluid Mech. **25**, 325 (1993).

[11] C. Nore, M. Abid, and M. E. Brachet, *Kolmogorov Turbulence in Low-Temperature Superflows*, Phys. Rev. Lett. **78**, 3896 (1997).

[12] M. C. Tsatsos, P. E. S. Tavares, A. Cidrim, A. R. Fritsch, M. A. Caracanhas, F. E. A. dos Santos, C. F. Barenghi, and V. S. Bagnato, *Quantum Turbulence in Trapped Atomic Bose–Einstein Condensates*, Phys. Rep. **622**, 1 (2016).

[13] A. N. Kolmogorov, *The Local Structure of Turbulence in Incompressible Viscous Fluid for Very Large Reynolds Numbers*, Dokl. Akad. Nauk SSSR **30**, 301 (1941); Proc. R. Soc. A **434**, 9 (1991).

[14] U. Frisch, *Turbulence: The Legacy of A.N. Kolmogorov*, 1st ed. (Cambridge University Press, Cambridge, England, 1995).

[15] K. R. Sreenivasan, A. Juneja, and A. K. Suri, *Scaling Properties of Circulation in Moderate-Reynolds-Number Turbulent Wakes*, Phys. Rev. Lett. **75**, 433 (1995).

[16] Q. Zhou, C. Sun, and K.-Q. Xia, *Experimental Investigation of Homogeneity, Isotropy, and Circulation of the Velocity Field in Buoyancy-Driven Turbulence*, J. Fluid Mech. **598**, 361 (2008).

[17] M. Umeki, *Probability Distribution of Velocity Circulation in Three-Dimensional Turbulence*, J. Phys. Soc. Jpn. **62**, 3788 (1993).

[18] N. Cao, S. Chen, and K. R. Sreenivasan, *Properties of Velocity Circulation in Three-Dimensional Turbulence*, Phys. Rev. Lett. **76**, 616 (1996).

[19] R. Benzi, L. Biferale, M. V. Struglia, and R. Tripiccione, *Self-Scaling Properties of Velocity Circulation in Shear Flows*, Phys. Rev. E **55**, 3739 (1997).

[20] K. P. Iyer, K. R. Sreenivasan, and P. K. Yeung, *Circulation in High Reynolds Number Isotropic Turbulence is a Bifractal*, Phys. Rev. X **9**, 041006 (2019).

[21] K. R. Sreenivasan and R. A. Antonia, *The Phenomenology of Small-Scale Turbulence*, Annu. Rev. Fluid Mech. **29**, 435 (1997).

[22] G. B. Apolinário, L. Moriconi, R. M. Pereira, and V. J. Valadão, *Vortex Gas Modeling of Turbulent Circulation Statistics*, Phys. Rev. E **102**, 041102(R) (2020).

[23] A. Migdal, *Clebsch Confinement and Instantons in Turbulence*, arXiv:2007.12468.

[24] K. P. Iyer, S. S. Bharadwaj, and K. R. Sreenivasan, *Area Rule for Circulation and Minimal Surfaces in Three-Dimensional Turbulence*, arXiv:2007.06723.

[25] J. Maurer and P. Tabeling, *Local Investigation of Superfluid Turbulence*, Europhys. Lett. **43**, 29 (1998).

[26] J. Salort, B. Chabaud, E. Lévêque, and P.-E. Roche, *Investigation of Intermittency in Superfluid Turbulence*, J. Phys. Conf. Ser. **318**, 042014 (2011).

[27] E. Rusaouen, B. Chabaud, J. Salort, and P.-E. Roche, *Intermittency of Quantum Turbulence with Superfluid Fractions from 0% to 96%*, Phys. Fluids **29**, 105108 (2017).

[28] E. Varga, J. Gao, W. Guo, and L. Skrbek, *Intermittency Enhancement in Quantum Turbulence in Superfluid* ^{4}He, Phys. Rev. Fluids **3**, 094601 (2018).

[29] C. Nore, M. Abid, and M. E. Brachet, *Decaying Kolmogorov Turbulence in a Model of Superflow*, Phys. Fluids **9**, 2644 (1997).

[30] N. Sasa, T. Kano, M. Machida, V. S. L'vov, O. Rudenko, and M. Tsubota, *Energy Spectra of Quantum Turbulence: Large-Scale Simulation and Modeling*, Phys. Rev. B **84**, 054525 (2011).

[31] N. P. Müller and G. Krstulovic, *Kolmogorov and Kelvin Wave Cascades in a Generalized Model for Quantum Turbulence*, Phys. Rev. B **102**, 134513 (2020).

[32] G. Krstulovic, *Grid Superfluid Turbulence and Intermittency at Very Low Temperature*, Phys. Rev. E **93**, 063104 (2016).

[33] P. C. di Leoni, P. D. Mininni, and M. E. Brachet, *Dual Cascade and Dissipation Mechanisms in Helical Quantum Turbulence*, Phys. Rev. A **95**, 053636 (2017).

[34] A. Villois, D. Proment, and G. Krstulovic, *Irreversible Dynamics of Vortex Reconnections in Quantum Fluids*, Phys. Rev. Lett. **125**, 164501 (2020).

[35] V. S. L'vov, S. V. Nazarenko, and O. Rudenko, *Bottleneck Crossover between Classical and Quantum Superfluid Turbulence*, Phys. Rev. B **76**, 024520 (2007).

[36] A. W. Baggaley, J. Laurie, and C. F. Barenghi, *Vortex-Density Fluctuations, Energy Spectra, and Vortical Regions in Superfluid Turbulence*, Phys. Rev. Lett. **109**, 205304 (2012).

[37] The Taylor microscale λ_T is formally defined by the longitudinal correlation function of the velocity field as the scale at which its parabolic approximation at the origin vanishes [38]. It can be seen as the scale at which velocity gradients become important and viscosity starts to act. It is related to the Kolmogorov length scale η, the scale at which the turbulent cascade ends, by the relationship $\lambda_T = 15^{1/4}\text{Re}_\lambda^{1/2}\eta$, with $\text{Re}_\lambda = v_\text{rms}\lambda_T/\nu$ the Taylor-scale Reynolds number [14]. It is often used by experimentalists and theoreticians, as it depends only on intrinsic properties of the turbulent flow and not on the forcing and dissipative mechanisms.

[38] S. B. Pope, *Turbulent Flows* (Cambridge University Press, Cambridge, England, 2000).

[39] M. Wilczek and R. Friedrich, *Dynamical Origins for Non-Gaussian Vorticity Distributions in Turbulent Flows*, Phys. Rev. E **80**, 016316 (2009).

[40] The previous discussion suggests normalizing distances using the Kolmogorov length $\eta = (\nu^3/\epsilon)^{1/4}$ instead of the Taylor microscale λ_T. However, for the sake of simplicity and consistency with Fig. 2, we use λ_T in Fig. 6.

[41] M. La Mantia, D. Duda, M. Rotter, and L. Skrbek, *Velocity Statistics in Quantum Turbulence*, Proc. IUTAM **9**, 79 (2013).

[42] T. Araki, M. Tsubota, and S. K. Nemirovskii, *Energy Spectrum of Superfluid Turbulence with No Normal-Fluid Component*, Phys. Rev. Lett. **89**, 145301 (2002).

[43] N. G. Parker and C. S. Adams, *Emergence and Decay of Turbulence in Stirred Atomic Bose-Einstein Condensates*, Phys. Rev. Lett. **95**, 145301 (2005).

[44] M. Kobayashi and M. Tsubota, *Kolmogorov Spectrum of Superfluid Turbulence: Numerical Analysis of the Gross-Pitaevskii Equation with a Small-Scale Dissipation*, Phys. Rev. Lett. **94**, 065302 (2005).

[45] M. Kobayashi and M. Tsubota, *Quantum Turbulence in a Trapped Bose-Einstein Condensate*, Phys. Rev. A **76**, 045603 (2007).

[46] J. Yepez, G. Vahala, L. Vahala, and M. Soe, *Superfluid Turbulence from Quantum Kelvin Wave to Classical Kolmogorov Cascades*, Phys. Rev. Lett. **103**, 084501 (2009).

[47] M. Tsubota, *Quantum Turbulence—From Superfluid Helium to Atomic Bose Condensates*, J. Phys. Condens. Matter **21**, 164207 (2009).

[48] C. F. Barenghi, V. S. L'vov, and P.-E. Roche, *Experimental, Numerical, and Analytical Velocity Spectra in Turbulent Quantum Fluid*, Proc. Natl. Acad. Sci. U.S.A. **111**, 4683 (2014).

[49] M. Tsubota, K. Fujimoto, and S. Yui, *Numerical Studies of Quantum Turbulence*, J. Low Temp. Phys. **188**, 119 (2017).

[50] L. Biferale, D. Khomenko, V. L'vov, A. Pomyalov, I. Procaccia, and G. Sahoo, *Turbulent Statistics and Intermittency Enhancement in Coflowing Superfluid* ^{4}He, Phys. Rev. Fluids **3,** 024605 (2018).

[51] S. Chen, G. L. Eyink, M. Wan, and Z. Xiao, *Is the Kelvin Theorem Valid for High Reynolds Number Turbulence?*, Phys. Rev. Lett. **97,** 144505 (2006).

[52] G. L. Eyink, *Turbulent Cascade of Circulations*, C.R. Phys. **7,** 449 (2006).

[53] R. J. Donnelly, A. N. Karpetis, J. J. Niemela, K. R. Sreenivasan, W. F. Vinen, and C. M. White, *The Use of Particle Image Velocimetry in the Study of Turbulence in Liquid Helium*, J. Low Temp. Phys. **126,** 327 (2002).

[54] T. Zhang and S. W. Van Sciver, *Large-Scale Turbulent Flow around a Cylinder in Counterflow Superfluid* ^{4}He *(He(II))*, Nat. Phys. **1,** 36 (2005).

[55] Y. A. Sergeev and C. F. Barenghi, *Particles-Vortex Interactions and Flow Visualization in* ^{4}He, J. Low Temp. Phys. **157,** 429 (2009).

[56] T. V. Chagovets and S. W. Van Sciver, *A Study of Thermal Counterflow Using Particle Tracking Velocimetry*, Phys. Fluids **23,** 107102 (2011).

[57] W. Guo, M. L. Mantia, D. P. Lathrop, and S. W. Van Sciver, *Visualization of Two-Fluid Flows of Superfluid Helium-4*, Proc. Natl. Acad. Sci. U.S.A. **111,** 4653 (2014).

[58] M. La Mantia, T. V. Chagovets, M. Rotter, and L. Skrbek, *Testing the Performance of a Cryogenic Visualization System on Thermal Counterflow by Using Hydrogen and Deuterium Solid Tracers*, Rev. Sci. Instrum. **83,** 055109 (2012).

[59] M. La Mantia and L. Skrbek, *Quantum Turbulence Visualized by Particle Dynamics*, Phys. Rev. B **90,** 014519 (2014).

[60] D. P. Meichle and D. P. Lathrop, *Nanoparticle Dispersion in Superfluid Helium*, Rev. Sci. Instrum. **85,** 073705 (2014).

[61] A. Marakov, J. Gao, W. Guo, S. W. Van Sciver, G. G. Ihas, D. N. McKinsey, and W. F. Vinen, *Visualization of the Normal-Fluid Turbulence in Counterflowing Superfluid* ^{4}He, Phys. Rev. B **91,** 094503 (2015).

[62] W. Guo, *Molecular Tagging Velocimetry in Superfluid Helium-4: Progress, Issues, and Future Development*, J. Low Temp. Phys. **196,** 60 (2019).

[63] W. Kubo and Y. Tsuji, *Statistical Properties of Small Particle Trajectories in a Fully Developed Turbulent State in He-II*, J. Low Temp. Phys. **196,** 170 (2019).

[64] X. Wen, S. R. Bao, L. McDonald, J. Pierce, G. L. Greene, L. Crow, X. Tong, A. Mezzacappa, R. Glasby, W. Guo, and M. R. Fitzsimmons, *Imaging Fluorescence of* He$_2^*$ *Excimers Created by Neutron Capture in Liquid Helium II*, Phys. Rev. Lett. **124,** 134502 (2020).

[65] J. Reneuve, J. Salort, and L. Chevillard, *Structure, Dynamics, and Reconnection of Vortices in a Nonlocal Model of Superfluids*, Phys. Rev. Fluids **3,** 114602 (2018).

[66] H. Homann, O. Kamps, R. Friedrich, and R. Grauer, *Bridging from Eulerian to Lagrangian Statistics in 3D Hydro- and Magnetohydrodynamic Turbulent Flows*, New J. Phys. **11,** 073020 (2009).

4.2.1 Discussion on low-order moments

One important difference of the circulation statistics between classical and quantum turbulence comes from the probability of finding zero values of circulation within a loop. In particular, as circulation in classical fluids takes continuous values, this probability is zero by definition. However, as in quantum fluids circulation takes discrete values, there are vortex cancellation events that lead to non-zero values for the probability of having zero circulation. In particular, doing a series expansion around $p = 0$, the circulation moments in a discrete system can be written as

$$\langle|\Gamma_r|^p\rangle = \sum_{\Gamma\neq0} |\Gamma|^p \mathcal{P}_r(\Gamma) = 1 - \mathcal{P}_r(0) + p \sum_{\Gamma\neq0} \log|\Gamma| \mathcal{P}_r(\Gamma) + o(p^2), \qquad (4.9)$$

where we used that $\sum_{\Gamma\neq0} \mathcal{P}_r(\Gamma) = 1 - \mathcal{P}_r(0)$. Here, it becomes evident that low-order moments are dominated by the probability of zero circulation values, which in quantum fluids is finite. In Fig. 4.3, we show the low-order moments obtained from DNS of the GP and the NS equations. Indeed, in quantum turbulence we observe that as $p \to 0$, the moments are completely prescribed by the probability of zero circulation, which follows $\mathcal{P}_r(0) \sim r^{-4/3}$ for large scales $r > \ell$ [MPK21]. As a consequence, there is a combination of power laws and it is therefore difficult to measure a clear exponent with a limited scaling range. In contrast, in NS simulations we observe a clear scaling for the moments of circulation, and they obey the K41 self-similar scaling, as reported by Iyer et al. [ISY19].

4.2.2 Comparison between GP and gGP models

The statistics of velocity circulation showed up to this point were obtained from numerical simulations of the gGP model, that includes a non-local interaction potential between bosons introducing a roton minimum in the excitation spectrum. This model differs from the standard GP model, in which the interaction between bosons
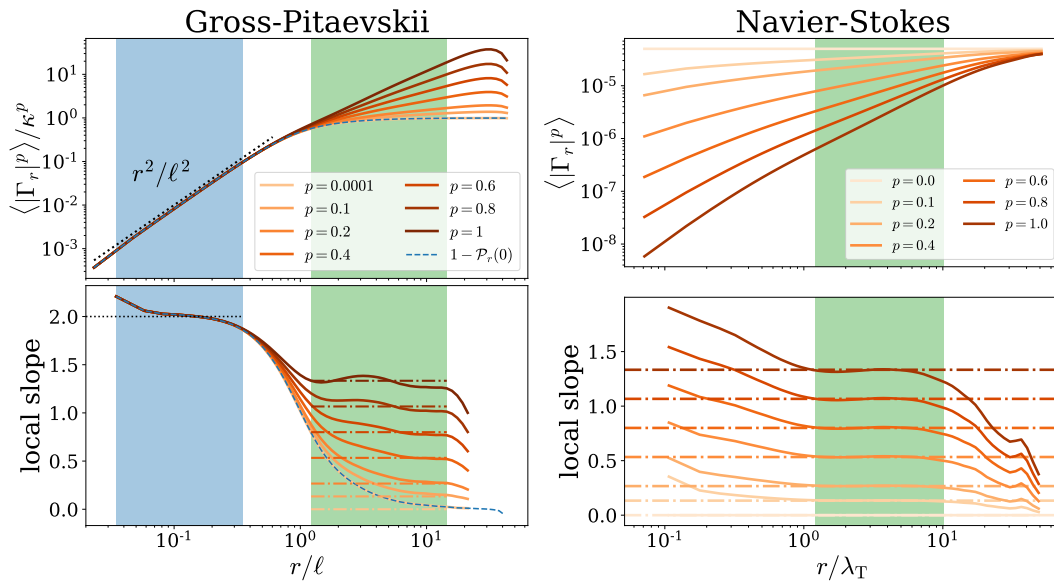

Figure 4.3: Circulation moments for $p \leq 1$ obtained from (left) GP simulations and (right) NS simulations. The dashed line corresponds to the scaling of zero-probability and dot-dashed lines to Kolmogorov prediction $\lambda_p^{K41} = 4p/3$. On the bottom panels, we show the local slopes $\mathrm{d}\log\langle|\Gamma_r|^p\rangle/\mathrm{d}\log r$.
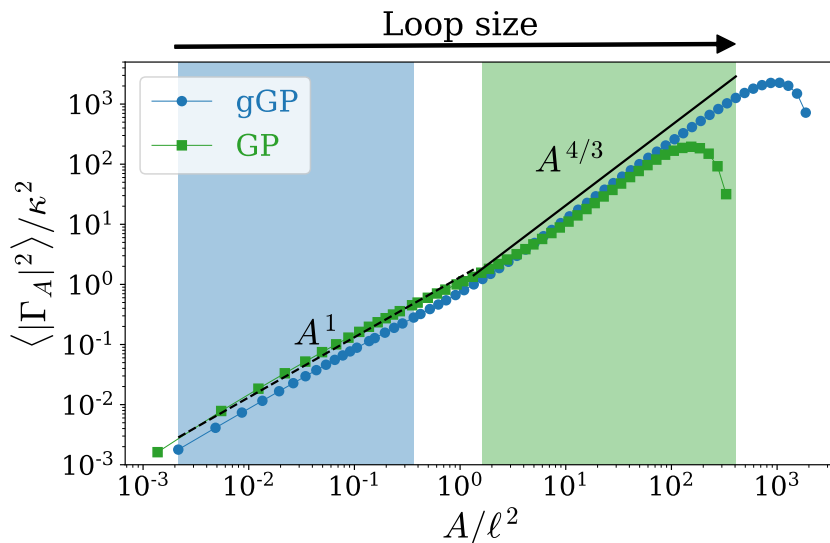
Figure 4.4: Circulation variance in the standard GP (green) and generalized GP (blue) models using 512^3 and 2048^3 collocation points, respectively. The blue and green area indicate the quantum and semi-classical inertial ranges, respectively. Both models seem to display the same turbulent properties.

is given by a δ-function and there is no roton minimum. To see if there are any differences in the turbulent properties of the velocity circulation between these models, we perform a single simulation of the standard GP equation using 512^3 collocation points. We generate an ABC flow and let it decay in time, in the same spirit as in the gGP simulations.

Figure 4.4 shows the circulation variance in both models. Both at large and small scales, the scaling properties of the turbulent flow display the same behavior. In particular, at small scales the scaling is governed by individual vortices as discussed in Müller, Polanco, and Krstulovic [MPK21], while at large scales it follows Kolmogorov scaling $r^{8/3}$. Note that the size of the inertial ranges might vary between the simulations as the resolution also does. One property that might vary between simulations is the intervortex distance. As discussed in Müller and Krstulovic [MK20], the intervortex distance in the non-local model can take smaller values than in the local model, modifying the sizes of the inertial ranges, making the semi-classical one larger.

This result suggests that the use of a local or a non-local interaction between bosons do not affect the scaling properties of velocity circulation neither at scales larger nor smaller than the intervortex distance. This, however, might not be the case for structure functions, where it was shown that the introduction of rotons enhance the development of the Kelvin wave cascade at small scales. This result might motivate new studies on the scaling of velocity circulation in the vortex filament model, where the reconnection process is introduced in an *ad hoc* manner.

4.3 Publication: *Vortex clustering, polarisation and circulation intermittency in classical and quantum turbulence*

After the empiric determination that velocity circulation statistics in classical and quantum turbulence display the same phenomenology, we decided to go a step further and try to disentangle the intermittent behavior of quantum flows [ISY19;

MPK21]. In this work, we use the same set of numerical simulations from the GP and NS equations as in the previous section.

Here, we first develop a simple model of circulation based on the contribution of n individual vortices

$$\Gamma_n = \sum_{i=1}^{n} \kappa s_i. \tag{4.10}$$

with κ the quantum of circulation of each vortex and $s_i = \pm 1$. In particular, we set $\kappa = 1$. The model, introduced in this publication and developed further in the supplementary material, is based on the idea that all vortices s_i are correlated, but the total circulation Γ_n is a Markovian process. The probability of adding a positive quantum vortex inside a loop depends on the circulation of the previous step given by $\mathcal{P}_n(s_n = 1|\Gamma_n = \Gamma) = (1 + \beta\Gamma/n)/2$, with β a polarization parameter. We can thus obtain analytically a scaling for the circulation moments as a function of the number of vortices that obeys [PMK21]

$$\langle \Gamma_n^p \rangle \sim n^{\gamma_p} \quad \text{with} \quad \gamma_p = \begin{cases} p/2 & \text{if } 0 \le \beta < 1/2 \\ \beta p & \text{if } 1/2 \le \beta \le 1 \end{cases} \tag{4.11}$$

If $\beta = 0$, the probability of adding a positive or negative vortex at each step is the same $(1/2)$ and vortices at large scales are completely uncorrelated, resembling a random walk and obtaining a diffusive scaling. If $\beta = 1$, the system will be fully polarized, with all the vortices with the same circulation sign and the system recovers a ballistic scaling. In particular, using that the mean number of vortices inside a loop of size r grows as $\langle n_r \rangle \sim r^2$, and taking the value $\beta = 2/3$, we obtain the K41 phenomenology, corresponding to a partial polarization of the vortices.

The model developed for the circulation moments (4.11) is built on individual vortices, and there is no notion of space on it. For the numerical data, we try to reproduce these ideas by studying the circulation based on the closest n vortices instead of the size of the loop r. For this, we first identify the position and sign of each individual vortex by computing the circulation around loops of the size of the vortices. With this information, we compute the circulation in each loop, and also count the number of vortices that it encloses, obtaining a joint PDF of $\mathcal{P}(\Gamma, r, n)$. We can thus compute the circulation moments for different loop sizes $\langle |\Gamma_r|^p \rangle$ as reported in Müller et al. [MPK21], and based on vortex proximity $\langle |\Gamma_n|^p \rangle$ as in the model, where there is no notion of space. Remarkably, we observe that the latter exhibits a self-similar scaling as in the model, suggesting that the anomalous scaling is caused by the complex spatial distribution of quantum vortices.

To further understand the model for circulation moments given by Eq. (4.11), we perform the following numerical experiment. For each 2D slab of the full 3D quantum turbulent flow, we randomize the sign of each quantum vortex, keeping its position fixed. By doing this, we expect to change the partial polarization $\beta = 2/3$ prescribed by Kolmogorov turbulence into a random system with $\beta = 0$. Indeed, we observe a change in the slope of the moments of Γ_n, keeping a self-similar scaling. More interestingly, we observe that the scaling exponents of $\langle |\Gamma_r|^p \rangle$ also change their slope, but still exhibiting an anomalous scaling, reinforcing the idea of intermittency is caused by the spatial distribution of vortices.

Finally, we study the moments of the number of vortices in loops of different sizes $\langle n_r^p \rangle$. We show that this quantity can be related with the coarse-grained energy dissipation rate in classical turbulence from a vortex gas model. In the inertial range, the PDFs of n_r exhibit a close to log-normal behavior and the moments present a

scaling that appear to be described by the scaling exponents τ_p, using either the log-normal or She-Lévêque models.

In the supplementary material published together with the paper, and included right after the publication, we show a generalization of the discrete model for circulation, a derivation for the relation between the coarse-grained energy dissipation and the number of vortices inside a loop, and the discrepancy between NS and GP scaling exponents of circulation and the classical OK62 theory. After the publication, we shortly discuss the correlation between vortices in the model.

Vortex clustering, polarisation and circulation intermittency in classical and quantum turbulence

Juan Ignacio Polanco [1,2✉], Nicolás P. Müller [1✉] & Giorgio Krstulovic [1✉]

The understanding of turbulent flows is one of the biggest current challenges in physics, as no first-principles theory exists to explain their observed spatio-temporal intermittency. Turbulent flows may be regarded as an intricate collection of mutually-interacting vortices. This picture becomes accurate in quantum turbulence, which is built on tangles of discrete vortex filaments. Here, we study the statistics of velocity circulation in quantum and classical turbulence. We show that, in quantum flows, Kolmogorov turbulence emerges from the correlation of vortex orientations, while deviations—associated with intermittency—originate from their non-trivial spatial arrangement. We then link the spatial distribution of vortices in quantum turbulence to the coarse-grained energy dissipation in classical turbulence, enabling the application of existent models of classical turbulence intermittency to the quantum case. Our results provide a connection between the intermittency of quantum and classical turbulence and initiate a promising path to a better understanding of the latter.

[1] Université Côte d'Azur, Observatoire de la Côte d'Azur, CNRS, Laboratoire J. L. Lagrange, Boulevard de l'Observatoire CS 34229 - F 06304 NICE Cedex 4, Paris, France. [2] Univ Lyon, CNRS, École Centrale de Lyon, INSA Lyon, Univ Claude Bernard Lyon 1, LMFA, UMR5509, 69130 Écully, France. ✉email: juan-ignacio.polanco@ec-lyon.fr; nmuller@oca.eu; krstulovic@oca.eu

V ortices are manifestly the most attractive feature of fluid flows occurring in the Nature. They are highly rotating zones of the fluid that often take the form of elongated filaments, of which tornadoes are one prominent example in atmospheric flows. Such structures can travel and interact with other vortex filaments, as well as with the surrounding fluid. In fact, the dynamics of vortex filaments in fluid flows is highly non-trivial, as they can reconnect changing the topology of the flow[1]. Their non-trivial arrangements may lead to very complex configurations and in particular to turbulence, an out-of-equilibrium state characterised by a large-scale separation between the scales at which energy is injected and the one at which it is dissipated. In three-dimensional flows, because of the inherently non-linear character of turbulence, energy initially injected at large scales is transferred towards the small scales through a cascade-like process.

In turbulent flows, the typical thickness of a vortex filament is comparable to the smallest active scale of turbulence[2], itself usually much smaller than the eddies carrying most of the energy content of the flow. Vortex filaments may thus be seen as the fundamental structure of turbulence, whose collective dynamics leads to the multi-scale complexity of such flows. Indeed, depending on their individual intensities and orientations, a set of vortex filaments located within a given spatial region may contribute constructively or destructively to the fluid rotation rate. In fluid dynamics, the rotation rate of a two-dimensional fluid patch is commonly quantified by the velocity circulation around the closed loop $\mathcal{C}$ surrounding the patch,

$$\Gamma(\mathcal{C}; \mathbf{v}) = \oint_{\mathcal{C}} \mathbf{v} \cdot d\mathbf{r}, \qquad (1)$$

where $\mathbf{v}$ is the fluid velocity field. Note that, by virtue of Stokes' theorem, the circulation is equal to the flux of vorticity, $\boldsymbol{\omega} = \nabla \times \mathbf{v}$, through the fluid patch.

The above view of vortex filaments as the fundamental unit of fluid flows is particularly appropriate in superfluids, such as low-temperature liquid helium and Bose–Einstein condensates (BECs). Indeed, in such fluids, vortices are well-defined discrete objects about which the circulation is quantised, taking values multiple of $\kappa = h/m$. Here h is Planck's constant and m is the mass of the bosons constituting the superfluid[3]. Such property arises from their quantum nature, as vortices are topological defects of the macroscopic wave function describing the system. For this reason, vortex filaments in superfluids are called quantum vortices.

One of the most striking properties of low-temperature superfluids is their total absence of viscosity. Despite this fact, quantum vortex reconnections are possible, since Helmholtz' theorem that forbids reconnections in classical inviscid fluids[1] breaks down due to the vanishing fluid density at the vortex core. This picture was first suggested by Feynman in 1955[4] and later confirmed numerically in the framework of the Gross–Pitaevskii (GP) equation[5]. Since then, quantum vortex reconnections have been observed experimentally in superfluid helium[6] and in BECs[7]. They are characterised by universal scaling laws[8,9] and have been linked to irreversibility, both in experiments[10] and in numerical simulations[11]. In the early vortex filament simulations by Schwarz[12], it was noticed that quantum vortex reconnections are a key physical process for the development of quantum turbulence, a state described by the complex interaction of a tangle of quantum vortices. Such a state is illustrated by the vortex filaments (in green and yellow) visualised in Fig. 1, obtained from the GP simulations performed in Ref. [13].

Quantum turbulence is characterised by a rich multi-scale physics. At small scales, between the vortex core size (about 1 Å in superfluid ^{4}He) and the mean inter-vortex distance ℓ (~1 μm), the physics is governed by the dynamics of individual quantised vortices[14]. At such scales, Kelvin waves (waves propagating along vortices) and vortex reconnections are the main physical processes carrying energy along scales[15,16]. In contrast, at scales larger than ℓ, the quantum nature of the superfluid becomes less important and a regime comparable to classical turbulence emerges. Indeed, at such scales, a Kolmogorov turbulent cascade is observed, provided that a large-scale separation exists between ℓ and the largest scale of the system. In particular, the scaling law predicted by Kolmogorov's celebrated K41 theory[17] for the kinetic energy spectrum has been observed in superfluid helium experiments[18,19] and in numerical simulations of quantum turbulence[20–22].

Previous studies have suggested that, in quantum turbulence, the emergence of K41 scaling laws is associated to a local *polarisation* of the vortex tangle[14,23–27]. In other words, within a given spatial region, the orientations of nearby vortices are not independent, but instead have some degree of correlation. This phenomenon is visible in Fig. 1, where vortex bundles—regions of same-coloured vortex filaments—can be clearly identified. This local polarisation is present even in ideally isotropic flows, and should not be confused with the preferential large-scale orientation of vortices, which typically occurs in anisotropic flows. A classic example of the latter is a rotating cylindrical vessel filled with superfluid helium[4].

In a recent work[13], we have shown that the quantitative similarities between classical and quantum turbulence go far beyond the Kolmogorov energy spectrum. Indeed, both systems display the emergence of extreme events that result in the breakdown of Kolmogorov's K41 theory—a phenomenon known as intermittency. Our work was motivated by the recent study of Iyer et al.[28], which suggested that intermittency has a relatively simple signature on the statistics of circulation in classical turbulence. In particular, the moments of the circulation measured over fluid patches of area $A \sim r^2$ follow a power law of the form

$$\langle |\Gamma|^p \rangle_A \sim r^{\lambda_p} \sim A^{\lambda_p/2}, \qquad (2)$$

with scaling exponents λ_p that increasingly deviate from the K41 prediction $\lambda_p^{\mathrm{K41}} = 4p/3$ as the moment order p increases. By performing simulations of a generalised GP equation, we have shown that the anomalous scaling exponents λ_p in the inertial scales of quantum turbulence closely match those observed in classical turbulence[13]. Note that, up until now, most of the advances in the understanding of intermittency have been made in terms of velocity increments. However, despite many theoretical efforts[17,29–31], there is still no first-principles theory able to explain this phenomenon. The above-cited findings suggest that circulation may provide an alternative path towards a better understanding of turbulence (as first hinted the by pioneering theoretical work of Migdal[32]), and eventually, to novel circulation-based theories of intermittency[33,34].

The strong similarity between the statistics of circulation in classical and quantum turbulence is particularly striking given the very different nature of vortices in both types of fluids. This statistical equivalence opens the way for an interpretation of the intermittency of classical turbulent flows in terms of the collective dynamics of discrete vortex filaments carrying a fixed circulation. With this idea in mind, we relate in this work the intermittent statistics of velocity circulation in classical and quantum turbulence. We start by investigating in quantum turbulence how local vortex polarisation, as well as the non-trivial spatial distribution of vortex filaments, affect circulation statistics. We address the following questions: Is it possible to study both effects separately? Do they contribute in the same way to the flow intermittency? We then provide a relation between the spatial distribution of discrete
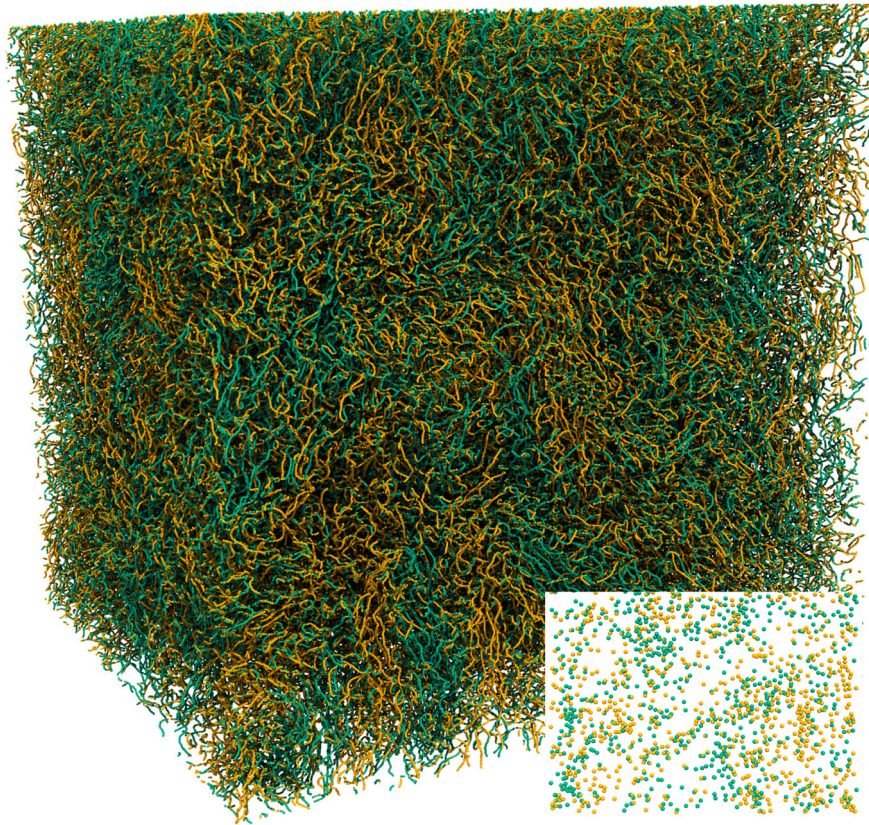
Fig. 1 Visualisation of a quantum turbulent vortex tangle. Instantaneous state obtained from GP simulations using 2048^3 collocation points. Green and yellow colours correspond to opposite orientations of the vortex lines with respect to the vertical direction. The inset shows a horizontal two-dimensional cut of the system. See "Methods" for the vortex identification algorithm.
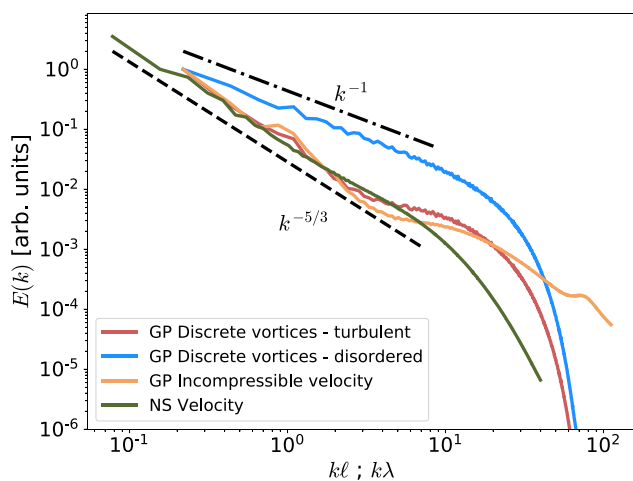

Fig. 2 Kinetic energy spectrum in quantum and classical turbulence. Spectra are obtained from simulations of the generalised Gross–Pitaevskii (GP) model and the incompressible Navier–Stokes (NS) equations. Wave numbers k are, respectively, normalised by the mean inter-vortex distance ℓ and by the Taylor micro-scale λ, while the vertical axis is in arbitrary units. In the GP case, the incompressible part of the kinetic energy is plotted[63]. Also shown are the energy spectra obtained after applying the vortex detection procedure to the GP fields (see "Methods" for details), both before and after the randomisation of the vortex orientations (turbulent and disordered cases, respectively). Dashed and dash-dotted lines, respectively, represent the Kolmogorov scaling $k^{-5/3}$ and the disordered scaling k^{-1}. Source data are provided as a Source Data file.

vortices, and the coarse-grained energy dissipation rate in classical turbulence, a quantity at the core of existent intermittency models.

In this work, quantum and classical turbulent systems are, respectively, studied using high-resolution direct numerical simulations of a generalised GP and the incompressible Navier–Stokes (NS) equations. Discrete vortices and their signs are extracted from the GP fields and then analysed. To disentangle the effects of polarisation and spatial vortex distribution, we additionally study a disordered turbulence state. Such state is generated from the discrete vortex data by randomly resetting the sign of each individual vortex while keeping its position fixed. To illustrate the differences between the turbulent (non-disordered) and the disordered turbulence states, we plot in Fig. 2 the kinetic energy spectrum associated to each vortex configuration (see "Methods" for details on the computation of the spectra from discrete vortices). First, we see that the turbulent case displays a clear $k^{-5/3}$ range, in agreement with the energy spectra obtained from the full GP and NS fields. Note that, in the case of GP fields, we show the incompressible kinetic energy spectrum, which contains 86% of the total energy of the system—the other components being the compressible, internal and quantum energy[20,22]. Secondly, the K41 scaling disappears once polarisation is artificially suppressed from the tangle, leading to a trivial k^{-1} scaling range for the disordered state (see "Methods" for a brief derivation). Note that this same scaling has already been observed in vortex filament simulations, once the vortex tangle has been decomposed into polarised and random components[26].
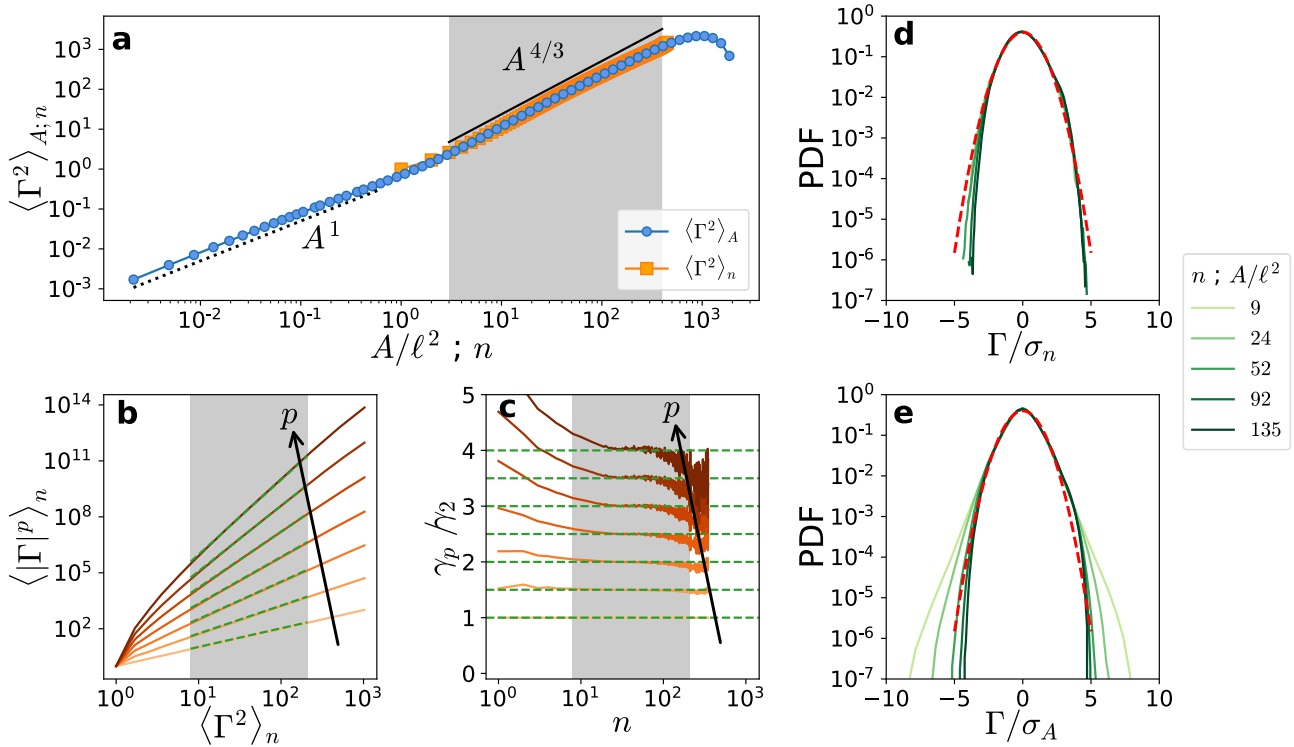
Fig. 3 Circulation statistics in quantum turbulence. a Circulation variance as a function of the area A of each loop and of the number n of neighbouring vortices. The dotted line represents the scaling A^1 observed at small scales of quantum turbulence[13]. **b, c** Moments and local slopes of $\langle|\Gamma|^p\rangle_n$ as a function of $\langle\Gamma^2\rangle_n$ according to the ESS approach, for $p \in [2, 8]$. Dashed green lines represent the K41 scaling $\gamma_p = 2p/3$. **d, e** PDFs of the circulation for different (**d**) numbers of vortices and (**e**) loop areas. All PDFs are normalised by the respective standard deviations. Dashed red lines represent a unit Gaussian distribution.

Results

A simple discrete model of circulation. Let us first consider a set of n discrete vortices, each of them carrying a circulation κs_i, where $s_i = \pm 1$ is the sign of each vortex. From now on we set the quantum of circulation to $\kappa = 1$ for simplicity. We propose to model the total circulation of the n-vortex collection, $\Gamma_n = \sum_{i=1}^{n} s_i$, as a biased one-dimensional random walk. Polarisation is naturally introduced by letting each random step s_i be positively correlated with the instantaneous position Γ_{i-1}, i.e. the total circulation of all previous vortices.

Concretely, we construct inductively the following toy model for the circulation. The sign of the first vortex, s_1, has equal probability of being positive or negative. Then, the sign of vortex $n + 1$ is positive with a probability p_{n+1}, which we set to depend on the total circulation at step n as $p_{n+1} = [1 + f(\Gamma_n/n)]/2$. Here, $f(z)$ is a suitable function (odd, non-decreasing, taking values in $[-1, 1]$), such that $p_n \in [0, 1]$ at each step n. For the sake of simplicity, we choose here $f(z) = \beta z$ (see the Supplementary information for the general case), where $\beta \in [0, 1]$ is an adjustable parameter that sets the polarisation of the system. When $\beta = 0$, one retrieves a standard random walk with scaling $\langle|\Gamma|^2\rangle_n \sim n$. Conversely, for $\beta = 1$, one recovers a fully polarised set of vortices behaving as $\langle|\Gamma|^2\rangle_n \sim n^2$.

The resulting model is a discrete Markov process, since the probability distribution of Γ_{n+1} only depends on the state $\{n, \Gamma_n\}$ via the probability p_{n+1}. Concretely, the probability $\mathcal{P}_n(\Gamma)$ of having $\Gamma_n = \Gamma$ obeys the master equation

$$\mathcal{P}_{n+1}(\Gamma) = \left(\frac{1}{2} + \beta\frac{\Gamma - 1}{2n}\right)\mathcal{P}_n(\Gamma - 1)$$
$$+ \left(\frac{1}{2} - \beta\frac{\Gamma + 1}{2n}\right)\mathcal{P}_n(\Gamma + 1). \qquad (3)$$

Multiplying this equation by Γ^2, summing over all Γ and, for the sake of simplicity, taking the limit of continuous n, one gets a closed equation for the circulation variance,

$$\frac{d\langle\Gamma^2\rangle_n}{dn} = 1 + \frac{2\beta}{n}\langle\Gamma^2\rangle_n, \qquad (4)$$

where averages are over all realisations after n steps. For large n, this equation predicts the scaling $\langle\Gamma^2\rangle_n \sim n$ for $\beta < 1/2$ (corresponding to a set of vortices with negligible polarisation), and $\langle\Gamma^2\rangle_n \sim n^{2\beta}$ otherwise. In particular, choosing $\beta = 2/3$, one recovers the Kolmogorov scaling by replacing $n \propto A$. This relation between the number of vortices n and the loop area A containing them is expected to hold on average under spatial homogeneity conditions, but neglects potentially important inhomogeneities in the spatial vortex distribution that may affect high-order moments of n. Besides, for the pth order moment, the model predicts the self-similar scaling $\langle|\Gamma|^p\rangle_n \sim n^{\gamma_p}$ with $\gamma_p = \beta p$. More generally, for any suitable function $f(z)$ defining the probability p_n of the model, one obtains the linear scaling $\gamma_p = p\min\{\max\{1/2, f'(0)\}, 1\}$ (see the Supplementary information for more details on the calculations).

The toy model introduced above shows in a very simple manner how a specific correlation (or polarisation) is responsible for the emergence of non-trivial scaling laws, as already suggested by previous works on quantum turbulence[24–26]. In addition, the model yields self-similar statistics, suggesting that polarisation is not sufficient to reproduce the observed intermittency of circulation in classical[28] and quantum[13] turbulent flows. At this point, we may speculate that the lack of intermittency in the model is likely associated with the missing notion of space. Indeed, on average one expects to have a number of vortices $\langle n \rangle \sim A/\ell^2$ crossing a loop of area A, where ℓ is the mean inter-

vortex distance. Yet, fluctuations in their spatial distribution—associated to the appearance of vortex clusters and voids—may strongly influence high-order moments. As seen in Fig. 1, such effects clearly take place in turbulent flows, where they are linked to the formation of coherent structures.

Comparison with quantum turbulence data. The ideas hinted at by our toy model can be verified using actual quantum turbulence data. With this aim, we identify all vortex filaments present in our GP simulations (see "Methods" for details), and compute circulation statistics as a function of the number n of considered vortices. Crucially, groups of vortices are chosen based on their spatial proximity, which is required to preserve the correlation between vortices. On the other hand, with such a conditioning, one may expect the effect of strong spatial fluctuations of the vortex distribution to be somewhat relaxed. In practice, for each two-dimensional cut of the simulation, we consider sets of n neighbouring vortices in order to compute the circulation moments $\langle |\Gamma|^p \rangle_n$. Then, to improve the statistics, we repeat such measurement for each cut and along the three Cartesian directions.

The resulting second-order moment $\langle \Gamma^2 \rangle_n$ is shown in Fig. 3a, along with the moment $\langle \Gamma^2 \rangle_A$ measured for different loop areas A (data from Müller et al.[13]). At small scales, $\langle \Gamma^2 \rangle_A \sim A^1$ due to the discrete nature of vortices[13]. In contrast, within the inertial range, both moments clearly exhibit the expected Kolmogorov scaling. In particular, $\langle \Gamma^2 \rangle_n \sim n^{\gamma_2}$ with $\gamma_2 = 4/3$. This result allows us to use the extended self-similarity (ESS) framework[35] to determine the scaling properties of higher-order moments via the relation $\langle |\Gamma|^p \rangle_n \sim n^{\gamma_p} \sim \langle \Gamma^2 \rangle_n^{\gamma_p/\gamma_2}$. Remarkably, as shown in Fig. 3b–c, the moments display a clear self-similar behaviour with $\gamma_p = 2p/3$, thus obeying Kolmogorov scaling for all orders. The self-similarity is also observed in the normalised probability density functions (PDFs) of Γ for different values of n (Fig. 3d), which nearly collapse and are close to Gaussian. This behaviour should be contrasted with the non-collapsing PDFs of Γ for different loop areas A (Fig. 3e). Note that, in both cases, the chosen values of A and n lay within the inertial range, represented by a grey background in Fig. 3a–c.

Disentangling polarisation and spatial vortex distribution. The fitted scaling exponents for the turbulent case $2\gamma_p^{\text{turb}}$, discussed above, are plotted in Fig. 4 (blue-filled stars) as a function of the moment order p. These exponents are compared to the measured values of λ_p^{turb} (blue-filled circles) obtained according to Eq. (2), where averages are performed for different loop areas A. The latter are the same as in Ref. [13]. The factor 2 in front of γ_p^{turb} comes from considering the relation $\langle n \rangle \sim A \sim r^2$. As discussed earlier, the moments averaged for different n closely follow the self-similar K41 scaling $2\gamma_p^{\text{turb}} \approx 4p/3$ (blue solid line), while the λ_p^{turb} exponents—affected by the spatial vortex distribution—show signs of intermittency[13].

To further distinguish the effects of polarisation and spatial vortex distribution on circulation statistics, we perform the following numerical experiment. We recompute the circulation in the quantum turbulent flow, but before doing this, we randomise the sign of each vortex on each analysed two-dimensional cut while keeping its position fixed. By doing this, we get rid of the system polarisation, while maintaining the non-trivial spatial distribution of vortices. We refer to this system as disordered turbulence. In our non-intermittent toy model, this setting would correspond to the unpolarised value $\beta = 0$, yielding the self-similar circulation scaling $\langle |\Gamma|^p \rangle_n \sim n^{p/2}$. In Fig. 4, we display the
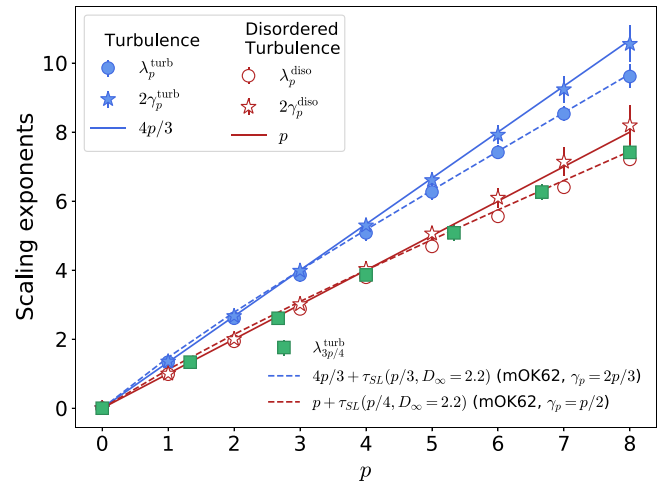

Fig. 4 Velocity circulation scaling exponents. Exponents of the turbulent (in blue) and the disordered turbulence (in red) cases. For each case, the scaling exponents are defined as $\langle |\Gamma|^p \rangle_A \sim r^{\lambda_p}$ (circles) and $\langle |\Gamma|^p \rangle_n \sim n^{\gamma_p}$ (stars). Error bars indicate 95% confidence intervals. Self-similar predictions for each case are shown as solid lines. Green squares show the relation between the turbulent and disordered systems given by Eq. (5). The blue and red dashed lines show the OK62 prediction combined with the She–Lévêque model (8) with $D_\infty = 2.2$ (termed "mOK62") for turbulence and disordered turbulence, respectively. Source data are provided as a Source Data file.

corresponding measured exponents of the disordered state λ_p^{diso} and $2\gamma_p^{\text{diso}}$ (red unfilled markers). Remarkably, even after suppressing vortex polarisation, λ_p^{diso} also presents intermittency deviations. In contrast, the scaling exponents γ_p^{diso} satisfy the expected self-similar behaviour $2\gamma_p^{\text{diso}} \approx p$ (red solid line).

The previous results suggest that the non-trivial polarisation of vortices, while being responsible for Kolmogorov scalings, has no major influence on the intermittency of the system. Furthermore, they indicate that the latter originates from fluctuations of the spatial distributions of vortices. From our above observations, one may therefore expect the scaling exponents of the circulation to be given by a composition of the polarisation and spatial distribution effects. That is, we may conjecture that the scaling exponents λ_p and γ_p are related by

$$\lambda_p = g(\gamma_p) \qquad (5)$$

where g is some yet unknown function.

In order to check this idea, we can try to relate the scaling exponents of the turbulent and disordered turbulent systems. If relationship (5) were to hold true, one should have that $\lambda_p^{\text{diso}} = \lambda_{3p/4}^{\text{turb}}$. Using this relation with the measured exponents of the turbulent case, one indeed recovers the intermittency exponents λ_p^{diso} of the disordered case, as shown by the green squared markers in Fig. 4. This result strongly highlights the importance of the fluctuations of vortex concentration on the intermittency of circulation.

Spatial vortex distribution and OK62 theory. As a first step towards relating the intermittency of classical and quantum turbulence, we now quantify the spatial distribution of vortices in the latter system. If vortices were homogeneously distributed in space, then the number n of vortices within loops of area A would be expected to follow a Poisson distribution with mean value $\langle n \rangle_A \propto A$. In that case, the moments of n would scale as $\langle n^p \rangle_A \sim$
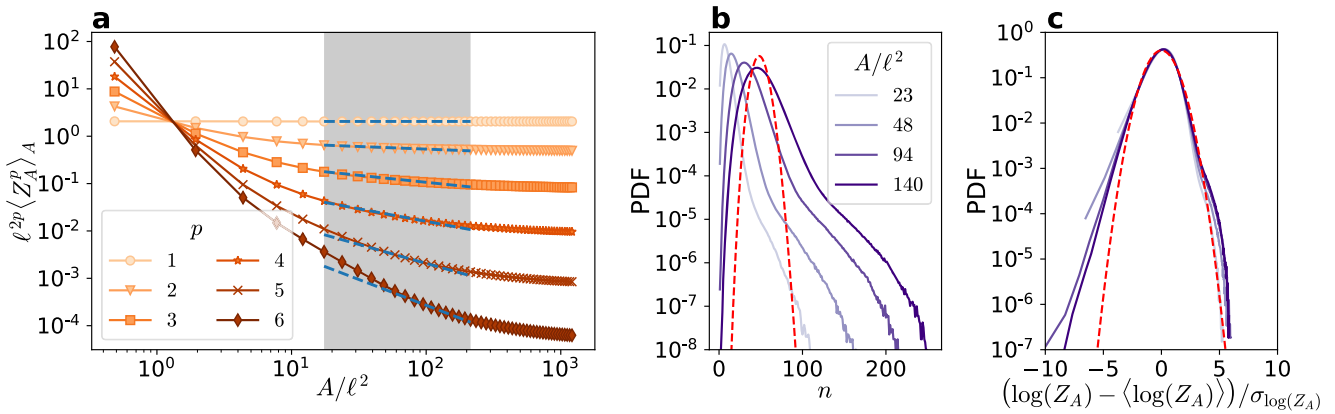
Fig. 5 Statistics of spatial vortex distribution in quantum turbulence. a Moments of the number of vortices normalised by the area that contains them, $Z_A = n/A$. Dashed lines correspond to the scaling of Eq. (7), using the She–Lévêque prediction[44] for the anomalous exponents $\tau(p)$ with $D_\infty = 1$. **b** PDFs of the number of vortices contained in loops of varying area A/ℓ^2. The dashed line corresponds to a Poisson distribution of mean equal to $\langle n \rangle_A$ at $A = 140\ell^2$. **c** Centred reduced PDFs of $\log(Z_A)$ for different values of A/ℓ^2. A log-normal distribution is shown as reference (red dashed line).

A^p for sufficiently large A. Equivalently, the number of vortices per unit area $Z_A = n/A$ would follow the trivial scalings $\langle Z_A^p \rangle_A \sim 1$ for all $p > 0$. As shown in Fig. 5a, this is clearly not the case, indicating that the spatial distribution of vortices is non-trivial in quantum turbulence (as may be inferred from the visualisation of Fig. 1). Indeed, while the first-order moment recovers a constant (consistently with the relation $\langle n \rangle_A \sim A$), higher-order moments of Z_A follow a different scaling with a negative exponent—a sign of anomalous behaviour. This is confirmed by the PDFs of n displayed in Fig. 5b, which are long-tailed and strongly differ from a Poisson distribution (dashed line).

In classical turbulence, it is today well accepted that the intermittency of velocity fluctuations is linked to the emergence of violent events, characterised by strong spatial fluctuations of the kinetic energy dissipation rate $\varepsilon(\mathbf{x})$. Such idea led Obukhov and Kolmogorov in 1962 to develop a refined similarity theory of turbulence, commonly referred to as OK62 theory, where such fluctuations are taken into account[17,36,37], unlike K41 theory which only deals with the mean value of $\varepsilon(\mathbf{x})$. This refined theory considers the scale-averaged (or coarse-grained) energy dissipation rate $\varepsilon_r(\mathbf{x}) = \frac{3}{4\pi r^3} \int_{B(\mathbf{x},r)} \varepsilon(\mathbf{x}') \, d^3\mathbf{x}'$, where $B(\mathbf{x}, r)$ is a ball of radius r centred at $\mathbf{x}$. When applied to the spatial velocity increments δv_r over a distance r, OK62 theory states that the statistics of $\delta v_r/(\varepsilon_r r)^{1/3}$ is self-similar and universal. Most intermittency models use ε_r to predict the anomalous scaling of velocity increment statistics[17]. Some early experiments in classical turbulence showed that, when velocity increments are conditioned on the coarse-grained dissipation, their statistics becomes Gaussian[38,39], proving that the intermittency of velocity fluctuations is hidden behind the distribution of energy dissipation. This observation was later confirmed by numerical simulations[40].

In the case of low-temperature quantum turbulence, such as the one studied here, energy is taken away from the inertial range and transferred towards small scales by the Kelvin wave cascade and vortex reconnections[9,41]. Furthermore, the velocity field diverges at the vortex core, and thus the definition of the dissipation field is delicate. Nevertheless, we can give a phenomenological interpretation of the dissipation by assuming that the system is well represented as a dilute point-vortex gas. Such a picture was recently used by Apolinário et al.[33] to model the velocity circulation in classical turbulence, and becomes particularly pertinent in quantum fluids. Although the superfluid is inviscid, one can model small-scale physics by some effective viscosity ν_{eff}[23,42], whose value is not important here. This approach allows us to directly estimate the coarse-grained

dissipation field by using its classical definition in terms of velocity gradients and a Dirac-like supported vorticity field (see Supplementary information). Given a disk of radius r crossed by n vortices, a straightforward calculation gives the estimate

$$\varepsilon_r \sim \frac{\nu_{\text{eff}} \kappa^2}{\xi^2} \frac{n}{A} = \frac{\nu_{\text{eff}} \kappa^2}{\xi^2} Z_A, \tag{6}$$

where ε_r is the average of the local dissipation rate $\varepsilon(\mathbf{x})$ over the disk, $A = \pi r^2$ is the disk area, ξ the typical vortex thickness and κ the quantum of circulation. The number of vortices per unit area $Z_A = n/A$ would then be the quantum analogous of the coarse-grained dissipation ε_r. Remarkably, and similarly to ε_r—which is known to exhibit log-normal statistics in classical turbulence[43]— the normalised PDFs of $\log(Z_A)$ almost collapse and are close to Gaussian in the bulk (Fig. 5c), reinforcing the pertinence of relation (6).

To make a stronger connection between classical and quantum turbulence, we recall that the classical coarse-grained energy dissipation rate is a highly fluctuating quantity that presents anomalous scaling laws traditionally denoted by $\langle \varepsilon_r^p \rangle \sim r^{\tau(p)}$. It follows from Eq. (6) that the number of vortices should satisfy

$$\langle n^p \rangle_A \sim r^{\alpha(p)} \sim A^{\alpha(p)/2}, \quad \text{with} \quad \alpha(p) = 2p + \tau(p). \tag{7}$$

Note that, because of homogeneity, $\tau(1) = 0$, which translates as $\langle n \rangle_A \sim A$ for the mean number of vortices. In the classical turbulence literature, there are several multifractal models for the anomalous exponents $\tau(p)$ that are able to reproduce experimental and numerical measurements[17]. Among those, the She–Lévêque model[44]

$$\tau_{\text{SL}}(p) = -2p/3 + (3 - D_\infty)\left[1 - \left(\frac{7/3 - D_\infty}{3 - D_\infty}\right)^p\right] \tag{8}$$

has one adjustable parameter D_∞ corresponding to the fractal dimension of the most singular structures of the system. In the original model, which closely matches existent turbulence measurements[35,44–46], these structures are assumed to be vortex filaments, hence $D_\infty = 1$. The combination of prediction (7) with the original She–Lévêque model, represented by the blue dashed lines in Fig. 5a, is in good agreement with our quantum turbulence data for sufficiently large A, although some deviations due to the limited scaling range may be present.

Classical turbulence and conditioned circulation. We now apply some of the previous ideas to classical turbulence. We perform a direct numerical simulation of the NS equations in a
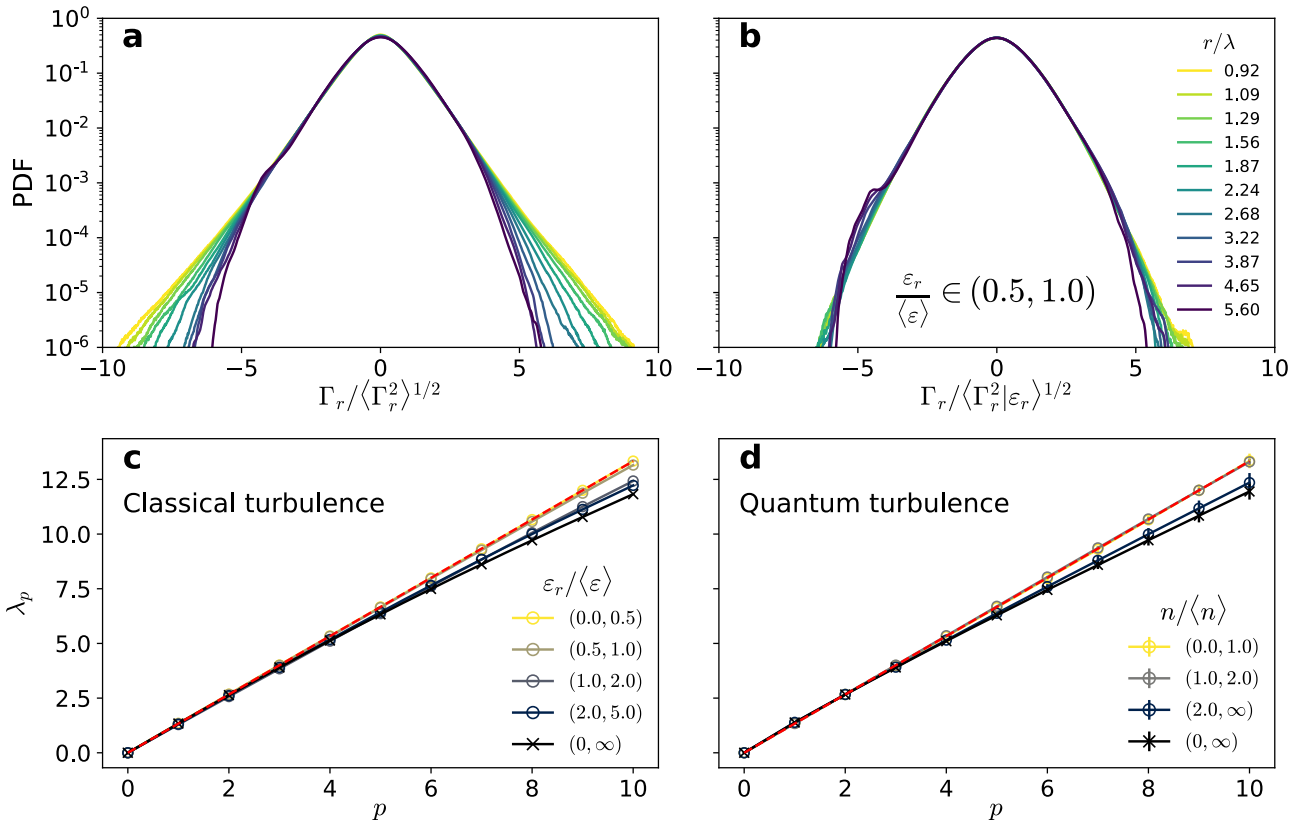
Fig. 6 Circulation intermittency and OK62 theory in classical and quantum turbulence. Top panels: PDFs of the circulation in classical turbulence as a function of the loop size r. **a** Unconditioned PDFs. **b** PDFs conditioned on low values of the local coarse-grained dissipation, $\varepsilon_r/\langle\varepsilon\rangle \in [0.5, 1]$. The different colours correspond to different loop sizes within the inertial range. **c, d** Scaling exponents of the circulation moments in (**c**) classical and (**d**) quantum turbulence. Different colours indicate a conditioning (**c**) on the local dissipation and (**d**) on the number of vortices within each loop. The unconditioned exponents are shown with black crosses. The Kolmogorov self-similar scaling is shown as reference (red dashed line). Error bars indicate 95% confidence intervals.

statistically steady state at a Taylor-based Reynolds number of $\mathrm{Re}_\lambda = 510$. The simulation is performed using 2048^3 collocation points. We then compute the velocity circulation over planar square loops of area $A = r^2$, and, following the framework of the OK62 refined similarity hypothesis, we condition its statistics on the coarse-grained dissipation field ε_r. The latter is obtained by averaging the local dissipation ε over the interior of each loop. See "Methods" for details on the numerical simulations and the data analysis.

We first consider the unconditioned velocity circulation PDFs, shown in Fig. 6a. The PDFs display heavy tails (associated with intermittency) which depend on the considered scale r/λ, with λ the Taylor micro-scale. This is consistent with the classical turbulence simulations of Iyer et al.[28,47]. The PDF tails are strongly suppressed when the statistics is conditioned on low values of the local coarse-grained dissipation, $\varepsilon_r/\langle\varepsilon\rangle \in [0.5, 1]$, as seen in Fig. 6b. The suppression of intermittency is also manifest in Fig. 6c, where the scaling exponents of circulation are displayed after conditioning on different intervals of ε_r. With no conditioning (black crosses), the scaling exponents match those of Iyer et al.[28], whereas when conditioning on low values of ε_r the K41 self-similar scaling is recovered.

Note that the above conditioning is slightly different from the one presented in Fig. 3, as here we are conditioning both on the loop area A and on the value of ε_r within such loops. In the case of quantum turbulence, the equivalent would be to study $\langle\Gamma^p|n\rangle_A$, i.e. to consider only loops of area A having n vortices. Such a double

conditioning is very restrictive, as it requires a very large amount of statistics. Nevertheless, we perform a similar analysis, considering loops having a low, average and high number of vortices relative to the mean. The respective scaling exponents are displayed in Fig. 6d. We find that, for loops with low and average number of vortices, the self-similar K41 scaling is recovered, whereas for loops having large vortex concentrations the statistics is still intermittent. The lack of self-similarity in regions of high dissipation (in classical flows) or high vortex concentration (in quantum flows) hints at the idea that not all such events contribute equally to circulation statistics.

Can OK62 theory describe circulation intermittency? Considering the relation introduced in Eq. (6) and the fact that the number of vortices per unit area follows the same intermittent behaviour as ε_r, one could try to apply OK62 theory to relate scaling exponents of circulation λ_p with those of dissipation $\tau(p)$, as traditionally done for velocity increments. Within this reasoning, $\Gamma \sim \varepsilon_r^{1/3} r^{4/3}$, yielding a OK62-based relation $\lambda_p = 4p/3 + \tau(p/3)$. However, such a relation is in strong disagreement with our data (classical and quantum turbulence, see Supplementary information) and with early NS studies[48]. Nevertheless, this disagreement is not in contradiction with the fact that the anomalous scaling of the number of vortices is well described by standard multifractal dissipation models (see Fig. 5). Indeed, if one considers a vortex dipole (two vortices of same magnitude and opposite sign), their

contribution to large fluctuations of the local dissipation field and to velocity increments may be very important. On the other hand, for the circulation, the dipole contribution is exactly zero due to vortex cancellation. This fact suggests that not all extreme dissipation events result in extreme circulation values. In particular, intense circulation events would be correlated to those highly dissipative structures in turbulence which carry a strong vortex polarisation, such as vortex sheets or bundles (at scales $r \gg \ell$). Note that, in classical fluids, the idea of vortex filaments organising into groups forming vortex sheets is consistent with the recently proposed sublayers' vortex picture of dissipation[49].

The previous observations motivate us to introduce a modified OK62 theory for the circulation ("mOK62" in the following), where the most relevant singular structures are not vortex filaments but structures of higher fractal dimension. To check this idea, we adapt the She–Lévêque model $\tau_{SL}(p)$ (Eq. (8)) by setting $D_\infty = 2.2$ instead of 1. The chosen dimensionality exactly corresponds to the monofractal fit obtained by Iyer et al.[28] and Müller et al.[13] for the high-order circulation moments ($p > 3$) in classical and quantum turbulence, and, as suggested in the former work, it may be linked to the effect of wrinkled vortex sheets. Note that, for large p, our mOK62 model simplifies to $\lambda_p \approx \frac{10}{9}p + (3 - D_\infty)$, which is equivalent to the monofractal fit by Iyer et al.[28]. In Fig. 4, it is shown that the adapted model matches strikingly well the anomalous exponents of circulation both in the turbulent and in the disordered cases for $p > 3$ (dashed lines), while for $p < 3$ there are some deviations.

Our mOK62 model can be generalised to an arbitrary degree of polarisation, which is fully determined by the exponent $\gamma_1 \in [1/2, 1]$. Using dimensional analysis and reintroducing the fundamental quantum of circulation κ, we have $\Gamma \sim \varepsilon_r^{\gamma_1/2} r^{2\gamma_1} \kappa^{1-3\gamma_1/2}$, leading to $\lambda_p = 2p\gamma_1 + \tau(p\gamma_1/2)$. Accordingly, the conjecture stated in Eq. (5) would be fulfilled with $g(x) = 2x + \tau(x/2)$. We recall that K41 turbulence corresponds to $\gamma_1 = 2/3$, in which case the dependence on κ consistently disappears. This model also accurately reproduces disordered turbulence data (see Fig. 4), which corresponds to $\gamma_1 = 1/2$. In this case, $\lambda_p = p + \tau(p/4)$, and intermittency corrections thus vanish at $p = 4$ (instead of $p = 3$ in the turbulent case).

The previous results provide a possible interpretation for the difference between the intermittency of velocity fluctuations and of circulation, based on the different topologies of the dissipative structures contributing to extreme events. We shall notice that an alternative interpretation is also possible, based on the recent works by Apolinário et al.[33] and Moriconi[34]. In this framework, the circulation should scale as $\varepsilon_r^{1/2}$, instead of $\varepsilon_r^{1/3}$, namely $\Gamma \sim \varepsilon_r^{1/2} \nu_r^{-1/2} r^2$, where ν_r is Kraichnan's eddy viscosity[50]. The latter is found by assuming that the energy spectrum takes the form $E(k) \sim \varepsilon^{2/3} k^{-5/3+\alpha}$ (where α is an intermittency correction), yielding $\nu_r \sim r^{4/3+\alpha}$. Note that this phenomenological approach mixes a mean-field approximation for determining ν_r with the fluctuations arising from $\varepsilon_r^{1/2}$. Moreover, in its present form, it does not directly account for vortex cancellations. Nevertheless, when combined with the standard She–Lévêque model (with $D_\infty = 1$), this model provides an expression for the exponents λ_p as accurate as our mOK62 model in the turbulent case. There is certainly a need to pursuit further investigations to understand how both models differ and complement each other.

Discussion

In this work, we have attempted at providing an interpretation for the intermittent statistics of velocity circulation in turbulent flows. We have done so by viewing turbulent flows as a polarised tangle of discrete and thin vortex filaments, each carrying a constant circulation. While this view is a priori only appropriate in low-temperature quantum fluids, we expect it to be a very pertinent model of classical turbulence, considering the strong similarities recently unveiled between both systems[13].

By introducing and solving a simple toy model and by analysing data of GP quantum turbulence simulations, we have shown that, in discrete-vortex systems, the Kolmogorov self-similar scalings result from a partial polarisation of the vortices (in agreement with previous quantum turbulence studies), while the intermittency of circulation statistics is linked to the non-trivial (non-Poissonian) spatial distribution of vortices. In fact, within fluid patches of varying area A in the inertial range of scales, the number of vortices n is found to be the quantum equivalent of the coarse-grained dissipation ε_r in classical turbulence, as they both follow the approximately log-normal distribution first hypothesised by the celebrated Obukhov–Kolmogorov OK62 theory for ε_r[43]. Quantitatively, we show that the intermittency of n is well described by the She–Lévêque model for ε_r, confirming the strong equivalence between both observables.

It is important to remark that the quantum turbulence simulations presented in this work have been performed on periodic domains, and are based on the GP equation describing an ideal superfluid at very low temperature. In contrast, most superfluid turbulence experiments using liquid helium are performed in confined systems and at finite temperatures[18,19], in a regime that may be described by a two-fluid model[51]. Early experimental studies showed that the signature of intermittency on velocity increments is nearly independent of the temperature, matching observations in classical fluids[52–54]. These observations were later contradicted by a recent experimental investigation, which showed an enhancement of velocity intermittency in the two-fluid regime compared to classical turbulence[55], in agreement with previous numerical simulations of related models[56,57]. Compared to velocity increments, we expect the circulation to be a much more robust observable in quantum fluids, as it does not display singular behaviour in the vicinity of vortices[13]. For this reason, measuring the scaling properties of circulation in future experiments may help disambiguate existent contradictions, and provide a clearer answer on the intermittency of finite-temperature quantum turbulence. Recent experiments have made initial attempts at reconstructing Eulerian velocity fields from Lagrangian particle tracking measurements in turbulent superfluid helium[55]. Such a technique could be used in principle to measure the velocity circulation in superfluid helium, although addressing high-order statistics might still be challenging. However, note that such an approach is delicate because, due to the two-fluid nature of finite-temperature superfluid helium, particles may fail to capture important Eulerian flow features[58,59], and further work is needed to determine its suitability.

Finally, using data from NS and GP simulations, we have confirmed that the classical OK62 theory does not fully account for the intermittency of the circulation in classical and quantum turbulence. We have provided an explanation based on the presumed topology of the turbulent structures that most contribute to extreme circulation events. We have then proposed a modified OK62 description of circulation, where relevant singular structures have a fractal dimension $D_\infty \approx 2.2$ associated to vortex sheets[28]. This value differs from the dimensionality $D_\infty = 1$ of isolated vortex filaments, used in the modelling of velocity increment statistics[44]. Using this idea, we have shown that the intermittency of circulation is well reproduced by a modified version of the She–Lévêque model, bringing support to the vortex sheet interpretation first proposed by Iyer et al.[28]. All the previous ideas were additionally tested by introducing a disordered turbulence state, obtained by artificially suppressing vortex polarisation from a GP numerical simulation.

There are still some questions that remain open for future works. In particular, further investigation on the topology of relevant structures for the intermittency of circulation is required. We have argued that the smallest structures significant for circulation are vortex sheets, as simpler structures are irrelevant due to vortex cancellation. One way of approaching this topic is by use of cancellation exponents[60–62], method that exploits the fact that circulation can take either negative or positive values. An alternative approach, based on recent works by Apolinário et al.[33] and Moriconi[34], suggests that the most relevant singular structures for velocity circulation should still be vortex filaments. Further investigations on the fractal dimension of circulation would help develop more accurate models of intermittency.

Our findings hint at the existence of a coarse-grained quantity different from ε_r, which may better encapsulate the intermittency of circulation in classical turbulence in the spirit of an OK62-like theory. Furthermore, it may be appropriate to investigate the relevance of quantities, such as the local vorticity magnitude (or enstrophy) or the local strain. Such coarse-grained quantity would be expected to display intermittent statistics with extreme values associated to the presence of quasi-two-dimensional structures such as vortex sheets.

More generally, our present results reinforce the strong equivalence between classical and quantum turbulence, and constitute an attempt at providing an explicit connection between the intermittency of both systems. We expect such a connection to provide a possible path to a simplified description of the intermittency of classical turbulence, a highly challenging topic from a modelling standpoint, yet extremely relevant to the understanding of fluid flows occurring in the Nature.

Methods

Numerical simulations. We study the dynamics of quantum turbulence in the framework of a generalised GP model

$$i\hbar \frac{\partial \psi}{\partial t} = -\frac{\hbar}{2m}\nabla^2\psi - \mu(1+\chi)\psi + g\left(\int V_1(\mathbf{x}-\mathbf{y})\,|\psi(\mathbf{y})|^2\;d^3y\right)\psi + g\chi\frac{|\psi|^{2(1+\gamma)}}{n_0^\gamma}\psi, \quad (9)$$

where ψ is the condensate wave function describing the dynamics of a compressible superfluid at zero temperature. Here, m is the mass of the bosons, μ is the chemical potential, n_0 the particle density and $g = 4\pi\hbar^2 a_s/m$ is the coupling constant proportional to the s-wave scattering length. The dimensionless parameters χ and γ correspond to the amplitude and order of beyond mean field corrections. The non-local interaction between bosons is given by the potential $V_1(\mathbf{x}-\mathbf{y})$ which is chosen, together with χ and γ, to reproduce the roton minimum in the excitation spectrum and the equation of state of superfluid helium. Details on the chosen parameters can be found in Ref. [22]. The use of a standard or a generalised GP model does not affect the statistics of velocity circulation[13].

The hydrodynamic interpretation of Eq. (9) stems from the Madelung transformation $\psi = \sqrt{\rho/m}e^{im\phi/\hbar}$, where ρ is the local density and ϕ the phase of the complex wave function. The velocity field is then given by $\mathbf{v} = \nabla\phi$. Note that ϕ is not defined at the locations where ψ vanishes, which implies that the velocity field is singular along quantum vortices[63].

The generalised GP equation (9) is solved in a three-dimensional periodic cube by direct numerical simulations using the Fourier pseudospectral code FROST, with an explicit fourth-order Runge–Kutta method for the time integration[22]. The quantum turbulent regime is studied in a freely decaying Arnold–Beltrami–Childress (ABC) flow[13,21] with 2048^3 collocation points. To reduce acoustic emissions, the initial condition is prepared using a minimisation process[20]. The box has a size $L = 1365\xi$ and the inter-vortex distance is $\ell \approx 28\xi$, with ξ the healing length.

We also perform direct numerical simulations of the incompressible NS equations

$$\frac{\partial \mathbf{v}}{\partial t} + \mathbf{v} \cdot \nabla\mathbf{v} = -\nabla p + \nu\nabla^2\mathbf{v} + \mathbf{f}, \quad (10)$$

$$\nabla \cdot \mathbf{v} = 0, \quad (11)$$

using the Fourier pseudospectral code LaTu[64] in a periodic cubic domain. The temporal advancement is performed with a third-order Runge-Kutta scheme.

Above, p is the pressure field, ν the fluid kinematic viscosity and $\mathbf{f}$ an external forcing stirring the fluid. The latter acts at large scales within a spherical shell of radius $|\mathbf{k}| \leq 2$ in Fourier space. The turbulent regime is studied once the simulation reaches a statistically steady state. The simulation is performed using 2048^3 collocation points at a Taylor-based Reynolds number of $\mathrm{Re}_\lambda = 510$.

Evaluation of circulation and coarse-grained dissipation. To obtain the circulation from GP and NS simulation data, we take advantage of the spectral nature of both solvers, and compute the circulation from the Fourier coefficients of the velocity fields. Namely, over a given L-periodic 2D cut of the physical domain, we write the circulation over a square loop of side r, centred at a point $\mathbf{x} = (x, y)$, as the convolution

$$\Gamma_r(\mathbf{x}) = \int_{B_r(\mathbf{x})} \omega(\mathbf{x}')\,d^2\mathbf{x}' = \iint_{[0,L]^2} H_r(\mathbf{x}-\mathbf{x}')\,\omega(\mathbf{x}')\,d^2\mathbf{x}', \quad (12)$$

where $\omega = (\nabla_{2D} \times \mathbf{v}) \cdot \hat{\mathbf{z}}$ is the out-of-plane vorticity field and $B_r(\mathbf{x})$ is a square of side r centred at $\mathbf{x}$. The convolution kernel can be written as the product of two rectangular functions, $H_r(\mathbf{x}) = \Pi(x/r)\,\Pi(y/r)$, where $\Pi(x) = 1$ for $|x| < \frac{1}{2}$ and 0 otherwise. Note that we have used Stokes' theorem to recast the contour integral (1) as a surface integral of vorticity. The convolution in Eq. (12) can be efficiently computed in Fourier space using the Fourier transform of the rectangular kernel, which may be written in terms of the normalised sinc function as $\hat{H}_r(k_x, k_y) = (r/L)^2\mathrm{sinc}\,(k_x r/2\pi)\,\mathrm{sinc}\,(k_y r/2\pi)$.

As mentioned earlier, the GP velocity field diverges at vortex locations. To minimise the numerical errors resulting from such singularities, we first resample each two-dimensional cut of the GP wave function field $\psi(\mathbf{x})$ into a very fine grid of resolution 32768^2, using Fourier interpolation. The velocity field is then evaluated in physical space using the Madelung transformation. This resampling procedure is described in more detail in Ref. [13].

In NS simulations, the above algorithm is also applied to compute the coarse-grained dissipation $\varepsilon_r(\mathbf{x})$ over squares of side r. Instead of the vorticity, the convoluted quantity is in this case the dissipation field $\varepsilon(\mathbf{x}) = 2\nu s_{ij}s_{ij}$, where $\mathbf{s}(\mathbf{x}) = [\nabla\mathbf{v} + (\nabla\mathbf{v})^T]/2$ is the three-dimensional strain-rate tensor.

Vortex detection from GP simulations. For a given two-dimensional cut of a GP velocity field, we identify the signs and locations of the quantum vortices crossing the cut as follows. First, the circulation is computed on a discrete grid following the procedure described above, taking small square loops of side $r \sim \xi \ll \ell$. The result is a discrete circulation field, where each circulation value is either zero if no vortex crosses the small loop centred at that position, or $\pm\kappa$ if a single vortex crosses it. For very small loop sizes, the former case is much more likely than the latter. As a result, the vortex distribution can be sparsely described by storing the locations and signs of the non-zero circulation values. By repeating this procedure over different cuts of the simulation, one can reconstruct the three-dimensional vortex structure, as visualised in Fig. 1.

Energy spectrum computation from discrete vortices. For each two-dimensional cut, once the positions $\mathbf{r}_i$ and the signs s_i of each vortex crossing the plane are determined, we first compute a regularised two-dimensional vorticity field $\omega(\mathbf{r}) = \kappa \sum_{i=1}^N s_i \delta_\eta(\mathbf{r} - \mathbf{r}_i)$, where N is the number of vortices on the 2D cut. Here, $\delta_\eta(\mathbf{r}) = \exp(-|\mathbf{r}|^2/2\eta^2)/2\pi\eta^2$, and η is the scale of the regularisation (we have used $\eta = \xi$ in Fig. 2). Then, the energy spectra are computed by noting that $|\hat{\mathbf{v}}(\mathbf{k})|^2 = |\hat{\omega}(\mathbf{k})|^2/|\mathbf{k}|^2$, where $\hat{\mathbf{v}}$ and $\hat{\omega}$ are the Fourier transforms at the wavevector $\mathbf{k}$ of the velocity field and of ω, respectively. Finally, by averaging over all 2D cuts and integrating over a shell $|\mathbf{k}| = k$, the energy spectrum reads

$$E(k) = \frac{\kappa^2 |\hat{\delta}_\eta(k)|^2}{2k} \int \left\langle \sum_{i,j} s_i s_j e^{i\mathbf{k}\cdot(\mathbf{r}_i - \mathbf{r}_j)} \right\rangle d\Omega, \quad (13)$$

where the integral is performed over all angles Ω. Note that the large-wavenumber range in Fig. 2 is determined by the regularised Dirac function δ_η and has no physical meaning.

For disordered turbulence, as there is no correlation between the signs and the vortex positions, it is easy to show that $\left\langle \sum_{i,j} s_i s_j e^{i\mathbf{k}\cdot(\mathbf{r}_i - \mathbf{r}_j)} \right\rangle = \langle N \rangle$, from where it follows $E(k) \sim k^{-1}$.

Data availability

Processed data used in the other figures are available from the corresponding authors upon request. Source data are provided with this paper.

Code availability

Code used to process solution fields from GP and NS simulations is openly available at https://github.com/jipolanco/Circulation.jl and on Zenodo[65], along with detailed installation instructions and a complete set of examples. The software is licensed under the open-source Mozilla Public License 2.0.

References

1. Kida, S. & Takaoka, M. Vortex reconnection. *Annu. Rev. Fluid Mech.* **26**, 169 (1994).
2. Jiménez, J., Wray, A. A., Saffman, P. G. & Rogallo, R. S. The structure of intense vorticity in isotropic turbulence. *J. Fluid Mech.* **255**, 65 (1993).
3. Barenghi, C. F., Skrbek, L. & Sreenivasan, K. R. Introduction to quantum turbulence. *Proc. Natl Acad. Sci. USA* **111**, 4647 (2014a).
4. Feynman, R. P. Application of quantum mechanics to liquid helium. In *Progress in Low Temperature Physics*, Vol. 1 (ed. Gorter, C. J.) 17–53 (Elsevier, 1955).
5. Koplik, J. & Levine, H. Vortex reconnection in superfluid helium. *Phys. Rev. Lett.* **71**, 1375 (1993).
6. Bewley, G. P., Lathrop, D. P. & Sreenivasan, K. R. Visualization of quantized vortices. *Nature* **441**, 588 (2006).
7. Serafini, S. et al. Vortex reconnections and rebounds in trapped atomic Bose-Einstein condensates. *Phys. Rev. X* **7**, 021031 (2017).
8. Villois, A., Proment, D. & Krstulovic, G. Universal and nonuniversal aspects of vortex reconnections in superfluids. *Phys. Rev. Fluids* **2**, 044701 (2017).
9. Galantucci, L., Baggaley, A. W., Parker, N. G. & Barenghi, C. F. Crossover from interaction to driven regimes in quantum vortex reconnections. *Proc. Natl Acad. Sci. USA* **116**, 12204 (2019).
10. Švančara, P. & La Mantia, M. Flight-crash events in superfluid turbulence. *J. Fluid Mech.* **876**, R2 (2019).
11. Villois, A., Proment, D. & Krstulovic, G. Irreversible dynamics of vortex reconnections in quantum fluids. *Phys. Rev. Lett.* **125**, 164501 (2020).
12. Schwarz, K. W. Three-dimensional vortex dynamics in superfluid ^{4}He: homogeneous superfluid turbulence. *Phys. Rev. B* **38**, 2398 (1988).
13. Müller, N. P., Polanco, J. I. & Krstulovic, G. Intermittency of velocity circulation in quantum turbulence. *Phys. Rev. X* **11**, 011053 (2021).
14. Barenghi, C. F., L'vov, V. S. & Roche, P.-E. Experimental, numerical, and analytical velocity spectra in turbulent quantum fluid. *Proc. Natl Acad. Sci. USA* **111**, 4683 (2014b).
15. Boué, L. et al. Exact solution for the energy spectrum of Kelvin-wave turbulence in superfluids. *Phys. Rev. B* **84**, 064516 (2011).
16. Krstulovic, G. Kelvin-wave cascade and dissipation in low-temperature superfluid vortices. *Phys. Rev. E* **86**, 055301 (2012).
17. Frisch, U. *Turbulence: The Legacy of A.N. Kolmogorov* 1st edn (Cambridge University Press, 1995).
18. Maurer, J. & Tabeling, P. Local investigation of superfluid turbulence. *Europhys. Lett.* **43**, 29 (1998).
19. Salort, J., Chabaud, B., Lévêque, E. & Roche, P.-E. Investigation of intermittency in superfluid turbulence. *J. Phys. Conf. Ser.* **318**, 042014 (2011).
20. Nore, C., Abid, M. & Brachet, M. E. Decaying Kolmogorov turbulence in a model of superflow. *Phys. Fluids* **9**, 2644 (1997a).
21. Clark di Leoni, P., Mininni, P. D. & Brachet, M. E. Dual cascade and dissipation mechanisms in helical quantum turbulence. *Phys. Rev. A* **95**, 053636 (2017).
22. Müller, N. P. & Krstulovic, G. Kolmogorov and Kelvin wave cascades in a generalized model for quantum turbulence. *Phys. Rev. B* **102**, 134513 (2020).
23. Vinen, W. F. & Niemela, J. J. Quantum turbulence. *J. Low Temp. Phys.* **128**, 167 (2002).
24. L'vov, V. S., Nazarenko, S. V. & Rudenko, O. Bottleneck crossover between classical and quantum superfluid turbulence. *Phys. Rev. B* **76**, 024520 (2007).
25. Roche, P.-E. & Barenghi, C. F. Vortex spectrum in superfluid turbulence: interpretation of a recent experiment. *EPL (Europhys. Lett.)* **81**, 36002 (2008).
26. Baggaley, A. W., Laurie, J. & Barenghi, C. F. Vortex-density fluctuations, energy spectra, and vortical regions in superfluid turbulence. *Phys. Rev. Lett.* **109**, 205304 (2012).
27. Baggaley, A. W. The importance of vortex bundles in quantum turbulence at absolute zero. *Phys. Fluids* **24**, 055109 (2012).
28. Iyer, K. P., Sreenivasan, K. R. & Yeung, P. K. Circulation in high Reynolds number isotropic turbulence is a bifractal. *Phys. Rev. X* **9**, 041006 (2019).
29. Zybin, K. P. & Sirota, V. A. Vortex filament model and multifractal conjecture. *Phys. Rev. E* **85**, 056317 (2012).
30. Zybin, K. P. & Sirota, V. A. Multifractal structure of fully developed turbulence. *Phys. Rev. E* **88**, 043017 (2013).
31. Sreenivasan, K. R. & Yakhot, V. Dynamics of three-dimensional turbulence from Navier-Stokes equations. *Phys. Rev. Fluids* **6**, 104604 (2021).
32. Migdal, A. A. Loop equation and area law in turbulence. *Int. J. Mod. Phys. A* **09**, 1197 (1994).
33. Apolinário, G. B., Moriconi, L., Pereira, R. M. & Valadão, V. J. Vortex gas modeling of turbulent circulation statistics. *Phys. Rev. E* **102**, 041102(R) (2020).
34. Moriconi, L. Multifractality breaking from bounded random measures. *Phys. Rev. E* **103**, 062137 (2021).
35. Benzi, R. et al. Extended self-similarity in turbulent flows. *Phys. Rev. E* **48**, R29 (1993).
36. Oboukhov, A. M. Some specific features of atmospheric tubulence. *J. Fluid Mech.* **13**, 77 (1962).
37. Kolmogorov, A. N. A refinement of previous hypotheses concerning the local structure of turbulence in a viscous incompressible fluid at high Reynolds number. *J. Fluid Mech.* **13**, 82 (1962).
38. Gagne, Y., Marchand, M. & Castaing, B. Conditional velocity pdf in 3-D turbulence. *J. Phys. II Fr.* **4**, 1 (1994).
39. Naert, A., Castaing, B., Chabaud, B., Hébral, B. & Peinke, J. Conditional statistics of velocity fluctuations in turbulence. *Phys. D.* **113**, 73 (1998).
40. Homann, H., Schulz, D. & Grauer, R. Conditional Eulerian and Lagrangian velocity increment statistics of fully developed turbulent flow. *Phys. Fluids* **23**, 055102 (2011).
41. Fonda, E., Meichle, D. P., Ouellette, N. T., Hormoz, S. & Lathrop, D. P. Direct observation of Kelvin waves excited by quantized vortex reconnection. *Proc. Natl Acad. Sci. USA* **111**, 4707 (2014).
42. Boué, L. et al. Energy and vorticity spectra in turbulent superfluid ^{4}He from $T = 0$ to T_λ. *Phys. Rev. B* **91**, 144501 (2015).
43. Dubrulle, B. Beyond Kolmogorov cascades. *J. Fluid Mech.* **867**, P1 (2019).
44. She, Z.-S. & Lévêque, E. Universal scaling laws in fully developed turbulence. *Phys. Rev. Lett.* **72**, 336 (1994).
45. Anselmet, F., Gagne, Y., Hopfinger, E. J. & Antonia, R. A. High-order velocity structure functions in turbulent shear flows. *J. Fluid Mech.* **140**, 63 (1984).
46. Boffetta, G., Mazzino, A. & Vulpiani, A. Twenty-five years of multifractals in fully developed turbulence: a tribute to Giovanni Paladin. *J. Phys. A* **41**, 363001 (2008).
47. Iyer, K. P., Bharadwaj, S. S. & Sreenivasan, K. R. The area rule for circulation in three-dimensional turbulence. *Proc. Natl Acad. Sci. USA* **118**, e2114679118 (2021).
48. Cao, N., Chen, S. & Sreenivasan, K. R. Properties of velocity circulation in three-dimensional turbulence. *Phys. Rev. Lett.* **76**, 616 (1996).
49. Elsinga, G. E., Ishihara, T. & Hunt, J. C. R. Extreme dissipation and intermittency in turbulence at very high Reynolds numbers. *Proc. R. Soc. A* **476**, 20200591 (2020).
50. Kraichnan, R. H. Eddy viscosity in two and three dimensions. *J. Atmos. Sci.* **33**, 1521 (1976).
51. Donnelly, R. J. The two-fluid theory and second sound in liquid helium. *Phys. Today* **62**, 34 (2009).
52. La Mantia, M. & Skrbek, L. Quantum turbulence visualized by particle dynamics. *Phys. Rev. B* **90**, 014519 (2014).
53. Švančara, P. & La Mantia, M. Flows of liquid ^{4}He due to oscillating grids. *J. Fluid Mech.* **832**, 578 (2017).
54. Rusaouen, E., Chabaud, B., Salort, J. & Roche, P.-E. Intermittency of quantum turbulence with superfluid fractions from 0% to 96%. *Phys. Fluids* **29**, 105108 (2017).
55. Tang, Y., Bao, S., Kanai, T. & Guo, W. Statistical properties of homogeneous and isotropic turbulence in He II measured via particle tracking velocimetry. *Phys. Rev. Fluids* **5**, 084602 (2020).
56. Boué, L., L'vov, V., Pomyalov, A. & Procaccia, I. Enhancement of intermittency in superfluid turbulence. *Phys. Rev. Lett.* **110**, 014502 (2013).
57. Biferale, L. et al. Turbulent statistics and intermittency enhancement in coflowing superfluid He 4. *Phys. Rev. Fluids* **3**, 024605 (2018).
58. Duda, D., La Mantia, M., Rotter, M. & Skrbek, L. On the visualization of thermal counterflow of He II past a circular cylinder. *J. Low Temp. Phys.* **175**, 331 (2014).
59. Outrata, O. et al. On the determination of vortex ring vorticity using Lagrangian particles. *J. Fluid Mech.* **924**, A44 (2021).
60. Ott, E., Du, Y., Sreenivasan, K. R., Juneja, A. & Suri, A. K. Sign-singular measures: fast magnetic dynamos, and high-Reynolds-number fluid turbulence. *Phys. Rev. Lett.* **69**, 2654 (1992).
61. Imazio, P. R. & Mininni, P. D. Cancellation exponents in helical and non-helical flows. *J. Fluid Mech.* **651**, 241 (2010).
62. Zhai, X. M., Sreenivasan, K. R. & Yeung, P. K. Cancellation exponents in isotropic turbulence and magnetohydrodynamic turbulence. *Phys. Rev. E* **99**, 023102 (2019).
63. Nore, C., Abid, M. & Brachet, M. E. Kolmogorov turbulence in low-temperature superflows. *Phys. Rev. Lett.* **78**, 3896 (1997b).
64. Homann, H., Kamps, O., Friedrich, R. & Grauer, R. Bridging from Eulerian to Lagrangian statistics in 3D hydro- and magnetohydrodynamic turbulent flows. *N. J. Phys.* **11**, 073020 (2009).

65. Polanco, J. I., Müller, N. P. & Krstulovic, G. Circulation.jl: tools for computing velocity circulation statistics from periodic 3D Navier–Stokes and Gross–Pitaevskii fields. Zenodo https://doi.org/10.5281/zenodo.5578953 (2021).

Author contributions
Navier–Stokes and Gross–Pitaevskii simulations were performed by J.I.P. and N.P.M., respectively. J.I.P. and N.P.M. post-processed data. J.I.P., N.P.M. and G.K. equally contributed to theoretical developments and writing the paper.

Competing interests
The authors declare no competing interests.

Additional information
Supplementary information The online version contains supplementary material available at https://doi.org/10.1038/s41467-021-27382-6.

Correspondence and requests for materials should be addressed to Juan Ignacio Polanco, Nicolás P. Müller or Giorgio Krstulovic.

Peer review information *Nature Communication* thanks the anonymous reviewers for their contribution to the peer review of this work. Peer reviewer reports are available.

Reprints and permission information is available at http://www.nature.com/reprints

Publisher's note Springer Nature remains neutral with regard to jurisdictional claims in published maps and institutional affiliations.

Supplementary Information for Vortex clustering, polarisation and circulation intermittency in quantum turbulence

Juan Ignacio Polanco,[1,2] Nicolás P. Müller,[1] and Giorgio Krstulovic[1]

[1]*Université Côte d'Azur, Observatoire de la Côte d'Azur, CNRS, Laboratoire Lagrange, Boulevard de l'Observatoire CS 34229 - F 06304 NICE Cedex 4, France*

[2]*Univ Lyon, CNRS, École Centrale de Lyon, INSA Lyon, Univ Claude Bernard Lyon 1, LMFA, UMR5509, 69130 Écully, France*

(Dated: November 2, 2021)

I.   TOY MODEL FOR VORTEX TANGLE POLARISATION AND CIRCULATION

In the main text, we have introduced a simple spin-like toy model for vortex polarisation based on a biased random walk. This model leads to different scaling laws for the circulation moments, which include Kolmogorov's 1941 theory (K41). We provide here more details on the analytical calculations.

The circulation of a loop enclosing n vortices is by definition

$$\Gamma_n = \sum_{i=1}^{n} s_i, \tag{1}$$

where $s_i = \pm 1$ is the polarization of the i-th vortex. As we have seen in the main text, the area A of the loop and the number of vortices can be related on average as $\langle n \rangle = A/\ell^2$, with ℓ the mean inter-vortex distance.

The model is defined as follows. The signs of the set of vortices $\{s_i\}_{i=1}^{n}$ are chosen inductively in a random manner:

- $n = 1$: the sign of the first vortex, s_1, is chosen randomly with equal probabilities;

- $n > 1$: after computing the circulation Γ_n at step n, the sign of vortex $n+1$ is set to $s_{n+1} = 1$ with probability $\frac{1}{2} + \frac{1}{2} f\left[\frac{\Gamma_n}{n}\right]$, and $s_{n+1} = -1$ with probability $\frac{1}{2} - \frac{1}{2} f\left[\frac{\Gamma_n}{n}\right]$.

In order to ensure that the probabilities of the vortices are well defined, the function f must satisfy $-1 \leq f[z] \leq 1$ for $|z| \leq 1$. Furthermore, to favour polarisation, i.e. to make it more likely for vortex s_{n+1} to be positive (resp. negative) if $\Gamma_n > 0$ (resp. $\Gamma_n < 0$), an additional condition is $f[z] > 0$ for $z > 0$ and $f[z] < 0$ for $z < 0$. Finally, as negative and positive circulation states are equally possible, one should have that $f[-z] = -f[z]$, and thus it suffices for f to be an odd non-decreasing function of z. Besides these general constrains, f can be arbitrary.

Clearly, in this model, the signs of all vortices are mutually correlated, but the circulation as a function of n is a Markov processes as $\Gamma_{n+1} = \Gamma_n + s_{n+1}$.

We denote by $\mathcal{P}_n(\Gamma)$ the probability that $\Gamma_n = \Gamma$. The master equation for $\mathcal{P}_n(\Gamma)$ can be directly computed using conditional probabilities

$$\mathcal{P}_{n+1}(\Gamma) = \sum_{\sigma=-\infty}^{\sigma=\infty} \mathcal{P}_{n+1}(\Gamma | \Gamma_n = \sigma) \, \mathcal{P}_n(\sigma) \tag{2}$$

$$= \mathcal{P}_{n+1}(\Gamma | \Gamma_n = \Gamma - 1) \, \mathcal{P}_n(\Gamma - 1) + \mathcal{P}_{n+1}(\Gamma | \Gamma_n = \Gamma + 1) \, \mathcal{P}_n(\Gamma + 1). \tag{3}$$

The infinite sum is reduced because $\mathcal{P}_{n+1}(\Gamma | \Gamma_n = \sigma)$ is the transition probability to a state where $\Gamma_{n+1} = \Gamma$, knowing that at the step n the circulation was σ. As circulation can only increase or decrease by one as an extra vortex is added, only two terms are non-zero. By construction of the model, we have for instance that $\mathcal{P}_{n+1}(\Gamma | \Gamma_n = \Gamma - 1) = \frac{1}{2} + \frac{1}{2} f\left[\frac{\Gamma - 1}{n}\right]$ as one needs a positive vortex to increase the circulation from $\Gamma - 1$ to Γ. It follows that

$$\mathcal{P}_{n+1}(\Gamma) = \left(\frac{1}{2} + \frac{1}{2} f\left[\frac{\Gamma - 1}{n}\right]\right) \mathcal{P}_n(\Gamma - 1) + \left(\frac{1}{2} - \frac{1}{2} f\left[\frac{\Gamma + 1}{n}\right]\right) \mathcal{P}_n(\Gamma + 1). \tag{4}$$

Multiplying by Γ^2 and summing over Γ we directly obtain an equation for the variance $\langle \Gamma^2 \rangle_n$

$$\langle \Gamma^2 \rangle_{n+1} = \langle \Gamma^2 \rangle_n + 1 + 2 \left\langle \Gamma f\left[\frac{\Gamma}{n}\right]\right\rangle_n \tag{5}$$

In the simple case of a linear function $f[z] = \beta z$, one gets a closed recurrence equation that can be solved exactly. It is simpler to take the continuous limit in n, which leads directly to equation (3) of the main text. For a general function f, it is natural to assume that f can be developed in series as $f[z] = \sum_{i=0}^{\infty} f_{2i+1} z^{2i+1}$. It follows that

$$\frac{d\langle \Gamma^2 \rangle}{dn} = 1 + 2f_1 \frac{\langle \Gamma^2 \rangle}{n} + 2f_3 \frac{\langle \Gamma^4 \rangle}{n^3} + \dots \tag{6}$$

We will show in the following that all the terms in the series but the one proportional to f_1 are subleading when n is large.

We express the circulation moments as

$$\langle \Gamma^p \rangle_n \sim a_p n^{\gamma_p}. \tag{7}$$

Inserting this Ansatz in Eq. (6) we obtain

$$a_2 \gamma_2 = n^{1-\gamma_2} + 2f_1 a_2 + \dots + 2f_{2p-1} a_{2p} n^{\gamma_{2p} - 2p - \gamma_2 + 2} + \dots \tag{8}$$

Now, making use of Cauchy–Schwarz's inequality $\langle \Gamma^{2p} \rangle = \langle \Gamma^{2(p-1)} \Gamma^2 \rangle \leq \langle \Gamma^{2(p-1)} \rangle \langle \Gamma^2 \rangle$, we have the general result for the scaling exponents $\gamma_{2p} \leq \gamma_{2(p-1)} + \gamma_2 \leq \gamma_{2(p-2)} + 2\gamma_2 \leq \dots \leq p\gamma_2$, for $p \geq 1$. We thus obtain

$$\gamma_{2p} - 2p - \gamma_2 + 2 \leq p\gamma_2 - 2p - \gamma_2 + 2 = (\gamma_2 - 2)(p - 1) \leq 0, \tag{9}$$

since $\Gamma_n \leq n$ and thus $\gamma_2 \leq 2$. As a consequence, all the terms of the series but the first one are subleading. Now, if $\gamma_2 > 1$ then taking the limit of large n from Eq. (8) we have that $\gamma_2 = \min[2f_1, 2]$. On the other hand, if $\gamma_2 \leq 1$ or equivalently $f_1 < 1/2$, all the terms depending on f can be neglected and we obtain $\langle \Gamma^2 \rangle_n = n$, and thus $\gamma_2 = 1$.

For high-order moments, a similar analysis can be performed and yields at the leading order the equation

$$\frac{d\langle \Gamma^p \rangle}{dn} = 1 + pf_1 \frac{\langle \Gamma^p \rangle}{n} + \dots. \tag{10}$$

In summary, for our model we obtain the self-similar exponents

$$\gamma_p = p \min\{\max[1/2, f'(0)], 1\}. \tag{11}$$

Note that performing the Laplace transform of (4), one obtains a linear partial differential equation that can be solved using the method of characteristics.

II. COARSE-GRAINED LOCAL ENERGY DISSIPATION AND ENSTROPHY FOR A DILUTED POINT-VORTEX GAS

Let us consider a two-dimensional system of n point vortices, each one carrying a positive or a negative circulation $\Gamma_i = \kappa s_i$, and located at the position $\mathbf{r}^i = (x^i, y^i)$. The corresponding vorticity field is given by

$$\omega(\mathbf{r}) = \kappa \sum_{i=1}^{n} s_i \delta_\xi(\mathbf{r} - \mathbf{r}^i), \tag{12}$$

where δ_ξ is regularisation of the two-dimensional Dirac δ-function at the scale ξ. Physically, ξ corresponds to the vortex core size where superfluid density vanishes or the Kolmogorov dissipative length scale in the case of classical turbulence. We assume that the system is diluted, meaning that the distance between vortices is much larger than their vortex core size $d^{ij} = |\mathbf{r}^i - \mathbf{r}^j| \gg \xi$.

To illustrate the spirit of the calculations, it is convenient to compute first the coarse-grained enstrophy at the scale r. By definition, this quantity is given by

$$\Omega_r = \frac{1}{\pi r^2} \int_B \omega(\mathbf{r}')^2 d^2\mathbf{r}' = \frac{\kappa^2}{\pi r^2} \sum_{i,j=1}^{n} s_i s_j \int_B \delta_\xi(\mathbf{r}' - \mathbf{r}^i) \delta_\xi(\mathbf{r}' - \mathbf{r}^j) d^2\mathbf{r}', \tag{13}$$

where B is ball of radius r containing all the vortices. The integral is divergent when $\xi \to 0$ for $i = j$. Indeed, using for instance a Gaussian regularisation of the δ-function [1], we have $\int_B \delta_\xi(\mathbf{r}' - \mathbf{r}^i) \delta_\xi(\mathbf{r}' - \mathbf{r}^j) d^2\mathbf{r}' \approx \delta_{\sqrt{2}\xi}(\mathbf{r}^i - \mathbf{r}^j)$. As $d^{ij} \gg \xi$, the contribution of the integral vanishes for $i \neq j$, and therefore it behaves as $\sim \delta_{ij}/\xi^2$. Using this results, the coarse-grained enstrophy becomes

$$\Omega_r \approx \frac{\kappa^2}{\pi r^2} \sum_{i,j=1}^{n} s_i s_j \frac{\delta_{ij}}{4\pi \xi^2} = \frac{\kappa^2 n}{4\pi^2 \xi^2 r^2}. \tag{14}$$

Computing the coarse-grained energy dissipation field requires a bit more of work as one needs to use the gradient of the velocity field, but the same scaling with n and r will be obtained. The velocity field generated by the vortex i, evaluated at a distance $\Delta r_i = |\mathbf{r} - \mathbf{r}^i| \gg \xi$ is given by

$$\mathbf{v}^i(x, y) = \frac{\kappa s_i}{2\pi(\Delta r_i)^2}(y^i - y, x - x^i) \tag{15}$$

The total velocity field generated by n vortices is then $\mathbf{v}(x, y) = \sum_{i=1}^{n} \mathbf{v}^i(x, y)$.

The local dissipation of a viscous fluid is by definition

$$\varepsilon(\mathbf{x}) = \frac{\nu_{\text{eff}}}{2}\left(\frac{\partial v_i}{\partial x_j} + \frac{\partial v_j}{\partial x_i}\right)^2 = 2\nu_{\text{eff}}\left[(\partial_x v_x)^2 + (\partial_y v_y)^2 + \frac{1}{2}(\partial_x v_y + \partial_y v_x)^2\right], \tag{16}$$

with ν_{eff} an effective viscosity of the system that takes place at small scales. In the last equality we make explicit use that the system is two-dimensional. Using the velocity field given in Eq. (15), one obtains

$$\partial_x v_x^i = -\partial_y v_y^i = \frac{\kappa s_i n_x^i n_y^i}{\pi \Delta r_i^2} \tag{17}$$

$$\partial_x v_y^i + \partial_y v_x^i = \frac{\kappa s_i}{\pi \Delta r_i^2}\left[(n_y^i)^2 - (n_x^i)^2\right], \tag{18}$$

with $\mathbf{n}^i = (\mathbf{r} - \mathbf{r}^i)/\Delta r_i$. By replacing these expressions in Eq. (16), we obtain the local energy dissipation of a point-vortex system

$$\varepsilon(\mathbf{x}) = \nu_{\text{eff}}\left[4\left(\sum_i^n \frac{\kappa s_i n_x^i n_y^i}{\pi \Delta r_i^2}\right)^2 + \left(\sum_i^n \frac{\kappa s_i}{\pi \Delta r_i^2}\left[(n_y^i)^2 - (n_x^i)^2\right]\right)^2\right]. \tag{19}$$

The coarse-grained energy dissipation ε_r is defined by averaging $\varepsilon(\mathbf{x})$ on a disk B of radius r containing all the vortices

$$\varepsilon_r = \frac{1}{\pi r^2}\int_B \varepsilon(\mathbf{r}')d^2\mathbf{r}' = \frac{\nu_{\text{eff}}\kappa^2}{\pi^3 r^2}\sum_{i=1}^n\sum_{j=1}^n s_i s_j \int_{B\setminus\cup_{k=1}^n B(\mathbf{r}^k,\xi)} \frac{\left[(n_y^i)^2 - (n_x^i)^2\right]\left[(n_y^j)^2 - (n_x^j)^2\right] + 4n_x^i n_y^i n_x^j n_y^j}{|\mathbf{r} - \mathbf{r}^i|^2|\mathbf{r} - \mathbf{r}^j|^2}d^2\mathbf{r}, \tag{20}$$

where $B(\mathbf{r}^k, \xi)$ is a small ball of radius ξ around vortex $\mathbf{r}^k$ and we omitted primes on the integration variables to simplify notation. Those balls are excluded to avoid the divergences of point vortices and it is justified by the regularisation of the vorticity. As we will see, the integrals are dominated by such divergences.

For $i = j$, the integral is simpler and becomes

$$\int_{B\setminus\cup_{k=1}^n B(\mathbf{r}^k,\xi)} \frac{\left[(n_y^i)^2 - (n_x^i)^2\right]^2 + 4n_x^i n_y^i n_x^i n_y^i}{|\mathbf{r} - \mathbf{r}^i|^4}d^2\mathbf{r} \approx \int_{B\setminus B(\mathbf{r}^i,\xi)} \frac{d^2\mathbf{r}}{|\mathbf{r} - \mathbf{r}^i|^4} \sim \frac{2\pi}{\xi^2}, \tag{21}$$

where we have used that $n_x^2 + n_y^2 = 1$, assumed that $r \gg \xi$ and kept only the dominant contribution. For $i \neq j$, the divergence is milder as in the denominator it intervenes the distance between two vortices d^{ij}, which is assumed to be much larger than ξ for a diluted system. Such terms contribute with a divergence of order $\log(\xi)/(d^{ij})^2$.

Finally, using Eq. (20) and keeping only dominant terms, we obtain at distances much larger than the inter-vortex distance

$$\varepsilon_r \sim \frac{\nu_{\text{eff}}\kappa^2}{\pi^3 r^2}\sum_{i=1}^n s_i^2 \frac{2\pi}{\xi^2} = \frac{2\nu_{\text{eff}}\kappa^2}{\pi^2 \xi^2}\frac{n}{r^2} \sim \frac{\nu_{\text{eff}}\kappa^2 n}{\xi^2 \pi r^2}. \tag{22}$$

Note that in terms of scaling laws, we could have used Eq. (14) and $\varepsilon_r \sim \nu_{\text{eff}}\Omega_r$ to obtain the same result.

III. SUITABILITY OF OK62 THEORY FOR CIRCULATION SCALING EXPONENTS

The celebrated K41 theory for turbulence describes a self-similar behavior for the scaling exponents of the high-order moments of the velocity increments [2]. This theory can also be adapted to describe the scaling exponents of velocity circulation $\langle|\Gamma|^p\rangle \sim r^{\lambda_p}$, resulting in the scaling $\lambda_p^{K41} = 4p/3$. However, it was observed that the self-similar hypothesis breaks down
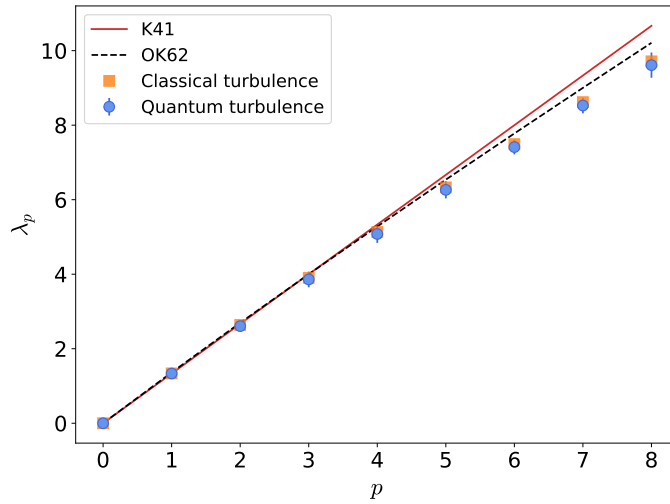
FIG. 1. Scaling exponents of the circulation moments defined as $\langle|\Gamma|^p\rangle \sim r^{\lambda_p}$ in numerical simulations of classical and quantum turbulence. As reference, the solid red line displays the Kolmogorov 1941 scaling $\lambda_p^{K41} = 4p/3$ and the dashed black line shows the OK62 scaling defined in (23) using the She–Lévêque model for the scaling of dissipation (24). Error bars indicate 95% confidence intervals.

generating deviations in the scaling exponents, in particular for high-order moments. It was later proposed by Obukhov and Kolmogorov in 1962 a refined similarity hypothesis [3, 4], that can also be applied to the circulation exponents as

$$\lambda_p^{OK62} = \frac{4p}{3} + \tau(p/3), \tag{23}$$

where $\tau(p)$ corresponds to the scaling exponents of the energy dissipation $\langle\epsilon^p\rangle_r \sim r^{\tau(p)}$. There are different models that describe the behavior of $\tau(p)$. In particular, in this work we use the She–Lévêque model [5]

$$\tau(p) = -\frac{2p}{3} + 2\left[1 - \left(\frac{2}{3}\right)^p\right], \tag{24}$$

that has no adjustable parameters.

Figure 1 shows the scaling exponents λ_p of the velocity circulation for moments up to order 8 obtained from numerical simulations of classical and quantum turbulence. Both numerical simulations were performed using 2048^3 collocation points, with a $Re_\lambda = 510$ in classical turbulence and a scale separation of $L/\xi = 1365$ in quantum turbulence. For high order moments, the scaling exponents deviate from both K41 and the refined OK62 models. These deviation were also observed in low-Reynolds numbers numerical simulations of the Navier–Stokes equation using the log-normal model for the scaling of dissipation [6].

[1] $\delta_\xi(\mathbf{r}) = \frac{1}{2\pi\xi^2} e^{-\frac{|\mathbf{r}|^2}{2\xi^2}}$.

[2] U. Frisch, *Turbulence: The Legacy of A.N. Kolmogorov*, 1st ed. (Cambridge University Press, 1995).

[3] A. M. Oboukhov, Some specific features of atmospheric tubulence, J. Fluid Mech. **13**, 77 (1962).

[4] A. N. Kolmogorov, A refinement of previous hypotheses concerning the local structure of turbulence in a viscous incompressible fluid at high Reynolds number, J. Fluid Mech. **13**, 82 (1962).

[5] Z.-S. She and E. Lévêque, Universal Scaling Laws in Fully Developed Turbulence, Phys. Rev. Lett. **72**, 336 (1994).

[6] N. Cao, S. Chen, and K. R. Sreenivasan, Properties of Velocity Circulation in Three-Dimensional Turbulence, Phys. Rev. Lett. **76**, 616 (1996).

4.3.1　Further comments on the Markovian model

In the previous section, we introduced a discrete model for velocity circulation that is able to describe Kolmogorov scaling for circulation moments assuming a partial polarization between vortices. In this model, the sign of all vortices are correlated, but the circulation Γ_n given by n quantum vortices follows a Markovian process that satisfies

$$P_{n+1}(\Gamma) = \frac{1}{2}\left[1 + f\left(\frac{\Gamma - 1}{n}\right)\right]P_n(\Gamma - 1) + \frac{1}{2}\left[1 - f\left(\frac{\Gamma + 1}{n}\right)\right]P_n(\Gamma + 1). \quad (4.12)$$

The function $f(z)$ can be any generic function that satisfies $f(z) > 0$ for $z > 0$, $f(z) < 0$ for $z < 0$, $f(-z) = -f(z)$ and $|f(z)| \leq 1$. In particular, in the remainder of this section, we will use the function $f(z) = \beta z$ with β a parameter that determines the circulation polarization. We will use this model to show how are vortices correlated, and to discuss the differences between the discrete and continuous models.

4.3.1.1　Correlation between vortices

Here, we show an exact solution for the correlation between two vortices obtained from this model.

We define the correlation function between a fixed and the nth vortex as

$$C_n = \langle s_1 s_n \rangle. \quad (4.13)$$

Using conditional probabilities, one can write the correlation as

$$
\begin{aligned}
C_{n+1} &= \sum_\Gamma \langle s_1 s_{n+1} | \Gamma_n = \Gamma, \Gamma_1 = +1 \rangle P(\Gamma_n = \Gamma, s_1 = +1) + \\
&\quad + \sum_\Gamma \langle s_1 s_{n+1} | \Gamma_n = \Gamma, \Gamma_1 = -1 \rangle P(\Gamma_n = \Gamma, s_1 = -1) = \\
&= \sum_\Gamma \langle s_{n+1} | \Gamma_n = \Gamma, \Gamma_1 = +1 \rangle P(\Gamma_n = \Gamma, s_1 = +1) - \\
&\quad - \sum_\Gamma \langle s_{n+1} | \Gamma_n = \Gamma, \Gamma_1 = -1 \rangle P(\Gamma_n = \Gamma, s_1 = -1),
\end{aligned} \quad (4.14)
$$

where we explicitly took the values $s_1 = \pm 1$, and $\Gamma_1 = s_1$. Using the Markovian property, one can reduce this expression to

$$C_{n+1} = \sum_\Gamma \langle s_{n+1} | \Gamma_n = \Gamma \rangle P_n^+(\Gamma)P(s_1 = 1) + \sum_\Gamma \langle s_{n+1} | \Gamma_n = \Gamma \rangle P_n^-(\Gamma)P(s_1 = -1), \quad (4.15)$$

with $P_n^\pm(\Gamma) = P(\Gamma_n = \Gamma | s_1 = \pm 1)$ to simplify the notation. Using the fact that the sign of the first vortex is $s_1 = \pm 1$ with probability $P(s_1 = \pm 1) = 1/2$, the correlation function reduces to

$$C_{n+1} = \frac{1}{2}\sum_\Gamma \langle s_{n+1} | \Gamma_n = \Gamma \rangle (P_n^+(\Gamma) - P_n^-(\Gamma)). \quad (4.16)$$

Following the model (4.12), the probability of $s_{n+1} = \pm 1$ given that $\Gamma_n = \Gamma$ is $(1 \pm \beta\Gamma/n)/2$. This leads to

$$C_{n+1} = \frac{1}{2} \sum_{\Gamma} \frac{1}{2} \left[\left(1 + \beta \frac{\Gamma}{n} \right) - \left(1 - \beta \frac{\Gamma}{n} \right) \right] (P_n^+(\Gamma) - P_n^-(\Gamma))$$

$$C_{n+1} = \frac{\beta}{2n} \sum_{\Gamma} \Gamma (P_n^+(\Gamma) - P_n^-(\Gamma)). \tag{4.17}$$

We can now use the master equation of the Markovian model for the circulation probability $P_n^\pm(\Gamma)$

$$P_n^\pm(\Gamma) = \frac{1}{2} \left(1 + \beta \frac{\Gamma - 1}{n - 1} \right) P_{n-1}^\pm(\Gamma - 1) + \frac{1}{2} \left(1 - \beta \frac{\Gamma + 1}{n - 1} \right) P_{n-1}^\pm(\Gamma + 1) \tag{4.18}$$

to obtain the following recurrence relation for the correlation function

$$C_{n+1} = \frac{\beta}{2n} \sum_{\Gamma} \Gamma \left(1 + \frac{\beta}{n - 1} \right) (P_{n-1}^+(\Gamma) - P_{n-1}^-(\Gamma))$$

$$\boxed{C_{n+1} = \frac{n - 1}{n} C_n + \frac{\beta}{n} C_n}, \quad \text{with} \quad C_0 = 1. \tag{4.19}$$

The recurrence relation (4.19) can be solved exactly, leading to

$$C_n = \begin{cases} \frac{\mathrm{Gamma}(\beta + n - 1)}{\mathrm{Gamma}(\beta)\mathrm{Gamma}(n - 1)} & \text{if } \beta \neq 0 \\ 1 & \text{if } \beta = 0 \end{cases} \tag{4.20}$$

where $\mathrm{Gamma}(z)$ is the gamma function. In the limit $n \gg 1$, it leads to the scaling

$$C_n \approx \frac{n^{\beta - 1}}{\mathrm{Gamma}(\beta)} \quad \text{for} \quad n \gg 1. \tag{4.21}$$

Note that the K41 value $\beta = 2/3$ leads to $C_n \sim n^{-1/3}$. We are not able to verify this relation in our numerical simulations as we do not count with enough vortex statistics to achieve good scaling properties.

4.3.1.2 Characteristic function for circulation

One way of determining the statistical properties of a random variable is by studying its characteristic function, defined as

$$\phi_n(\theta) = \langle e^{i\theta\Gamma} \rangle_n = \sum_\gamma e^{i\theta\gamma} P_n(\gamma), \tag{4.22}$$

where here the circulation Γ is a real-valued random variable. One of the main properties of this characteristic function is that the moments of the random variable are related with its derivatives as

$$\langle \Gamma^p \rangle_n = i^{-p} \left. \frac{\mathrm{d}^p \phi_n}{\mathrm{d}\theta^p} \right|_{\theta = 0}. \tag{4.23}$$

In this section, we will find an expression and study some of the properties of the characteristic function given by the discrete Markovian model.
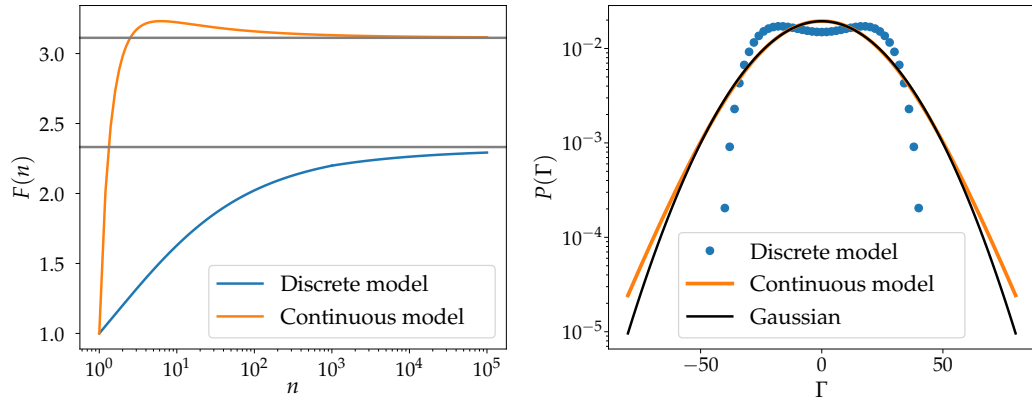
Figure 4.5: Left panel: Circulation flatness for the discrete Markovian model (blue line) and the continuous model (orange line). Right panel: Probability distributions of the discrete (blue) and continuous model (orange). A Gaussian distribution is shown as reference.

Replacing the probability distribution given by the model in Eq. (4.12) in the definition of the characteristic function (4.22), we obtain the following recursive expression (see Appendix B for details on the derivation)

$$\phi_{n+1}(\theta) = \cos\theta\,\phi_n(\theta) + \frac{\beta}{n}\sin\theta\frac{\partial\phi_n}{\partial\theta}, \tag{4.24}$$

Note that the initial condition is given by $\phi_1(\theta) = \cos\theta$. Using the property (4.23), one can easily obtain a recursion for the circulation moments of order p

$$\langle\Gamma^p\rangle_{n+1} = \frac{1}{2n}\sum_{k=0}^{p}\left[1+(-1)^{k+p}\right]\left[\beta\binom{p}{k-1}+n\binom{p}{k}\right]\langle\Gamma^k\rangle_n, \tag{4.25}$$

with $\binom{p}{k} = p!/(k!(p-k)!)$ the binomial coefficients. Note that this expression can also be obtained from the model (4.12) and that all moments satisfy $\langle\Gamma^p\rangle_1 = 1$. Equation (4.25) can be solved exactly for all orders. In particular, we will focus here on the flatness $F(n) = \langle\Gamma^4\rangle_n/\langle\Gamma^2\rangle_n^2$. The moments of order two and four are obtained from Eq. (4.25), which for $\beta = 2/3$ reduce to

$$\langle\Gamma^2\rangle_n = -3n + \frac{4\text{Gamma}(n+4/3)}{\text{Gamma}(n)\text{Gamma}(7/3)}, \tag{4.26}$$

$$\langle\Gamma^4\rangle_n = \frac{3}{5}n(34+45n)+ \tag{4.27}$$

$$+ \frac{8}{5\text{Gamma}(n)}\left[-\frac{5(10+9n)\text{Gamma}\left(n+\frac{4}{3}\right)}{\text{Gamma}(7/3)}+\frac{66\text{Gamma}\left(n+\frac{8}{3}\right)}{\text{Gamma}(11/3)}\right].$$

In the limit of a large number of vortices, the flatness can be written as

$$F(n) = 2.33196 + 1.19309n^{-1/3} + o(n^{-2/3}). \tag{4.28}$$

Figure 4.5 shows the flatness in this discrete model (blue solid line), which tends to the asymptotic value 2.33196 for $n \to \infty$.

In the limit of a large number of vortices, one can assume that the circulation and the number of vortices become continuous, and the moments of order two and four from Eq. (4.25) can be rewritten to satisfy

$$\frac{d\langle \Gamma^2 \rangle_n}{dn} = 1 + \frac{2\beta}{n}\langle \Gamma^2 \rangle_n, \tag{4.29}$$

$$\frac{d\langle \Gamma^4 \rangle_n}{dn} = 1 + 6\langle \Gamma^2 \rangle_n + \frac{4\beta}{n}\langle \Gamma^2 \rangle_n + \frac{4\beta}{n}\langle \Gamma^4 \rangle_n. \tag{4.30}$$

Solving these partial differential equations with $\beta = 2/3$ lead to the flatness in the continuous model

$$F(n) = \frac{249}{80} + \frac{27}{160n^{1/3}} + o(n^{-2/3}), \tag{4.31}$$

which is shown in Fig. 4.5 (orange solid line). The discrete and continuous flatness differ for all n. One of the possible reasons of this discrepancy is that in the discrete model the circulation is bounded by the total number of vortices, while in the continuous model it is not bounded as circulation can take any real value, leading to heavier tails in the probability distribution and larger values of the flatness.

The characteristic function can also be used to obtain the probability distribution of circulation, which is defined as

$$P_n(\Gamma) = \frac{1}{2\pi} \int_0^{2\pi} \phi_n(\theta) e^{-i\theta\Gamma} d\theta. \tag{4.32}$$

In the continuous model, the characteristic function is obtained by solving the partial differential equation

$$\frac{\partial \phi_n}{\partial n} = (\cos\theta - 1)\phi_n(\theta) + \frac{\beta}{n}\sin\theta\frac{\partial \phi_n}{\partial\theta}, \tag{4.33}$$

which admits an exact solution. The PDFs obtained from the discrete and continuous models for $\beta = 2/3$ are shown in Fig. 4.5. As discussed before, in the discrete model the circulation is bounded by the maximum number of vortices, while in the continuous model it is not. Moreover, the PDF in the discrete model shows a bimodal behavior due to the partial polarization in the system. Note that this bimodal behavior is not observed in the PDFs obtained from the numerical simulations reported in publications [MPK21; PMK21], although they approach better the one obtained from the continuous model which is closer to Gaussian.

4.3.1.3 Stochastic model for circulation

In the discrete Markovian model, the circulation given by $n + 1$ vortices is

$$\Gamma_{n+1} = \Gamma_n + s_{n+1}, \tag{4.34}$$

with $s_{n+1} = \pm 1$ the value of circulation of the $n + 1$ vortex. In classical fluids, the circulation around vortices can take any continuous value, in the sense that

$$d\Gamma_n = s_{n+1}. \tag{4.35}$$

Let us assume now that Γ_n is a stochastic process with n and Γ taking any continuous value. Its evolution will be governed by the noise s_{n+1} that has a given drift $\mu(\Gamma, n)$ and variance $\sigma^2(\Gamma, n)$. Motivated by the discrete model, these quantities can be taken as

$$\mu(\Gamma, n) = \langle s_{n+1} \rangle = \frac{1}{2}\left[1 + f\left(\frac{\Gamma}{n}\right)\right] - \frac{1}{2}\left[1 - f\left(\frac{\Gamma}{n}\right)\right] = f\left(\frac{\Gamma}{n}\right), \tag{4.36}$$

$$\sigma^2(\Gamma, n) = \langle s_{n+1}^2 \rangle - \langle s_{n+1} \rangle^2 = 1 - f^2\left(\frac{\Gamma}{n}\right). \tag{4.37}$$

Note that the function f must satisfy $|f(z)| \leq 1$ as the variance takes positive values. Based on these observations, we propose to express the circulation as a stochastic Itô process that follows the stochastic differential equation

$$\frac{d\Gamma}{dn} = f\left(\frac{\Gamma}{n}\right) + \sqrt{1 - f^2\left(\frac{\Gamma}{n}\right)}\,\xi(n), \tag{4.38}$$

where $\xi(n)$ is a white noise that satisfies $\langle \xi(n)\xi(n') \rangle = \delta(n - n')$. To simplify, we choose the function $f(z) = \beta z$ with β the polarization parameter. The circulation moments of order p are determined by the differential equation

$$\frac{d\langle \Gamma^p \rangle}{dn} = \frac{p\beta}{n}\langle \Gamma^p \rangle + \frac{p(p-1)}{2}\langle \Gamma^{p-2} \rangle + \frac{\beta^2 p(p-1)}{2n^2}\langle \Gamma^p \rangle \tag{4.39}$$

In particular, the variance in the limit of large n leads to

$$\frac{d\langle \Gamma^2 \rangle}{dn} = 1 + \frac{2\beta}{n}\langle \Gamma^2 \rangle \tag{4.40}$$

which coincides with the variance in the continuous model given by Eq. (4.29). For high order moments, the same scaling $\langle \Gamma^p \rangle \sim n^{\gamma_p}$ is recovered, with

$$\gamma_p = \begin{cases} \beta p & \text{if} \quad 1/2 \leq \beta \leq 1 \\[2mm] \beta/2 & \text{if} \quad \beta \leq 1/2 \end{cases} \tag{4.41}$$

We perform some numerical analysis on this model for different values of β. The moments of circulation are shown in Fig. 4.6. In particular, the scaling in Eq. (4.41) is observed for $n \gg 1$. This simple stochastic model recovers the proper scaling of circulation in quantum and classical turbulence for low-order moments. However, it predicts a self-similar scaling, which differ for high-order moments. In principle, one could also include extra terms in the stochastic model to take into account intermittent corrections.

4.4   Publication: *Velocity circulation intermittency in finite-temperature turbulent superfluid helium*

The first experimental study of the intermittent behavior of superfluid helium was carried out by Maurer and Tabeling [MT98]. The authors studied a turbulent flow generated by two counter-rotating disks in a range of temperatures between 1.4 and 2.3 K. They observed that superfluid helium presents an intermittent behavior that is consistent with classical turbulence, with no temperature dependence. Since then, several experiments were carried out using different forcings and at different temperature regimes, in agreement with the behavior observed by Maurer and Tabeling [SRL11; RCS+17]. In a different experiment of grid turbulence in superfluid helium, it was observed that at an intermediate temperature $T = 1.85$ K, the system displays
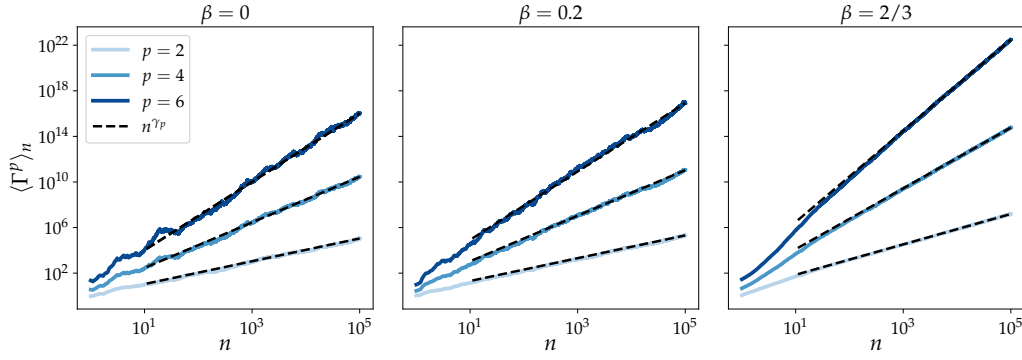
Figure 4.6: Moments of circulation obtained from numerical simulations of the stochastic model (4.38) for different values of the polarization parameter β. The black dashed lines show the predicted scaling γ_p in Eq. (4.41).

an apparent intermittent enhancement, while for the other temperatures between 1.45 and 2.15 K it is compatible with classical turbulence [VGG⁺18].

Numerical simulations of superfluid turbulence at finite temperature displayed a wide variety of behaviors. For instance, studies using shell-model simulations based on the two-fluid HVBK equations have shown that the intermittent behavior peaks at an intermediate temperature [BLP⁺13; SP16]. However, the first of these works showed an enhanced intermittent behavior, while the second one a reduced one. Direct numerical simulations of the HVBK model also showed an enhancement at an intermediate temperature in which both normal and superfluid densities have a similar fraction, and hence the energy transfer due to mutual friction force is maximal [BKL⁺18]. Simulations of grid turbulence in the GP framework at zero temperature have shown a more intermittent behavior [Krs16]. Due to the wide variety of observations, there is still a lack of consensus on whether intermittency in superfluid turbulence is consistent with classical turbulence in the whole range of temperatures or if at intermediate temperatures it deviates as a consequence of mutual friction.

In this work, we analyze the intermittent behavior of superfluid helium using velocity circulation statistics obtained from experimental data performed by the group of Wei Guo in Tallahassee specifically to address this problem, and numerical data from the HVBK model performed in my group. The experiments in superfluid helium are performed by exciting the flow with a moving grid at two different temperatures $T = 1.65$ K and $T = 1.95$ K. To probe the flow, we use particle tracking velocimetry (PTV) measurements and then average the velocity of each particle to recover Eulerian velocity fields of the superfluid at different times, and compute the circulation from them. We observe that, up to $p = 4$, circulation moments display a similar behavior as in classical turbulence, and the same for both temperatures.

To provide information about higher-order moments and at a wider range of temperatures, we perform seven numerical simulations of the coarse-grained two-fluid HVBK model at temperatures between 1.3 and 2.1 K using 1024^3 collocation points. From the DNS, we observe no temperature dependence of the intermittent behavior of velocity circulation, which is compatible to simulations in classical turbulence up to $p = 8$. Thus, we provide the first experimental measurements of circulation statistics in superfluid ⁴He. Our results are compatible with previous observations on the structure functions in experiments in superfluid helium [MT98; RCS⁺17].

Velocity circulation intermittency in finite-temperature turbulent superfluid helium

Nicolás P. Müller [1], Yuan Tang [2,3] Wei Guo [2,3] and Giorgio Krstulovic [1]

[1]*Université Côte d'Azur, Observatoire de la Côte d'Azur, CNRS, Laboratoire Lagrange,*
Boulevard de l'Observatoire CS 34229 - F 06304 NICE Cedex 4, France
[2]*National High Magnetic Field Laboratory, 1800 East Paul Dirac Drive, Tallahassee,*
Florida 32310, USA
[3]*Mechanical Engineering Department, FAMU-FSU College of Engineering,*
Florida State University, Tallahassee, Florida 32310, USA

We study intermittency of circulation moments in turbulent superfluid helium by using experimental grid turbulence and numerical simulations of the Hall-Vinen-Bekarevich-Khalatnikov model. More precisely, we compute the velocity circulation Γ_r in loops of size r laying in the inertial range. For both experimental and numerical data, the circulation variance shows a clear Kolmogorov scaling $\langle \Gamma_r^2 \rangle \sim r^{8/3}$ in the inertial range, independently of the temperature. Scaling exponents of high-order moments are comparable, within error bars, to previously reported anomalous circulation exponents in classical turbulence and low-temperature quantum turbulence numerical simulations.

I. INTRODUCTION

Turbulence, the disordered and chaotic motion of fluids, is an ubiquitous phenomenon in nature taking place at very different length scales, from astrophysical to microscales [1]. Its dynamics is described by complex velocity fields dominated by vortices, regions of the flow with a strong local rotation. Despite great efforts and improvements made on its understanding over the last two centuries, there is still no full theory able to describe the dynamics of turbulent flows completely.

The most traditional way of characterizing velocity fluctuations in classical turbulence (CT) at a given scale $r = |\boldsymbol{r}|$ is using the so-called structure functions $S_p(r) = \langle [\boldsymbol{v}(\boldsymbol{x} + \boldsymbol{r}) - \boldsymbol{v}(\boldsymbol{x})]^p \rangle$, where the brackets indicate an average in space, time, or over different ensembles. When a large scale separation exists between the forcing scale L and the dissipative scale η, the structure function displays power laws as $S_p(r) \sim r^{\zeta_p}$ for $\eta \ll r \ll L$. For homogeneous isotropic flows, in 1941 Kolmogorov predicted the self-similar scaling $\zeta_p^{\mathrm{K41}} = p/3$ (K41 prediction) [2]. Such a prediction is based on a mean-field approach and simply based on dimensional analysis. Experiments and numerical simulations on homogeneous isotropic CT have, however, showed some deviations from K41 theory [3]. This breakdown of self-similarity is usually attributed to the highly intermittent nature of velocity fluctuations at small scales. There are several phenomenological theories based on multifractality intending to describe the intermittency of turbulent flows [4–6].

A different system with a manifest intermittency is quantum turbulence (QT), the turbulence taking place in superfluids [7]. When liquid ^{4}He is cooled below the critical temperature of $T_\lambda = 2.17$ K, it undergoes a phase transition into a superfluid state [8]. Its dynamics at nonzero temperatures can be interpreted as two-fluid systems that mutually interact between themselves: a superfluid component with a velocity field $\boldsymbol{v}_\mathrm{s}$ that presents no viscosity, and a normal viscous component $\boldsymbol{v}_\mathrm{n}$ that is described by the classical Navier–Stokes equations [9]. These two components

can move in phase (coflow) or in counterphase (counterflow). In the first case, it has been observed both in experiments and numerical simulations that the statistical properties of the flow at large scales follows a behavior similar to classical fluids [10]. On the other hand, counterflow turbulence dynamics differs from classical fluids, displaying an inverse energy cascade and a breakdown of isotropy at small scales [11,12].

In superfluid ^{4}He, the relative densities between the normal and superfluid components depend on temperature, and therefore there is an open discussion on whether or not there is a dependence of intermittency on the temperature. Experimental studies on QT at the wake of a disk in superfluid ^{4}He at temperatures between 1.3 K $\leqslant T \leqslant T_\lambda$ show that there is no temperature dependence on the intermittency [13]. Other sets of experiments on homogeneous isotropic QT show that there is no temperature dependence up to $p = 6$, but there are some deviations from CT [14,15]. Numerical simulations on QT using different models like the Gross-Pitaevskii (GP) equation, shell models, or the HVBK (Hall-Vinen-Bekarevich-Khalatnikov) equations show a clear temperature dependence that is amplified at intermediate temperatures of $1.8 \leqslant T \leqslant 2$ K, where the density fractions of each component approach each other [16,17]. However, some HVBK-based shell models show an enhancement of intermittency on this temperature range while others show some decrease or even nonintermittent behavior [18,19]. Given the lack of consensus between experiments and numerical simulations, further studies are required on this subject.

An alternative way of studying intermittency in turbulent flows is using moments of the velocity circulation instead of the velocity increments [20–23]. The velocity circulation around a closed loop $\mathcal{C}$ enclosing an area A is defined by

$$\Gamma_A(\mathcal{C}; \boldsymbol{v}) = \oint_{\mathcal{C}} \boldsymbol{v} \cdot d\boldsymbol{l} = \iint_A \boldsymbol{\omega} \cdot \boldsymbol{n} \, dS, \tag{1}$$

where in the second equality we make use of the Stokes theorem, with $\boldsymbol{\omega} = \nabla \times \boldsymbol{v}$ the vorticity field. First theoretical studies on the statistics of velocity circulation suggested that the probability density function (PDF) follows the area rule, that is, within the inertial range of scales, they depend only on the minimal area circumscribed by the closed loop [20,24]. Further numerical studies at low Reynolds numbers suggested that velocity circulation is a highly intermittent quantity, as well as velocity increments [21–23]. These results were also observed in experiments of homogeneous and isotropic turbulence in classical fluids [25]. It was recently shown using high-resolution numerical simulations of the Navier–Stokes equations that the moments of circulation present a clear scaling,

$$\langle \Gamma_r^p \rangle \sim r^{\lambda_p}, \text{ for } \quad \eta \ll r \ll L, \tag{2}$$

with $r = \sqrt{A}$, which deviate from Kolmogorov-based prediction $\lambda_p^{K41} = 4p/3$ for larger moments [26]. Moreover, in numerical simulations of the GP equation, a model for low-temperature superfluids, a very similar behavior between CT and QT was observed [27]. The advantage of using the velocity circulation to study intermittency is that it is an integral quantity, and allows for the development of new theories for intermittency [28–30]. To our knowledge, there is still no experimental studies in superfluid ^{4}He of the scaling laws of velocity circulation.

In this paper, we study intermittency of superfluid ^{4}He from the point of view of velocity circulation. We measure the circulation scaling in experiments of grid turbulence in superfluid ^{4}He and compare them with numerical simulations of the coarse-grained HVBK equations at different temperatures (see Sec. II for details on the experimental and numerical methods). The analysis is performed for large-scale statistics of QT. We show that for both experiments and numerical simulations, the scaling exponents of low-order moments do not depend significantly on the temperature of the superfluid. In particular, for numerical simulations we show that high-order moments display the same intermittent behavior as in CT. These results are in agreement with the experimental observations of the velocity increments [13,31]. This paper is organized as follows. In Sec. II, we provide details of our experimental and numerical methods, including the model we use and the algorithm for computing the velocity circulation. Then, in Sec. III we present our
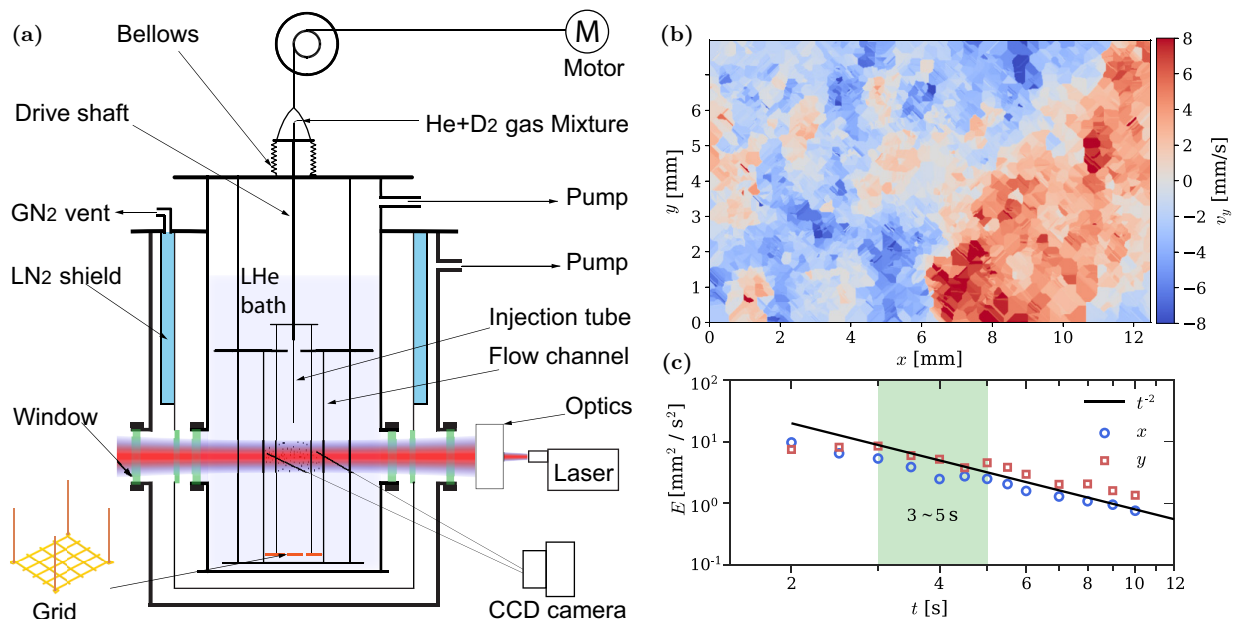
FIG. 1. (a) Experimental apparatus for grid turbulence of the superfluid ^{4}He. (b) Typical experimental velocity field obtained from the PTV measurements of grid turbulence in superfluid ^{4}He following the procedure described in Sec. II A. (c) Turbulent kinetic energy density as a function of decay time for a typical acquisition at $T = 1.95$ K.

experimental and numerical results. Finally, in Sec. IV we summarize our results and discuss known results on the circulation intermittency.

II. EXPERIMENTAL SETUP AND MATHEMATICAL MODEL

A. Experimental setup

To examine the circulation statistics experimentally, we have conducted velocity-field measurements in quasiclassical turbulence generated in He II by a towed grid using the particle tracking velocimetry (PTV) method [15]. The experimental apparatus, shown in Fig. 1(a), consists of a transparent cast acrylic flow channel with a cross-section area of 1.6×1.6 cm^2 and a length of 33 cm immersed vertically in a He II bath (more details of the setup can be found in Ref. [32]). The bath temperature is controlled by regulating the vapor pressure. A brass mesh grid with a spacing of 3 mm and 40% solidity is suspended in the flow channel by stainless-steel thin wires at the four corners. A linear motor outside the cryostat can pull the wires and hence the grid at a speed up to 60 cm/s. In the current paper, we used a fixed grid speed at 30 cm/s. To probe the flow, we adopt the PTV method using solidified D$_2$ tracer particles with a mean diameter of about 5 μm [32]. These particles are entrained by the viscous normal-fluid flow due to their small sizes and hence small Stokes number [15,33,34], but they can also get trapped on quantized vortices in the superfluid [35–38]. A continuous-wave laser sheet (thickness: 200 μm, height: 9 mm) passes through the center of two opposite side walls of the channel to illuminate the particles. The motion of the particles is then capture by a CCD camera at 200 frames per second at an angle perpendicular to both the flow channel and the laser sheet. The pixel size of the camera is 7.5 μm $\times$ 7.5 μm with a full view resolution of 2560×1440 pixels. We install a Nikon Micro-Nikkor 105 mm f/2.8 lens to the camera so the view region is coupled to the camera sensor at a ratio of nearly 1:1. The exact length scale in the images can be calibrated by measuring the pixel distance between the two side walls of the channel. We set $t = 0$ when the grid passes the center of the view window and typically record the particle motion continuously for 40 s. A modified feature-point tracking routine [32] is adopted to extract the trajectories of the tracer particles from the sequence of images. In the

current paper, we focus on analyzing the data obtained in the time interval $t = 3$ s to $t = 5$ s at two bath temperatures, i.e., $T = 1.65$ K and 1.95 K. The turbulence at these decay times appears to be reasonably homogeneous and isotropic, and its turbulence intensity is relatively high such that an inertial range exists [15].

For circulation analysis, it is more convenient to have two-dimensional Eulerian velocity field. To generate this information using the spatially sparse PTV data, we adopt the method reported in Ref. [39]. We first combine the velocity data $\boldsymbol{v}(x, y)$ obtained from 11 successive images into a single velocity-field image. This procedure assumes that during the acquisition time of these 11 images (i.e., 50 ms), the velocity field does not change considerably, so these data describe a single instantaneous velocity field. Then we divide the combined image into square cells with side length $\Delta = 0.02$ mm so most of the cells have at least 1–2 data points. The velocity assigned to the center of each cell is calculated as the Gaussian-averaged velocity of particles inside the cell with a Gaussian-profile variance $\sigma \approx \Delta/2$ to ensure that the Gaussian weight drops to near zero at the cell's edge. Occasionally, there may not be any particles that fall inside a particular cell. In this case, we increase the size of this cell by a factor of 2, and this process may be repeated until a few particles fall in the enlarged cell so the velocity at the cell center can be determined. A representative resulted velocity field $\boldsymbol{v}(x, y)$ obtained at $T = 1.95$ K is shown in Fig. 1(b) . In Fig. 1(c), we show the time evolution of the turbulent kinetic energy density, defined as $E_{x,y} = \langle \boldsymbol{v}_{x,y}^2 \rangle / 2$. At $t \geqslant 3$ s, the kinetic energy density of the velocity components in both x and y directions are comparable, suggesting that the flow is relatively isotropic. Furthermore, a decay scaling $E_{x,y} \propto t^{-2}$ at $t \geqslant 3$ s is clearly visible. This scaling is a characteristic feature of the homogeneous and isotropic turbulence in He II when the size of the energy containing eddies are saturated by the channel width [40]. Here we specifically analyze the data at 3 s $\leqslant t \leqslant 5$ s, since the flow is reasonably homogeneous and isotropic and the turbulent kinetic energy density is relatively large such that a clear inertial range may exist.

To aid the discussion of the statistical analysis, we have also calculated the Taylor microscale $\lambda_{\mathrm{T}} = \sqrt{15\nu/\epsilon}\, v_{\mathrm{rms}}$ and the Taylor Reynolds number $\mathrm{Re}_\lambda = v_{\mathrm{rms}}\lambda_{\mathrm{T}}/\nu$. These calculations involve the evaluation of the energy dissipation rate ϵ. As explained in more detail in our previous work [15], we calculate the energy dissipation rate based on the measured velocity derivatives in the x-y plane. The obtained Re_λ is 40–60, and the corresponding Taylor microscale is 0.15–0.17 mm for 3 s $\leqslant t \leqslant 5$ s at both 1.65 K and 1.95 K.

B. Model for superfluid helium

The dynamics of superfluid helium at finite temperatures and scales larger than the intervortex distance can be described by the coarse-grained HVBK equations [9,18,34,41]:

$$\frac{\partial \boldsymbol{v}_{\mathrm{n}}}{\partial t} + \boldsymbol{v}_{\mathrm{n}} \cdot \nabla \boldsymbol{v}_{\mathrm{n}} = -\frac{1}{\rho_{\mathrm{n}}} \nabla p_{\mathrm{n}} + \nu_{\mathrm{n}} \nabla^2 \boldsymbol{v}_{\mathrm{n}} - \frac{\rho_s}{\rho_n} \boldsymbol{f}_{\mathrm{ns}} + \boldsymbol{\Phi}_{\mathrm{n}}, \tag{3}$$

$$\frac{\partial \boldsymbol{v}_{\mathrm{s}}}{\partial t} + \boldsymbol{v}_{\mathrm{s}} \cdot \nabla \boldsymbol{v}_{\mathrm{s}} = -\frac{1}{\rho_{\mathrm{s}}} \nabla p_{\mathrm{s}} + \nu_{\mathrm{s}} \nabla^2 \boldsymbol{v}_{\mathrm{s}} + \boldsymbol{f}_{\mathrm{ns}} + \boldsymbol{\Phi}_{\mathrm{s}}, \tag{4}$$

$$\nabla \cdot \boldsymbol{v}_{\mathrm{n}} = \nabla \cdot \boldsymbol{v}_{\mathrm{s}} = 0. \tag{5}$$

This incompressible two-fluid model describes the motion of the normal ($\boldsymbol{v}_{\mathrm{n}}$) and superfluid ($\boldsymbol{v}_{\mathrm{s}}$) components via two coupled Navier–Stokes equations. The kinematic viscosity is related to the dynamic one via $\nu_{\mathrm{n}} = \mu/\rho_{\mathrm{n}}$, $p_{\mathrm{n,s}}$ is the hydrodynamic pressure of each component, and the total density of the fluid is $\rho = \rho_{\mathrm{n}} + \rho_{\mathrm{s}}$. The superfluid component also dissipates via an effective viscosity ν_{s} that takes into account dissipative effects taking place at small scales that the HVBK model is not able to resolve, like quantum vortex reconnections and Kelvin waves [42–46]. Both Navier–Stokes equations are coupled through the mutual friction force between both velocity components $\boldsymbol{f}_{\mathrm{ns}} = \alpha \Omega_0 (\boldsymbol{v}_{\mathrm{n}} - \boldsymbol{v}_{\mathrm{s}})$, with $\alpha = \alpha(T)$ the mutual friction coefficient that depends on the temperature of the system. The frequency $\Omega_0 = \kappa \mathcal{L}$ is proportional to the vortex line density $\mathcal{L}$ and to the quantum of circulation of the vortices κ, and can be estimated using the enstrophy Ω as

TABLE I. Table of parameters for the numerical simulations of the HVBK equations. N corresponds to the linear resolution on each direction, T is the temperature of the HVBK system expressed in Kelvin units, α the mutual friction coefficient, ρ_s and ρ_n the superfluid and normal densities, respectively, ν_s/ν_n the ratio of the kinematic viscosities, and $\text{Re}_\lambda^{n,s}$ to the Taylor-microscale Reynolds number $\text{Re}_\lambda = v_{rms}\lambda_T/\nu$ of the normal and superfluid components, respectively. The Reynolds number Re_λ^{tot} is associated to the total velocity $\boldsymbol{v}_{tot} = (\rho_s\boldsymbol{v}_s + \rho_n\boldsymbol{v}_n)/\rho$. The integral length scale is defined as $L_I^{tot} = \int k^{-1}E(k)dk / \int E(k)dk$.

RUN	N	T (K)	α	ρ_s/ρ	ρ_n/ρ	ν_s/ν_n	Re_λ^n	Re_λ^s	Re_λ^{tot}	L_I^{tot}
I	1024	1.3	0.034	0.952	0.048	0.043	34	412	418	0.56
II	1024	1.5	0.072	0.889	0.111	0.2	187	651	628	0.57
III	1024	1.79	0.156	0.696	0.304	0.8	358	427	389	0.57
IV	1024	1.9	0.206	0.574	0.426	1.25	500	419	462	0.53
V	1024	1.96	0.244	0.504	0.496	1.50	550	410	545	0.57
VI	1024	2.05	0.347	0.362	0.638	1.87	550	345	495	0.54
VII	1024	2.1	0.481	0.259	0.741	2.5	406	193	344	0.56

$\Omega_0^2 \approx \Omega = \langle|\boldsymbol{\omega}_s|^2\rangle/2$ with $\boldsymbol{\omega}_s = \nabla \times \boldsymbol{v}_s$ the superfluid vorticity and $\langle.\rangle$ denoting a spatial average [17,34]. Thus, it is possible to find an estimation of the mean intervortex distance of the flow as $\ell = \mathcal{L}^{-1/2}$. It is important to remark that this relation is not obtained from first principles. An alternative approach is to assume that the intervortex distance is of the order of the Taylor microscale of the turbulent flow $\ell \sim \lambda_T = \sqrt{5E/\Omega}$, with $E = \langle|\boldsymbol{v}|^2\rangle/2$ the mean kinetic energy and $\Omega = \Omega_0^2$ the enstrophy of the flow [47]. We use two independent large-scale constant-in-time Gaussian random forces $\boldsymbol{\Phi}_n(\boldsymbol{x})$ and $\boldsymbol{\Phi}_s(\boldsymbol{x})$ to excite both fluid components and obtain a stationary state.

We study the scaling of velocity circulation in superfluid ^{4}He at different temperatures by solving numerically the HVBK Eqs. (3)–(5) using a fully dealiased Fourier pseudospectral code in a periodic cubic domain and a third-order Runge-Kutta integration in time (see Ref. [48] for details). We perform seven numerical simulations of these equations for temperatures that vary between $T = 1.3$ K and $T = 2.1$ K, using $N = 1024$ linear collocation points in each direction. All the parameters used for each numerical simulation are shown in Table I. The mutual friction, normal, and superfluid density fractions and viscosity ratios were chosen to reproduce the typical values observed experimentally in superfluid helium at each temperature [49,50]. We report the Reynolds number associated to the Taylor-microscale $\text{Re}_\lambda^{n,s,tot} = v_{rms}^{n,s,tot}\lambda_T/\nu_{n,s,tot}$, where the superscripts correspond to the normal, superfluid and total components, respectively. The total velocity is defined as $\boldsymbol{v}_{tot} = (\rho_n\boldsymbol{v}_n + \rho_s\boldsymbol{v}_s)/\rho$.

For comparison, we also use data from Refs. [27,28]. In particular, we use the circulation exponents of CT obtained by integrating the Navier-Stokes equations with a Taylor-microscale Reynolds number of $\text{Re}_\lambda = 510$, and zero-temperature QT generated by using the GP model, with a separation between the integral length scale L_I and the healing length ξ of $L_I/\xi = 820$. Using the intervortex distance ℓ as the equivalent of the Taylor microscale in the GP model, we can obtain a microscale Reynolds number of $\text{Re}_\lambda^{GP} \equiv 15L_I/\ell = 440$. In both cases, the numerical simulations have a linear spatial resolution of $N = 2048$.

C. Data analysis

The velocity circulation for the HVBK numerical simulations is computed using the Fourier coefficients of the velocity fields of each component using our openly available code [51]. Over each two-dimensional L-periodic slab of the system, in three different orientations, we compute the circulation over square loops of different sizes r centered at each point $\boldsymbol{x} = (x, y)$ of the domain as

the convolution [28]

$$\Gamma_r(\boldsymbol{x}) = \int_{S_r(\boldsymbol{x})} \omega_{\mathrm{n,s}}(\boldsymbol{x}')d^2\boldsymbol{x}' = \iint H_r(\boldsymbol{x} - \boldsymbol{x}')\omega_{\mathrm{n,s}}(\boldsymbol{x}')d^2\boldsymbol{x}, \qquad (6)$$

where $\omega_{\mathrm{n,s}} = (\boldsymbol{\nabla}_{2\mathrm{D}} \times \boldsymbol{v}_{\mathrm{n,s}}) \cdot \hat{z}$ is the two-dimensional vorticity of the normal or superfluid component for each slab and $S_r(\boldsymbol{x})$ a squared planar surface of linear size r centered at $\boldsymbol{x}$. The convolution kernel is defined as $H_r(\boldsymbol{x}) = \Pi(x/r)\Pi(y/r)$, where $\Pi(x) = 1$ for $|x| < 1/2$ and 0 otherwise, so it can be written in Fourier space in terms of the normalized sinc function as $\hat{H}_r(k_x, k_y) = (r/L)^2 \mathrm{sinc}(k_x r/2\pi)\mathrm{sinc}(k_y r/2\pi)$.

This method can be used to compute the simulations for the normal and superfluid components obtained from the numerical simulations of the HVBK equations due to their periodicity. However, the velocity fields obtained from experiments are not periodic. Therefore, instead of using the Fourier coefficients, we compute the circulation directly from the velocity field following the first equality in Eq. (1). We have checked that the analysis done using this nonperiodic method leads to the same quantitative results for the circulation moments and their scaling exponents obtained using the Fourier coefficients and periodic boundary conditions. In particular, we tested these methods using the velocity fields from the numerical simulations of the HVBK equations.

III. RESULTS

A. Low order statistics from experimental data

We analyze the data obtained from several realizations of grid turbulence in superfluid helium at temperatures $T = 1.65$ K and $T = 1.95$ K following the experimental setup described in Sec. II A. We determine that the system reaches a regime of fully developed turbulence between three and five seconds after the grid passes through the center of the region. We study and obtain a two-dimensional Eulerian velocity field every 0.1 s within this time interval on a rectangular window of 7.98×12.48 mm, following the procedure described in Sec. II A. These velocity fields allow us to compute the velocity circulation around squared planar loops of different linear sizes r, as described in Sec. II C. As the velocity field is not periodic, we analyze a reduced window of $(L_x - r, L_y - r)$, obtaining a reduced amount of statistics for larger loops. In Fig. 1(c), we show that the energy injected may vary between different realizations of the flow, and that within the time interval studied it shows a consistent decaying. Averaging the different realizations and the circulation obtained at different times would give a stronger weight to some realizations and to early times of the evolution. Therefore, we normalize each realization and each time step by the circulation at large scales $\Gamma_0 = v_{\mathrm{rms}}L_{\mathrm{I}}$, with the root mean square velocity field $v_{\mathrm{rms}} = \sqrt{(2v_x^2 + v_y^2)/3}$ of each time step and the mean integral length scale $L_{\mathrm{I}} = \int k^{-1}E(k)dk / \int E(k)dk$, with $E(k)$ the energy spectrum. The typical integral length scale in our experiments is $L_{\mathrm{I}} = 4.5$ mm and the typical root-mean-square velocity is $v_{\mathrm{rms}} = 1.7$ mm/s. Figure 2 shows the variance of the normalized circulation $\bar{\Gamma} = \Gamma/\Gamma_0$ obtained from the averaged measurements as a function of the linear size of the loop normalized by the Taylor-microscale $\lambda_{\mathrm{T}} \approx 0.16$ mm. In the inertial range, represented by the green-shaded region, the circulation variance follows a scaling that approximates the Kolmogorov one $\lambda_2^{\mathrm{K41}} = 8/3$ for both temperatures. Moreover, when the variances are compensated by λ_2^{K41}, they approach to a plateau. Note that scales in this range are larger than the laser sheet thickness and should be little affected by the construction of the Eulerian field using experimental data.

Figure 3 shows the PDFs of the velocity circulation for both temperatures and for different loop sizes (in green). At small scales, the PDFs present heavy tails, a clear signature of intermittency. As the size of the loop increases, they collapse and approach a Gaussian distribution (red dashed line). This behavior is similar to the one observed for the velocity circulation in numerical simulations of the Navier–Stokes and GP equations [26–28], and experiments in classical fluids [25].

The study of high-order moments of the circulation $\langle \Gamma^p \rangle$ usually requires a large amount of data for statistical convergence [52]. Measured moments of order p cannot be trusted if the integrands
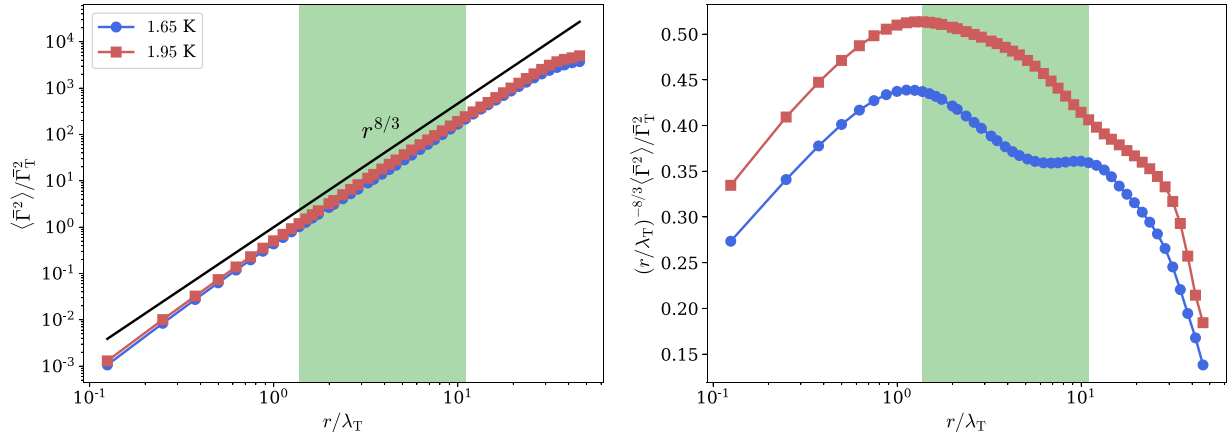
FIG. 2. Left panel: Circulation variance for the average of the experimental acquisitions at temperatures $T = 1.65$ K (blue circles) and $T = 1.95$ K (red squares). The green shaded area indicates the inertial range. The black solid line corresponds to Kolmogorov scaling law $r^{8/3}$. Right panel: Circulation variance compensated by Kolmogorov scaling.

$\Gamma^p P_r(\Gamma)$, for a given length scale within the inertial range, do not go to zero for the largest measured value of Γ, since the assumption $\langle \Gamma^p \rangle = \int_{-\infty}^{\infty} \Gamma^p P_r(\Gamma) d\Gamma \approx \int_{-\Gamma_c}^{\Gamma_c} \Gamma^p P_r(\Gamma) d\Gamma$, with Γ_c the circulation cut-off, breaks down. In Fig. 3, we also show the circulation integrands of the experimental measurements up to fourth order (in blue) for length scales within the inertial range. In
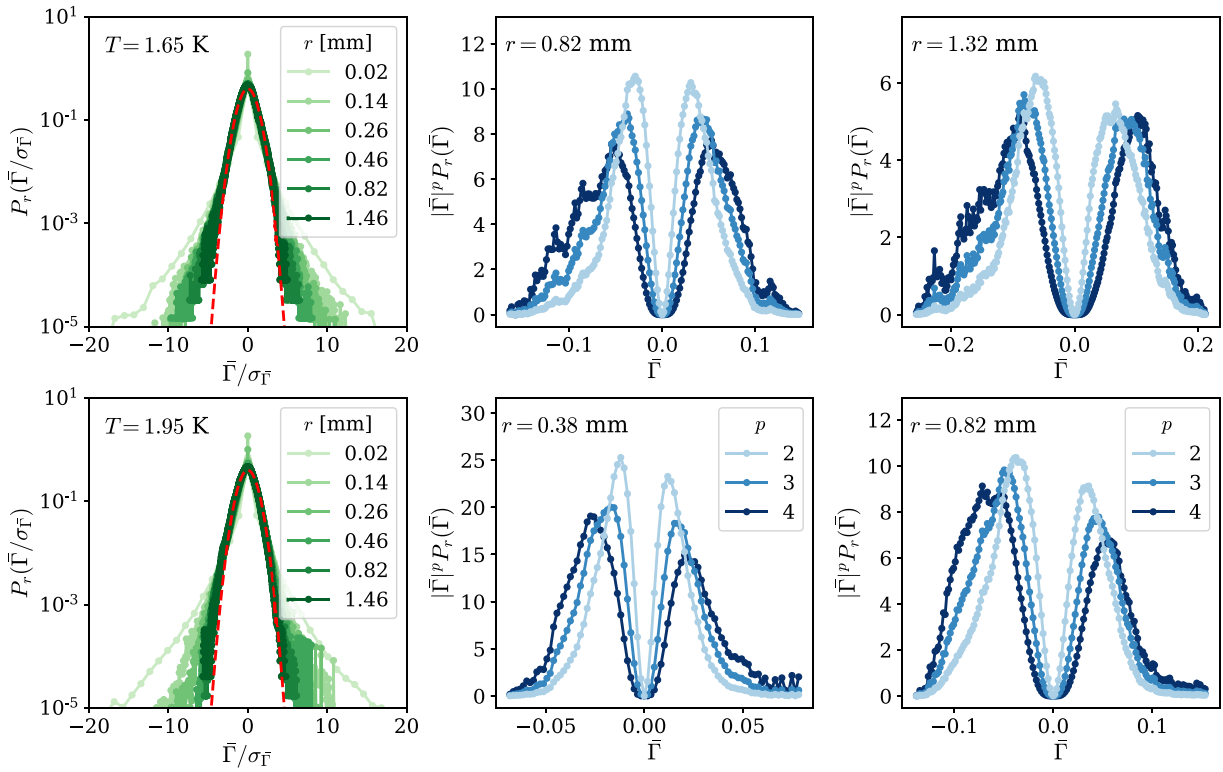
FIG. 3. Left panel: Experimental PDFs of the velocity circulation at different length scales. Each row corresponds to a different temperature. Middle and right panels: Circulation integrands up to moment four for two different length scales laying within the inertial range. The statistical convergence starts to fail on the fourth moment.
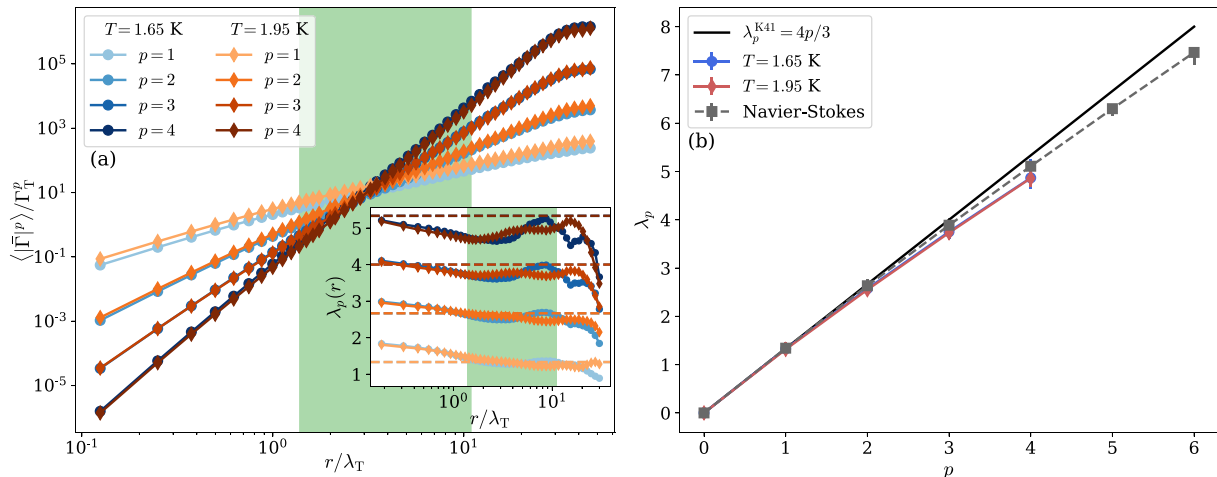
FIG. 4. (a) Circulation moments for the experimental data up to order four for temperatures $T = 1.65$ K (blue circles) and $T = 1.95$ K (orange diamonds). The inset shows the local slope of the circulation moments and Kolmogorov scaling as dashed horizontal lines. Green shaded areas indicate the inertial range for both temperatures. (b) Scaling exponents of the experimental measurements. The error bars indicate the maximum and minimum values of the local slope within the inertial range. As reference, we show Kolmogorov scaling $\lambda_p^{\mathrm{K41}} = 4p/3$ and the scaling exponents of classical turbulence obtained from numerical simulations of the Navier–Stokes equations (gray squares).

particular, for the highest order shown here, the tails fail to converge for some scales. This behavior suggests that, at best, moment of order four are borderline in terms of statistical converge.

The circulation moments up to the fourth order for $T = 1.65$ K (blue circles) and for $T = 1.95$ K (orange diamonds) are shown in Fig. 4(a). Odd-order moments of circulation shall vanish as there is no preferential rotation of the flow inducing a symmetry breaking. Therefore, we study their absolute values $\langle |\Gamma|^p \rangle$. The local slopes, defined as the logarithmic derivative $\lambda_p(r) = d\log\langle|\Gamma|^p\rangle/d\log r$, approach to a plateau within the inertial range, obtaining the scaling exponents λ_p shown in Fig. 4(b). The error bars correspond to the maximum and minimum values of the local slopes in the inertial range. Up to the third order, the scaling exponents seem to follow the Kolmogorov scaling law for the circulation $\lambda^{\mathrm{K41}} = 4p/3$. For higher orders, they start deviating from this prediction, taking smaller values and hence a stronger intermittency. As a reference, we show the scaling exponents of CT obtained from numerical simulations of the incompressible Navier–Stokes equations, taken from Ref. [28]. Our experimental data starts deviating from the classical limit for increasing order moments. However, data does not allow us to enforce this claim due to a possible lack of statistics to compute the fourth-order moment, as shown in Fig. 3. See Sec. IV for a further discussion.

B. HVBK results

The experimental results presented in Sec. III A provide evidence of circulation scaling in superfluid helium turbulence for low-order moments, in particular, observing a Kolmogorov scaling up to third order. However, the analysis of high-order moments cannot be completely trusted due to the lack of statistics. To provide insight on this aspect, we perform numerical simulations of the coarse-grained HVBK Eqs. (3)–(5) using typical parameters for superfluid ^{4}He (see Table I). We force the system with two independent random forces to obtain a stationary state of homogeneous isotropic QT (see Sec. II B for details on the model and numerical simulations). The two-fluid HVBK model describes the motion of the normal and the superfluid components at finite temperatures. Therefore, the turbulent properties of the flow may differ between them, so each velocity component, in principle, should be studied independently. Figure 5 shows the energy
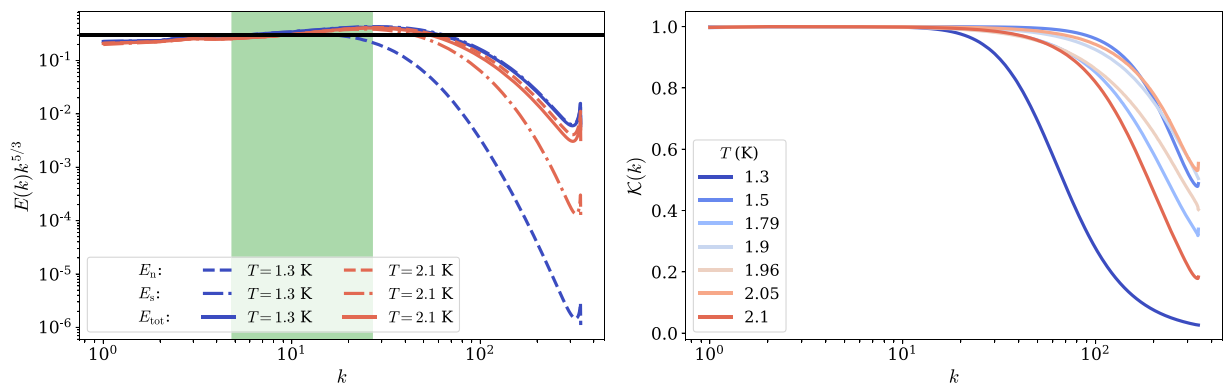
FIG. 5. Left panel: Spectra of the different energy components for the lowest and highest temperature of the simulations. Right panel: Velocity cross-correlation defined in Eq. (7) for different temperatures.

spectra of each velocity component in a statistically steady turbulent regime for two temperatures, the highest and lowest ones studied in this work. For both temperatures and velocity components, the energy spectra display a scaling close to Kolmogorov one $E_{n,s} \sim k^{-5/3}$ within an inertial range that varies depending on the temperature and the velocity component. The reason for these variations is that the normal and effective superfluid viscosities vary, and also present a different temperature dependence. One way of defining a homogeneous inertial range to facilitate the analysis of these two velocity components is by studying the total velocity field $\boldsymbol{v}_{\text{tot}} = \boldsymbol{j}/\rho$ with $\boldsymbol{j} = \rho_s \boldsymbol{v}_s + \rho_n \boldsymbol{v}_n$ the total momentum density.

The use of the total velocity could be valid under the assumption of *locking* between both velocity components, in the sense of $\boldsymbol{v}_n \approx \boldsymbol{v}_s$ [50,53]. One way of quantifying the scale-by-scale locking is with the velocity cross-correlation, [17,18]

$$\mathcal{K}(k) = \frac{2E_{\text{ns}}(k)}{E_n(k) + E_s(k)}, \qquad (7)$$

with $E_{\text{ns}}(k)$ the cross-velocity energy spectrum associated to $\boldsymbol{v}_n \cdot \boldsymbol{v}_s$. If the cross correlation is equal to one, it indicates that both components are completely locked, while if it approaches to zero the superfluid and normal velocities are statistically independent. Figure 5(b) shows that for all temperatures the velocity components are locked with $\mathcal{K}(k) > 0.95$ at least up to $k \approx 50$ except for the lowest temperature case $T = 1.3$ K, where the locking stops at $k \approx 20$ as a consequence of the small proportion of normal density. In the inertial range, where the energy spectrum obeys Kolmogorov scaling, both fluid components are locked, so the study of the normal, superfluid, or total velocities should be statistically equivalent. Therefore, most of the following analysis on the velocity circulation is done using the total velocity.

The PDFs of the total velocity circulation normalized by its standard deviation $\sigma = \langle \Gamma^2 \rangle^{1/2}$ for different length scales are presented in Fig. 6. Here, length scales are normalized by the lambda microscale $\lambda_T = \sqrt{5E/\Omega}$ with $E = \int v^2/2 dV$ the total energy of the system and $\Omega = \int |\boldsymbol{\omega}|^2/2 dV$ the enstrophy. For all temperatures, the PDFs follow a qualitatively similar behavior as the one observed in the experiments discussed in Sec. III A (Fig. 3), with heavy tails for small scales and approaching a Gaussian for large scales. The circulation integrands show a good convergence up to order eight.

The circulation variance for different temperatures is shown in Fig. 7. The circulation is normalized by $\Gamma_T^2 = (\lambda_T^4/3)\langle |\boldsymbol{\omega}|^2 \rangle$, which corresponds to the small-scale prediction [27]. In this manner, when the normalized circulation variance is plotted as a function r/λ_T, the data collapses for all temperatures. For each individual temperature, the inertial range extends to a full decade. The green region corresponds to the intersection of all inertial ranges, corresponding also to scales where $\mathcal{K} > 0.95$. For all temperatures, the circulation variance follows a scaling close to the Kolmogorov one $\langle \Gamma^2 \rangle \sim r^{8/3}$. In the right panel, we show that the local slope approaches a plateau of 8/3 within
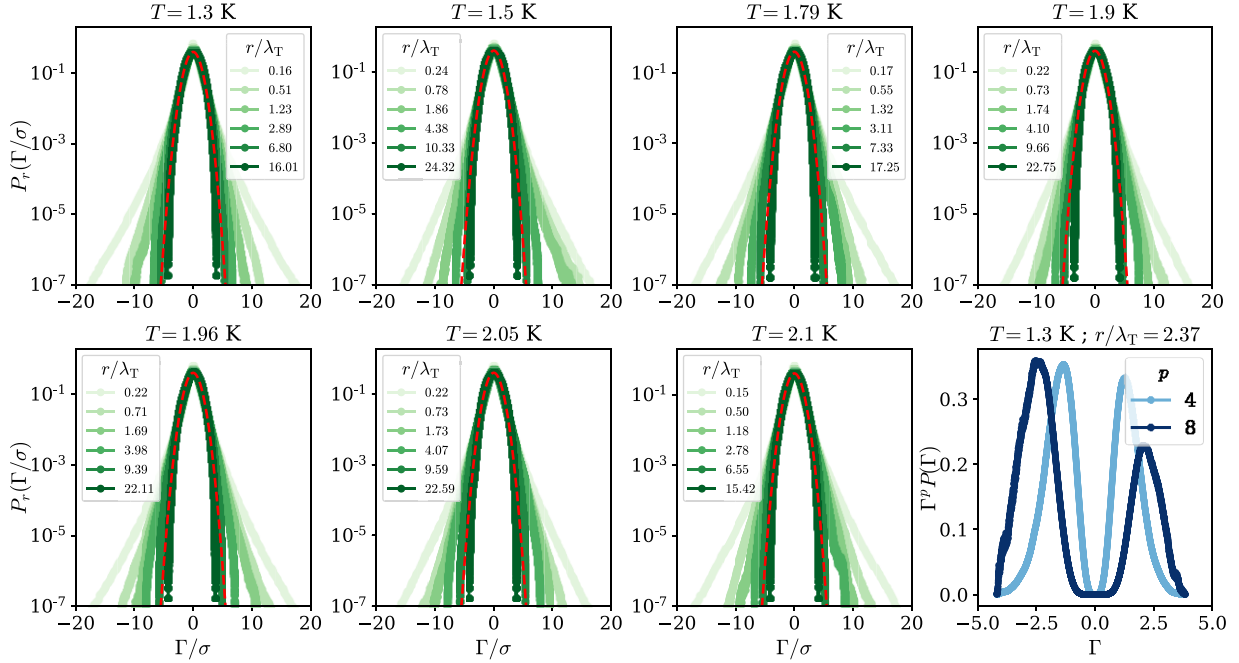
FIG. 6. Normalized PDFs of the velocity circulation Γ for different loop sizes at different temperatures. In red dashed lines, we show as reference a Normal distribution. The last panel shows the circulation integrands up to order eight for $T = 1.3$ K and a length scale within the inertial range.

the inertial range of scales. To analyze more in detail the temperature dependence of the system, we show the scaling exponents of the circulation variance as a function of the superfluid density ρ_s/ρ for the different velocity components in Fig. 8. The error bars correspond to the maximum and minimum values of the local slope in the inertial range. The different velocity components display no significant difference between themselves, supporting the argument of velocity locking. Also, in all cases there is no apparent temperature dependence and the exponents approach to Kolmogorov $\lambda_2^{K41} = 8/3$. The temperature $T = 1.3$ K is removed from the normal velocity scaling due to the fact that the normal mass density is very small, displaying no clear scaling.

For high-order moments, the scaling exponents of the system seem to follow the same behavior observed in numerical simulations of the Navier–Stokes and GP equations [26,27], the latter represented by the shaded area in Fig. 9(a) which accounts for the error bars of data from Ref. [28]. For
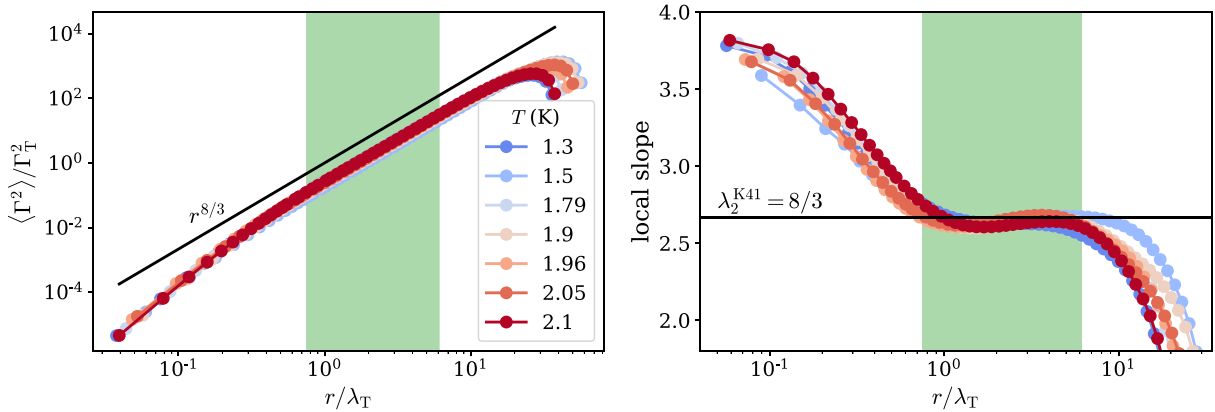

FIG. 7. Circulation variance of the total velocity $\boldsymbol{v}_{\text{tot}}$ for different temperatures. Black solid lines correspond to Kolmogorov scaling. On the right, the local slope of the circulation variance, defined as the logarithmic derivative $d \log\langle\Gamma^2\rangle/d \log r$.
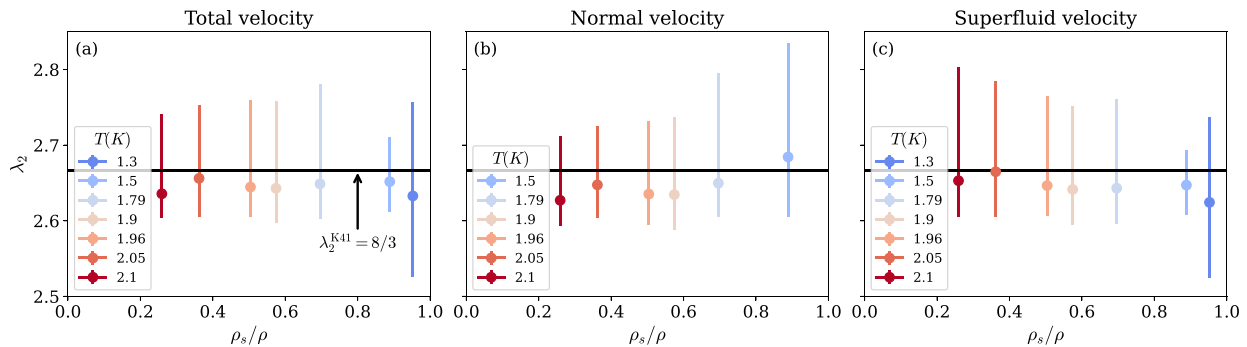
FIG. 8. Scaling exponents of the second-order moment of the velocity circulation at different temperatures for (a) the total velocity, (b) the normal velocity, and (c) the superfluid velocity fields. As a reference, the solid black line shows Kolmogorov scaling $\lambda_2^{\text{K41}} = 8/3$. Error bars indicate the maximum and minimum value of the local slope within the inertial range. The lowest temperature is removed from the middle panel due to the low mass density of the normal component.

$p \leqslant 3$, the scaling exponents of the velocity circulation follow Kolmogorov scaling $\lambda_p^{\text{K41}} = 4p/3$, while for higher-order moments up to $p = 8$ the scaling can be described by different multifractal models [26,28,29]. Figure 9(b) shows the scaling exponents from $p = 2$ to $p = 8$ as a function of the superfluid density. Horizontal dashed lines correspond to the exponents obtained in CT, and the gray area including its error bars. Here, it is clear that there is no apparent temperature dependence on the circulation scaling even for high-order moments, following in all cases the same behavior as in CT.

IV. DISCUSSION AND CONCLUSIONS

In this paper, we have addressed the scaling of circulation moments in superfluid helium at different temperatures. We have used superfluid grid turbulence experiments and numerical simulations of the HVBK model. We have compared the resulting circulation scaling exponents with those of Navier-Stokes (CT) and GP (zero-temperature QT) simulations from Ref. [28].

We obtained the scaling exponents for experiments at temperatures $T = 1.65$ K and $T = 1.95$ K up to order four. Remarkably, we have observed a clear Kolmogorov scaling for the circulation variance, and there is no apparent temperature dependence within the error bars. For the HVBK
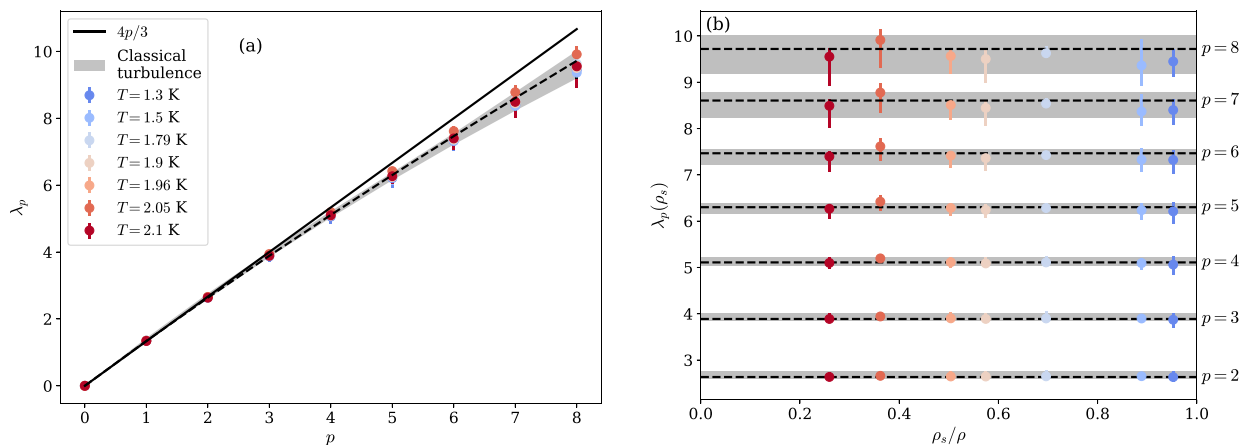

FIG. 9. Scaling exponent of the p-order moments of the velocity circulation at different temperatures. As a reference, the solid black line shows Kolmogorov scaling $\lambda_p^{\text{K41}} = 4p/3$ and gray shaded area shows the scaling obtained from numerical simulations of the Navier–Stokes equations, with the black dashed line its mean value.
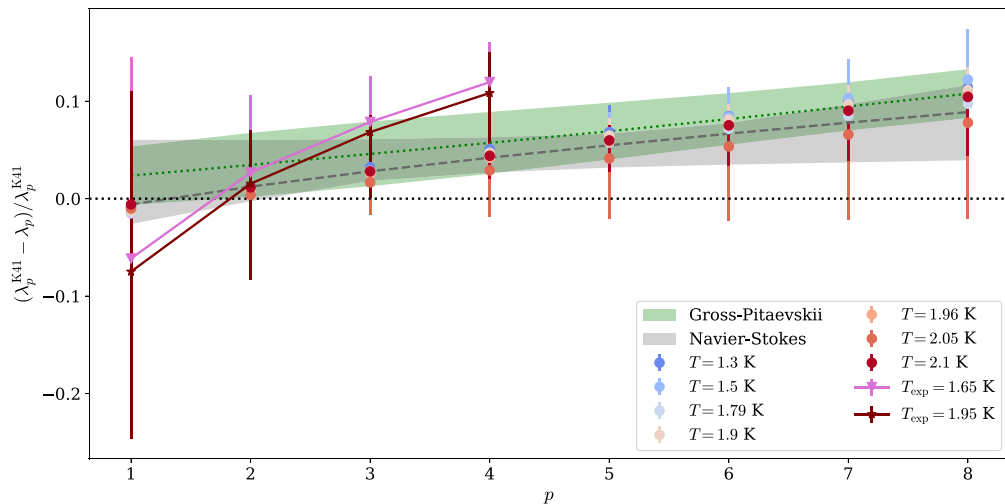
FIG. 10. Relative deviation of the circulation scaling exponents λ_p with respect to K41 prediction $\lambda_p^{K41} = 4p/3$. Data corresponds to superfluid grid turbulence experiments and numerical simulations of the HVBK, Gross-Pitaevskii, and Navier-Stokes models. Grid superfluid experiments are realized at two different temperatures ($T_{exp} = 1.65$K and $T_{exp} = 1.95$K). Exponents obtained from HVBK data of the current paper are at temperatures $T = 1.3$K-2.1K. Error bars are obtained by measuring the maximum and minimum of the local slope in the inertial range (see text). Classical and zero-temperature quantum turbulence exponents are taken from Navier-Stokes and Gross-Pitaevskii simulations of Ref. [28]. The green and gray areas show the error bars for those data sets, respectively.

numerical simulations, we have varied the temperature in the range $1.3 \leqslant T \leqslant 2.1$ K and observed that there is no clear temperature dependence either on the intermittent behavior both for low and high-order moments of velocity circulation. Furthermore, experimental and HVBK data coincide, within error bars, with classical and low-temperature QT simulations. This result is consistent with experimental observations of the velocity increments in superfluid helium [13,31]. Figure 10 presents the relative deviation $(\lambda_p^{K41} - \lambda_p)/\lambda_p^{K41}$ of the circulation exponents λ_p with respect to the Kolmogorov scaling λ_p^{K41} for all available data.

Note that if one drops error bars, there is a slight systematic departure of the experimentally measured circulation exponents from those obtained using HVBK simulations. First, one could be tempted to claim that such a deviation origins from the HVBK description of superfluid helium which might fail to capture the whole physics of superfluids. Indeed, the HVBK model provides only a coarse-grained description of superfluids and does not incorporate the dynamics of quantized vortices. Quantum vortices are related to singularities of the velocity field, which could impact high-order statistics. Whereas such singularities could affect velocity increments, they have no impact on circulation as it is perfectly well-defined for quantum vortices (it is actually quantized); see Ref. [27] for further discussion. Second, the available statistics used to compute high-order moments might not be enough to observe clean power laws in the inertial range, which could undoubtedly induce some errors. Finally, the circulation was computed using Eulerian fields constructed from Lagrangian particles. Several issues can arise from this method. For instance, a lack of particles in a given location of the flow could induce larger regions of constant velocity with abrupt jumps, affecting circulation values. Such regions are visible in the experimental Eulerian fields in Fig. 1(b). Moreover, particles might be trapped by superfluid vortices [34,36,37,43]. In that case, they cannot be considered perfect tracers, which will affect the determination of the Eulerian fields for which this assumption is crucial [54]. All those effects are difficult to quantify. On the other hand, the fact that the variance displays such a clear K41 scaling validates the current method and motivates its use for further studies. Whether the slight intermittency enhancement observed in experiments

has an actual physical origin or arises from the construction of the Eulerian fields is an interesting question that should be addressed in the future.

ACKNOWLEDGMENTS

---

[1] P. A. Davidson, *Turbulence in Rotating, Stratified and Electrically Conducting Fluids* (Cambridge University Press, Cambridge, 2013).

[2] A. N. Kolmogorov, Dissipation of energy in the locally isotropic turbulence, Proc. R. Soc. London A: Mathematical and Physical Sciences **434**, 15 (1991).

[3] U. Frisch, *Turbulence: The Legacy of A.N. Kolmogorov*, 1st ed. (Cambridge University Press, Cambridge, 1995).

[4] A. N. Kolmogorov, A refinement of previous hypotheses concerning the local structure of turbulence in a viscous incompressible fluid at high Reynolds number, J. Fluid Mech. **13**, 82 (1962).

[5] R. Benzi, G. Paladin, G. Parisis, and A. Vulpiani, On the multifractal nature of fully developed turbulence and chaotic systems, J. Phys. A: Math. Gen. **17**, 3521 (1984).

[6] Z.-S. She and E. Lévêque, Universal Scaling Laws in Fully Developed Turbulence, Phys. Rev. Lett. **72**, 336 (1994).

[7] C. F. Barenghi, L. Skrbek, and K. R. Sreenivasan, Introduction to quantum turbulence, Proc. Natl. Acad. Sci. **111**, 4647 (2014).

[8] L. P. Pitaevskii and S. Stringari, *Bose-Einstein Condensation and Superfluidity* (Oxford University Press, Oxford, 2016), Vol. 164.

[9] R. J. Donnelly, *Quantized Vortices in Helium II* (Cambridge University Press, Cambridge, 1991).

[10] J. Maurer and P. Tabeling, Local investigation of superfluid turbulence, Europhys. Lett. **43**, 29 (1998).

[11] L. Biferale, D. Khomenko, V. L'vov, A. Pomyalov, I. Procaccia, and G. Sahoo, Superfluid Helium in Three-Dimensional Counterflow Differs Strongly from Classical Flows: Anisotropy on Small Scales, Phys. Rev. Lett. **122**, 144501 (2019).

[12] J. I. Polanco and G. Krstulovic, Counterflow-Induced Inverse Energy Cascade in Three-Dimensional Superfluid Turbulence, Phys. Rev. Lett. **125**, 254504 (2020).

[13] E. Rusaouen, B. Chabaud, J. Salort, and P.-E. Roche, Intermittency of quantum turbulence with superfluid fractions from 0% to 96%, Phys. Fluids **29**, 105108 (2017).

[14] E. Varga, J. Gao, W. Guo, and L. Skrbek, Intermittency enhancement in quantum turbulence in superfluid He 4, Phys. Rev. Fluids **3**, 094601 (2018).

[15] Y. Tang, S. Bao, T. Kanai, and W. Guo, Statistical properties of homogeneous and isotropic turbulence in He II measured via particle tracking velocimetry, Phys. Rev. Fluids **5**, 084602 (2020).

[16] G. Krstulovic, Grid superfluid turbulence and intermittency at very low temperature, Phys. Rev. E **93**, 063104 (2016).

[17] L. Biferale, D. Khomenko, V. L'vov, A. Pomyalov, I. Procaccia, and G. Sahoo, Turbulent statistics and intermittency enhancement in coflowing superfluid ^{4}He, Phys. Rev. Fluids **3**, 024605 (2018).

[18] L. Boué, V. L'vov, A. Pomyalov, and I. Procaccia, Enhancement of Intermittency in Superfluid Turbulence, Phys. Rev. Lett. **110**, 014502 (2013).

[19] V. Shukla and R. Pandit, Multiscaling in superfluid turbulence: A shell-model study, Phys. Rev. E **94**, 043101 (2016).

[20] A. Migdal, Clebsch confinement and instantons in turbulence, Int. J. Mod. Phys. A **35**, 2030018 (2020).

[21] K. R. Sreenivasan, A. Juneja, and A. K. Suri, Scaling Properties of Circulation in Moderate-Reynolds-Number Turbulent Wakes, Phys. Rev. Lett. **75**, 433 (1995).

[22] N. Cao, S. Chen, and K. R. Sreenivasan, Properties of Velocity Circulation in Three-Dimensional Turbulence, Phys. Rev. Lett. **76**, 616 (1996).

[23] R. Benzi, L. Biferale, M. V. Struglia, and R. Tripiccione, Self-scaling properties of velocity circulation in shear flows, Phys. Rev. E **55**, 3739 (1997).

[24] K. P. Iyer, S. S. Bharadwaj, and K. R. Sreenivasan, The area rule for circulation in three-dimensional turbulence, Proc. Natl. Acad. Sci. **118**, e2114679118 (2021).

[25] Q. Zhou, C. Sun, and K.-Q. Xia, Experimental investigation of homogeneity, isotropy, and circulation of the velocity field in buoyancy-driven turbulence, J. Fluid Mech. **598**, 361 (2008).

[26] K. P. Iyer, K. R. Sreenivasan, and P. K. Yeung, Circulation in High Reynolds Number Iisotropic Turbulence is a Bifractal, Phys. Rev. X **9**, 041006 (2019).

[27] N. P. Müller, J. I. Polanco, and G. Krstulovic, Intermittency of Velocity Circulation in Quantum Turbulence, Phys. Rev. X **11**, 011053 (2021).

[28] J. I. Polanco, N. P. Müller, and G. Krstulovic, Vortex clustering, polarisation and circulation intermittency in classical and quantum turbulence, Nat. Commun. **12**, 7090 (2021).

[29] L. Moriconi, Multifractality breaking from bounded random measures, Phys. Rev. E **103**, 062137 (2021).

[30] G. B. Apolinário, L. Moriconi, R. M. Pereira, and V. J. Valadão, Vortex gas modeling of turbulent circulation statistics, Phys. Rev. E **102**, 041102(R) (2020).

[31] J. Salort, B. Chabaud, E. Lévêque, and P.-E. Roche, Investigation of intermittency in superfluid turbulence, J. Phys.: Conf. Ser. **318**, 042014 (2011).

[32] B. Mastracci and W. Guo, An apparatus for generation and quantitative measurement of homogeneous isotropic turbulence in He II, Rev. Sci. Instrum. **89**, 015107 (2018).

[33] B. Mastracci and W. Guo, Exploration of thermal counterflow in He II using particle tracking velocimetry, Phys. Rev. Fluids **3**, 063304 (2018).

[34] J. I. Polanco and G. Krstulovic, Inhomogeneous distribution of particles in coflow and counterflow quantum turbulence, Phys. Rev. Fluids **5**, 032601(R) (2020).

[35] B. Mastracci and W. Guo, Characterizing vortex tangle properties in steady-state He II counterflow using particle tracking velocimetry, Phys. Rev. Fluids **4**, 023301 (2019).

[36] Y. Tang, S. Bao, and W. Guo, Superdiffusion of quantized vortices uncovering scaling laws in quantum turbulence, Proc. Natl. Acad. Sci. **118**, e2021957118 (2021).

[37] U. Giuriato and G. Krstulovic, Interaction between active particles and quantum vortices leading to Kelvin wave generation, Sci. Rep. **9**, 4839 (2019).

[38] U. Giuriato and G. Krstulovic, Active and finite-size particles in decaying quantum turbulence at low temperature, Phys. Rev. Fluids **5**, 054608 (2020).

[39] Y. Tang, W. Guo, V. S. L'vov, and A. Pomyalov, Eulerian and Lagrangian second-order statistics of superfluid ^{4}He grid turbulence, Phys. Rev. B **103**, 144506 (2021).

[40] S. R. Stalp, L. Skrbek, and R. J. Donnelly, Decay of Grid Turbulence in a Finite Channel, Phys. Rev. Lett. **82**, 4831 (1999).

[41] L. Biferale, D. Khomenko, V. L'vov, A. Pomyalov, I. Procaccia, and G. Sahoo, Local and nonlocal energy spectra of superfluid 3He turbulence, Phys. Rev. B **95**, 184510 (2017).

[42] J. Koplik and H. Levine, Vortex Reconnection in Superfluid Helium, Phys. Rev. Lett. **71**, 1375 (1993).

[43] G. P. Bewley, M. S. Paoletti, K. R. Sreenivasan, and D. P. Lathrop, Characterization of reconnecting vortices in superfluid helium, Proc. Natl. Acad. Sci. U.S.A. **105**, 13707 (2008).

[44] A. Villois, D. Proment, and G. Krstulovic, Irreversible Dynamics of Vortex Reconnections in Quantum Fluids, Phys. Rev. Lett. **125**, 164501 (2020).

[45] G. Krstulovic, Kelvin-wave cascade and dissipation in low-temperature superfluid vortices, Phys. Rev. E **86**, 055301(R) (2012).

[46] E. Fonda, D. P. Meichle, N. T. Ouellette, S. Hormoz, and D. P. Lathrop, Direct observation of Kelvin waves excited by quantized vortex reconnection, Proc. Natl. Acad. Sci. **111**, 4707 (2014).

[47] C. Nore, M. Abid, and M. E. Brachet, Decaying Kolmogorov turbulence in a model of superflow, Phys. Fluids **9**, 2644 (1997).

[48] H. Homann, O. Kamps, R. Friedrich, and R. Grauer, Bridging from Eulerian to Lagrangian statistics in 3D hydro- and magnetohydrodynamic turbulent flows, New J. Phys. **11**, 073020 (2009).

[49] R. J. Donnelly and C. F. Barenghi, The observed properties of liquid helium at the saturated vapor pressure, J. Phys. Chem. Ref. Data **27**, 1217 (1998).

[50] L. Boué, V. S. L'vov, Y. Nagar, S. V. Nazarenko, A. Pomyalov, and I. Procaccia, Energy and vorticity spectra in turbulent superfluid ^{4}He from T $= 0$ to T$_\lambda$, Phys. Rev. B **91**, 144501 (2015).

[51] J. I. Polanco, N. P. Müller, and G. Krstulovic, Circulation.jl: Tools for computing velocity circulation statistics from periodic 3D Navier–Stokes and Gross–Pitaevskii fields, Zenodo (2021), https://doi.org/10.5281/ZENODO.5578953.

[52] F. Anselmet, Y. Gagne, E. J. Hopfinger, and R. A. Antonia, High-order velocity structure functions in turbulent shear flows, J. Fluid Mech. **140**, 63 (1984).

[53] W. F. Vinen and J. J. Niemela, Quantum turbulence, J. Low Temperature Physics **128**, 167 (2002).

[54] P. Švančara, D. Duda, P. Hrubcová, M. Rotter, L. Skrbek, M. L. Mantia, E. Durozoy, P. Diribarne, B. Rousset, M. Bourgoin, and M. Gibert, Ubiquity of particle–vortex interactions in turbulent counterflow of superfluid helium, J. Fluid Mech. **911**, 22 (2021).

4.5 Two-dimensional quantum turbulence

Intermittency of velocity circulation statistics in three-dimensional (3D) quantum turbulence (QT) displays a similar behavior as in 3D classical turbulence (CT). Naturally, it would be interesting to understand the circulation statistics two-dimensional (2D) quantum turbulence. In 2D fluids, as a consequence of the absence of vortex stretching, energy is transferred towards large scales and enstrophy towards small scales (see chapter 2). These phenomena are known as inverse energy cascade (IEC), with the energy spectrum satisfying $E(k) \sim k^{-5/3}$, and direct enstrophy cascade (DEC), with the energy spectrum satisfying $E(k) \sim k^{-3}$, obviating logarithmic corrections. It has been observed through DNS of the NS equations that the IEC presents a self-similar scaling in the structure functions, in a sharp contrast with 3D turbulence where the system is intermittent, displaying anomalous exponents [BE12]. The concentration of energy at large scales leads to the formation of vortex clusters, also known as Onsager cluster [GRY+19; JGS+19].

In this section, we show some preliminary results of the scaling of velocity circulation in 2D decaying quantum turbulence. We perform two sets of DNS using the GP equation with 8192^2 collocation points. Each set consists of an ensemble of 8 statistically equivalent flows. In the first set of simulations, we generate an initial condition with most of its energy concentrated at the largest scales $k_f \approx 1 - 2$ to study the DEC. In the second set, the initial energy is concentrated at intermediate scales $k_f \approx 30 - 40$ to focus on the IEC. To initialize the flow, we make use of the Clebsch potentials to generate a velocity field with a minimized acoustic contribution, which I developed during my Licenciatura in Buenos Aires [MBA+20]. A typical visualization of the quantum vortices extracted from the full wavefunction ψ of these two different quantum flows is shown in Fig. 4.7. The large-scale eddy turnover time of each flow is defined using the injection scale as $\tau = L_f / v_{\rm rms}$. The dynamics of the DEC is typically much faster than the IEC. As a consequence, we evolved the flow excited at intermediate scales for longer times to be able to study
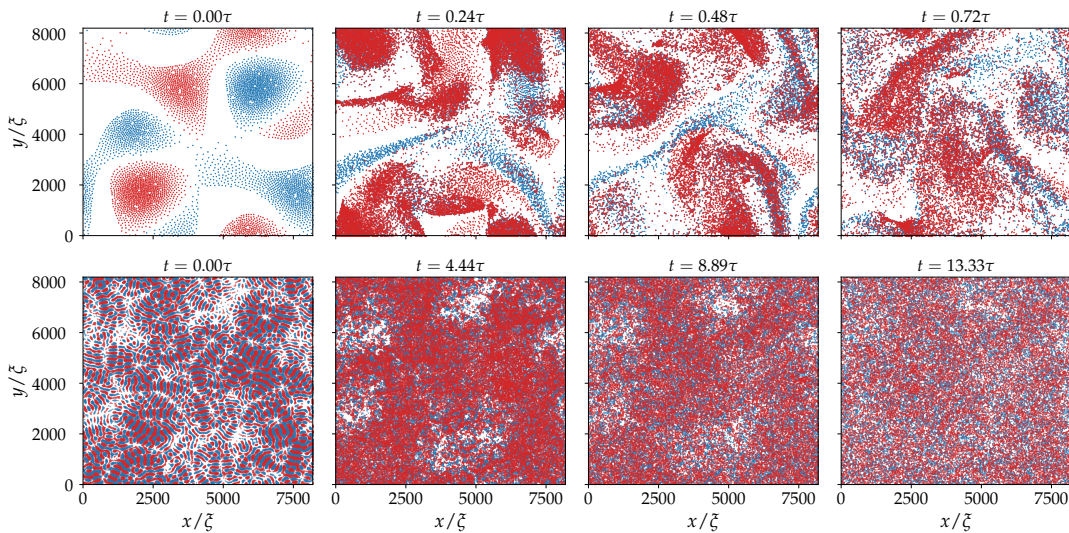

Figure 4.7: Evolution of the point vortices extracted from the wavefunction obtained from DNS of the GP equation using 8192^2 grid points. Red and blue points correspond to a positive and a negative vortices, respectively. Top panels: Evolution for the initial condition at large scales. Bottom panels: Evolution for the initial condition at intermediate scales.
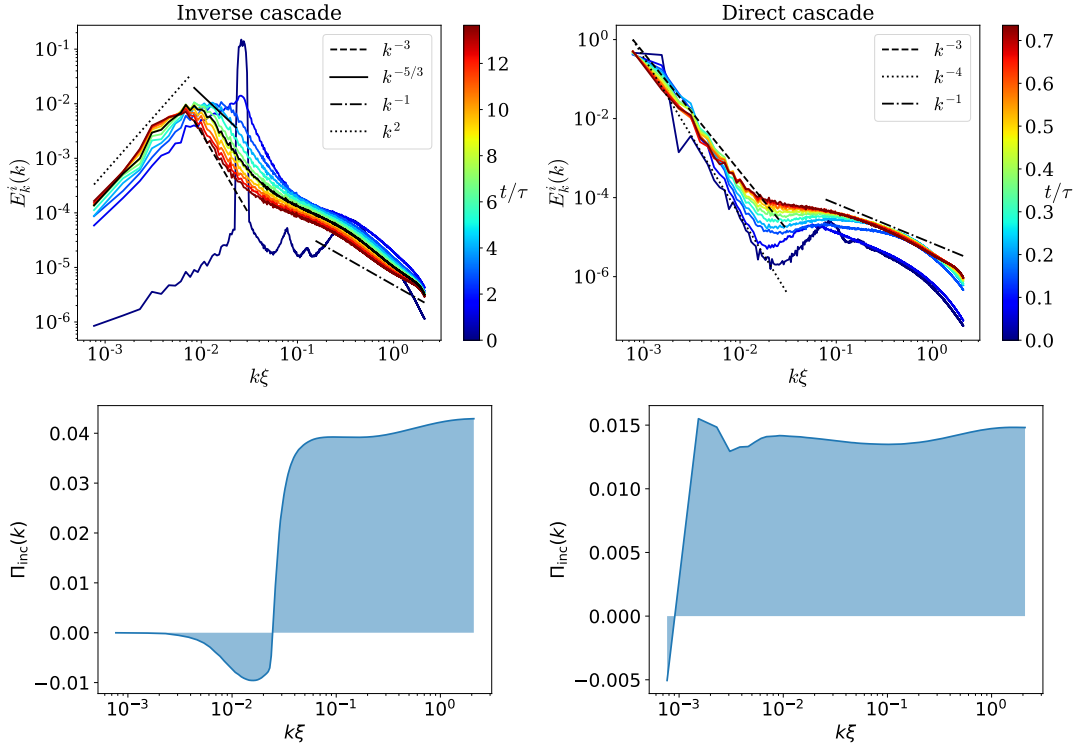
Figure 4.8: Top panels: Incompressible energy spectrum at different times for (left) the inverse cascade and (right) the direct cascade. Bottom panels: Time-averaged incompressible energy flux for the inverse cascade (left) and direct cascade (right).

the IEC. Note that the initial number of vortices for the flow excited at intermediate scales is much larger than the one forced at large scales. As the system evolves, vortices start to interact and annihilate, and the number of vortices at long times decreases.

The incompressible energy spectra at different times averaged over the whole ensemble of runs are shown in Fig. 4.8. For the IEC, we observe that the initial energy is concentrated at intermediate scales and, as the system evolves, energy is transferred towards larger scales. This is manifested in the incompressible energy flux, defined as

$$\Pi_{\text{inc}}(k) = -\frac{\text{d}}{\text{d}t} \int_0^k E_k^i(\tilde{k}) \text{d}\tilde{k}, \tag{4.42}$$

which takes negative values for $k > k_f$. Another quantity that indicates the presence of an IEC is the evolution of the integral length scale. In particular, it is shown that the peak of the incompressible kinetic energy spectrum starts at $k_{\text{peak}}\xi \approx 0.025$ and at a later stage is found at around $k_{\text{peak}}\xi \approx 0.007$. At the largest scales, we observe a scaling k^2 which should not be confused to the scaling of a thermalized system, as in 2D it goes as k^1. In particular, the scaling in this region might depend on the type of forcing or, in this case, on the initial condition [AB19]. Between k_{peak} and the intervortex wavenumber, there seems to be a range of scales in which the spectrum develops a k^{-3} power law associated to the direct enstrophy cascade, which is better developed in the set of simulations initialized at large scales. At small scales, it follows a scaling closer to k^{-1} given by the velocity field generated by individual vortices. However, we observe no development of $k^{-5/3}$ power law. This can be explained as the total energy associated to a developed inverse cascade is
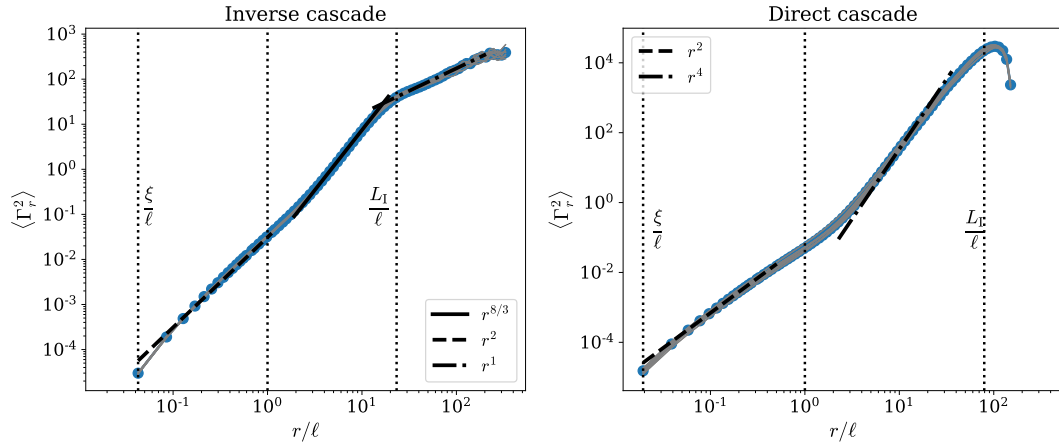
Figure 4.9: Circulation variance for the (left) inverse and (right) direct cascades. In gray are the different realizations of the flow, and in blue the ensemble average.

$$E = \int_{k_0}^{k_f} E(k)\mathrm{d}k = \frac{3C}{2}\epsilon^{2/3}(k_0^{-2/3} - k_f^{-2/3}), \qquad (4.43)$$

with C a dimensionless constant, k_0 the largest scale of the system and ϵ the energy flux. In the case that $k_0 \ll k_f$, it can be approached as $E \approx 3C(\epsilon/k_0)^{2/3}/2$. If the injected initial energy is smaller than this value, the IEC will not achieve the largest scale of the system and the energy spectrum will not be fully developed. To observe the Kolmogorov-like power law, one should either increase the injected energy or decrease the value of k_f, reducing the inverse inertial range. The results presented here are still an ongoing work, and we plan to perform several simulations with different initial conditions in the near future.

One of the main advantages of velocity circulation is that this integral quantity is able to display clear power laws over the range of scales. We study then the statistics of velocity circulation over squared loops of different sizes. Figure 4.9 shows the circulation variance averaged over a time window and the ensemble of runs, as a function of the loop size normalized by the intervortex distance ℓ. For both the DEC and the IEC at small scales, we recover the trivial scaling given by single vortex lines $\langle \Gamma^p \rangle \sim r^2$, proportional to the probability of finding a vortex inside the loop. We are interested however in the behavior at large scales, where the formation of coherent structure might display a similar behavior as in classical turbulence. For instance, for the inverse cascade, between the intervortex distance and the integral length scale L_I, there is a scaling law $r^{8/3}$ associated to an inverse energy cascade. This is surprising as the $k^{-5/3}$ scaling is not clearly observed in the energy spectrum. At scales larger than the integral scale $r > L_I$, we observe a power-law scaling r^1 associated to the k^2 energy spectrum, that is smaller than the scaling of uncorrelated structures. For the direct cascade, the energy spectrum $E(k) \sim k^{-3}$ is associated to the scaling of velocity increments of a smooth field $\langle \delta v_r^2 \rangle \sim r^2$. Therefore, one would expect a scaling for the circulation variance $\langle \Gamma_r^2 \rangle \sim r^4$. This is not exactly the case for the data shown in Fig. 4.9, that seems to present a less steep scaling [Kra67; BE12].

Time and ensemble averaged moments of circulation are shown in Fig. 4.10. We study the moments of the absolute value of circulation to avoid cancellation events that considerably reduce the amplitude and the scaling properties. For the inverse cascade we observe almost no deviations from Kolmogorov scaling on the range of scales of the inverse cascade. This becomes evident by studying the local slopes
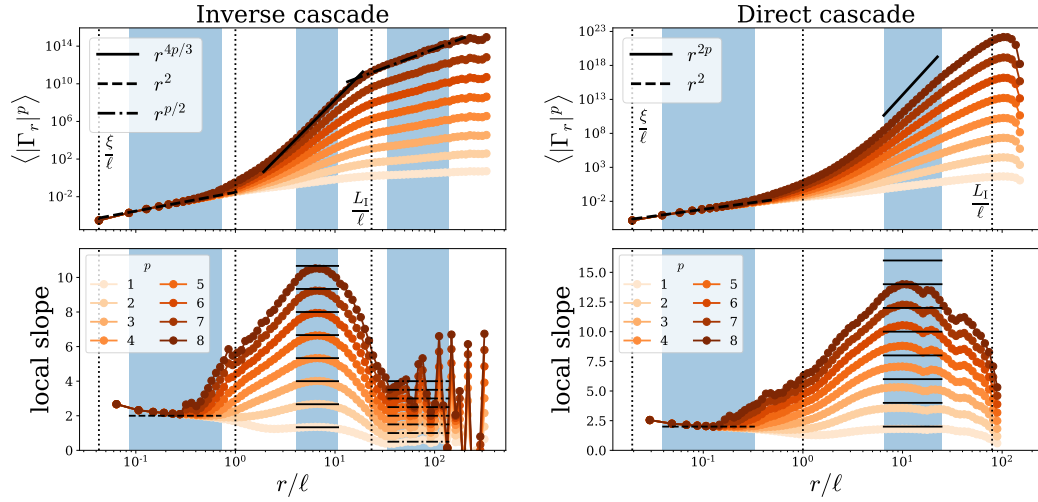
Figure 4.10: Circulation moments averaged over 8 different flow realizations and in time for (left) the inverse cascade and (right) the direct cascade. The bottom panels show the local slopes given by $d\log(\langle|\Gamma_r|^p\rangle)/d\log r$.
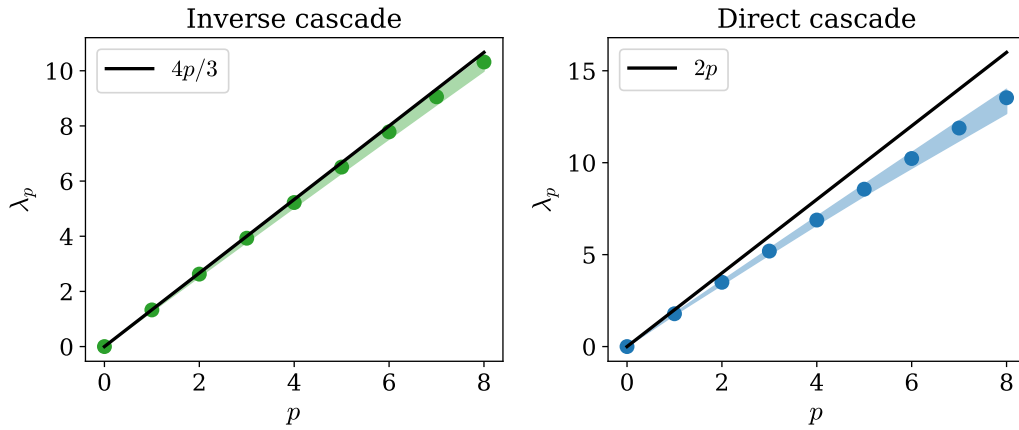

Figure 4.11: Scaling exponents of velocity circulation moments for (left) the direct cascade and (right) the inverse cascade.

$d\log(\langle|\Gamma_r|^p\rangle)/d\log r$. On the other hand, for the direct cascade at large scales, we clear observe some deviation from the scaling of a smooth field $\langle|\Gamma_r|^p\rangle \sim r^{2p}$. The scaling exponents of the circulation moments are shown in Fig. 4.11. As already discussed, the direct enstrophy cascade displays an intermittent behavior that deviates from the smooth scaling. In contrast, for the inverse cascade we observe the expected self-similar scaling that is also recovered for the structure functions in classical turbulence [BE12]. These preliminary results are encouraging and are now being contrasted with NS data provided by the group of G. Boffetta.

Chapter 5

Vortex nucleation in a model with rotons

In this chapter, we characterize the process of vortex nucleation in the generalized Gross–Pitaevskii model we introduced in chapter 3. We present the publication "Critical velocity for vortex nucleation and roton emission in a generalized model for superfluids" [MK22]. Using a branch following Newton-Raphson method, we compute the bifurcation diagrams of stable and unstable stationary solutions for moving disks of different diameters. Thus, we can determine the critical velocity predicted by the Landau criterion for superfluidity in a model with rotons. In particular, we distinguish the process of vortex nucleation from the roton emission.

5.1 Landau criterion for superfluidity

As a superfluid at zero temperature has no viscosity, a moving object would experience no drag force. Landau proposed that this picture of superfluidity is valid only for low velocities, and that there exists a critical velocity above which the moving object would generate elementary excitations, losing part of its kinetic energy. This idea is known as Landau criterion for superfluidity [LL87].

In chapter 1, we formally introduced this criterion, showing that the spontaneous creation of an elementary excitation with energy $\epsilon_{\mathbf{p}}$ and momentum $\mathbf{p}$ in a superfluid moving at a velocity $\mathbf{u}$ is energetically favorable if it satisfies relation (1.2) [PS08; PS16]. Let us rewrite this relation in terms of the dispersion relation of the superfluid $\omega(\mathbf{k}) = \epsilon_{\mathbf{p}}/\hbar$ and the wavenumber $\mathbf{k} = \mathbf{p}/\hbar$ as

$$\omega(\mathbf{k}) + \mathbf{k} \cdot \mathbf{u} < 0. \tag{5.1}$$

This condition is satisfied when $|\mathbf{u}| > \omega(\mathbf{k})/|\mathbf{k}|$ and $\mathbf{k} \cdot \mathbf{u} < 0$, that is, when the direction of propagation of the excitation is opposite to the fluid, and the fluid velocity exceeds the critical value

$$u_{\mathrm{c}} = \min_{\mathbf{k}} \frac{\omega(\mathbf{k})}{|\mathbf{k}|}. \tag{5.2}$$

Below this velocity, it is impossible to create excitations and, consequently, there is no mechanism for degrading the motion of impurities, so the liquid will exhibit superfluidity.

Landau criterion for superfluidity shows that the dispersion relation of the condensate plays an important role for the definition of superfluidity. Let us consider some examples. In an ideal gas of bosons with mass m, the dispersion relation of free particles is $\omega(\mathbf{k}) = \hbar k^2/(2m)$ leading to a critical velocity $u_{\mathrm{c}} = 0$. This result shows
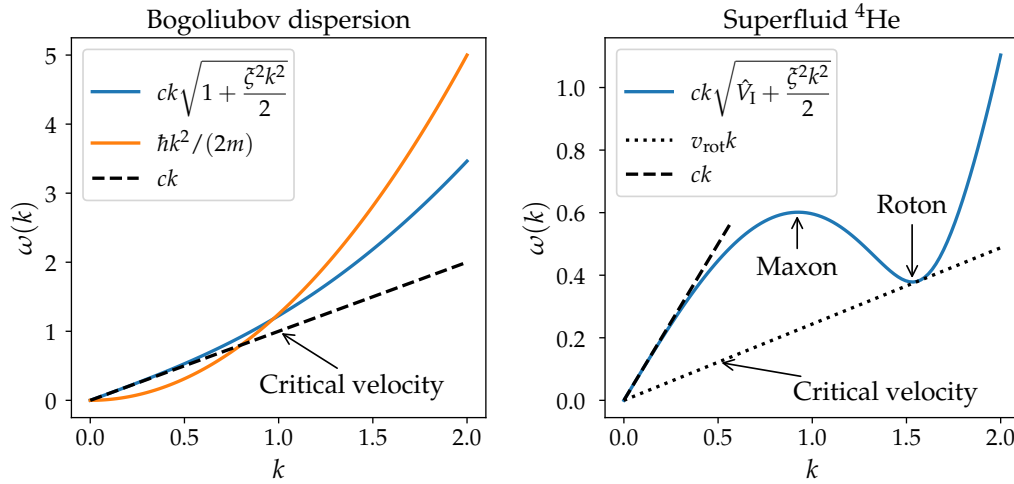
Figure 5.1: Schematic picture of the dispersion relation in (a) an ideal (orange) and a weakly interacting (blue) BEC and (b) superfluid helium. We also indicate the critical velocity of the system, with $v_{\text{rot}} \approx 0.25c$.

that in an ideal Bose gas superfluidity is not possible. For a weakly interacting Bose gas, the system obeys the Bogoliubov dispersion relation

$$\omega_{\text{B}}(k) = ck\sqrt{1 + \frac{\xi^2 k^2}{2}}, \tag{5.3}$$

where we recall that $c = \sqrt{gn_0/m}$ is the speed of sound and $\xi = \hbar/\sqrt{2mgn_0}$ the healing length of the superfluid, with m the mass of the bosons, g the coupling between bosons and n_0 the particles density of the ground state. Replacing Bogoliubov dispersion into Eq. (5.2) leads to a critical velocity $u_{\text{c}} = c$, exciting long-wavelength sound waves.

One last important example is superfluid helium. The dispersion relation in this system differs from Bogoliubov dispersion relation, displaying a maximum and a minimum known as maxon and roton, respectively (see Fig. 5.1). The latter prescribes Landau critical velocity. In superfluid helium, the critical velocity is around $u_{\text{c}} \approx 60 \text{ ms}^{-1}$, which is around $c/4$ with $c = 238 \text{ ms}^{-1}$ the speed of sound of ^{4}He, indicating that rotons are more easily excited than phonons. The dispersion relation in this system can be reproduced in the gGP model using a non-local interaction potential V_{I} as described in chapter 3.

Landau criterion is based only on considerations of energy and momentum, and provides a lower bound for u_{c}. However, it only involves excitations that are described by the dispersion relation, while other excitations such as quantum vortices are not taken into account. In particular, it has been observed numerically and experimentally that when an object of finite size moves through the condensate, it can nucleate quantum vortices in its wake [FPR92; HB97; RKO+99]. The critical value at which this process takes place depends on the size and the shape of the obstacle, and is typically smaller than the speed of sound. One possible explanation of this smaller value is that the fluid exceeds locally the speed of sound around the moving obstacle.

5.2 Publication: *"Critical velocity for vortex nucleation and roton emission in a generalized model for superfluids"*

In this work, we study the process of vortex nucleation in two and three dimensions in the gGP equation. We use this model to investigate how the roton minimum in the excitation spectrum modifies the superfluid critical velocity. We also compare this behavior for different values of the high-order non-linearities with a local interaction (without rotons).

We perform different sets of numerical simulations in 2D in which we include a disk-shaped external potential of diameters between $D = 5\xi$ and $D = 400\xi$ moving at different Mach numbers $M = U/c$ to determine if it introduces any excitation in the superfluid. The maximum amplitude V_0 of the external potential is chosen much larger than the chemical potential μ of the condensate to completely deplete the superfluid. Applying a Newton-Raphson method, we recover the stable stationary solutions of the condensate, in which only the obstacle is moving, and unstable solutions, in which the obstacle is accompanied by two, four, or six vortices. One should not confuse these unstable solutions that initially count with some vortices with the process of vortex nucleation. In this case, the evolution of the moving obstacle and the vortices is stationary, and the moving obstacle does not excite any vortices in its wake. Computing the energy branches of stable and unstable solutions leads to the characterization of bifurcation diagrams that determine the critical velocity of the superfluid.

We first analyze the case with a local interaction potential (without rotons) for different values of the non-linearities. We determine that the critical Mach number $M_c = U_c/c$ decreases for increasing values of the non-linear parameters. Note that the absolute value of the speed of sound c also increases with these parameters, so the absolute critical velocity also increases. In the local GP model, the only way to break down superfluidity is by the nucleation of quantum vortices. When the roton minimum is introduced, we observe two different behaviors depending on the size of the obstacle. For large diameters $D \gtrsim 80\xi$, the critical velocity follows a similar behavior as in the local case, and is determined by the nucleation of vortices in the wake of the moving obstacle. For small diameters $D \lesssim 80\xi$, the critical velocity saturates to the roton velocity given by Landau criterion for superfluidity $u_c \approx 0.25c$. In this regime, there is a range of velocities in which the obstacle excites only rotons and there is no quantum vortex nucleation. Indeed, we verify that the wavenumber of these excitations satisfy Eq. (5.1) for a velocity $\mathbf{U} = U\mathbf{y}$. Finally, we also verify that the nucleation of vortices in three dimensions is qualitatively the same as in 2D.

Critical velocity for vortex nucleation and roton emission in a generalized model for superfluids

Nicolás P. Müller and Giorgio Krstulovic
Université Côte d'Azur, Observatoire de la Côte d'Azur, CNRS, Laboratoire Lagrange,
Boulevard de l'Observatoire CS 34229, F 06304 Nice Cedex 4, France

We study numerically the process of vortex nucleation in the wake of a moving object in superfluids using a generalized and nonlocal Gross-Pitaevskii model. The nonlocal potential is set to reproduce the roton minimum present in the excitation spectrum of superfluid helium. By applying numerically a Newton-Raphson method we determine the bifurcation diagram for different types of nonlinearities and object sizes which allow for determining the corresponding critical velocities. In the case of a nonlocal potential, we observe that for small object sizes the critical velocity is simply determined by the Landau criterion for superfluidity, whereas for large objects there is little difference between all models studied. Finally, we study dynamically in two and three dimensions how rotons and vortices are excited in the nonlocal model of superfluid.

I. INTRODUCTION

One of the most interesting features of superfluids is their total absence of viscosity. This means that a particle traveling in a superfluid experiences no drag force and moves freely with no friction. However, it took not long for Landau to realize that if a moving impurity exceeds a certain velocity, known as Landau's critical velocity [1]

$$v_L = \min_{\boldsymbol{k}} \frac{\omega(\boldsymbol{k})}{|\boldsymbol{k}|}, \tag{1}$$

with $\omega(\boldsymbol{k})$ being the dispersion relation of the superfluid and $\boldsymbol{k}$ being the wave vector, it generates the spontaneous creation of elementary excitations that act as a dissipative mechanism on the impurity. This is known as Landau's criterion for superfluidity. In a noninteracting Bose-Einstein condensate (BEC), the dispersion relation is proportional to k^2, so Landau's velocity is zero and superfluidity cannot take place. In a weakly interacting BEC, the system follows the Bogoliubov dispersion relation [2] and Landau's velocity is given by the speed of sound of the superfluid $v_L = c$, while in superfluid ^{4}He, Landau's critical velocity is smaller than the speed of sound as a consequence of the well-known roton minimum appearing in its excitation spectrum [3,4].

In classical compressible fluids, velocities above the speed of sound would lead to the formation of shock waves [5]. However, shock waves in superfluids are suppressed due to the dispersive nature of the system. Instead, these structures are replaced by the nucleation of vortices. In the early 90s it was first observed numerically in weakly interacting BECs that a particle traveling through a superfluid may experience a drag force if it exceeds a critical velocity v_c [6], nucleating vortices in its wake. This critical velocity was found to be smaller than the speed of sound. The reason for this is that the local velocity of the flow exceeds the speed of sound somewhere around the surface of the obstacle. Since then, several efforts have been carried out to provide a better description of the mechanisms of vortex nucleation, in particular, in the

determination of the critical velocity of superfluids and its dependence on the size of the moving obstacle [7–13]. The nucleation of vortices is a process that takes place in different quantum flows, like BECs [14,15], superfluid of light [16,17], and superfluid ^{4}He [18]. Numerical simulations in models of BECs and dipolar BECs showed that the obstacle can create regular or irregular vortex patterns in its wake, in particular, the creation of a Bénard-von Kármán vortex street [19–22].

Understanding the process of vortex nucleation is very important for its practical applications. For instance, it can be used as a mean of injecting vortices and energy into a system as in grid turbulence [23,24] and is also a relevant process on the study of lift force of a flow around an airfoil [25]. The study of vortices in superfluid ^{4}He presents some difficulties given that there is not a simple microscopic description of it. However, it is possible to study some of its phenomenology assuming a nonlocal interaction between the bosons constituting the superfluid [26–29]. In this framework, a moving obstacle is allowed to emit some density excitations known as rotons [29–31].

In this work, we focus on the determination of the critical velocity for the nucleation of vortices in different zero-temperature models for superfluids. In particular, we study a model that better describes weakly interacting BECs where compressibility effects can vary and a model that incorporates a roton minimum in the excitation spectrum. In particular, we show the differences between the vortex nucleation and roton creation processes. In Sec. II we introduce the different models used in this work and, in particular, with the presence of a moving obstacle. In Sec. III we present the results obtained in the study of the vortex nucleation in these different models both in the stationary and dynamical regimes in two and three dimensions and, finally, in Sec. IV we present our conclusions.

II. MODEL FOR SUPERFLUID ^{4}He

A superfluid at zero temperature constituted by bosons of mass m can be described by the generalized Gross-Pitaevskii

(gGP) equation [26,28,32]

$$
i\hbar \frac{\partial \psi}{\partial t} = -\frac{\hbar^2}{2m}\nabla^2\psi - \mu(1+\chi)\psi
$$
$$
+ g\left(\int V_\mathrm{I}(\boldsymbol{x}-\boldsymbol{y})|\psi(\boldsymbol{y})|^2 d^3y\right)\psi + g\chi\frac{|\psi|^{2(1+\gamma)}}{n_0^\gamma}\psi,
$$
$$(2)$$

where ψ is the macroscopic wave function of the condensate, μ is the chemical potential, $g = 4\pi\hbar^2 a_s/m$ is the coupling constant fixed by the s-wave scattering length a_s, and n_0 is the particle density of the ground state. The last term is a high-order correction of the mean-field approximation, with χ and γ being two dimensionless parameters corresponding to its amplitude and order, respectively. The chemical potential has been renormalized so that $|\psi_0|^2 = n_0$ remains the ground state of the system. The interaction potential between bosons V_I is normalized such that $\int V_\mathrm{I}(\boldsymbol{x})d^3x = 1$. Note that by choosing a δ-function interaction potential $V_\mathrm{I}(\boldsymbol{x}-\boldsymbol{y}) = \delta(\boldsymbol{x}-\boldsymbol{y})$, and setting $\chi = 0$, one recovers the standard Gross-Pitaevskii (GP) equation [1]. We refer to the local gGP model as the case where the interaction potential is a δ function, but the beyond-mean-field corrections are not neglected, i.e., $\chi \neq 0$, the local gGP model.

Perturbing the system around the ground state recovers the generalized Bogoliubov dispersion relation of the system

$$
\omega_B(\boldsymbol{k}) = ck\sqrt{\frac{\xi^2 k^2}{2} + \frac{\hat{V}_\mathrm{I}(\boldsymbol{k}) + \chi(\gamma+1)}{1+\chi(\gamma+1)}}, \qquad (3)
$$

where k is the wave number of the perturbation and $\hat{V}_\mathrm{I} = \int e^{i\boldsymbol{k}\cdot\boldsymbol{r}}V_\mathrm{I}(\boldsymbol{r})d^3r$ is the Fourier transform of the interaction potential normalized such that $\hat{V}_\mathrm{I}(k=0) = 1$. The speed of sound and the healing length of the system are respectively given by

$$
c = c_0\sqrt{f_{\chi,\gamma}}, \qquad (4)
$$

$$
\xi = \frac{\xi_0}{\sqrt{f_{\chi,\gamma}}}, \qquad (5)
$$

with $c_0 = \sqrt{gn_0/m}$ and $\xi_0 = \hbar/\sqrt{2mgn_0}$ being the speed of sound and the healing length of the standard GP model, respectively. The factor $f_{\chi,\gamma} = 1 + \chi(\gamma+1)$ is a rescaling parameter of the system. Larger values of χ or γ correspond to stronger interactions between bosons, thus making the fluid more incompressible. As a consequence, the speed of sound increases at the same rate as the healing length decreases. Note that the product between c and ξ is independent of the high-order corrections and is associated with the quanta of circulation $\kappa = c\xi 2\pi\sqrt{2} = h/m$ that depends only on the mass of the bosons constituting the superfluid.

The gGP model (2) can be rewritten in terms of the relevant parameters of the system as

$$
\frac{\partial \psi}{\partial t} = -i\frac{c}{\xi\sqrt{2}f_{\chi,\gamma}}\left[-f_{\chi,\gamma}\xi^2\nabla^2\psi - (1+\chi)\psi\right.
$$
$$
\left. + \frac{1}{n_0}(V_\mathrm{I}*|\psi|^2)\psi + \frac{\chi}{n_0^{\gamma+1}}|\psi|^{2(\gamma+1)}\psi\right]. \qquad (6)
$$

This generalized model can be used to provide a better phenomenological description of different systems like superfluid ^{4}He [28], dipolar gases [33], or even the supersolid state of matter [34]. In the particular case of superfluid ^{4}He, the following isotropic potential [27,32],

$$
\hat{V}_\mathrm{I}(\boldsymbol{k}) = \left[1 - V_1\left(\frac{k}{k_\mathrm{rot}}\right)^2 + V_2\left(\frac{k}{k_\mathrm{rot}}\right)^4\right]\exp\left(-\frac{k^2}{2k_\mathrm{rot}^2}\right), \quad (7)
$$

can reproduce the excitation spectrum observed experimentally [4,35]. Here $k_\mathrm{rot} = 2\pi/a_\mathrm{rot}$ is the wave number associated with the roton minimum length scale of ^{4}He, $a_\mathrm{rot} = 3.26$ Å, and together with the dimensionless parameters, V_1 and V_2 are determined to mimic its experimental dispersion relation [35]. In this work, this fit was done by considering that Eq. (6) is written in terms of the healing length of ^{4}He, $\xi = 0.8$ Å, and the turnover time at small scales, $\tau = \xi/c = 3.36 \times 10^{-13}$ s, being the speed of sound in ^{4}He, $c = 238$ ms^{-1}. Using this system of units it is possible to determine the values of V_1, V_2, and k_rot to recover the roton minimum in the excitation spectrum [28]. The beyond-mean-field correction was implemented to avoid the development of instabilities of wave numbers close to the roton minimum [27]. In the following sections, all simulations with a nonlocal interaction were done with $\gamma = 2.8$, $\chi = 0.1$, $V_1 = 4.54$, $V_2 = 0.01$, and $k_\mathrm{rot}\xi = 1.638$. This particular choice of γ is set so that the long-wavelength sound waves are proportional to $\rho^{2.8}$ according to experiments [26,36].

A. Superfluid with a moving obstacle

In superfluid ^{4}He, Landau's critical velocity is determined by the roton minimum in the excitation spectrum and is associated with the emission of density fluctuations. In the case of an obstacle moving with a velocity $\boldsymbol{U} = U\hat{y}$, assuming energy and momentum conservation, Landau's criterion for superfluidity can be rewritten as [31]

$$
\boldsymbol{k}\cdot\boldsymbol{v} - \omega(\boldsymbol{k}) = k_y U - \omega(\boldsymbol{k}) = 0, \qquad (8)
$$

showing that there is some anisotropy and a range of excited wave numbers.

We can describe an obstacle moving in a superfluid with the Gaussian potential $V_\mathrm{obs}(\boldsymbol{r}-\boldsymbol{U}t) = V_0 e^{-\frac{1}{2}\frac{|\boldsymbol{r}-\boldsymbol{U}t|^2}{\Delta^2}}$, which describes a disk (sphere) in two (three) dimensions. The size of the obstacle in the Thomas-Fermi approximation is determined by $\Delta = D/[2\sqrt{2\log(V_0)}]$, with D being its diameter. The amplitude of the potential is chosen as $V_0 \gg 1$ so that the obstacle completely depletes the superfluid. Thus, the equation of motion of a superfluid with a moving obstacle becomes

$$
\frac{\partial \psi}{\partial t} = -i\frac{c}{\xi\sqrt{2}f_{\chi,\gamma}}\left\{-f_{\chi,\gamma}\xi^2\nabla^2 - [1+\chi - V_\mathrm{obs}(\boldsymbol{r}-\boldsymbol{U}t)]\right.
$$
$$
\left. + \frac{1}{n_0}(V_\mathrm{I}*|\psi|^2) + \frac{\chi}{n_0^{\gamma+1}}|\psi|^{2(\gamma+1)}\right\}\psi, \qquad (9)
$$

with the total energy of the system being

$$\mathcal{E} = \frac{c^2}{n_0 V f_{\chi,\gamma}} \int \left\{ f_{\chi,\gamma} \xi^2 |\nabla \psi|^2 + \frac{|\psi|^2}{2n_0} (V_{\mathrm{I}} * |\psi|^2) \right.$$

$$\left. - [1 + \chi - V_{\mathrm{obs}}(\boldsymbol{r} - \boldsymbol{U}t)] |\psi|^2 + \frac{\chi |\psi|^{2(\gamma+2)}}{n_0^{\gamma+1}(\gamma+2)} \right\} d^3 r. \tag{10}$$

To determine the critical velocity of the superfluid, it is convenient to study solutions of the system that are stationary in the frame of reference of the moving particle [7,11]. To do this, we look for steady solutions of the wave function of the form $\psi(\boldsymbol{r}, t) = \Psi(\boldsymbol{r} - \boldsymbol{U}t) = \Psi(\tilde{\boldsymbol{r}})$ with boundary conditions such that $\psi \xrightarrow{r \to \infty} \sqrt{n_0}$. The equation obtained after performing this transformation is

$$\boldsymbol{U} \cdot \nabla_{\tilde{r}} \Psi = i \frac{c}{\xi \sqrt{2} f_{\chi,\gamma}} \left\{ - f_{\chi,\gamma} \xi^2 \nabla^2 - [1 + \chi - V_{\mathrm{obs}}(\tilde{\boldsymbol{r}})] \right.$$

$$\left. + \frac{1}{n_0} (V_{\mathrm{I}} * |\Psi|^2) + \frac{\chi}{n_0^{\gamma+1}} |\Psi|^{2(\gamma+1)} \right\} \Psi. \tag{11}$$

III. VORTEX NUCLEATION

In this section, we study the different dynamics of an object moving at a constant velocity of $\boldsymbol{U} = U\hat{y}$ in a superfluid at rest. We determine the critical velocity U_c or the critical Mach number $M_c = U_c/c$ of the system for different diameters D of the disk, above which it starts nucleating vortices. To do this, we perform two-dimensional numerical simulations with periodic boundary conditions of the gGP model with a moving particle (9). In all cases we solve the system with a spatial resolution of $\Delta x = \xi$ in a squared domain with a size of $L > 5D$ to minimize spurious effects that may surge as a consequence of periodicity, using a number of collocation points that go from 512^2 to 2048^2. We study the differences of the phenomenon of vortex nucleation for the standard GP model, the local gGP (9) for different values of χ and γ, and the nonlocal gGP with the interaction potential (7) that supports roton excitations.

A. Critical velocity in the local gGP model

As discussed in Sec. II A, the determination of the critical velocity can be done by studying the stationary solutions of the system. A superfluid with a moving obstacle has different sets of steady solutions, some of them stable and some others unstable [7,11]. The stable stationary solutions of the system can be obtained by solving the imaginary time gGP model, i.e., by replacing $t \to -it$ in Eq. (11). However, this method only recovers states with minimal energy; that is, it can only be used to recover stable stationary solutions. Therefore, we implement a Newton-Raphson method to be also able to obtain unstable stationary solutions of the system (see the Appendix for details).

Figure 1 shows different energy branches $\mathcal{E} - \mathcal{E}$ ($U = 0$) of stationary solutions obtained as the Mach number of the disk $M = U/c$ varies. Each of these values was obtained using a Newton-Raphson method to solve the standard GP (local
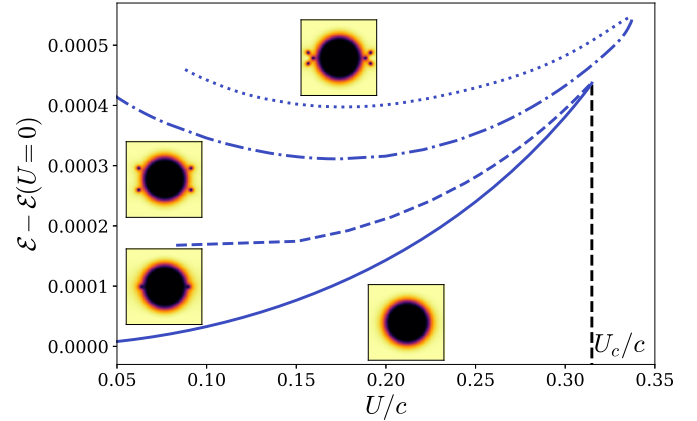

FIG. 1. Bifurcation diagram of the energy of stationary solutions in the standard GP model with a disk diameter of $D = 40\xi$ moving at different velocities U. The stable branch (solid line) and the two-vortex (dashed line), four-vortex (dot-dashed line), and six-vortex (dotted line) unstable branches are shown. The insets show the density fields of the different branches. Dark colors correspond to regions where the density vanishes.

interaction potential with $\chi = 0$) and with a disk diameter of $D = 40\xi$. The other energy branches correspond to unstable solutions in which two (dashed line), four (dot-dashed line), or six (dotted) vortices are nucleated. The time evolution of each of these solutions is stationary in the frame of reference of the moving disk; i.e., the number of vortices in the system will not change. The interesting aspect of the bifurcation diagram of the system is that it provides a way to determine the critical Mach of the superfluid M_c for a particular disk size D. Such a value corresponds to the Mach number where the stable and unstable branches merge together, being in this case $M_c \approx 0.315$. Beyond this critical velocity there is no stationary solution, meaning that the disk would nucleate vortices and experience some drag force. The bifurcation diagram observed here is similar to the one obtained in previous works [7,11], but the exact values may differ due to a different choice on the potential describing the disk.

To understand how the high-order nonlinear term affects the dynamics of the system, we study the critical velocity U_c of the superfluid for different values of χ and γ. Here, we use in all cases a local interaction potential of $V_{\mathrm{I}}(\boldsymbol{x} - \boldsymbol{y}) = \delta(\boldsymbol{x} - \boldsymbol{y})$, a disk of diameter of $D = 5\xi$, and values of χ that go between 1 and 5 with $\gamma = 1$ or $\gamma = 2.8$. We also compare with the standard GP model ($\chi = 0$). Note that the speed of sound and the healing length of the system depend on the values of χ and γ according to Eqs. (4) and (5). In particular, we fixed in all the simulations $c = 1$ and $\xi = \Delta x$. Therefore, the speed of sound varies between $c = 1c_0$ ($\chi = 0$) and $c = 4.54c_0$ (for $\chi = 5$ and $\gamma = 2.8$). As a consequence, the critical velocity U_c in the gGP system can take relative values that are larger than c_0, as shown in Fig. 2(a), where solid and dashed lines correspond to stable and two-vortex unstable solutions of the system, respectively. The increase of the relative values of U_c is due to the changes in the properties of the flow, as the speed of sound of the superfluid c relative to c_0 increases. However, when the velocity is normalized by the speed of sound of the superfluid c, the critical Mach number
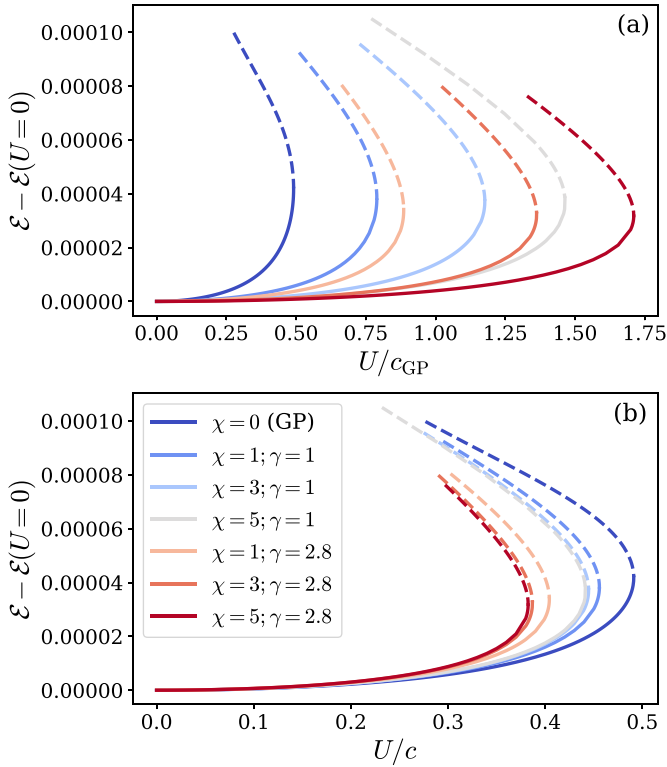
FIG. 2. Bifurcation diagrams of the energy of stationary solutions of the local gGP model (10) for a disk of diameter $D = 5\xi$ moving at different velocities U. The velocity is normalized by (a) the GP speed of sound $c_0 = \sqrt{gn_0/m}$ and (b) the superfluid speed of sound c. Different diagrams correspond to different values of the amplitude χ and the order γ of the nonlinearity. The stable (solid lines) and two-vortex unstable (dashed lines) branches are shown.

M_c rescales in a nontrivial manner, as shown in Fig. 2(b). In particular, M_c decreases with the nonlinearities.

As already shown in Figs. 1 and 2, the critical Mach number varies according to the size of the obstacle [7,19]. Figure 3 shows the bifurcation diagram of a flow around a disk of diameters varying between $D = 5\xi$ and $D = 40\xi$. The blue curves correspond to the bifurcation diagram of the standard GP model ($\chi = 0$) and the red curves correspond to the local gGP with $\chi = 5$ and $\gamma = 2.8$. Solid lines correspond to the stable branch and dashed lines correspond to unstable solutions with two vortices. As the particle size D increases, the critical Mach number M_c decreases.

B. Rotons

We now focus on a system with the nonlocal interaction potential introduced in Eq. (7), which is able to reproduce the roton minimum in the dispersion relation (3). The parameters for the high-order nonlinear terms are chosen as described in Sec. II. The bifurcation diagram of the model with rotons (yellow lines) for a disk of diameter $D = 10\xi$ is shown in Fig. 4 and is compared with the local gGP (red lines) and the standard GP (blue lines). The stable branch in the case with rotons presents an abrupt stop at a Mach number of $M_c \approx 0.248$. This value is close to Landau's Mach number $M_L \approx 0.245$, obtained from applying Eq. (1) to the dispersion relation of
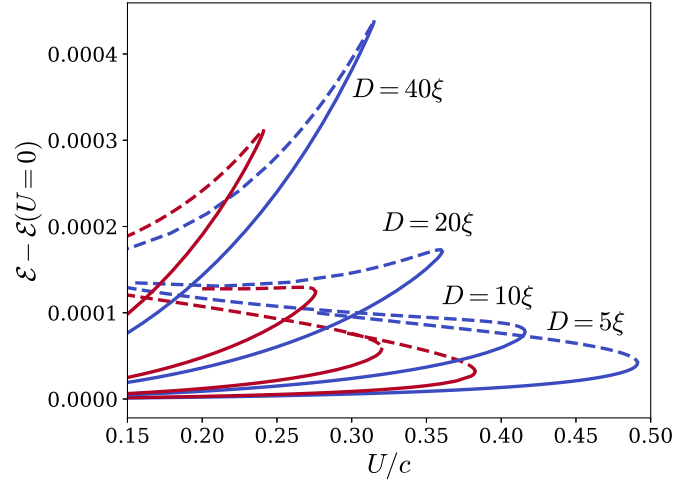

FIG. 3. Bifurcation diagram of the energy of stationary solutions of a superfluid with a disk moving at a constant velocity U for different diameters for the disk. Simulations of the GP model (blue lines) and the local gGP model with $\chi = 5$ and $\gamma = 2.8$ (red lines) are shown. The solid and dashed lines correspond to the stable and unstable branches, respectively.

the gGP system (3) with the nonlocal potential (7) with the parameters discussed below that expression, and Landau's Mach number of ^{4}He $M_L^{\text{He}} = 0.252$ assuming $c = 238$ ms^{-1} and $v_L = 60$ ms^{-1} [4,35]. Indeed, when the disk is moving at a velocity that is greater than but still close to the Landau velocity, we observe the emission of density modulations on the fluid, which can be associated with rotons. However, if the velocity of the disk is not large enough, there is no nucleation of vortices. This result suggests that there are two kinds of excitations when a nonlocal interaction potential is introduced: rotons and vortices.

As discussed in Sec. III A, the critical velocity for vortex nucleation depends on the size of the obstacle. Here, we study the dependence of the critical Mach number for a wide range
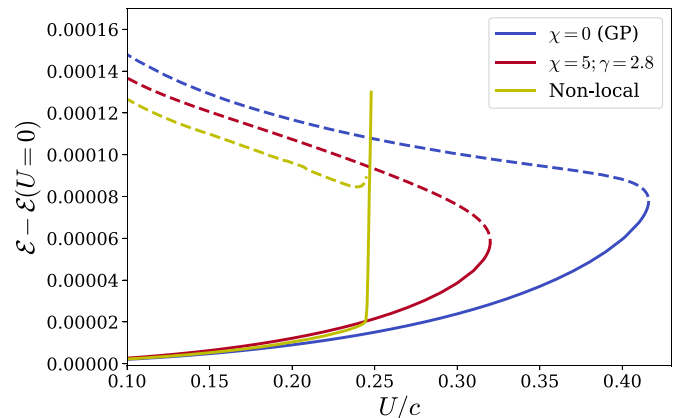

FIG. 4. Bifurcation diagram of a moving disk of diameter $D = 10\xi$ for a local interaction with $\chi = 0$ (blue lines) and $\chi = 5$ and $\gamma = 2.8$ (red lines) and for the isotropic nonlocal potential defined in Eq. (7) (yellow lines) that reproduces the roton minimum in the excitation spectrum. The solid and dashed lines correspond to the stable and unstable branches, respectively.
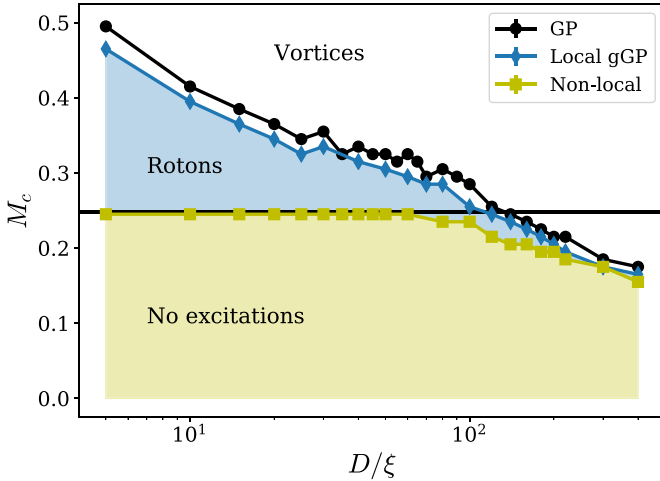
FIG. 5. Critical Mach number as a function of the diameter of the disk for the standard GP model (black) and the local (blue) and nonlocal gGP (yellow) models. The horizontal solid black line indicates Landau's Mach number of the system, $M_L = 0.248$.

of disk diameters in the nonlocal gGP model (yellow line) and compare it with the same system with a local potential (blue lines) (Fig. 5). For comparison reasons, we also show the critical velocity dependence in the standard GP model (black line). This last one follows a behavior similar to that of the local gGP simulation but with larger critical values. The system presents an interesting behavior in the case where rotons are supported. If the disk diameter is smaller than $D \approx 100\xi$, there is a range of velocities in which the disk in the nonlocal gGP model emits rotons but no vortices. As the diameter increases, the critical velocities for systems with and without roton minimum tend to collapse, presenting a similar behavior for large obstacles.

According to experiments [18], the critical velocity in superfluid ^{4}He is of the order of $v_c \approx 10$ cm/s, a value that is much smaller than Landau's velocity $v_L \approx 60$ m/s. However, the experiments were performed with a fork of size $D = 0.4$ mm $\approx 4 \times 10^6 \xi$, a value 4 orders of magnitude larger than the largest one studied in this work of $D = 400\xi$. The regime where only rotons are emitted would correspond to a particle size smaller than 10 nm in superfluid ^{4}He, which, to our knowledge, to this day has not been studied. However, it is important to remark that the presence of the roton minimum seems to be irrelevant in the process of vortex nucleation for sufficiently large obstacles.

C. Temporal evolution of a moving obstacle

The solutions introduced in Sec. III A provide us with a better understanding of the system for the study of its temporal evolution. To do this, we start from a two-dimensional initial condition at rest with a disk of size $D = 20\xi$ and let it evolve using the nonlocal gGP equation (6) with a roton minimum in its excitation spectrum. We apply an external force to the particle until it achieves the desired velocity. Note that we do not include a two-way coupling in the system [37]; i.e., the particle will not slow down after the nucleation of vortices or the emission of rotons. During the acceleration regime, the
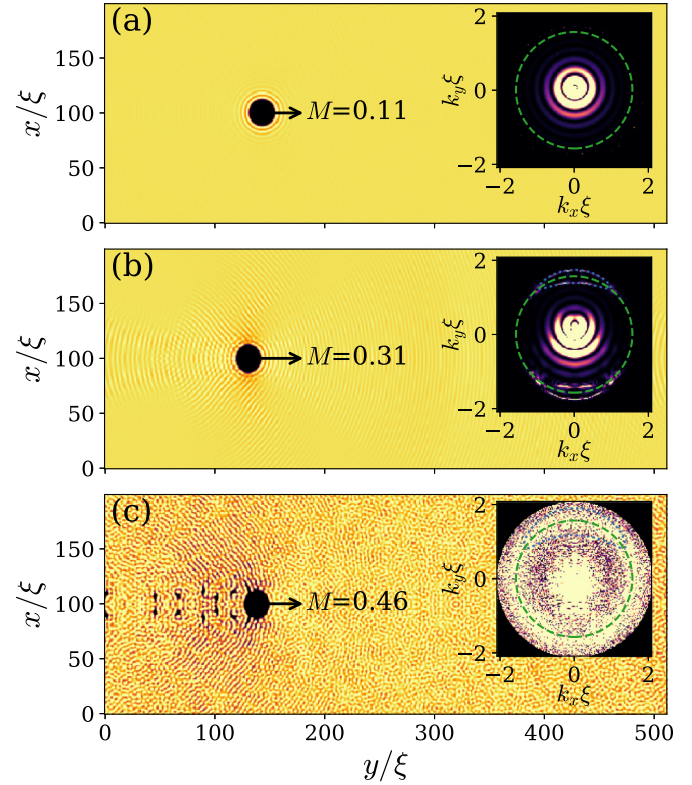

FIG. 6. Two-dimensional density fields of nonlocal superfluid with a disk of diameter $D = 20\xi$. Dark zones correspond to regions where the superfluid is depleted. The disk is moving at a Mach number at which (a) the system is stationary, (b) rotons are emitted, and (c) vortices are nucleated. The insets show the two-dimensional Fourier transform of the density field. Green dashed lines show the wave number of the roton minimum k_{rot} and the blue dotted lines show solutions of Eq. (8).

disk introduces small density perturbations on the flow. To mitigate spurious effects caused by these perturbations, we apply some dissipation during this regime and turn it off as soon as the target velocity is achieved.

Previous works have already studied the dynamical process of vortex nucleation in the standard GP model in either two-dimensional [7,11] or three-dimensional systems [9], observing the regular or irregular emission of vortices in the wake of the moving obstacle [19–21]. Here, we focus on the nonlocal gGP model and the different regimes of roton or vortex emission. Figure 6 shows snapshots of the disk moving at different Mach numbers. In black we show the regions where the superfluid is depleted, corresponding to either the obstacle or the vortices. For a velocity that is smaller than Landau's velocity $M_L \approx 0.245$, there are no excitations on the flow [Fig. 6(a)]. Note that there are some stationary density modulations around the disk as a consequence of the nonlocal interaction [26,38], which keep their shape around the disk as it moves without causing any drag force on it. The inset shows the two-dimensional density spectrum $|\hat{\psi}|^2(k_x, k_y)$ of the superfluid. The excited modes correspond to the density modulations around the disk. These patterns have already been observed around small obstacles and vortices in previous works [26,27,30]. More interestingly, when the particle moves
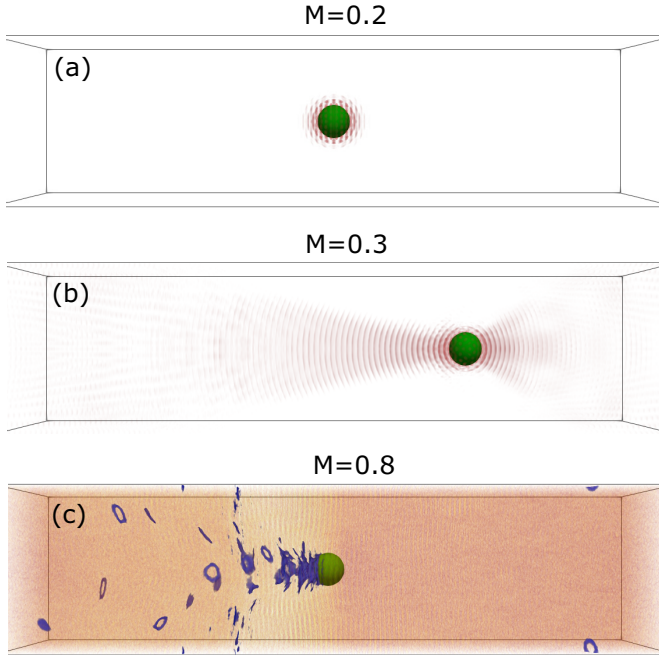
FIG. 7. Three-dimensional density field of a superfluid with a roton minimum in the excitation spectrum. In green, we show a sphere of diameter $D = 20\xi$ moving to the right at Mach numbers $M = 0.2$ (a), $M = 0.3$ (b), and $M = 0.8$ (c). In red, we show density fluctuations around the equilibrium and in blue we show low values of the density. We can identify three different regimes, one of them stationary (a), one in which rotons in the shape of a cone are emitted (b), and one where vortices are nucleated (c).

at a velocity of $M \gtrsim M_L$ [Fig. 6(b)], it introduces some density fluctuations on the superfluid. The excited wave numbers obey the anisotropic expression in Eq. (8) computed using the dispersion relation with rotons, shown as blue dotted lines in the inset of Fig. 6(b). Finally, for a velocity of $M \gg M_L$ [Fig. 6(c)], the disk emits rotons but also it starts nucleating vortices. Due to the mutual interaction between vortices and the rotons, vortices can annihilate emitting phonons. Thus, there is a wide range of modes that are excited, as shown in the inset.

In conclusion, we show here that, at velocities above Landau's critical one, the moving obstacle introduces some elementary excitations with wave numbers that obey Eq. (8). We can thus identify these excitations with rotons. For larger velocities, the disk starts nucleating vortices, emitting rotons and other excitations in a wide range of wave numbers.

D. Three-dimensional system

All of the results discussed until now were obtained from two-dimensional simulations of the nonlocal gGP model. A similar behavior can be obtained in three-dimensional systems. In particular, we studied the motion of a sphere of diameter $D = 20\xi$ in the z direction in an elongated domain with $L_z = 4L_\perp$ and a spatial resolution of $256 \times 256 \times 1024$. In the case of the sphere moving at a velocity of $M = 0.2$, below Landau's Mach number, there is no quasiparticle emission [Fig. 7(a)]. The density fluctuations in red around the sphere create a pattern induced by the roton minimum but that do
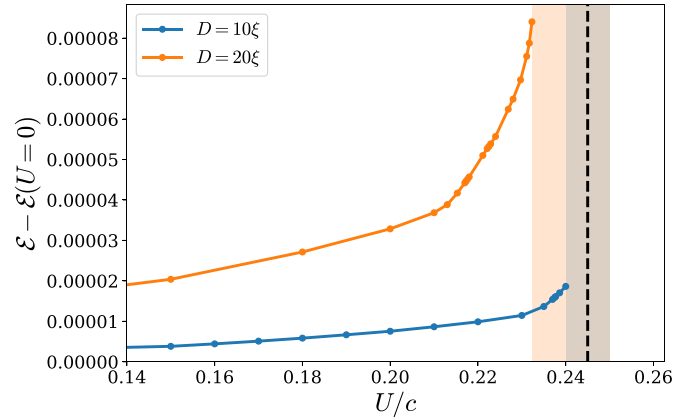

FIG. 8. Stable stationary solutions of a moving sphere of two different diameters D. The highlighted regions correspond to the intervals where we estimate the critical Mach number should be found, with the lower bound being the maximum value obtained using the Newton-Raphson method and the upper bound obtained using the imaginary time evolution of Eq. (9). The vertical black dashed line indicates Landau's Mach number of the system, $M_L = 0.245$.

not emit any excitation on the flow. In the case of the sphere moving at a velocity of $M = 0.3$, just above Landau's Mach number, it starts emitting rotons in the shape of a cone, shown as red density fluctuations above the equilibrium in Fig. 7(b). Note that the cone is emitted in both upstream and downstream directions, consistent with negative solutions in the wave numbers shown in the inset of Fig. 6(b). For a larger velocity of $M = 0.8$, the particle starts nucleating vortices [blue rings in Fig. 7(c)]. The depletion of the superfluid is stronger in the wake of the sphere, where vortices are nucleated. In this region, many vortex rings reconnect and collapse due to the interaction with strong density fluctuations introduced by the roton minimum, shown in red.

We also perform an analysis on the critical velocity in the three-dimensional case for two sphere diameters, $D = 10\xi$ and $D = 20\xi$. These sizes correspond to the small-particle limit discussed in the two-dimensional case and are chosen in this way to avoid spurious effects introduced by the boundary conditions. Larger particle sizes require larger computational boxes that are prohibitive. The critical velocity of the system can be determined by the Mach number where the stable and unstable branches merge. The unstable branch can only be obtained using a Newton-Raphson method that is too expensive in three dimensions and is out of the scope of this work. Therefore, we only show the stable branch in Fig. 8 for both particle sizes. The stable branch allows us to determine a lower bound of the critical Mach value, corresponding to the maximum value of M at which the Newton-Raphson method converges. We have checked that the imaginary time evolution of the gGP model, obtained by replacing $t \to -it$ in Eq. (9), does not converge for $M = 0.25$, which is slightly above the theoretical value for roton emission, $M_L = 0.245$. Therefore, we can estimate that the critical Mach belongs to the interval $M_c \in [0.24, 0.25]$ for $D = 10\xi$ and $M_c \in [0.231, 0.25]$ for $D = 20\xi$ (highlighted regions in Fig. 8). These results are consistent with the ones obtained in two dimensions for small particles of $D < 100\xi$. A more precise determination of the

critical value in three dimensions and the study of the unstable branch are left for a future study.

IV. CONCLUSIONS

In this work, we study the process of vortex nucleation in the wake of a moving obstacle in a generalized Gross-Pitaevskii (gGP) model [28,34] in periodic two-dimensional systems. We determine the critical velocity of the superfluid, the velocity above which superfluidity breaks down, for moving disks of diameters between $D = 2.5\xi$ and $D = 400\xi$ by analyzing the bifurcation diagram of stationary solutions of the system [7,11]. In particular, we study the role of the beyond-mean-field corrections and the introduction of a nonlocal interaction potential that can reproduce the roton minimum in the excitation spectrum, observed in superfluid ^{4}He and in dipolar BECs [4,33], and compare them with the standard GP model.

Varying the amplitude and order of the high-order non-linear terms in the local gGP model, we show that the role of beyond-mean-field corrections is to reduce compressible effects in the system, increasing the value of the speed of sound c and decreasing the core size of the vortices. As the absolute value of the speed of sound increases, the critical velocity also does. However, it does not do it in a trivial way as the critical Mach number decreases with the nonlinearities.

In the case of a nonlocal interaction potential, we show that the superfluid presents two characteristic velocities, one of them associated with the emission of rotons and the other related with the vortex nucleation. In the case of impenetrable disks of diameter $D \lesssim 100\xi$, the critical velocity is a consequence of the roton minimum in the excitation spectrum. Above $M_L \approx 0.25$, the disk starts emitting rotons that, in the case of the particle moving in the y direction, satisfy the dispersion relation (8). For small obstacles, there is a range of velocities where only rotons are emitted and no vortices are nucleated. In this case, rotons are the reason for the breakdown of superfluidity. For larger obstacles of diameter $D \gtrsim 100\xi$, the critical velocity for nucleation of vortices becomes smaller than the one for emission of rotons, and its value for the different models tend to collapse, suggesting that for large obstacles the rotons are not relevant in the mechanism of vortex nucleation. In the case of a three-dimensional system, the dynamics of a moving sphere immersed in a superfluid is consistent with the behavior observed in the two-dimensional case, although the study is limited to small particles because of computational constraints. We identify the presence of three regimes for different particle velocities, one in which the moving particle does not perturb the flow, one in which it emits rotons, and a third one in which it nucleates vortices

perturbing the flow in the whole range of scales. The critical velocity in the limit of small particles is consistent with Landau's critical velocity of the system.

APPENDIX: NEWTON-RAPHSON METHOD

In order to find the critical velocity at which a superfluid breaks down, i.e., the velocity above which vortices are nucleated, we can study stationary solutions of the system of either maximum or minimum of the energy $\mathcal{E}$ (10). One way of doing this is to study the imaginary time gGP, obtained by replacing $t \to -it$ in Eq. (11). The evolution of this equation allows one to obtain a ground state of the system, which corresponds to a stable stationary solution of the system. However, for the vortex nucleation problem we expect to find a bifurcation diagram with stable and unstable solutions of the gGP equation [7,11], so this method would only allow us to obtain the stable branch of the system.

An alternative way of computing the stationary solutions of Eq. (11) is by using the Newton-Raphson method [39]. To find both stable and unstable steady states, we study an equation of the form

$$\frac{\partial \Psi}{\partial t} = 0 = L\Psi + N(\Psi) + A(\Psi), \tag{A1}$$

where L corresponds to a linear operator, $N(\Psi)$ is an arbitrary function involving multiplicative and nonlinear terms, and $A(\Psi)$ corresponds to the advective term. The Newton-Raphson method consists of finding iteratively a solution of the above problem. We start from an initial guess Ψ, which is then perturbed as $\Psi - \delta\psi$, with $\delta\psi$ small. By linearizing Eq. (A1) for small $\delta\psi$, we obtain the following linear equation:

$$[L + DW(\Psi)]\delta\psi = L\Psi + W(\Psi), \tag{A2}$$

with $DW(\Psi)$ being the Jacobian of $W(\Psi) = N(\Psi) + A(\Psi)$ at Ψ, acting on $\delta\psi$. To solve numerically this equation, we use an iterative biconjugate gradient stabilized method with a preconditioner $\mathcal{P} = (I - \Delta t L)^{-1}$, where Δt is an arbitrary parameter used to improve convergence [39]. The Newton-Raphson method can only be used when a good estimation of the steady state is provided as an initial guess.

[1] L. P. Pitaevskii and S. Stringari, *Bose-Einstein Condensation and Superfluidity*, International Series of Monographs on Physics Vol. 164 (Oxford University, Oxford, England, 2016).

[2] F. Dalfovo, S. Giorgini, L. P. Pitaevskii, and S. Stringari, Rev. Mod. Phys. **71**, 463 (1999).

[3] R. J. Donnelly, *Quantized Vortices in Helium II* (Cambridge University, Cambridge, England, 1991).

[4] H. Godfrin, K. Beauvois, A. Sultan, E. Krotscheck, J. Dawidowski, B. Fåk, and J. Ollivier, Phys. Rev. B **103**, 104516 (2021).

[5] L. D. Landau and E. M. Lifshitz, *Fluid Mechanics*, 2nd ed., Course of Theoretical Physics Vol. 6 (Elsevier, Amsterdam, 1987).

[6] T. Frisch, Y. Pomeau, and S. Rica, Phys. Rev. Lett. **69**, 1644 (1992).

[7] C. Huepe and M. E. Brachet, C. R. Acad. Sci. **325**, 195 (1997).

[8] T. Winiecki, J. F. McCann, and C. S. Adams, Europhys. Lett. **48**, 475 (1999).

[9] T. Winiecki, B. Jackson, J. F. McCann, and C. S. Adams, J. Phys. B: At., Mol. Opt. Phys. **33**, 4069 (2000).

[10] C. Huepe and M.-E. Brachet, Phys. D (Amsterdam, Neth.) **140**, 126 (2000).

[11] C.-T. Pham, C. Nore, and M.-E. Brachet, Phys. D (Amsterdam, Neth.) **210**, 203 (2005).

[12] S. Rica, Phys. D (Amsterdam, Neth.) **148**, 221 (2001).

[13] A. Villois and H. Salman, Phys. Rev. B **97**, 094507 (2018).

[14] C. Raman, M. Köhl, R. Onofrio, D. S. Durfee, C. E. Kuklewicz, Z. Hadzibabic, and W. Ketterle, Phys. Rev. Lett. **83**, 2502 (1999).

[15] W. J. Kwon, J. H. Kim, S. W. Seo, and Y. Shin, Phys. Rev. Lett. **117**, 245301 (2016).

[16] A. Eloy, O. Boughdad, M. Albert, P.-É. Larr, F. Mortessagne, M. Bellec, and C. Michel, Europhys. Lett. **134**, 26001 (2021).

[17] I. Carusotto and C. Ciuti, Rev. Mod. Phys. **85**, 299 (2013).

[18] V. B. Efimov, D. Garg, O. Kolosov, and P. V. E. McClintock, J. Low Temp. Phys. **158**, 456 (2010).

[19] K. Sasaki, N. Suzuki, and H. Saito, Phys. Rev. Lett. **104**, 150404 (2010).

[20] G. W. Stagg, N. G. Parker, and C. F. Barenghi, J. Phys. B: At., Mol. Opt. Phys. **47**, 095304 (2014).

[21] M. T. Reeves, T. P. Billam, B. P. Anderson, and A. S. Bradley, Phys. Rev. Lett. **114**, 155302 (2015).

[22] Z.-H. Xi, Y.-Z. Zhao, and Y.-R. Shi, Phys. A (Amsterdam, Neth.) **572**, 125866 (2021).

[23] J. Salort, C. Baudet, B. Castaing, B. Chabaud, F. Daviaud, T. Didelot, P. Diribarne, B. Dubrulle, Y. Gagne, F. Gauthier, A. Girard, B. Hébral, B. Rousset, P. Thibault, and P.-E. Roche, Phys. Fluids **22**, 125102 (2010).

[24] G. Krstulovic, Phys. Rev. E **93**, 063104 (2016).

[25] S. Musser, D. Proment, M. Onorato, and W. T. M. Irvine, Phys. Rev. Lett. **123**, 154502 (2019).

[26] N. G. Berloff and P. H. Roberts, J. Phys. A: Math. Gen. **32**, 5611 (1999).

[27] J. Reneuve, J. Salort, and L. Chevillard, Phys. Rev. Fluids **3**, 114602 (2018).

[28] N. P. Müller and G. Krstulovic, Phys. Rev. B **102**, 134513 (2020).

[29] N. G. Berloff and P. H. Roberts, Phys. Lett. A **274**, 69 (2000).

[30] Y. Pomeau and S. Rica, Phys. Rev. Lett. **71**, 247 (1993).

[31] E. B. Kolomeisky, J. Colen, and J. P. Straley, arXiv:2106.00821.

[32] N. G. Berloff, M. Brachet, and N. P. Proukakis, Proc. Natl. Acad. Sci. USA **111**, 4675 (2014).

[33] T. Lahaye, C. Menotti, L. Santos, M. Lewenstein, and T. Pfau, Rep. Prog. Phys. **72**, 126401 (2009).

[34] A. Gallemí, S. M. Roccuzzo, S. Stringari, and A. Recati, Phys. Rev. A **102**, 023322 (2020).

[35] R. J. Donnelly and C. F. Barenghi, J. Phys. Chem. Ref. Data **27**, 1217 (1998).

[36] J. S. Brooks and R. J. Donnelly, J. Phys. Chem. Ref. Data **6**, 51 (1977).

[37] U. Giuriato and G. Krstulovic, Sci. Rep. **9**, 4839 (2019).

[38] S. Villerot, B. Castaing, and L. Chevillard, J. Low Temp. Phys. **169**, 1 (2012).

[39] L. Tuckerman, C. Huepe, and M.-E. Brachet, in *Instabilities and Nonequilibrium Structures IX* (Kluwer, Dordrecht, 2004), pp. 75–83.

Conclusions

In this Thesis, we investigated systematically the statistical properties of quantum turbulence by performing extensive direct numerical simulations (DNS) of different models for superfluidity. We used the standard Gross–Pitaevskii (GP) equation, a generalized GP (gGP) model that incorporates a non-local interaction potential between bosons, and the two-fluid HVBK equations. We also compared some of the results with DNS of the incompressible Navier–Stokes (NS) equations. The main body of the results concerns the dynamics of rotons in a superfluid at very low temperatures and the intermittent nature of velocity circulation statistics in classical and quantum turbulence.

In the study on quantum turbulence in a model with a roton minimum [MK20], we first introduced the gGP equation, a model originally proposed to study the properties of superfluid ^{4}He [BR99]. It includes a non-local interaction potential between bosons, which in this Thesis was chosen to fit the roton minimum in the excitation spectrum in superfluid ^{4}He [DB98; RSC18]. This equation also incorporates a beyond mean-field correction which models strong interactions between bosons. In practice, this high-order non-linear term mitigates the development of certain instabilities that lead to a crystallization state with no background superfluid [RSC18]. In chapter 3 we showed that the roton minimum introduces some well-known density modulations on the vortex profile around the ground state [BR99; RSC18]. All the model variations (standard GP, local GP with beyond mean-field correction but without rotons, and gGP including rotons) exhibit the same statistical properties at scales larger than the intervortex distance $r > \ell$, following the phenomenology of Kolmogorov turbulence. At small scales $r < \ell$, however, the introduction of the roton minimum enhances the energy spectrum in the Kelvin-wave cascade, following the weak-wave turbulence prediction not only for the scaling of the wavenumber $k^{-5/3}$ but also for the prefactor, that depends on the energy dissipation rate ϵ, the intervortex distance ℓ and the quantum of circulation κ. We conclude from this work that the phenomenology of Kolmogorov turbulence is independent of the modelling at small scales, while rotons and high-order non-linearities enhance the propagation of Kelvin waves.

The main work developed in this Thesis is devoted to the study of velocity circulation statistics in classical and quantum turbulence. These results lead to three different publications [MPK21; PMK21; MTG$^+$22] that are discussed in detail in chapter 4. In particular, performing high-resolution DNS of the gGP model, we have shown that at scales larger than the intervortex distance, the intermittent behavior of velocity circulation in quantum turbulence is similar to the one observed in classical fluids [ISY19]. The behavior differs at small scales due to the discrete nature of circulation in quantum vortices. In this range, the scaling of circulation moments only depends on the probability of finding a vortex in a loop of area A, which is independent of the moment order p. We also show that these results are independent of the non-local interaction potential used in the gGP model, and that the same phenomenology for velocity circulation statistics is obtained using the standard GP

equation. The large-scale behavior observed in the gGP model is contrasted with experimental measurements on grid turbulence in superfluid ^{4}He at 1.65 K and 1.95 K, performed by the group of Wei Guo in Tallahassee [MTG$^+$22]. We have shown that circulation statistics in superfluid ^{4}He is also similar to the one of classical fluids, and is independent of the temperature. These results are also consistent with DNS of the HVBK equations, where we analyze higher-order moments and a wide range of temperatures.

Motivated by the previous results, we developed a discrete Markovian model for the circulation, in which the signs of all individual quantum vortices are correlated [PMK21]. This model predicts that the scaling of circulation moments is determined by the polarization between vortices, recovering the K41 phenomenology for a partial polarization. One notable property of quantum fluids is that it is possible to identify the position and sign of each individual vortex for a given 2D slab, and thus compute the circulation in two different ways: as a function of the loop size, or based on vortex proximity. In particular, the first method leads to an intermittent behavior of circulation, reported in the previous work [MPK21], while the moments of circulation based on vortex proximity exhibit a self-similar scaling, similarly to our Markovian model, where the notion of space is absent. We derived a relation between the number of vortices enclosed by a loop and the coarse-grained energy dissipation, with both quantities displaying a log-normal distribution [Dub19]. Based on these results, we proposed that the scaling exponents of velocity circulation can be described as a composition of two effects: a partial polarization between vortices, that leads to the self-similar K41 scaling, and a complex spatial distribution of vortices, with voids and clusters that are the reason for the anomalous deviations. To test this idea, we performed a numerical experiment in which we randomized the circulation value of each vortex, keeping their position fixed. As there is no polarization in this new configuration, it leads to a different scaling motivated by the Markovian model (a simple random walk), and still exhibits an intermittent scaling. We conclude that the discrete nature of circulation in quantum fluids is very useful for the development of analytical models describing the circulation statistics in quantum turbulence. These models can also be useful for the understanding of classical turbulence.

Concerning two-dimensional quantum turbulence, we presented some preliminary results on the circulation statistics in the inverse energy cascade and the direct enstrophy cascade regimes. In the former, we observe a self-similar scaling for circulation moments. This result is consistent with previous observations for the structure function in 2D classical turbulence [BE12]. Even though the enstrophy is not a regular quantity in quantum fluids, one can establish a relation between the enstrophy and the number of vortices in the system. Therefore, one would still expect the development of an enstrophy cascade given by a coarse-grained vorticity field, provided a large scale separation between the initial pump and the vortex core size [BRA$^+$14; RBY$^+$17]. In particular, the scaling exponents of circulation moments display some deviations from the smooth field prediction given by the enstrophy spectrum. In the near future, we plan to characterize more in detail the circulation statistics in 2D quantum turbulence. In particular, it would be interesting to analyze the spatial vortex distribution in both cascade regimes and see if the intermittent or non-intermittent nature of the flow modifies the vortex distribution. Moreover, there is currently no study on velocity circulation statistics in 2D classical fluids that we are aware of, and a comparison with this system is necessary.

Finally, in the last publication of this Thesis [MK22], we characterized the process of vortex nucleation in the gGP model. Landau criterion of superfluidity determines that the introduction of the roton minimum reduces the critical velocity of the system from the speed of sound to the velocity of roton propagation, which in superfluid ^{4}He differ by a factor 4. We study the stationary solutions of 2D flows with a disk-shaped obstacle moving at a constant velocity using a Newton-Raphson method, and determine the bifurcation diagrams for different obstacles sizes [HB00]. For large disk diameters, the critical velocity in both the GP and gGP models is determined by the process of vortex nucleation, leading to a critical value that is typically smaller than Landau criterion. Instead, for small disk diameters, the critical velocity in the gGP model follows Landau criterion, determined by the roton velocity. This result shows that the modelling at small scales does not affect the process of vortex nucleation at large scales, and rotons are only relevant at small scales. In the case of a moving sphere immersed in a superfluid in three dimensions, these results seem to be consistent with the 2D case.

To conclude, the gGP equation studied in this Thesis is a very rich model that can be useful to study different systems, whether they admit rotons or not. In particular, choosing the right parameters for the beyond mean-field correction and the proper non-local interaction potential, this model can be used to describe dipolar BECs [LMS$^+$09; GRS$^+$20]. This anisotropic quantum fluid attracted a great interest in the low-temperature physics community, as it was recently observed in 1D and 2D systems that it might display supersolid properties [CPI$^+$19; BSW$^+$19; TLF$^+$19; BPP$^+$22]. Supersolidity is an exotic state of matter characterized by the formation of a periodic structure immersed in a superfluid. In particular, we speculate that the origin of this phase results from the development of instabilities generated by the roton minimum in the excitation spectrum. The implementation of the gGP model in the FROST code (Full solveR Of Superfluid Turbulence) allows us, in principle, to study different properties of supersolidity, such as the ground state either in a periodic or a confined system. It is also possible to study its dynamics, including different excitations as waves, quantum vortices or the interaction with particles.

We stress that the characterization of velocity circulation statistics in quantum turbulence is a young area of research, and there are still a lot of questions that remain open for future investigations. In particular, circulation is a signed quantity leading to cancellation events that can be characterized using cancellation exponents [ODS$^+$92; IM10; ZSY19]. This study might provide some information on the fractal dimension of structures contributing to circulation. In the work of Iyer et al. [ISY19], the authors suggested that the scaling exponents of circulation follow a bifractal behavior, with a fractal dimension associated to wrinkled vortex sheets. The study of vortex clustering may also provide some insight on the fractal dimension, making use for instance of box counting algorithms [HP83].

Understanding the circulation statistics in quantum fluids can be helpful to describe the dynamics of different regimes of superfluid turbulence. In particular, Vinen turbulence is characterized by the presence of vortex rings with a random polarization, displaying an energy spectrum that differs from Kolmogorov picture. It can be achieved numerically studying the long-time evolution of the GP model in the decaying regime [VPK16], or experimentally by injecting vortex rings into the superfluid in a controlled way [WG08]. In principle, there is no reason to think that Vinen turbulence exhibits an intermittent behavior, and it would be interesting to study the transition between Kolmogorov and Vinen turbulence. An exhaustive analysis on the velocity circulation statistics may provide useful insight on the polarization and intermittent nature of this regime. For instance, these two regimes can

be studied using the vortex filament method. Under proper conditions, this model is able to reproduce properly the energy spectrum of Kolmogorov and Vinen turbulence [BLB12], and the computations of circulation statistics in this system would be straightforward. Another interesting system is counterflow turbulence, one of the most popular techniques to study superfluid ^{4}He turbulence [GCN$^+$10; LMDR$^+$13]. In particular, it is excited by imposing a temperature gradient in the superfluid. Numerical simulations have shown that a mean counterflow develops anisotropies at small scales, and displays some 2D phenomenology as an inverse energy cascade [BKL$^+$19a; PK20a]. To analyze the circulation statistics in this system, one has to be careful with the anisotropy of the system. This study could be useful to understand whether counterflow turbulence exhibits an intermittent behavior or not.

As a last remark, circulation is an integral quantity that, in quantum turbulence, displays more clear power laws than the velocity increments. Structure functions in the GP framework actually exhibit a stronger intermittent behavior than classical turbulence [Krs16]. One possible reason for this enhancement of intermittency is that the velocity field is singular, diverging at the vortices cores, and these structures may contaminate the scaling properties of the flow. In particular, we count with high-resolution DNS that, with a careful analysis, can provide useful measurements on the statistics of velocity increments. In contrast, these singularities for the velocity increments are regularized to discrete values for the circulation, leading to better scaling properties and resulting in an ideal framework for intermittency investigations.

Appendix A

Numerical methods

In this Appendix, we will discuss about the numerical simulations performed in this Thesis to study quantum turbulent flows using the Gross–Pitaevskii equation. This model describes the dynamics of a compressible superfluid. However, we would like to focus mainly on the turbulent properties of the superfluid described by the incompressible component of the velocity field. To do this, we need a regime with a small Mach number $M = v/c_\mathrm{s}$, and with the minimum amount of acoustic perturbations. To do this, we generate an initial condition for the condensate wavefunction ψ following a complex velocity field and let it evolve freely in time. As the system evolves, quantum vortices will start to reconnect, emitting sound pulses (see 1.4.2 for details). For very long times, this density fluctuations will eventually dominate the dynamics of the flow attenuating the vortex dynamics [KB11]. The properties of the turbulent flow are then analyzed in a time window where the initial condition is not dominating the flow, and where the acoustic emissions are still subdominant.

In the publications [MK20; MPK21; PMK21], we mostly study the decaying of an Arnold-Bertrami-Childress (ABC) flow

$$
\begin{aligned}
\mathbf{u}_{\mathrm{ABC}} = \{ &[B\cos(ky) + C\sin(kz)]\hat{x}+ \\
&+[A\sin(kx) + C\cos(kz)]\hat{y}+ \\
&+[A\cos(kx) + B\sin(ky)]\hat{z} \}.
\end{aligned}
\tag{A.1}
$$

The values of amplitudes are $(A, B, C) = U_0(0.9, 1, 1.1)/\sqrt{3}$ with $U_0 = 0.5c$ [CMB16]. The motivation of using this initial condition is that it has a maximal helicity, in the sense $\nabla \times \mathbf{u}_{\mathrm{ABC}} = k\mathbf{u}_{\mathrm{ABC}}$. The wavefunction associated to this velocity field is the generated as a product of several modes $\psi_{\mathrm{ABC}} = \psi_{\mathrm{ABC}}^{(k_1)} \times \psi_{\mathrm{ABC}}^{(k_2)}$, with $\psi_{\mathrm{ABC}}^{(k)} = \psi_{\mathrm{A,k}}^{x,y,z} \times \psi_{\mathrm{B,k}}^{y,z,x} \times \psi_{\mathrm{C,k}}^{z,x,y}$ and

$$
\psi_{\mathrm{A,k}}^{x,y,z} = \exp\left\{ i\left[\frac{A\sin(kx)}{c\xi\sqrt{2}}\right]\frac{2\pi y}{L} + i\left[\frac{A\cos(kx)}{c\xi\sqrt{2}}\right]\frac{2\pi z}{L} \right\}
\tag{A.2}
$$

where the brackets [] indicate the integer value closest to the argument to ensure periodicity. This wavefunction is a good ansatz to initialize the phase and the density field of the quantum flow, where the zeros of the wavefunction correspond to the positions of the quantum vortices. However, to set properly the density profile of the quantum vortices and to minimize the density fluctuations in the flows, we first evolve ψ_{ABC} using the advective real Ginzburg-Landau equation (ARGL, also known as imaginary time evolution in a locally Galilean transformed system of reference) [NAB97a]

$$\partial_t \psi = -\frac{c}{\xi\sqrt{2}} \left[-\xi^2 \nabla^2 \psi - \psi + \frac{|\psi|^2}{n_0} \psi \right] - i\mathbf{u}_{\mathrm{ABC}} \cdot \boldsymbol{\nabla} \psi - \frac{(\mathbf{u}_{\mathrm{ABC}})^2}{2\sqrt{2}c\xi} \psi \qquad (\mathrm{A.3})$$

where c is the speed of sound, ξ the healing length and n_0 the particles density of the ground state. The final state of the evolution of this equation leads to a wavefunction with a minimal amount of sound emission that follows the incompressible velocity field $\mathbf{u}_{\mathrm{ABC}}$. Once the initial condition is generated using this equation, it is then evolved using the GP or the gGP equations.

In classical fluids, the most used method to study turbulence is to use an external forcing that, together with the dissipation term described by the Navier–Stokes equations, allows the generation of a steady state. In the GP framework, the generation of stationary turbulence is more complicated. First of all, the forcing would excite both vortices and sound waves. As the total energy of the system is conserved, one should introduced some damping mechanism into the system to prevent the energy to diverge. One way of doing this is to consider that the condensate is in contact with a thermal reservoir and interchanges particles with the thermal cloud [ZNG99; KT05; Tsu09]. This model, together with the introduction of a forcing, has been used to study statistical steady turbulence in two-dimensions [RBA⁺13], or to study the Kelvin-wave cascade [PNO12]. One of the counterparts of this method is that this dissipation mechanism acts at all scales on all the energy components of the system, including the vortices. This, together with the energy transfer to sound due to reconnections, still makes that for long times the system becomes dominated by acoustic waves.

Appendix B

Characteristic function in the Markovian model

By definition, the characteristic function of a real-valued random variable is given by

$$\phi(n+1,\theta) \equiv \langle e^{i\theta\Gamma}\rangle_{n+1} = \sum_{\gamma} e^{i\theta\gamma} P_{n+1}(\gamma), \tag{B.1}$$

where we took the circulation Γ as a random variable. Determining the characteristic function is an alternative way of specifying the probability distribution and the moments, that are prescribed by

$$\langle \Gamma^p \rangle = i^{-p} \frac{d^p\phi}{d\theta^p}\Big|_{\theta=0} \tag{B.2}$$

In chapter 4, we introduced a discrete Markovian model for circulation, in which the probability distribution of circulation Γ for $n+1$ vortices satisfies the recurrence

$$P_{n+1}(\Gamma) = \frac{1}{2}\left[1 + f\left(\frac{\Gamma-1}{n}\right)\right] P_n(\Gamma-1) + \frac{1}{2}\left[1 - f\left(\frac{\Gamma+1}{n}\right)\right] P_n(\Gamma+1), \tag{B.3}$$

where $f(z)$ is an arbitrary function that satisfies $f(z) > 0$ for $z > 0$, $f(z) < 0$ for $z < 0$, $f(-z) = -f(z)$, and $|f(z)| \leq 1$. Introducing the probability (B.3) into Eq. (B.1) leads to

$$\phi(n+1,\theta) = \frac{1}{2}\sum_{\gamma} e^{i\theta\gamma}\left\{\left[1 + f\left(\frac{\gamma-1}{n}\right)\right] P_n(\gamma-1) + \left[1 - f\left(\frac{\gamma+1}{n}\right)\right] P_n(\gamma+1)\right\} \tag{B.4}$$

$$= \frac{1}{2}\sum_{\gamma}\left\{e^{i\theta(\gamma+1)}\left[1 + f\left(\frac{\gamma}{n}\right)\right] + e^{i\theta(\gamma-1)}\left[1 - f\left(\frac{\gamma}{n}\right)\right]\right\} P_n(\gamma) \tag{B.5}$$

$$= \sum_{\gamma}\left\{\frac{e^{i\theta} + e^{-i\theta}}{2} + f\left(\frac{\gamma}{n}\right)\frac{e^{i\theta} - e^{-i\theta}}{2}\right\} e^{i\theta\gamma} P_n(\gamma). \tag{B.6}$$

This expression can be simplified taking an explicit definition for the function $f(z) = \beta z$, where β is a polarization parameter. This choice of the function f resembles a biased random walk, which for $\beta = 0$ recovers the standard random walk. Thus, this last expression can be written in terms of trigonometric functions as

$$\boxed{\phi(n+1,\theta) = \cos(\theta)\phi(n,\theta) + \frac{\beta}{n}\sin(\theta)\frac{\partial}{\partial\theta}\phi(n,\theta),} \tag{B.7}$$

where we used the property $\gamma e^{i\gamma\theta} = -i\mathrm{d}e^{i\gamma\theta}/\mathrm{d}\theta$. As a boundary condition, the characteristic function satisfies

$$\phi(1,\theta) = \langle e^{i\theta\Gamma} \rangle_1 = \frac{e^{i\theta} + e^{-i\theta}}{2} = \cos(\theta). \qquad (B.8)$$

Equation (B.7) can be used to obtain a recurrence for the circulation moments and to recover the probability distribution of circulation, which is defined as

$$P_n(\Gamma) = \frac{1}{2\pi} \int_0^{2\pi} \phi(n,\theta) e^{-i\theta\Gamma} \mathrm{d}\theta. \qquad (B.9)$$

Bibliography

[AB18]   A. Alexakis and L. Biferale. Cascades and transitions in turbulent flows. *Physics Reports* **767–769**, 1–101 (2018) (cit. on p. 41).

[AB19]   A. Alexakis and M.-E. Brachet. On the thermal equilibrium state of large-scale flows. *Journal of Fluid Mechanics* **872**, 594–625 (2019) (cit. on p. 140).

[AEBM22]   J. Amette Estrada, M. E. Brachet, and P. D. Mininni. Turbulence in rotating Bose-Einstein condensates. *Physical Review A* **105**, 063321 (2022) (cit. on p. 49).

[AEM⁺95]   M. H. Anderson, J. R. Ensher, M. R. Matthews, C. E. Wieman, and E. A. Cornell. Observation of Bose-Einstein Condensation in a Dilute Atomic Vapor. *Science* **269**, 198–201 (1995) (cit. on pp. 2, 10).

[AH65]   R. J. Arms and F. R. Hama. Localized-Induction Concept on a Curved Vortex and Motion of an Elliptic Vortex Ring. *Physics of Fluids* **8**, 553 (1965) (cit. on p. 29).

[AM38]   J. F. Allen and A. D. Misener. Flow of Liquid Helium II. *Nature* **141**, 75–75 (1938) (cit. on pp. 1, 7, 8).

[AMP⁺20]   G. B. Apolinário, L. Moriconi, R. M. Pereira, and V. J. Valadão. Vortex gas modeling of turbulent circulation statistics. *Physical Review E* **102**, 041102(R) (2020) (cit. on p. 82).

[ATN02]   T. Araki, M. Tsubota, and S. K. Nemirovskii. Energy Spectrum of Superfluid Turbulence with No Normal-Fluid Component. *Physical Review Letters* **89**, 145301 (2002) (cit. on pp. 3, 28, 44).

[BA12]   A. S. Bradley and B. P. Anderson. Energy Spectra of Vortex Distributions in Two-Dimensional Quantum Turbulence. *Physical Review X* **2**, 041001 (2012) (cit. on p. 51).

[Bat00]   G. K. Batchelor. *An Introduction to Fluid Dynamics*. Cambridge Mathematical Library. Cambridge Univ. Press, Cambridge, 1. cambridge mathematical ed., 14. print edition, 2000 (cit. on p. 36).

[BB11]   A. W. Baggaley and C. F. Barenghi. Spectrum of turbulent Kelvin-waves cascade in superfluid helium. *Physical Review B* **83**, 134509 (2011) (cit. on pp. 28, 45).

[BBC⁺06]   D. Bernard, G. Boffetta, A. Celani, and G. Falkovich. Conformal invariance in two-dimensional turbulence. *Nature Physics* **2**, 124–128 (2006) (cit. on p. 43).

[BBP14]   N. G. Berloff, M. Brachet, and N. P. Proukakis. Modeling quantum fluid dynamics at nonzero temperatures. *Proceedings of the National Academy of Sciences of the United States of America* **111**, 4675–4682 (2014) (cit. on p. 27).

[BBS12]   A. W. Baggaley, C. F. Barenghi, and Y. A. Sergeev. Quasiclassical and ultraquantum decay of superfluid turbulence. *Physical Review B* **85**, 060501 (2012) (cit. on pp. 48, 49, 60).

[BBS⁺97]   R. Benzi, L. Biferale, M. V. Struglia, and R. Tripiccione. Self-scaling properties of velocity circulation in shear flows. *Physical Review E* **55**, 3739–3742 (1997) (cit. on p. 81).

[BCF⁺06]   D. I. Bradley, D. O. Clubb, S. N. Fisher, A. M. Guénault, R. P. Haley, C. J. Matthews, G. R. Pickett, V. Tsepelin, and K. Zaki. Decay of Pure Quantum Turbulence in Superfluid He 3 - B. *Physical Review Letters* **96**, 035301 (2006) (cit. on p. 48).

[BCM⁺02]   G. Boffetta, A. Celani, S. Musacchio, and M. Vergassola. Intermittency in two-dimensional Ekman-Navier-Stokes turbulence. *Physical Review E* **66**, 026304 (2002) (cit. on p. 43).

[BCV00]   G. Boffetta, A. Celani, and M. Vergassola. Inverse energy cascade in two-dimensional turbulence: Deviations from Gaussian behavior. *Physical Review E* **61**, R29–R32 (2000) (cit. on p. 43).

[BDL⁺11]   L. Boué, R. Dasgupta, J. Laurie, V. L'vov, S. Nazarenko, and I. Procaccia. Exact solution for the energy spectrum of Kelvin-wave turbulence in superfluids. *Physical Review B* **84**, 064516 (2011) (cit. on pp. 3, 28, 45, 47).

[BDV⁺01]   C. F. Barenghi, R. J. Donnelly, W. F. Vinen, R. Beig, J. Ehlers, U. Frisch, K. Hepp, W. Hillebrand, D. Imboden, R. L. Jaffe, R. Kippenhahn, R. Lipowsky, H. v. Löhneysen, I. Ojima, H. A. Weidenmüller, J. Wess, and J. Zittartz, editors. *Quantized Vortex Dynamics and Superfluid Turbulence*, volume 571 of *Lecture Notes in Physics*. Springer Berlin Heidelberg, Berlin, Heidelberg, 2001 (cit. on p. 28).

[BDZ08]   I. Bloch, J. Dalibard, and W. Zwerger. Many-body physics with ultracold gases. *Reviews of Modern Physics* **80**, 885–964 (2008) (cit. on p. 2).

[BE12]   G. Boffetta and R. E. Ecke. Two-Dimensional Turbulence. *Annual Review of Fluid Mechanics* **44**, 427–451 (2012) (cit. on pp. 41–43, 139, 141, 142, 156).

[Ber00]   D Bernard. Influence of friction on the direct cascade of the 2d forced turbulence. *Europhysics Letters (EPL)* **50**, 333–339 (2000) (cit. on p. 43).

[Ber04]   N. G. Berloff. Padé approximations of solitary wave solutions of the Gross–Pitaevskii equation. *Journal of Physics A: Mathematical and General* **37**, 1617–1632 (2004) (cit. on p. 25).

[Ber99]   D. Bernard. Three-point velocity correlation functions in two-dimensional forced turbulence. *Physical Review E* **60**, 6184–6187 (1999) (cit. on p. 43).

[BK07]   J Bec and K Khanin. Burgers turbulence. *Physics Reports* **447**, 1–66 (2007) (cit. on p. 55).

[BK61]   I. L. Bekarevich and I. M. Khalatnikov. Phenomenological derivation of the equations of vortex motion in He II. *Sov. Phys. JETP* **13**, 643 (1961) (cit. on pp. 3, 31).

[BKL⁺18]   L. Biferale, D. Khomenko, V. L'vov, A. Pomyalov, I. Procaccia, and G. Sahoo. Turbulent statistics and intermittency enhancement in coflowing superfluid He 4. *Physical Review Fluids* **3**, 024605 (2018) (cit. on pp. 31, 32, 44, 123).

[BKL⁺19a] L. Biferale, D. Khomenko, V. L'vov, A. Pomyalov, I. Procaccia, and G. Sahoo. Superfluid Helium in Three-Dimensional Counterflow Differs Strongly from Classical Flows: Anisotropy on Small Scales. *Physical Review Letters* **122**, 144501 (2019) (cit. on pp. 3, 32, 158).

[BKL⁺19b] L. Biferale, D. Khomenko, V. S. L'vov, A. Pomyalov, I. Procaccia, and G. Sahoo. Strong anisotropy of superfluid He 4 counterflow turbulence. *Physical Review B* **100**, 134515 (2019) (cit. on p. 49).

[BL14] A. W. Baggaley and J. Laurie. Kelvin-wave cascade in the vortex filament model. *Physical Review B* **89**, 014504 (2014) (cit. on pp. 28, 30, 33, 45, 47).

[BLB12] A. W. Baggaley, J. Laurie, and C. F. Barenghi. Vortex-Density Fluctuations, Energy Spectra, and Vortical Regions in Superfluid Turbulence. *Physical Review Letters* **109**, 205304 (2012) (cit. on pp. 3, 28, 30, 47–49, 158).

[BLN⁺15] L. Boué, V. S. L'vov, Y. Nagar, S. V. Nazarenko, A. Pomyalov, and I. Procaccia. Energy and vorticity spectra in turbulent superfluid ^{4}He from T=0 to T$_\lambda$. *Physical Review B* **91**, 144501 (2015) (cit. on p. 31).

[BLP⁺13] L. Boué, V. L'vov, A. Pomyalov, and I. Procaccia. Enhancement of Intermittency in Superfluid Turbulence. *Physical Review Letters* **110**, 014502 (2013) (cit. on p. 123).

[BLS06] G. P. Bewley, D. P. Lathrop, and K. R. Sreenivasan. Visualization of quantized vortices. *Nature* **441**, 588–588 (2006) (cit. on pp. 2, 24, 28).

[BM10] G. Boffetta and S. Musacchio. Evidence for the double cascade scenario in two-dimensional turbulence. *Physical Review E* **82**, 016307 (2010) (cit. on p. 43).

[BMV08] G Boffetta, A Mazzino, and A Vulpiani. Twenty-five years of multifractals in fully developed turbulence: a tribute to Giovanni Paladin. *Journal of Physics A: Mathematical and Theoretical* **41**, 363001 (2008) (cit. on pp. 54, 56).

[BN15] M. D. Bustamante and S. Nazarenko. Derivation of the Biot-Savart equation from the nonlinear Schrödinger equation. *Physical Review E* **92**, 053019 (2015) (cit. on p. 29).

[Bog47] N Bogoliubov. On the theory of superfluidity. *Journal of Physics* **11**, 10 (1947) (cit. on p. 15).

[Bol02] S. Boldyrev. Kolmogorov-Burgers Model for Star-forming Turbulence. *The Astrophysical Journal* **569**, 841–845 (2002) (cit. on p. 57).

[Bos24] S. N. Bose. Plancks Gesetz und Lichtquantenhypothese. *Zeitschrift für Physik* **26**, 178–181 (1924) (cit. on pp. 1, 10).

[BPP⁺22] T. Bland, E. Poli, C. Politi, L. Klaus, M. A. Norcia, F. Ferlaino, L. Santos, and R. N. Bisset. Two-Dimensional Supersolid Formation in Dipolar Condensates. *Physical Review Letters* **128**, 195302 (2022) (cit. on p. 157).

[BPP⁺84] R Benzi, G Paladin, G Parisi, and A Vulpiani. On the multifractal nature of fully developed turbulence and chaotic systems. *Journal of Physics A: Mathematical and General* **17**, 3521–3531 (1984) (cit. on pp. 54, 56).

[BPS+08]   G. P. Bewley, M. S. Paoletti, K. R. Sreenivasan, and D. P. Lathrop. Characterization of reconnecting vortices in superfluid helium. *Proceedings of the National Academy of Sciences of the United States of America* **105**, 13707–13710 (2008) (cit. on p. 34).

[BR99]   N. G. Berloff and P. H. Roberts. Motions in a bose condensate: VI. Vortices in a nonlocal model. *Journal of Physics A: Mathematical and General* **32**, 5611–5625 (1999) (cit. on pp. 4, 5, 27, 62, 63, 155).

[BRA+14]   T. P. Billam, M. T. Reeves, B. P. Anderson, and A. S. Bradley. Onsager-Kraichnan Condensation in Decaying Two-Dimensional Quantum Turbulence. *Physical Review Letters* **112**, 145301 (2014) (cit. on pp. 51, 156).

[BSB16]   C. F. Barenghi, Y. A. Sergeev, and A. W. Baggaley. Regimes of turbulence without an energy cascade. *Scientific Reports* **6**, 35701 (2016) (cit. on p. 49).

[BSB+97]   C. F. Barenghi, D. C. Samuels, G. H. Bauer, and R. J. Donnelly. Superfluid vortex lines in a model of turbulent flow. *Physics of Fluids* **9**, 2631–2643 (1997) (cit. on p. 28).

[BSS14]   C. F. Barenghi, L. Skrbek, and K. R. Sreenivasan. Introduction to quantum turbulence. *Proceedings of the National Academy of Sciences* **111**, 4647–4652 (2014) (cit. on pp. 2, 32, 44, 49).

[BSW+19]   F. Böttcher, J.-N. Schmidt, M. Wenzel, J. Hertkorn, M. Guo, T. Langen, and T. Pfau. Transient Supersolid Properties in an Array of Dipolar Quantum Droplets. *Physical Review X* **9**, 011051 (2019) (cit. on pp. 26, 157).

[CC13]   I. Carusotto and C. Ciuti. Quantum fluids of light. *Reviews of Modern Physics* **85**, 299–366 (2013) (cit. on pp. 1, 15).

[CCS96]   N. Cao, S. Chen, and K. R. Sreenivasan. Properties of Velocity Circulation in Three-Dimensional Turbulence. *Physical Review Letters* **76**, 616–619 (1996) (cit. on pp. 58, 80, 81).

[CFF+23]   L. Chomaz, I. Ferrier-Barbut, F. Ferlaino, B. Laburthe-Tolra, B. L. Lev, and T. Pfau. Dipolar physics: a review of experiments with magnetic quantum gases. *Reports on Progress in Physics* **86**, 026401 (2023) (cit. on pp. 26, 28).

[Cha17]   N. Chamel. Superfluidity and Superconductivity in Neutron Stars. *Journal of Astrophysics and Astronomy* **38**, 43 (2017) (cit. on p. 15).

[CMB16]   P. Clark di Leoni, P. D. Mininni, and M. E. Brachet. Helicity, topology, and Kelvin waves in reconnecting quantum knots. *Physical Review A* **94**, 043605 (2016) (cit. on pp. 33, 159).

[CMB17]   P. Clark di Leoni, P. D. Mininni, and M. E. Brachet. Dual cascade and dissipation mechanisms in helical quantum turbulence. *Physical Review A* **95**, 053636 (2017) (cit. on pp. 3, 45–47, 60, 64).

[CPI+19]   L. Chomaz, D. Petter, P. Ilzhöfer, G. Natale, A. Trautmann, C. Politi, G. Durastante, R. M. W. van Bijnen, A. Patscheider, M. Sohmen, M. J. Mark, and F. Ferlaino. Long-Lived and Transient Supersolid Behaviors in Dipolar Quantum Gases. *Physical Review X* **9**, 021012 (2019) (cit. on pp. 26, 157).

[CTS⁺18]   C. R. Cabrera, L. Tanzi, J. Sanz, B. Naylor, P. Thomas, P. Cheiney, and L. Tarruell. Quantum liquid droplets in a mixture of Bose-Einstein condensates. *Science* **359**, 301–304 (2018) (cit. on p. 25).

[CWA⁺17]   A. Cidrim, A. C. White, A. J. Allen, V. S. Bagnato, and C. F. Barenghi. Vinen turbulence via the decay of multicharged vortices in trapped atomic Bose-Einstein condensates. *Physical Review A* **96**, 023617 (2017) (cit. on p. 49).

[Dav13]   P. A. Davidson. *Turbulence in Rotating, Stratified and Electrically Conducting Fluids*. Cambridge University Press, Cambridge, 2013 (cit. on pp. 36, 40–42).

[DB98]   R. J. Donnelly and C. F. Barenghi. The observed properties of liquid helium at the saturated vapor pressure. *Journal of Physical and Chemical Reference Data* **27**, 1217–1274 (1998) (cit. on pp. 8, 10, 61, 155).

[DGP⁺99]   F. Dalfovo, S. Giorgini, L. P. Pitaevskii, and S. Stringari. Theory of Bose-Einstein condensation in trapped gases. *Reviews of Modern Physics* **71**, 463–512 (1999) (cit. on pp. 5, 15, 26).

[DHY10]   H. Deng, H. Haug, and Y. Yamamoto. Exciton-polariton Bose-Einstein condensation. *Reviews of Modern Physics* **82**, 1489–1537 (2010) (cit. on p. 60).

[DMA⁺95]   K. B. Davis, M. O. Mewes, M. R. Andrews, N. J. van Druten, D. S. Durfee, D. M. Kurn, and W. Ketterle. Bose-Einstein Condensation in a Gas of Sodium Atoms. *Physical Review Letters* **75**, 3969–3973 (1995) (cit. on pp. 2, 10).

[DMM22]   S. Das, K. Mukherjee, and S. Majumder. Vortex formation and quantum turbulence with rotating paddle potentials in a two-dimensional binary Bose-Einstein condensate. *Physical Review A* **106**, 023306 (2022) (cit. on p. 51).

[Don91]   R. J. Donnelly. *Quantized Vortices in Helium II*. Cambridge University Press, Cambridge, 1991 (cit. on pp. 1, 3, 8, 24, 28, 31, 43).

[Don93]   R. J. Donnelly. Quantized Vortices and Turbulence in Helium II. *Annual Review of Fluid Mechanics* **25**, 325–371 (1993) (cit. on pp. 29, 43).

[Dub19]   B. Dubrulle. Beyond Kolmogorov cascades. *Journal of Fluid Mechanics* **867**, P1 (2019) (cit. on pp. 2, 5, 39, 40, 156).

[Dub94]   B. Dubrulle. Intermittency in fully developed turbulence: Log-Poisson statistics and generalized scale covariance. *Physical Review Letters* **73**, 959–962 (1994) (cit. on pp. 56, 57).

[Ein25]   A. Einstein. Quantentheorie des idealen einatomigen gases, zweite abhandlung.pdf. *Quantentheorie des idealen einatomigen gases, zweite abhandlung*, 3–14 (1925) (cit. on pp. 1, 10).

[ES06]   G. L. Eyink and K. R. Sreenivasan. Onsager and the theory of hydrodynamic turbulence. *Reviews of Modern Physics* **78**, 87–135 (2006) (cit. on p. 49).

[Fey55]   R. P. Feynman. Application of Quantum Mechanics to Liquid Helium. In C. J. Gorter, editor, *Progress in Low Temperature Physics*. Volume 1, pages 17–53. Elsevier, 1955 (cit. on pp. 2, 24, 33, 43).

[FHG⁺01]   S. N. Fisher, A. J. Hale, A. M. Guénault, and G. R. Pickett. Generation and Detection of Quantum Turbulence in Superfluid H 3 e - B. *Physical Review Letters* **86**, 244–247 (2001) (cit. on p. 44).

[Fjø53]   R. Fjørtoft. On the Changes in the Spectral Distribution of Kinetic Energy for Twodimensional, Nondivergent Flow. *Tellus* **5**, 225–230 (1953) (cit. on p. 42).

[FMO⁺14]   E. Fonda, D. P. Meichle, N. T. Ouellette, S. Hormoz, and D. P. Lathrop. Direct observation of Kelvin waves excited by quantized vortex reconnection. *Proceedings of the National Academy of Sciences* **111**, 4707–4710 (2014) (cit. on pp. 2, 32, 33, 45, 47).

[FPR92]   T. Frisch, Y. Pomeau, and S. Rica. Transition to dissipation in a model of superflow. *Physical Review Letters* **69**, 1644–1647 (1992) (cit. on pp. 6, 28, 144).

[Fri95]   U. Frisch. *Turbulence: The Legacy of A.N. Kolmogorov*. Cambridge University Press, Cambridge, first edition, 1995 (cit. on pp. 2, 36–38, 40, 41, 51, 52, 56–58, 80).

[FSL19]   E. Fonda, K. R. Sreenivasan, and D. P. Lathrop. Reconnection scaling in quantum fluids. *Proceedings of the National Academy of Sciences* **116**, 1924–1928 (2019) (cit. on pp. 24, 34).

[FSN78]   U. Frisch, P.-L. Sulem, and M. Nelkin. A simple dynamical model of intermittent fully developed turbulence. *Journal of Fluid Mechanics* **87**, 719 (1978) (cit. on p. 52).

[FW12]   A. L. Fetter and J. D. Walecka. *Quantum Theory of Many-Particle Systems*. Courier Corporation, 2012 (cit. on p. 15).

[GBB⁺20]   L. Galantucci, A. W. Baggaley, C. F. Barenghi, and G. Krstulovic. A new self-consistent approach of quantum turbulence in superfluid helium. *The European Physical Journal Plus* **135**, 547 (2020) (cit. on p. 30).

[GBP⁺19]   L. Galantucci, A. W. Baggaley, N. G. Parker, and C. F. Barenghi. Crossover from interaction to driven regimes in quantum vortex reconnections. *Proceedings of the National Academy of Sciences* **116**, 12204–12211 (2019) (cit. on pp. 2, 34).

[GCN⁺10]   W. Guo, S. B. Cahn, J. A. Nikkel, W. F. Vinen, and D. N. McKinsey. Visualization Study of Counterflow in Superfluid He 4 using Metastable Helium Molecules. *Physical Review Letters* **105**, 045301 (2010) (cit. on p. 158).

[GGV16]   J. Gao, W. Guo, and W. F. Vinen. Determination of the effective kinematic viscosity for the decay of quasiclassical turbulence in superfluid He 4. *Physical Review B* **94**, 094502 (2016) (cit. on p. 45).

[GK19]   U. Giuriato and G. Krstulovic. Interaction between active particles and quantum vortices leading to Kelvin wave generation. *Scientific Reports* **9**, 4839 (2019) (cit. on pp. 32, 44).

[GK20]   U. Giuriato and G. Krstulovic. Active and finite-size particles in decaying quantum turbulence at low temperature. *Physical Review Fluids* **5**, 054608 (2020) (cit. on p. 33).

[GKB23]   L. Galantucci, G. Krstulovic, and C. F. Barenghi. Friction-enhanced lifetime of bundled quantum vortices. *Physical Review Fluids* **8**, 014702 (2023) (cit. on p. 30).

[GML⁺14] W. Guo, M. L. Mantia, D. P. Lathrop, and S. W. Van Sciver. Visualization of two-fluid flows of superfluid helium-4. *Proceedings of the National Academy of Sciences* **111**, 4653–4658 (2014) (cit. on pp. 3, 24, 44).

[Gro61] E. P. Gross. Structure of a quantized vortex in boson systems. *Il Nuovo Cimento* **20**, 454–477 (1961) (cit. on pp. 3, 15, 24).

[GRS⁺20] A. Gallemí, S. M. Roccuzzo, S. Stringari, and A. Recati. Quantized vortices in dipolar supersolid Bose-Einstein-condensed gases. *Physical Review A* **102**, 023322 (2020) (cit. on pp. 63, 157).

[GRY⁺19] G. Gauthier, M. T. Reeves, X. Yu, A. S. Bradley, M. A. Baker, T. A. Bell, H. Rubinsztein-Dunlop, M. J. Davis, and T. W. Neely. Giant vortex clusters in a two-dimensional quantum fluid. *Science* **364**, 1264–1267 (2019) (cit. on pp. 51, 139).

[GSB15] L. Galantucci, M. Sciacca, and C. F. Barenghi. Coupled normal fluid and superfluid profiles of turbulent helium II in channels. *Physical Review B* **92**, 174530 (2015) (cit. on p. 30).

[GSB17] L. Galantucci, M. Sciacca, and C. F. Barenghi. Large-scale normal fluid circulation in helium superflows. *Physical Review B* **95**, 014509 (2017) (cit. on p. 30).

[GSP⁺16] A. J. Groszek, T. P. Simula, D. M. Paganin, and K. Helmerson. Onsager vortex formation in Bose-Einstein condensates in two-dimensional power-law traps. *Physical Review A* **93**, 043614 (2016) (cit. on p. 51).

[Hal58] H. Hall. An Experimental and theoretical study of torsional oscillations in uniformly rotating liquid helium II. *Proceedings of the Royal Society of London. Series A. Mathematical and Physical Sciences* **245**, 546–561 (1958) (cit. on p. 24).

[HB00] C. Huepe and M.-E. Brachet. Scaling laws for vortical nucleation solutions in a model of superflow. *Physica D: Nonlinear Phenomena* **140**, 126–140 (2000) (cit. on p. 157).

[HB97] C. Huepe and M. Brachet. Solutions de nucleation tourbillonnaires dans un modèle d'écoulement superfluide. *Comptes Rendus de l'Académie des Sciences - Series IIB - Mechanics-Physics-Chemistry-Astronomy* **325**, 195–202 (1997) (cit. on pp. 6, 28, 144).

[Hoh67] P. C. Hohenberg. Existence of Long-Range Order in One and Two Dimensions. *Physical Review* **158**, 383–386 (1967) (cit. on p. 14).

[HP83] H. Hentschel and I. Procaccia. The infinite number of generalized dimensions of fractals and strange attractors. *Physica D: Nonlinear Phenomena* **8**, 435–444 (1983) (cit. on p. 157).

[Hua87] K. Huang. *Statistical Mechanics, 2nd Edition*. 1987 (cit. on p. 10).

[HV56] H. edgar Hall and W. F. Vinen. The rotation of liquid helium II II. The theory of mutual friction in uniformly rotating helium II. *Proceedings of the Royal Society of London. Series A. Mathematical and Physical Sciences* **238**, 215–234 (1956) (cit. on pp. 2, 3, 31, 43).

[IBS21] K. P. Iyer, S. S. Bharadwaj, and K. R. Sreenivasan. The area rule for circulation in three-dimensional turbulence. *Proceedings of the National Academy of Sciences* **118**, e2114679118 (2021) (cit. on p. 82).

[IGK09]   T. Ishihara, T. Gotoh, and Y. Kaneda. Study of High–Reynolds Number Isotropic Turbulence by Direct Numerical Simulation. *Annual Review of Fluid Mechanics* **41**, 165–180 (2009) (cit. on pp. 39, 51, 52).

[IM10]   P. R. Imazio and P. D. Mininni. Cancellation exponents in helical and non-helical flows. *Journal of Fluid Mechanics* **651**, 241–250 (2010) (cit. on pp. 58, 157).

[ISY19]   K. P. Iyer, K. R. Sreenivasan, and P. K. Yeung. Circulation in High Reynolds Number Isotropic Turbulence is a Bifractal. *Physical Review X* **9**, 041006 (2019) (cit. on pp. 81, 82, 84, 85, 99, 100, 155, 157).

[ISY20]   K. P. Iyer, K. R. Sreenivasan, and P. K. Yeung. Scaling exponents saturate in three-dimensional isotropic turbulence. *Physical Review Fluids* **5**, 054605 (2020) (cit. on pp. 52, 57).

[IT21]   S. Inui and M. Tsubota. Coupled dynamics of quantized vortices and normal fluid in superfluid He 4 based on the lattice Boltzmann method. *Physical Review B* **104**, 214503 (2021) (cit. on p. 30).

[IWB+00]   O. C. Idowu, A. Willis, C. F. Barenghi, and D. C. Samuels. Local normal-fluid helium II flow due to mutual friction interaction with the superfluid. *Physical Review B* **62**, 3409–3415 (2000) (cit. on p. 30).

[JGS+19]   S. P. Johnstone, A. J. Groszek, P. T. Starkey, C. J. Billington, T. P. Simula, and K. Helmerson. Evolution of large-scale flow from turbulence in a two-dimensional superfluid. *Science* **364**, 1267–1271 (2019) (cit. on pp. 51, 139).

[Kap38]   P. Kapitza. Viscosity of Liquid Helium below the λ-Point. *Nature* **141**, 74–74 (1938) (cit. on pp. 1, 7).

[KB11]   G. Krstulovic and M. Brachet. Dispersive Bottleneck Delaying Thermalization of Turbulent Bose-Einstein Condensates. *Physical Review Letters* **106**, 115303 (2011) (cit. on pp. 59, 60, 159).

[KBL11]   M. Kursa, K. Bajer, and T. Lipniacki. Cascade of vortex loops initiated by a single reconnection of quantum vortices. *Physical Review B* **83**, 014515 (2011) (cit. on p. 34).

[KBS00]   D. Kivotides, C. F. Barenghi, and D. C. Samuels. Triple Vortex Ring Structure in Superfluid Helium II. *Science* **290**, 777–779 (2000) (cit. on p. 30).

[KG21]   T. Kanai and W. Guo. True Mechanism of Spontaneous Order from Turbulence in Two-Dimensional Superfluid Manifolds. *Physical Review Letters* **127**, 095301 (2021) (cit. on p. 51).

[KHO+06]   M. Kumakura, T. Hirotani, M. Okano, Y. Takahashi, and T. Yabuzaki. Topological formation of a multiply charged vortex in the Rb Bose-Einstein condensate: Effectiveness of the gravity compensation. *Physical Review A* **73**, 063605 (2006) (cit. on p. 25).

[Kiv15]   D. Kivotides. Decay of Finite Temperature Superfluid Helium-4 Turbulence. *Journal of Low Temperature Physics* **181**, 68–76 (2015) (cit. on p. 30).

[KKL+15]   D. Khomenko, L. Kondaurova, V. S. L'vov, P. Mishra, A. Pomyalov, and I. Procaccia. Dynamics of the density of quantized vortex lines in superfluid turbulence. *Physical Review B* **91**, 180504 (2015) (cit. on pp. 28, 29).

[KL93]   J. Koplik and H. Levine. Vortex reconnection in superfluid helium. *Physical Review Letters* **71**, 1375–1378 (1993) (cit. on pp. 28, 33).

[Kol41]   A. N. Kolmogorov. The local structure of turbulence in incompressible viscous fluid for very large Reynolds numbers. *Doklady Akademii Nauk* **30**, 301–305 (1941) (cit. on pp. 2, 38).

[Kol62]   A. N. Kolmogorov. A refinement of previous hypotheses concerning the local structure of turbulence in a viscous incompressible fluid at high Reynolds number. *Journal of Fluid Mechanics* **13**, 82–85 (1962) (cit. on pp. 55, 57).

[Kra67]   R. H. Kraichnan. Inertial Ranges in Two-Dimensional Turbulence. *Physics of Fluids* **10**, 1417 (1967) (cit. on pp. 42, 43, 141).

[Krs12]   G. Krstulovic. Kelvin-wave cascade and dissipation in low-temperature superfluid vortices. *Physical Review E* **86**, 055301(R) (2012) (cit. on pp. 33, 45, 47, 60).

[Krs16]   G. Krstulovic. Grid superfluid turbulence and intermittency at very low temperature. *Physical Review E* **93**, 063104 (2016) (cit. on pp. 83, 123, 158).

[KS09]   E. V. Kozik and B. V. Svistunov. Theory of Decay of Superfluid Turbulence in the Low-Temperature Limit. *Journal of Low Temperature Physics* **156**, 215–267 (2009) (cit. on p. 47).

[KT05]   M. Kobayashi and M. Tsubota. Kolmogorov Spectrum of Superfluid Turbulence: Numerical Analysis of the Gross-Pitaevskii Equation with a Small-Scale Dissipation. *Physical Review Letters* **94**, 065302 (2005) (cit. on pp. 44, 60, 85, 160).

[KVS+01]   D. Kivotides, J. C. Vassilicos, D. C. Samuels, and C. F. Barenghi. Kelvin Waves Cascade in Superfluid Turbulence. *Physical Review Letters* **86**, 3080–3083 (2001) (cit. on pp. 28, 45).

[KVS+02]   D Kivotides, C. J Vassilicos, D. C Samuels, and C. F Barenghi. Velocity spectra of superfluid turbulence. *Europhysics Letters (EPL)* **57**, 845–851 (2002) (cit. on p. 44).

[Lan41]   L. Landau. Theory of the Superfluidity of Helium II. *Physical Review* **60**, 356–358 (1941) (cit. on pp. 1, 8).

[LCL+19]   N. Lundblad, R. A. Carollo, C. Lannert, M. J. Gold, X. Jiang, D. Paseltiner, N. Sergay, and D. C. Aveline. Shell potentials for microgravity Bose–Einstein condensates. *npj Microgravity* **5**, 30 (2019) (cit. on p. 51).

[Leg01]   A. J. Leggett. Bose-Einstein condensation in the alkali gases: Some fundamental concepts. *Reviews of Modern Physics* **73**, 307–356 (2001) (cit. on p. 2).

[Leg04]   A. J. Leggett. Nobel Lecture: Superfluid He 3 : the early days as seen by a theorist. *Reviews of Modern Physics* **76**, 999–1011 (2004) (cit. on pp. 1, 15).

[LHY57]   T. D. Lee, K. Huang, and C. N. Yang. Eigenvalues and Eigenfunctions of a Bose System of Hard Spheres and Its Low-Temperature Properties. *Physical Review* **106**, 1135–1145 (1957) (cit. on pp. 5, 26).

[Lin99]   E. Lindborg. Can the atmospheric kinetic energy spectrum be explained by two-dimensional turbulence? *Journal of Fluid Mechanics* **388**, 259–288 (1999) (cit. on p. 43).

[LL87]   L. D. Landau and E. M. Lifshits. *Fluid Mechanics*, number v. 6 in Course of Theoretical Physics. Pergamon Press, Oxford, England ; New York, 2nd ed., 2nd english ed., rev edition, 1987 (cit. on pp. 1, 31, 143).

[LLN⁺10]   J. Laurie, V. S. L'vov, S. Nazarenko, and O. Rudenko. Interaction of Kelvin waves and nonlocality of energy transfer in superfluids. *Physical Review B* **81**, 104526 (2010) (cit. on p. 47).

[LMDR⁺13]   M. La Mantia, D. Duda, M. Rotter, and L. Skrbek. Lagrangian accelerations of particles in superfluid turbulence. *Journal of Fluid Mechanics* **717**, R9 (2013) (cit. on p. 158).

[LMS14]   M. La Mantia and L. Skrbek. Quantum turbulence visualized by particle dynamics. *Physical Review B* **90**, 014519 (2014) (cit. on p. 44).

[LMS⁺09]   T Lahaye, C Menotti, L Santos, M Lewenstein, and T Pfau. The physics of dipolar bosonic quantum gases. *Reports on Progress in Physics* **72**, 126401 (2009) (cit. on pp. 28, 157).

[LN10]   V. S. L'vov and S. Nazarenko. Spectrum of Kelvin-wave turbulence in superfluids. *JETP Letters* **91**, 428–434 (2010) (cit. on pp. 45, 47, 64).

[LNR07]   V. S. L'vov, S. V. Nazarenko, and O. Rudenko. Bottleneck crossover between classical and quantum superfluid turbulence. *Physical Review B* **76**, 024520 (2007) (cit. on p. 45).

[Lon38]   F. London. On the Bose-Einstein Condensation. *Physical Review* **54**, 947–954 (1938) (cit. on pp. 1, 8, 10).

[LWS⁺01]   M. Leadbeater, T. Winiecki, D. C. Samuels, C. F. Barenghi, and C. S. Adams. Sound Emission due to Superfluid Vortex Reconnections. *Physical Review Letters* **86**, 1410–1413 (2001) (cit. on p. 34).

[Mad26]   E. Madelung. Eine anschauliche Deutung der Gleichung von Schr\"odinger. *Die Naturwissenschaften* **14**, 1004–1004 (1926) (cit. on p. 21).

[MAP08]   P. D. Mininni, A. Alexakis, and A. Pouquet. Nonlocal interactions in hydrodynamic turbulence at high Reynolds numbers: The slow emergence of scaling laws. *Physical Review E* **77**, 036306 (2008) (cit. on pp. 38, 39).

[MBA⁺20]   N. P. Müller, M.-E. Brachet, A. Alexakis, and P. D. Mininni. Abrupt Transition between Three-Dimensional and Two-Dimensional Quantum Turbulence. *Physical Review Letters* **124**, 134501 (2020) (cit. on pp. 51, 139).

[MGG⁺15]   A. Marakov, J. Gao, W. Guo, S. W. Van Sciver, G. G. Ihas, D. N. McKinsey, and W. F. Vinen. Visualization of the normal-fluid turbulence in counterflowing superfluid ^{4}He. *Physical Review B* **91**, 094503 (2015) (cit. on p. 44).

[Mig94]   A. A. Migdal. Loop Equation and Area Law in Turbulence. *International Journal of Modern Physics A* **09**, 1197–1238 (1994) (cit. on p. 81).

[MK20]   N. P. Müller and G. Krstulovic. Kolmogorov and Kelvin wave cascades in a generalized model for quantum turbulence. *Physical Review B* **102**, 134513 (2020) (cit. on pp. ix, 5, 27, 28, 33, 46, 47, 59, 61, 63, 100, 155, 159).

[MK22]   N. P. Müller and G. Krstulovic. Critical velocity for vortex nucleation and roton emission in a generalized model for superfluids. *Physical Review B* **105**, 014515 (2022) (cit. on pp. ix, 6, 10, 27, 28, 143, 157).

[MKD⁺21]   T. Mithun, K. Kasamatsu, B. Dey, and P. G. Kevrekidis. Decay of two-dimensional quantum turbulence in binary Bose-Einstein condensates. *Physical Review A* **103**, 023301 (2021) (cit. on p. 51).

[MMC⁺21]   Á. V. M. Marino, L. Madeira, A. Cidrim, F. E. A. dos Santos, and V. S. Bagnato. Momentum distribution of Vinen turbulence in trapped atomic Bose–Einstein condensates. *The European Physical Journal Special Topics* **230**, 809–812 (2021) (cit. on p. 49).

[MP13]   P. D. Mininni and A. Pouquet. Inverse cascade behavior in freely decaying two-dimensional fluid turbulence. *Physical Review E* **87**, 033002 (2013) (cit. on p. 43).

[MPK21]   N. P. Müller, J. I. Polanco, and G. Krstulovic. Intermittency of Velocity Circulation in Quantum Turbulence. *Physical Review X* **11**, 011053 (2021) (cit. on pp. ix, 5, 27, 28, 45, 61, 79, 99–101, 121, 155, 156, 159).

[MPV22]   L. Moriconi, R. M. Pereira, and V. J. Valadão. Circulation statistics and the mutually excluding behavior of turbulent vortex structures. *Physical Review E* **106**, L023101 (2022) (cit. on p. 82).

[MS87]   C. Meneveau and K. R. Sreenivasan. Simple multifractal cascade model for fully developed turbulence. *Physical Review Letters* **59**, 1424–1427 (1987) (cit. on p. 57).

[MT83]   K. P. Martin and J. T. Tough. Evolution of superfluid turbulence in thermal counterflow. *Physical Review B* **27**, 2788–2799 (1983) (cit. on p. 30).

[MT98]   J Maurer and P Tabeling. Local investigation of superfluid turbulence. *Europhysics Letters (EPL)* **43**, 29–34 (1998) (cit. on pp. 2, 44, 84, 122, 123).

[MTG⁺22]   N. P. Müller, Y. Tang, W. Guo, and G. Krstulovic. Velocity circulation intermittency in finite-temperature turbulent superfluid helium. *Physical Review Fluids* **7**, 15 (2022) (cit. on pp. ix, 5, 79, 155, 156).

[MW66]   N. D. Mermin and H. Wagner. Absence of Ferromagnetism or Antiferromagnetism in One- or Two-Dimensional Isotropic Heisenberg Models. *Physical Review Letters* **17**, 1133–1136 (1966) (cit. on p. 14).

[MYL81]   A. S. Monin, A. M. Yaglom, and J. L. Lumley. *Statistical Fluid Mechanics: Mechanics of Turbulence. Bd. 2: Statistical Fluid Mechanics: Mechanics of Turbulence*. MIT Press, Cambridge, 2. aufl edition, 1981 (cit. on pp. 2, 36, 38).

[MZ68]   J. B. Mehl and W. Zimmermann. Flow of Superfluid Helium in a Porous Medium. *Physical Review* **167**, 214–229 (1968) (cit. on pp. 1, 8).

[NAB97a]   C. Nore, M. Abid, and M. E. Brachet. Decaying Kolmogorov turbulence in a model of superflow. *Physics of Fluids* **9**, 2644–2669 (1997) (cit. on pp. 2, 18, 60, 159).

[NAB97b]   C. Nore, M. Abid, and M. E. Brachet. Kolmogorov Turbulence in Low-Temperature Superflows. *Physical Review Letters* **78**, 3896–3899 (1997) (cit. on pp. 44, 45, 85).

[Naz11]   S. Nazarenko. *Wave Turbulence*, number 825 in Lecture Notes in Physics. Springer, Heidelberg, 2011 (cit. on pp. 33, 45, 46, 61).

[Nem13]   S. K. Nemirovskii. Quantum turbulence: Theoretical and numerical problems. *Physics Reports* **524**, 85–202 (2013) (cit. on pp. 28, 34).

[NEZ⁺19]   N. Navon, C. Eigen, J. Zhang, R. Lopes, A. L. Gaunt, K. Fujimoto, M. Tsubota, R. P. Smith, and Z. Hadzibabic. Synthetic dissipation and cascade fluxes in a turbulent quantum gas. *Science* **366**, 382–385 (2019) (cit. on p. 61).

[NGS⁺16]   N. Navon, A. L. Gaunt, R. P. Smith, and Z. Hadzibabic. Emergence of a turbulent cascade in a quantum gas. *Nature* **539**, 72–75 (2016) (cit. on p. 61).

[NOA⁺00]   K. Nam, E. Ott, T. M. Antonsen, and P. N. Guzdar. Lagrangian Chaos and the Effect of Drag on the Enstrophy Cascade in Two-Dimensional Turbulence. *Physical Review Letters* **84**, 5134–5137 (2000) (cit. on p. 43).

[Obo62]   A. M. Oboukhov. Some specific features of atmospheric tubulence. *Journal of Fluid Mechanics* **13**, 77–81 (1962) (cit. on pp. 55, 57).

[ODS⁺92]   E. Ott, Y. Du, K. R. Sreenivasan, A. Juneja, and A. K. Suri. Sign-singular measures: Fast magnetic dynamos, and high-Reynolds-number fluid turbulence. *Physical Review Letters* **69**, 2654–2657 (1992) (cit. on pp. 58, 80, 157).

[Onn08]   H. K. Onnes. The Condensation of Helium. *Nature* **77**, 581–581 (1908) (cit. on pp. 1, 7).

[Ons49]   L. Onsager. Statistical hydrodynamics. **6**, 279–287 (1949) (cit. on pp. 2, 23, 49).

[PA85]   D. Pines and M. A. Alpar. Superfluidity in neutron stars. *Nature* **316**, 27–32 (1985) (cit. on p. 1).

[PB11]   R. K. Pathria and P. D. Beale. *Statistical Mechanics*. Elsevier/Academic Press, Amsterdam ; Boston, 3rd ed edition, 2011 (cit. on p. 10).

[PBS⁺05]   D. R. Poole, C. F. Barenghi, Y. A. Sergeev, and W. F. Vinen. Motion of tracer particles in He II. *Physical Review B* **71**, 064514 (2005) (cit. on p. 44).

[PCM⁺22]   R. Panico, P. Comaron, M. Matuszewski, A. S. Lanotte, D. Trypogeorgos, G. Gigli, M. De Giorgi, V. Ardizzone, D. Sanvitto, and D. Ballarini. Onset of vortex clustering and inverse energy cascade in dissipative quantum fluids. *arXiv:2205.02925 [cond-mat]* (2022). arXiv: 2205.02925 [cond-mat] (cit. on p. 51).

[Pet15]   D. S. Petrov. Quantum Mechanical Stabilization of a Collapsing Bose-Bose Mixture. *Physical Review Letters* **115**, 155302 (2015) (cit. on p. 25).

[PFL10]   M. Paoletti, M. E. Fisher, and D. Lathrop. Reconnection dynamics for quantized vortices. *Physica D: Nonlinear Phenomena* **239**, 1367–1377 (2010) (cit. on p. 34).

[PFS⁺08]   M. S. Paoletti, M. E. Fisher, K. R. Sreenivasan, and D. P. Lathrop. Velocity Statistics Distinguish Quantum Turbulence from Classical Turbulence. *Physical Review Letters* **101**, 154501 (2008) (cit. on pp. 34, 44).

[Pit61]   L. P. Pitaevskii. Vortex lines in an imperfect Bose gas. *Sovietic Physics JETP* (1961) (cit. on pp. 3, 15, 24).

[PJ08]   N. P. Proukakis and B. Jackson. Finite-temperature models of Bose–Einstein condensation. *Journal of Physics B: Atomic, Molecular and Optical Physics* **41**, 203002 (2008) (cit. on p. 15).

[PK20a]   J. I. Polanco and G. Krstulovic. Counterflow-Induced Inverse Energy Cascade in Three-Dimensional Superfluid Turbulence. *Physical Review Letters* **125**, 254504 (2020) (cit. on pp. 3, 32, 49, 158).

[PK20b]   J. I. Polanco and G. Krstulovic. Inhomogeneous distribution of particles in coflow and counterflow quantum turbulence. *Physical Review Fluids* **5**, 032601(R) (2020) (cit. on p. 31).

[PK20c]   D. Proment and G. Krstulovic. Matching theory to characterize sound emission during vortex reconnection in quantum fluids. *Physical Review Fluids* **5**, 104701 (2020) (cit. on pp. 33, 34).

[PL11]   M. S. Paoletti and D. P. Lathrop. Quantum Turbulence. *Annual Review of Condensed Matter Physics* **2**, 213–234 (2011) (cit. on p. 34).

[PMD+21] R. Panico, G. Macorini, L. Dominici, A. Gianfrate, A. Fieramosca, M. De Giorgi, G. Gigli, D. Sanvitto, A. S. Lanotte, and D. Ballarini. Dynamics of a Vortex Lattice in an Expanding Polariton Quantum Fluid. *Physical Review Letters* **127**, 047401 (2021) (cit. on pp. 51, 60).

[PMK21]   J. I. Polanco, N. P. Müller, and G. Krstulovic. Vortex clustering, polarisation and circulation intermittency in classical and quantum turbulence. *Nature Communications* **12**, 7090 (2021) (cit. on pp. ix, 5, 27, 28, 61, 79, 82, 101, 121, 155, 156, 159).

[PNO12]   D. Proment, S. Nazarenko, and M. Onorato. Sustained turbulence in the three-dimensional Gross–Pitaevskii model. *Physica D: Nonlinear Phenomena* **241**, 304–314 (2012) (cit. on pp. 60, 160).

[Pop00]   S. B. Pope. *Turbulent Flows*. Cambridge University Press, Cambridge ; New York, 2000 (cit. on pp. 36–38, 40).

[PR93]   Y. Pomeau and S. Rica. Model of superflow with rotons. *Physical Review Letters* **71**, 247–250 (1993) (cit. on pp. 4, 62).

[PS08]   C. Pethick and H. Smith. *Bose-Einstein Condensation in Dilute Gases*. Cambridge University Press, Cambridge ; New York, 2nd ed edition, 2008 (cit. on pp. 1, 15, 25, 26, 143).

[PS16]   L. P. Pitaevskii and S. Stringari. *Bose-Einstein Condensation and Superfluidity*, volume 164. Oxford University Press, Oxford, 2016 (cit. on pp. 1, 10, 15, 25, 143).

[PT98]   J. Paret and P. Tabeling. Intermittency in the two-dimensional inverse cascade of energy: Experimental observations. *Physics of Fluids* **10**, 3126–3136 (1998) (cit. on p. 43).

[RBA+13] M. T. Reeves, T. P. Billam, B. P. Anderson, and A. S. Bradley. Inverse Energy Cascade in Forced Two-Dimensional Quantum Turbulence. *Physical Review Letters* **110**, 104501 (2013) (cit. on pp. 51, 60, 160).

[RBD+14] B. Rousset, P. Bonnay, P. Diribarne, A. Girard, J. M. Poncet, E. Herbert, J. Salort, C. Baudet, B. Castaing, L. Chevillard, F. Daviaud, B. Dubrulle, Y. Gagne, M. Gibert, B. Hébral, T. Lehner, P.-E. Roche, B. Saint-Michel, and M. Bon Mardion. Superfluid high REynolds von Kármán experiment. *Review of Scientific Instruments* **85**, 103908 (2014) (cit. on pp. 3, 15).

[RBL09]   P.-E. Roche, C. F. Barenghi, and E. Leveque. Quantum turbulence at finite temperature: The two-fluids cascade. *EPL (Europhysics Letters)* **87**, 54006 (2009) (cit. on pp. 32, 44).

[RBY+17]   M. T. Reeves, T. P. Billam, X. Yu, and A. S. Bradley. Enstrophy Cascade in Decaying Two-Dimensional Quantum Turbulence. *Physical Review Letters* **119**, 184502 (2017) (cit. on pp. 51, 156).

[RCS+17]   E. Rusaouen, B. Chabaud, J. Salort, and P.-E. Roche. Intermittency of quantum turbulence with superfluid fractions from 0% to 96%. *Physics of Fluids* **29**, 105108 (2017) (cit. on pp. 6, 84, 122, 123).

[Ric01]   S. Rica. A remark on the critical speed for vortex nucleation in the nonlinear Schrödinger equation. *Physica D: Nonlinear Phenomena* **148**, 221–226 (2001) (cit. on p. 28).

[RKO+99]   C. Raman, M. Köhl, R. Onofrio, D. S. Durfee, C. E. Kuklewicz, Z. Hadzibabic, and W. Ketterle. Evidence for a Critical Velocity in a Bose-Einstein Condensed Gas. *Physical Review Letters* **83**, 2502–2505 (1999) (cit. on p. 144).

[Rob03]   P. H. Roberts. On vortex waves in compressible fluids. II. The condensate vortex. *Proceedings of the Royal Society of London. Series A: Mathematical, Physical and Engineering Sciences* **459**, 597–607 (2003) (cit. on p. 33).

[RS39]   B. Rollin and F. Simon. On the "film" phenomenon of liquid helium II. *Physica* **6**, 219–230 (1939) (cit. on pp. 1, 8).

[RSB99]   R. L. Ricca, D. C. Samuels, and C. F. Barenghi. Evolution of vortex knots. *Journal of Fluid Mechanics* **391**, 29–44 (1999) (cit. on p. 28).

[RSC18]   J. Reneuve, J. Salort, and L. Chevillard. Structure, dynamics, and reconnection of vortices in a nonlocal model of superfluids. *Physical Review Fluids* **3**, 114602 (2018) (cit. on pp. 4, 5, 27, 61–63, 155).

[SA16]   A. Skaugen and L. Angheluta. Vortex clustering and universal scaling laws in two-dimensional quantum turbulence. *Physical Review E* **93**, 032106 (2016) (cit. on p. 51).

[Sal18]   L. Salasnich. Self-Consistent Derivation of the Modified Gross-Pitaevskii Equation with Lee-Huang-Yang Correction. *Applied Sciences* **8**, 1998 (2018) (cit. on p. 26).

[Sch85]   K. W. Schwarz. Three-dimensional vortex dynamics in superfluid He 4 : Line-line and line-boundary interactions. *Physical Review B* **31**, 5782–5804 (1985) (cit. on pp. 3, 28).

[Sch88]   K. W. Schwarz. Three-dimensional vortex dynamics in superfluid ^{4}He: Homogeneous superfluid turbulence. *Physical Review B* **38**, 2398–2417 (1988) (cit. on pp. 3, 28, 44).

[SD90]   D. C. Samuels and R. J. Donnelly. Dynamics of the interactions of rotons with quantized vortices in helium II. *Physical Review Letters* **65**, 187–190 (1990) (cit. on p. 30).

[SFM+18]   G. Semeghini, G. Ferioli, L. Masi, C. Mazzinghi, L. Wolswijk, F. Minardi, M. Modugno, G. Modugno, M. Inguscio, and M. Fattori. Self-Bound Quantum Droplets of Atomic Mixtures in Free Space. *Physical Review Letters* **120**, 235301 (2018) (cit. on p. 25).

[SGI+17]   S. Serafini, L. Galantucci, E. Iseni, T. Bienaimé, R. N. Bisset, C. F. Barenghi, F. Dalfovo, G. Lamporesi, and G. Ferrari. Vortex Reconnections and Rebounds in Trapped Atomic Bose-Einstein Condensates. *Physical Review X* **7**, 021031 (2017) (cit. on pp. 28, 34).

[SJS95]　K. R. Sreenivasan, A. Juneja, and A. K. Suri. Scaling Properties of Circulation in Moderate-Reynolds-Number Turbulent Wakes. *Physical Review Letters* **75**, 433–436 (1995) (cit. on pp. 58, 81).

[SL94]　Z.-S. She and E. Lévêque. Universal scaling laws in fully developed turbulence. *Physical Review Letters* **72**, 336–339 (1994) (cit. on p. 56).

[ŠLM19]　P. Švančara and M. La Mantia. Flight-crash events in superfluid turbulence. *Journal of Fluid Mechanics* **876**, R2 (2019) (cit. on p. 34).

[SLN22]　J. Skipp, J. Laurie, and S. Nazarenko. Hamiltonian derivation of the point vortex model from the two-dimensional nonlinear Schr\"odinger equation, 2022. arXiv: `2208.10412 [cond-mat, physics:math-ph, physics:nlin, physics:physics]` (cit. on p. 50).

[SMK+19]　V. Shukla, P. D. Mininni, G. Krstulovic, P. C. Di Leoni, and M. E. Brachet. Quantitative estimation of effective viscosity in quantum turbulence. *Physical Review A* **99**, 043605 (2019) (cit. on pp. 46, 64).

[SND00]　L. Skrbek, J. J. Niemela, and R. J. Donnelly. Four Regimes of Decaying Grid Turbulence in a Finite Channel. *Physical Review Letters* **85**, 2973–2976 (2000) (cit. on p. 48).

[SP16]　V. Shukla and R. Pandit. Multiscaling in superfluid turbulence: A shell-model study. *Physical Review E* **94**, 043101 (2016) (cit. on p. 123).

[Sre95]　K. R. Sreenivasan. On the universality of the Kolmogorov constant. *Physics of Fluids* **7**, 2778–2784 (1995) (cit. on p. 39).

[SRL11]　J. Salort, P.-E. Roche, and E. Leveque. Mesoscale equipartition of kinetic energy in quantum turbulence. *EPL (Europhysics Letters)* **94**, 24001 (2011) (cit. on p. 122).

[SS04]　C. Sulem and P.-L. Sulem, editors. *The Nonlinear Schrödinger Equation: Self-Focusing and Wave Collapse*, volume 139 of *Applied Mathematical Sciences*. Springer New York, New York, NY, 2004 (cit. on pp. 18, 20).

[SS95]　K. R. Sreenivasan and G. Stolovitzky. Turbulent cascades. *Journal of Statistical Physics* **78**, 311–333 (1995) (cit. on p. 57).

[SSD99]　S. R. Stalp, L. Skrbek, and R. J. Donnelly. Decay of grid turbulence in a finite channel. *Physical Review Letters* **82**, 4831–4834 (1999) (cit. on pp. 31, 48).

[SSL03]　L. Santos, G. V. Shlyapnikov, and M. Lewenstein. Roton-Maxon Spectrum and Stability of Trapped Dipolar Bose-Einstein Condensates. *Physical Review Letters* **90**, 250403 (2003) (cit. on pp. 28, 61).

[SW95]　Z.-S. She and E. C. Waymire. Quantized Energy Cascade and Log-Poisson Statistics in Fully Developed Turbulence. *Physical Review Letters* **74**, 262–265 (1995) (cit. on p. 57).

[Tab02]　P Tabeling. Two-dimensional turbulence: a physicist approach. *Physics Reports* **362**, 1–62 (2002) (cit. on pp. 42, 43).

[TAD+20]　S. L. Tang, R. A. Antonia, L. Djenidi, and Y. Zhou. Scaling of the turbulent energy dissipation correlation function. *Journal of Fluid Mechanics* **891**, A26 (2020) (cit. on p. 57).

[TH09]　M. Tsubota and W. P. Halperin. *Progress in Low Temperature Physics: Quantum Turbulence*. Elsevier, Amsterdam, 2009 (cit. on pp. 44, 48).

[Tho80]   W. Thomson. XXIV. *Vibrations of a columnar vortex*. *The London, Edinburgh, and Dublin Philosophical Magazine and Journal of Science* **10**, 155–168 (1880) (cit. on p. 32).

[Tis38]   L. Tisza. Transport Phenomena in Helium II. *Nature* **141**, 913–913 (1938) (cit. on pp. 1, 8).

[TL72]   H. Tennekes and J. L. Lumley. *A First Course in Turbulence*. MIT Press, 1972 (cit. on p. 40).

[TLF+19]   L. Tanzi, E. Lucioni, F. Famà, J. Catani, A. Fioretti, C. Gabbanini, R. N. Bisset, L. Santos, and G. Modugno. Observation of a Dipolar Quantum Gas with Metastable Supersolid Properties. *Physical Review Letters* **122**, 130405 (2019) (cit. on pp. 26, 157).

[Tsu09]   M. Tsubota. Quantum turbulence—from superfluid helium to atomic Bose–Einstein condensates. *Journal of Physics: Condensed Matter* **21**, 164207 (2009) (cit. on pp. 48, 60, 160).

[TTC+16]   M. C. Tsatsos, P. E. Tavares, A. Cidrim, A. R. Fritsch, M. A. Caracanhas, F. E. A. dos Santos, C. F. Barenghi, and V. S. Bagnato. Quantum turbulence in trapped atomic Bose–Einstein condensates. *Physics Reports* **622**, 1–52 (2016) (cit. on pp. 2, 15, 44).

[TTF+22]   G. D. Telles, P. E. S. Tavares, A. R. Fritsch, A Cidrim, and V. S. Bagnato. Dynamical evolution and decay of multi-charged quantum vortex in a Bose–Einstein condensate. *Laser Physics Letters* **19**, 015501 (2022) (cit. on p. 25).

[Ume93]   M. Umeki. Probability distribution of velocity circulation in three-dimensional turbulence. *Journal of the Physical Society of Japan* **62**, 3788–3791 (1993) (cit. on p. 81).

[Vas15]   J. C. Vassilicos. Dissipation in Turbulent Flows. *Annual Review of Fluid Mechanics* **47**, 95–114 (2015) (cit. on pp. 2, 39).

[VCC12]   S. Villerot, B. Castaing, and L. Chevillard. Static Spectroscopy of a Dense Superfluid. *Journal of Low Temperature Physics* **169**, 1–14 (2012) (cit. on pp. 61, 62).

[VGG+18]   E. Varga, J. Gao, W. Guo, and L. Skrbek. Intermittency enhancement in quantum turbulence in superfluid He 4. *Physical Review Fluids* **3**, 094601 (2018) (cit. on p. 123).

[Vin57]   W. F. Vinen. Mutual friction in a heat current in liquid helium II III. Theory of the mutual friction. *Proceedings of the Royal Society of London. Series A. Mathematical and Physical Sciences* **242**, 493–515 (1957) (cit. on pp. 47–49).

[Vin61]   W. F. Vinen. The detection of single quanta of circulation in liquid helium II. *Proceedings of the Royal Society of London. Series A. Mathematical and Physical Sciences* **260**, 218–236 (1961) (cit. on p. 24).

[VN02]   W. F. Vinen and J. J. Niemela. Quantum Turbulence. *Journal of Low Temperature Physics* **128**, 167–231 (2002) (cit. on pp. 2, 3, 34, 48).

[VPK16]   A. Villois, D. Proment, and G. Krstulovic. Evolution of a superfluid vortex filament tangle driven by the Gross-Pitaevskii equation. *Physical Review E* **93**, 061103 (2016) (cit. on pp. 45, 49, 157).

[VPK17]   A. Villois, D. Proment, and G. Krstulovic. Universal and nonuniversal aspects of vortex reconnections in superfluids. *Physical Review Fluids* **2**, 044701 (2017) (cit. on p. 28).

[VPK20]   A. Villois, D. Proment, and G. Krstulovic. Irreversible dynamics of vortex reconnections in quantum fluids. *Physical Review Letters* **125**, 164501 (2020) (cit. on pp. 28, 32, 34, 45).

[VS18]   A. Villois and H. Salman. Vortex nucleation limited mobility of free electron bubbles in the Gross-Pitaevskii model of a superfluid. *Physical Review B* **97**, 094507 (2018) (cit. on p. 28).

[WG08]   P. M. Walmsley and A. I. Golov. Quantum and Quasiclassical Types of Superfluid Turbulence. *Physical Review Letters* **100**, 245301 (2008) (cit. on pp. 47–49, 60, 157).

[WGH⁺07]   P. M. Walmsley, A. I. Golov, H. E. Hall, A. A. Levchenko, and W. F. Vinen. Dissipation of Quantum Turbulence in the Zero Temperature Limit. *Physical Review Letters* **99**, 265302 (2007) (cit. on p. 44).

[WP74]   G. A. Williams and R. E. Packard. Photographs of Quantized Vortex Lines in Rotating He II. *Physical Review Letters* **33**, 280–283 (1974) (cit. on pp. 2, 24).

[Yak01]   V. Yakhot. Mean-field approximation and a small parameter in turbulence theory. *Physical Review E* **63**, 026307 (2001) (cit. on p. 57).

[YGP79]   E. J. Yarmchuk, M. J. V. Gordon, and R. E. Packard. Observation of Stationary Vortex Arrays in Rotating Superfluid Helium. *Physical Review Letters* **43**, 214–217 (1979) (cit. on p. 24).

[YKT⁺20]   S. Yui, H. Kobayashi, M. Tsubota, and W. Guo. Fully Coupled Two-Fluid Dynamics in Superfluid He 4 : Anomalous Anisotropic Velocity Fluctuations in Counterflow. *Physical Review Letters* **124**, 155301 (2020) (cit. on p. 30).

[YR17]   R. M. B. Young and P. L. Read. Forward and inverse kinetic energy cascades in Jupiter's turbulent weather layer. *Nature Physics* **13**, 1135–1140 (2017) (cit. on p. 50).

[YTK18]   S. Yui, M. Tsubota, and H. Kobayashi. Three-Dimensional Coupled Dynamics of the Two-Fluid Model in Superfluid He 4 : Deformed Velocity Profile of Normal Fluid in Thermal Counterflow. *Physical Review Letters* **120**, 155301 (2018) (cit. on p. 30).

[ZCB⁺12]   S. Zuccher, M. Caliari, A. W. Baggaley, and C. F. Barenghi. Quantum vortex reconnections. *Physics of Fluids* **24**, 125108 (2012) (cit. on pp. 2, 28, 34).

[ZNG99]   E. Zaremba, T. Nikuni, and A. Griffin. Dynamics of Trapped Bose Gases at Finite Temperatures. *Journal of Low Temperature Physics* **116**, 277–345 (1999) (cit. on pp. 60, 160).

[ZSX08]   Q. Zhou, C. Sun, and K.-Q. Xia. Experimental investigation of homogeneity, isotropy, and circulation of the velocity field in buoyancy-driven turbulence. *Journal of Fluid Mechanics* **598**, 361–372 (2008) (cit. on p. 81).

[ZSY19]   X. M. Zhai, K. R. Sreenivasan, and P. K. Yeung. Cancellation exponents in isotropic turbulence and magnetohydrodynamic turbulence. *Physical Review E* **99**, 023102 (2019) (cit. on pp. 58, 80, 157).